Citation: Benson, C. E. (2022). Investigating Rho dysregulation in Adams-Oliver syndrome as a model of vascular development. (Unpublished Doctoral thesis, St George's, University of London)

Investigating Rho dysregulation in Adams-Oliver syndrome as a model of vascular development

Clare Elizabeth Benson

Institute of Molecular and Clinical Sciences
St. George’s, University of London

A thesis submitted for the degree of Doctor of Philosophy
June 2022

Declaration

I, Clare Benson, declare that the work presented in this thesis is my own. Any contributions from collaborators or where information has been derived from other sources is explicitly referenced in the text.

Signed: [redacted]

Pandemic impact statement

Owing to the Covid-19 pandemic, approximately 7 months of working time were lost, although over this time I was able to publish a literature review, “The DOCK protein family in vascular development and disease” (Benson and Southgate, 2021). The time lost includes the months spent in isolation from March 2020-July 2020 when the university labs were closed, the experiments I'd been developing over January and February 2020 which needed to be restarted post-lockdown and the time taken for the zebrafish to start producing embryos again post-lockdown for my experiments. Additional disruption was caused by three separate Covid isolation periods throughout 2021, amounting to around 30 days of experimental time lost and restarting numerous experiments which were ongoing when the isolation periods began.

Abstract

Adams-Oliver syndrome (AOS) is a rare developmental disorder, predominantly characterised by scalp and limb anomalies. A wide range of additional clinical features, including neurological, vascular and/or cardiac defects, are observed. Of the six known causal genes, *ARHGAP31* and *DOCK6* encode Rho GTPase regulators for Cdc42 and Rac1 activity. Nonetheless, the molecular mechanisms underlying Cdc42/Rac1 dysregulation in AOS remain largely unexplored.

AOS is hypothesised to be a disorder of vasculogenesis, therefore I sought to model ARHGAP31 and DOCK6 dysfunction using zebrafish to examine the mechanisms underlying perturbed vascularisation. Normal *dock6* and *arhgap31* expression during embryogenesis were characterised using quantitative PCR, whole-mount *in situ* hybridisation and a novel *dock6* transgenic line. Vascular development in morpholino- and CRISPR-mediated disease models was quantified using microangiography and a tg(*fli1*:EGFP) transgenic zebrafish line. To investigate the cellular mechanisms underpinning vascular defects in AOS, siRNA-mediated *DOCK6* knockdown was evaluated in human vascular smooth muscle and epidermal keratinocyte cell lines.

Expression of *arhgap31* and *dock6* localised to some vascular and neural crest-derived structures throughout embryogenesis. Gene knockdown promoted cardiovascular and neural crest-related defects. Reduced *arhgap31* expression impaired enlargement of the brain ventricles and increased Notch signalling, indicating a potential novel overlap between the Rho and Notch pathways in AOS. Both disease models exhibited impaired intersegmental vessel (ISV) and optic vessel sprouting, asymmetric and truncated ISVs. Vessel leakage and limited vessel perfusion implied a critical role for *arhgap31* and *dock6* during zebrafish vascularisation. In human cell lines, *DOCK6* knockdown disrupted cell adhesion and phalloidin staining revealed defective cytoskeletal, lamellipodia and filopodia formation.

Together, this work suggests a model of impaired cell adhesion impeding normal vascular development in AOS, with a potential origin in the neural crest. These novel findings confirm vascular disruption as a key factor in AOS pathogenesis, advancing our understanding of the mechanisms underpinning this debilitating disorder.

Table of contents

Table of Tables

Table of Movies

Table of Figures

Abbreviations

µg	Microgram
µM	Micromole
AA	Aortic arches
ACC	Aplasia cutis congenita
ACeV	Anterior cerebral vein
actb2	actin beta 2
ADAM	A disintegrin and metalloproteinase
A-E2	arhgap31-E2
A-E3	arhgap31-E3
AKT	RAC-alpha serine/threonine-protein kinase
ALM	Anterior lateral plate mesoderm
ARHGAP31	Rho GTPase Activating Protein 31
ARP2/3	Actin Related Protein 2/3 complex
ASPA	Animals (Scientific Procedures) Act 1986
BMP	Bone morphogenetic protein
bp	Base pair
BRAF	Serine/threonine-protein kinase B-Raf
CA	Caudal aorta
CaV	Cardinal vein
CCtA	Cerebellar central arteries
CDC42	Cell Division Cycle 42
CDGAP	Cdc42 GTPase activating protein
cDNA	Complementary DNA
CMTC	Cutis marmorata telangiectatica congenita
CNC	Cranial neural crest
CNS	Central nervous system
CRISPR	Clustered regularly interspaced short palindromic repeats
crRNA	Crispr RNA
CSF	Cerebrospinal fluid
CSL	CBF1, Suppressor of Hairless, Lag-1
CV	Caudal vein
CVP	Caudal vein plexus
DA	Dorsal aorta
DCV	Dorsal ciliary vein
D-E1	Dock6-E1
D-E2	Dock6-E2
DHH	Desert hedgehog
DHR	Dock homology region
DLAV	Dorsal longitudinal anastomotic vessels
DLL4	Delta-like ligand 4
DLV	Dorsal lateral vein
DNA	deoxyribonucleic acid
DOCK6	Dedicator of cytokinesis 6

Dpf	Days post fertilisation
DSL	Delta/Serrate/lag-2
EC	Endothelial cell
ECM	Extracellular matrix
EDTA	Ethylenediaminetetraacetic acid
Eef1a1	Eukaryotic Translation Elongation Factor 1 Alpha 1
EOGT	EGF domain-specific O-linked N-acetylglucosamine transferase
ERK	Extracellular signal-regulated kinase
ETS	E26 transformation-specific
ETSRP	ETS1-related protein
FB	Forebrain
FGF	Fibroblast growth factor
FGFR	FGF receptor
Fli1	Friend leukemia integration 1
FLT1	Fms Related Receptor Tyrosine Kinase 1
GAP	GTPase activating protein
GAPDH	Glyceraldehyde-3-Phosphate Dehydrogenase
GDI	Guanine dissociation inhibitor
GEF	Guanine exchange factor
GFP	Green fluorescent protein
gRNA	Guide RNA
GSK-3	Glycogen synthase kinase 3
HaCat	Human adult keratinocyte
HB	Hindbrain
HH	Hedgehog
Hpf	Hours post fertilisation
Hr	Hour
HUVEC	Human umbilical vein endothelial cell
IHH	Indian hedgehog
iPSC	Induced pluripotent stem cell
ISG15	Interferon-stimulated gene 15
ISV	Intersegmental vessel
Kb	Kilobase
KDa	Kilodalton
KDRL	Kinase insert domain receptor like
LB	Luria broth
MAPK	Mitogen-activated protein kinase
MB	Midbrain
MCeV	Middle cerebral vein
MCS	Multiple cloning site
MEK	MAP kinase kinase
MHB	Midbrain hindbrain boundary
Min	Minute
Mitfa	Melanocyte inducing transcription factor a
Ml	Millilitre
MMCtA	Middle mesencephalic central artery

MMP	Matrix metalloprotease
MO	Morpholino
MsV	Mesencephalic vein
MtA	Metencephalic artery
MTT	3-(4,5-dimethylthiazol-2-yl)-2,5-diphenyltetrazolium bromide
NBT/BCIP	P-nitroblue tetrazolium chloride/p-nitroblue tetrazolium chloride
NC	Notochord
NCA	Nasal ciliary artery
NCC	Neural crest cell
NeC	Neural crest
NECD	Notch extracellular domain
NEXT	Notch extracellular truncation
ng	Nanogram
NICD	Notch intracellular domain
nl	Nanolitre
NT	Neural tube
OV	Optic vessel
PA	Pharangeal arches
PAGE	Polyacrylimide gel electrophoresis
PAR	Protease-activated receptors
PCeV	Posterior cerebral vein
PCR	Polymerase chain reaction
PCV	Posterior cardinal vein
Pg	Picogram
PHBC	Primordial hindbrain channel
PI3K	Phosphoinositide 3-kinase
PIP3	Phosphatidylinositol 3,4,5-triphosphate
PMBC	Primordial midbrain channel
PP2A	Protein phosphatase 2
PrA	Prosencephalic artery
PTEN	Phosphatase and tensin homolog
PTU	N-phenylthiourea
qPCR	Quantitative PCR
RAC1	Ras-related C3 botulinum toxin substrate 1
RBPJ	Recombination Signal Binding Protein For Immunoglobulin Kappa J Region
RNA	Ribonucleic acid
RNP	Ribonucleoprotein
ROS	Reactive oxygen species
Rpm	Revolutions per minute
RT-PCR	Reverse-transcriptase PCR
S	Second
SD	Standard deviation
sgRNA	Single guide RNA
SH3	Src homology 3 domain
SHH	Sonic hedghog

SiRNA	Small interfering RNA
SNT	Single neurite tracer
SVP	Subintestinal vessel plexus
TGF-B	Transforming growth factor-beta
Tm	Melting temperature
Tsg	Twisted gastrulation
TTLD	Transverse terminal limb defect
UTR	Untranslated region
VEGF	Vascular endothelial growth factor
VEGFR	VEGF receptor
VSMC	Vascular smooth muscle cell
WASP	Wiskott-Aldrich syndrome protein
WAVE	Wiskott-Aldrich syndrome protein family member
WISH	Wholemount *in situ* hybridisation
WT	Wild-type
YY1AP1	YY1-associated protein 1

Acknowledgements

I would first like to extend my profound gratitude to my supervisor Dr Laura Southgate, for her confidence in me, her unwavering dedication in supporting me throughout this process and for her invaluable guidance. Laura's motivation and encouragement throughout has shaped me as a researcher and inspired me to pursue a career in academia.

I offer my sincerest thanks to Dr. Dan Osborn for his invaluable zebrafish expertise and abundant research ideas. Thank you for all your support, wisdom and giggles throughout this project. Thank you to Prof. Guy Whitley for his invaluable input and for providing the VSMC line which contributed towards this thesis and to Dr. Anissa Chikh for gifting the HaCaT cell line which led to the completion of Chapter 6.

To St. George's, University of London, for offering me a funded studentship, facilities and the support to enable my development as a researcher over the last few years. A huge thank you to the Graduate School team, Mark, Carwyn and Derilyn, whose hard work and empathy ensured continued funding for my project following some very trying times.

Thank you to the SGUL BRF staff, Rob, Emma, Rene and Louise, for their hard work in maintaining the fish facility over my project. Similarly, thank you to the UCL fish facility staff for taking us in and supporting my experiments, in particular Karen, Heather, Carole and Jenna. I extend an additional thank you to Paul Frankel for the use of his tg(*fli1*:GFP) fish, which contributed significantly to this work. To Greg in the IRF, thank you for your invaluable patience, support and guidance throughout this project.

To my fellow fish friend Gideon, whose boundless enthusiasm has inspired me throughout and to Fatima, for her wonderful company in the lab and her kindness and support over the last year.

An almighty thank you to my wonderful SGUL buddies Sally, Emily and Ben, for their moral support, warmth and belief in me and to Nick, Nathan, Claire, Stas, Mads, Julia, Ella and so many others over the last few years. Your friendship means the world to me and I’m so grateful.

To the wonderful Eve, Rachel and Elizabeth who shaped my academic journey, patiently listened to me ramble about my work for the last four years and continue to make life so much more joyous.

I extend my eternal gratitude to my Mum and Dad, who have given me unconditional support throughout all my studies and showed constant belief in my abilities; thank you, I couldn’t have made it here without you. To my wonderful big sister and best friend Jenny; thank you for being you and for making life brighter and delightfully random. In memory of my lovely grandparents, who offered me continuous support and encouragement as I grew up.

Finally, I offer my perpetual gratitude to Antony. Your patience, kindness and encouragement every day has lifted me through each challenge and I couldn’t have completed this without you.

Chapter 1:
Introduction

1.1 Adams-Oliver syndrome

Adams-Oliver syndrome (AOS) is a rare heterogeneous genetic disorder observed in approximately 1 in 220,000 live births (Adams and Oliver, 1945). AOS is predominantly defined by the congenital absence of skin on the scalp, known as aplasia cutis congenita (ACC), and terminal transverse limb defects (TTLD) (Dudoignon et al., 2020; Hassed et al., 2017). Both ACC and TTLD occur at a frequency of approximately 81% in AOS and display a wide range of severity (Southgate, 2019). ACC presents in several forms including alopecia, absent skin on the scalp and underlying bony defects leading to haemorrhaging and brain herniation (Hassed et al., 2017). Similarly, TTLD can vary from mild hypoplasia of the phalanges and nails to syndactyly, brachydactyly and termination of limbs at the wrists and ankles (Dudoignon et al., 2020; Hassed et al., 2017; Shaheen et al., 2011). These primary features may occur in concert with characteristics such as neurological or ocular defects, dependent upon the genetic origin. Importantly, cardiac and vascular anomalies are each observed in approximately 20% of AOS cases (Dudoignon et al., 2020; Hassed et al., 2017; Meester et al., 2018). The mechanisms underlying ACC, TTLD and other AOS-associated characteristics are currently unclear. However it is widely hypothesised that a disruption to the vascular supply during embryogenesis, likely due to defective vasculo- or angiogenic functions, contributes towards the abnormal development of structures in AOS (Hassed et al., 2017; Patel et al., 2004; Southgate, 2019; Swartz et al., 1999).

1.1.1 The vascular hypothesis in AOS

Though the major characteristics of AOS are mainly confined to ACC and TTLD, the high incidence of vascular and cardiac anomalies in patients points towards a potential role for angiopathies in the pathology of AOS (Southgate, 2019). Vascular abnormalities observed in AOS patients vary widely in severity and include vessel stenosis, pulmonary hypertension, ischaemia and calcifications in the brain (Bilginer et al., 2008; Dadzie et al., 2007; Lehman et al., 2014; Piazza et al., 2004; Swartz et al., 1999; Toriello et al., 1988). The most frequently observed vascular defect in AOS is cutis marmorata telangiectatica congenita (CMTC), which is reported in approximately 20% of patients (Bilginer et al., 2008; Dadzie et al., 2007; Patel et al., 2004). In addition to vascular defects, a similar proportion of AOS patients present with congenital heart defects (CHD). As with AOS-related abnormalities affecting other body systems during development, CHDs vary in severity and include Tetralogy of Fallot, patent foramen ovale, atrial and ventricular septal defects, and polyvalvular dysplasia (Bilginer et al., 2008; Dadzie et al., 2007; Patel et al., 2004; Swartz et al., 1999).

Several hypotheses exist for the mechanisms underpinning vascular and other developmental defects in AOS. It has been suggested that thrombotic obstruction to large vessels induces the development of AOS characteristics, as several studies have identified a disruption to the early embryonic blood supply *in utero*¸ in some instances coinciding with the incidence of thrombi in the large fetal vessels (Girard et al., 2005; Lehman et al., 2014). Others have indicated a likelihood for endothelial defects causing decreased stability of embryonic blood vessels, resulting in a disruption of blood flow which initiates TTLD, ACC and vascular and cardiac abnormalities (Bilginer et al., 2008; Papadopoulou et al., 2008; Silva et al., 2012; Swartz et al., 1999).

Another potential mechanism underlying AOS-related vasculopathies has been highlighted in patients showing abnormal pericyte (see Section 1.2.2.1) recruitment and thickness to the muscle wall surrounding the vessels, which may also account for the decreased vessel stability observed in other studies (Dadzie et al., 2007; Lehman et al., 2014; Papadopoulou et al., 2008; Patel et al., 2004; Piazza et al., 2004). In particular, vessel stenosis is frequently displayed in AOS patients with vascular and cardiac complications (Dadzie et al., 2007; Lehman et al., 2014; Patel et al., 2004; Silva et al., 2012; Swartz et al., 1999). A number of other genetic disorders also present with vessel stenosis and in the case of Grange syndrome, this is caused by the reduced proliferation and differentiation of vascular smooth muscle cells (VSMCs) in response to mutations in the YY1-associated protein 1 (*YY1AP1*) gene (Guo et al., 2017). Incidentally, Grange syndrome patients also display TTLD, CNS defects and hypertension induced by the narrowing of arteries due to VSMC-related stenosis, comparable to the characteristics caused by AOS (Ciuffetelli Alamo et al., 2019; Guo et al., 2017; Raggio et al., 2021; Rath et al., 2019). This suggests a potential overlap in the mechanisms effectuating both Grange syndrome and AOS. Of further interest, defective pericyte migration is suspected to increase the severity of foot TTLD compared with hand TTLD in AOS, as the feet are further away from the pericyte origin (Patel et al., 2004).

1.1.2 Genetics of AOS

AOS has diverse genetic origins whereby it can manifest in an autosomal dominant or recessive manner and arise either sporadically or with familial clustering (Renfree and Dell, 2016; Sukalo et al., 2015). Thus far, six genes have been identified as causal for AOS: the Rho GTPase pathway-related genes Rho GTPase-activating protein 31 (*ARHGAP31*) and dedicator of cytokinesis 6 (*DOCK6*) and the Notch pathway-related Notch receptor 1 (*NOTCH1*), Delta-like canonical notch ligand 4 (*DLL4*), EGF domain specific O-linked N-acetylglucosamine transferase (*EOGT*) and recombination signal binding protein for immunoglobulin kappa J region (*RBPJ*) (Cohen et al., 2014; Hassed et al., 2012; Lehman et al., 2014; Meester et al., 2015; Shaheen et al., 2013, 2011; Southgate et al., 2015, 2011; Stittrich et al., 2014; Sukalo et al., 2015). However there is much scope for the identification of novel AOS-causing mutations, as it is predicted that these genes account for only ~36% of cases of AOS (Meester et al., 2018; Southgate, 2019). The notable involvement of the Notch and Rho pathways and co-occurrence of vascular abnormalities suggests that AOS pathogenicity could originate from a currently unknown mechanism common to both pathways (Lehman et al., 2014). While an extensive body of research exists on the role of the Notch signalling pathway in vascular development, there are relatively few studies dedicated to examining the roles of the Rho pathway, specifically ARHGAP31 and DOCK6, in early vascularisation. Therefore, the mechanisms underpinning vascular defects in Rho-associated AOS patients are currently poorly understood.

1.1.3 Rho pathway

The Rho signalling pathway regulates the activity of Rho GTPases, a family of small G proteins of which the best characterised are RhoA, Ras-related C3 botulinum toxin substrate 1 (Rac1) and cell division cycle 42 (Cdc42) (Bryan et al., 2010; Bryan and D'Amore, 2007; Caron et al., 2016). Rho GTPases are expressed ubiquitously across eukaryotes and there are known to be approximately 20 members of the Rho GTPase family in mammals (Heasman and Ridley, 2008). They are known to play crucial roles in many biological processes, including cell polarity establishment, membrane trafficking, transcriptional regulation, cell growth and cytoskeletal organisation (Van Aelst et al., 1997; Mack and Georgiou, 2014). Rho GTPases function as molecular switches, which cycle between an active (guanosine-5'-triphosphate (GTP)-bound) and inactive (guanosine diphosphate (GDP)-bound) form controlled by the respective actions of guanine nucleotide exchange factors (GEFs), GTPase-activating proteins (GAPs) and guanine nucleotide dissociation inhibitors (GDIs) (Cherfils and Zeghouf, 2013; Côté and Vuori, 2002). GEFs activate small GTPases by catalysing the exchange of GDP for GTP. Conversely, GAPs induce the intrinsic GTPase activity of Rho GTPases, leading to their inactivation. In a similar fashion, GDIs bind to and stabilise GDP-bound small GTPases, sequestering them in the cytoplasm to prevent the spontaneous and GEF-catalysed release of GDP (Sastre et al., 2020). The Rho GEF and GAP families comprise approximately 80 and 65 members, respectively, and have been most heavily implicated in the development of cancers and neurological disorders (Ellenbroek and Collard, 2007; Endris et al., 2002; Kamai et al., 2003; Nadif Kasri and Van Aelst, 2008; Parri and Chiarugi, 2010).

1.1.4 Rho-related AOS

In the Rho pathway, DOCK6 and ARHGAP31 have opposing functions in regulating the activity of the small GTPases Rac1 and Cdc42 (Figure 1) (Tcherkezian et al., 2006; Van Buul et al., 2014). Through its role as a GAP, ARHGAP31 inactivates Rac1 and Cdc42 (Caron et al., 2016; Lamarche-Vane and Hall, 1998), whereas the GEF DOCK6 increases levels of active, GTP-bound Rac1 and Cdc42 (Cherfils and Zeghouf, 2013; Tcherkezian and Lamarche-Vane, 2007; Van Buul et al., 2014).

The cellular mechanisms underlying *ARHGAP31*- and *DOCK6*-related AOS are poorly understood. However, existing studies support a model of impaired vascular development in Rho-related AOS, indicating that this pathway requires further interrogation to gain greater insight into the molecular mechanisms underlying AOS. Stimulation of the small Rho GTPases by vascular endothelial growth factor (VEGF)

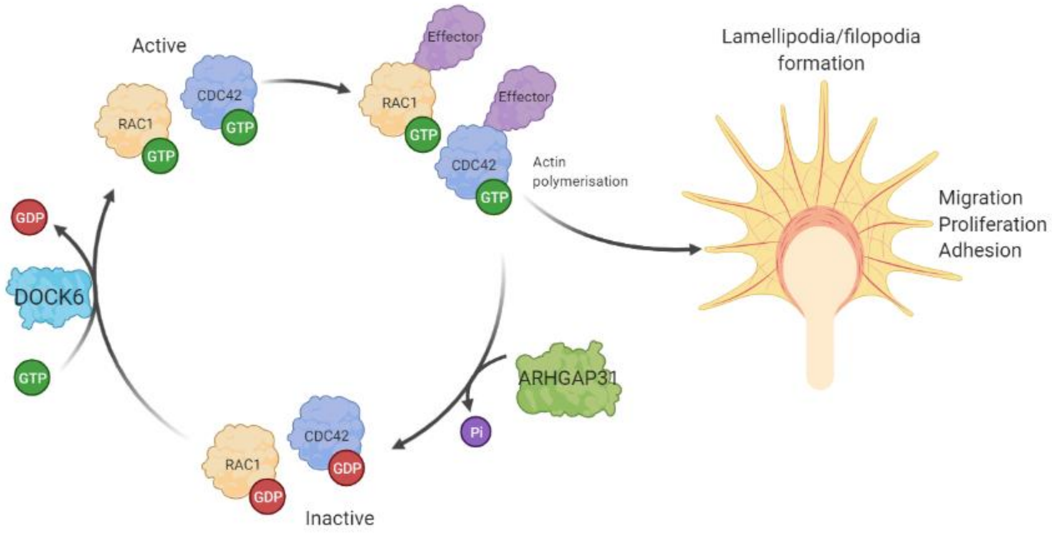

Figure 1: DOCK6 and ARHGAP31 activity in Rac1 and Cdc42 regulation.

DOCK6 is a guanine exchange factor which exchanges the GDP on inactive Rac1 or Cdc42 for GTP. This increases Rac1/Cdc42 activity leading to lamellipodia and filopodia formation and promoting cell functions such as migration, proliferation and adhesion. Conversely, ARHGAP31 decreases active Rac1 and Cdc42 levels through its function as a GTPase-activating protein, converting GTP to GDP. Figure created with BioRender.com.

leads to an increased active GTP-bound state and their enhanced membrane localisation, indicating a crucial function for the Rho pathway as a key mediator of VEGF-induced capillary formation. Activated Rho GTPases contribute to dynamic actin cytoskeletal assembly and rearrangement, which forms the basis of cell-cell adhesion and migration (Barry et al., 2015; Kesavan et al., 2009). Rac1 and Cdc42 induce lamellipodia and filopodia formation, which are critical for cell migration during angiogenic vessel remodelling. The lamellipodial network is a sheet-like network comprised of crosslinked actin filaments at the leading edge of a cell and filopodia are actin-rich protrusions that extend from the lamellipodial network in the plasma membrane. Additionally, Cdc42 and Rac1 have roles in cell motility, polarity, adhesion and migration, processes necessary during vasculogenesis and angiogenesis (Caron et al., 2016; Cascone et al., 2003; Tan et al., 2008).

1.1.4.1 Overview of the roles of Cdc42

Cdc42 is part of a complex signalling network that spatially and temporally regulates many dynamic cellular processes. Specifically, Cdc42 aids mediation of cell polarity, cytokinesis and actin reorganisation by inducing processes such as actin polymerisation, membrane ruffling and filopodia formation. Additionally, Cdc42 regulates cell adhesion, migration and invasion in many cell types, including neurons, endothelial cells and VSMCs (Barry et al., 2015; Davis et al., 2002; Kesavan et al., 2009). Through interactions with various effector molecules, for example receptor tyrosine kinases, scaffold proteins and adhesion molecules, Cdc42 is recruited to the cell surface and mediates nucleation of actin filaments and therefore actin polymerisation through various effectors, including actin-related protein 2/3 complex (Arp2/3) and N-WASP (see section 1.1.5.2) (Ma et al., 1998; Mullins et al., 2000). The deletion of Cdc42 and subsequent disruption of Cdc42s many downstream effectors in embryonic stem cells mediates disorganised filamentous actin (F-actin) and failed actin polymerisation, highlighting the complex nature of Cdc42 involvement in actin cytoskeleton organisation (Chen et al., 2000). Cdc42 plays a critical role in endothelial cell morphogenesis during vessel lumen formation, whereby the lumen develops by the formation of Cdc42-mediated vacuoles which coalesce to form the luminal compartment (Bayless and Davis, 2002; Norden et al., 2016). Cdc42 also has an essential role in cell polarity, as shown in experiments demonstrating recruitment of Cdc42 to the apical domain of epithelial cells following phosphatase and tensin homolog (PTEN) signalling (Martin-Belmonte et al., 2007). Polarisation is closely associated with the establishment of cell contacts such as tight junctions, requiring complex rearrangement of the actin cytoskeleton (Bauer et al., 2014). *Cdc42*-null mice are small and embryonic lethal by E5.5, displaying a disorganised anterior-posterior body axis and diffuse actin (Chen et al., 2000). These mice lack the early primitive endoderm and their embryonic stem cells were unable to initiate actin polymerisation under stimulation (Chen et al., 2000; Duquette and Vane, 2014). Of note, *Cdc42* deletion in the limb bud mesenchyme gave rise to shorter limbs and skeletal abnormalities including syndactyly, likely caused by impaired interdigital programmed cell death (Kühn et al., 2015). This indicates a critical role for Cdc42 during limb development (Kühn et al., 2015).

1.1.4.2 Overview of the roles of Rac1

Initially described in the promotion of phagocytosis and membrane-ruffle formation, Rac1 has since been shown to promote migration, adhesion, angiogenic sprouting and the permeability responses of endothelial cells to VEGF both *in vitro* and *in vivo*

(Caron et al., 2016; Kesavan et al., 2009; Tan et al., 2008). However, Rac1 activity is dispensable for filopodial formation and is instead essential in the formation of lamellipodia. In cell migration, Rac1 is recruited to the leading edge of the cell to promote actin polymerisation through downstream effectors, including Arp2/3 and the Scar/WAVE family (see section 1.1.5.2) (Bear et al., 1998). This requires tight spatio-temporal regulation thus Rac1 is known to be activated by over 30 different GEFs, including DOCK proteins 1-8, in addition to other regulatory mechanisms, for example the interaction of Rac1 with PIP3 to localise Rac1 to the leading edge of migrating cells (Tong et al., 2013). In the vasculature, Rac1 is essential for blood vessel formation due to its role in vacuole development during endothelial cell lumenogenesis (Bayless and Davis, 2002; Cascone et al., 2003; Norden et al., 2016; Waterman-Storer et al., 1999). Like Cdc42, Rac1 is essential in cell polarisation, stimulated upstream by molecules including the protease-activated receptor (Par) complex, and also plays a role in the establishment of tight junctions (Bauer et al., 2014; Wang et al., 2012).

In a *Rac1*-null mouse model, epiblast explants lacked lamellipodia and the anterior-posterior body axis was impaired due to defective migration of anterior visceral endoderm cells (Duquette and Vane, 2014). In addition, Rac1 appears to be crucial in neurulation as *Rac1* depletion leads to neural tube defects in the developing mouse embryo. This is likely due to defective cell shape change, cytoskeletal protrusion and cell-cell adhesion during neural plate formation caused by loss of Rac1 activity (Duquette and Vane, 2014). Interestingly, *Rac1* deletion in the embryonic limb bud ectoderm also led to TTLDs including syndactyly in the mouse, due to absent interdigital programmed cell death (Kühn et al., 2015).

Therefore, both Cdc42 and Rac1 demonstrate roles in cellular processes critical for vasculogenesis and angiogenesis by contributing towards actin cytoskeleton reorganisation. Of note, both Rac1- and Cdc42-null mouse models demonstrate features analogous to AOS characteristics, such as impaired angiogenesis, cardiac defects and limb malformations (Suzuki et al., 2013; Tan et al., 2008).

1.1.5 ARHGAP31

ARHGAP31, also known as CdGAP, encodes a serine- and proline-rich Rho GAP protein (Figure 2). It contains an N-terminal GAP domain and two C-terminal proline-rich domains (Figure 2) and harbours five consensus Src homology 3 domain (SH3)-binding sites (Lamarche-Vane and Hall, 1998). ARHGAP31 activity is thought to be regulated through phosphorylation of the N-terminal GAP domain by extracellular signal-regulated kinase (ERK) and has been seen to induce plasma membrane blebbing, cytoskeleton-regulated cell protrusions that suggest a role for ARHGAP31 in apoptosis (Tcherkezian et al., 2006, 2005). In zebrafish, *arhgap31* has been found to be regulated by the angiogenic E26 transformation-specific (Ets) transcription factor family, implicating *arhgap31* in vascular development (Gomez et al., 2012; Randi et al., 2009).

1.1.5.1 ARHGAP31 in AOS

ARHGAP31 was identified as the first causative gene for AOS by genome-wide sequencing of two families in which ACC and TTLD were segregating in an autosomal dominant manner (Southgate et al., 2011). In both families, heterozygous truncating variants were identified in the terminal exon 12 of *ARHGAP31* (Southgate et al., 2011).

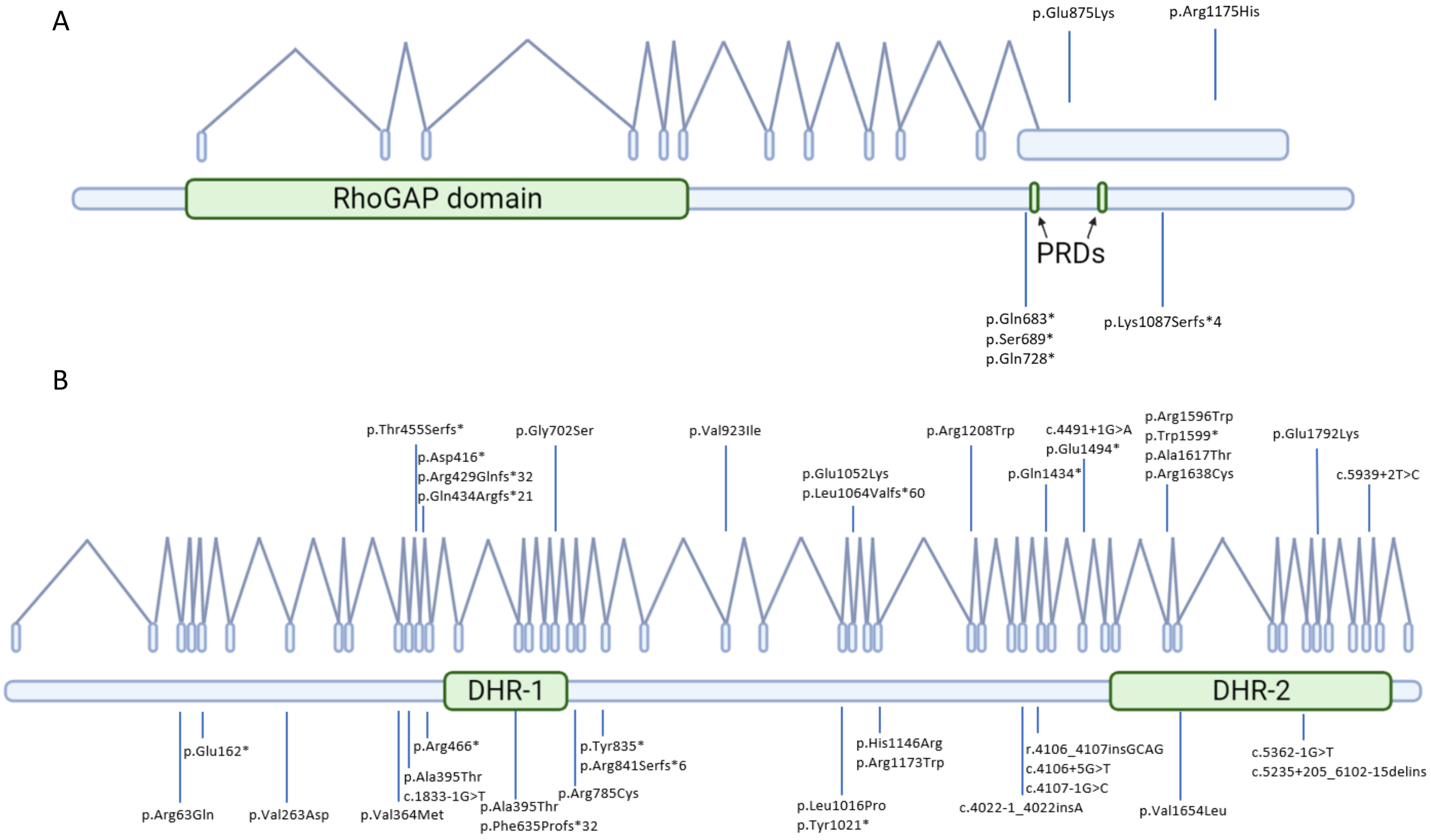

Figure 2: Schematic displaying the structures and AOS mutations of *ARHGAP31* and *DOCK6*.

ARHGAP31 (**A**) contains 12 exons, a RhoGAP domain and two proline-rich domains (PRD) in the terminal exon 12. *DOCK6* (**B**) is a gene containing 48 exons and two functional domains, DHR-1 and DHR-2. Mutations associated with AOS are indicated as vertical lines along each gene. Figure created using Biorender.

To date, a total of eight AOS-related *ARHGAP31* mutations have been reported, including a frameshift mutation, five nonsense and two missense mutations (“ClinVar,” 2022; Isrie et al., 2014; Southgate et al., 2011). Currently, only six are known to be pathogenic (Figure 2) and these are confined exon 12 (“ClinVar,” 2022; Southgate, 2019; Southgate et al., 2011). *ARHGAP31* variation accounts for <5% of all reported AOS cases and are predicted to be gain-of-function, although this remains to be independently validated (Southgate, 2019). ARHGAP31 gain-of-function in AOS was originally demonstrated by G-LISA assays, identifying a decrease in GTP-bound Cdc42 abundance in human embryonic kidney (HEK) 293 cells transiently transfected with AOS-associated *ARHGAP31* mutant constructs (Southgate et al., 2011). The predicted constitutive inactivation of its targets, Rac1 and Cdc42, likely results in downstream effects associated with impaired cytoskeleton organisation (Cau and Hall, 2005; Davis et al., 2002; Southgate et al., 2011; Tapon and Hall, 1997).

Preliminary work in *ARHGAP31*-related AOS patient-derived fibroblasts has identified disruption in cell proliferation and migration (Southgate et al., 2011). Wound-healing assays demonstrated defective migration patterns in fibroblasts carrying a heterozygous p.Gln683* variant in addition to a decrease in cell proliferation and a cell rounding phenotype, implying disruption to the actin cytoskeleton (Southgate et al., 2011). Together, these findings support an impact of ARHGAP31 gain-of-function on cellular function in the development of ACC and TTLD. However, similar investigations have not yet been conducted to examine the effects of AOS-specific *ARHGAP31* mutations in vascular-related cells. An in-depth study in cells pertinent to vasculogenesis and angiogenesis is therefore required to elucidate the mechanisms behind abnormalities in these processes.

1.1.5.2 Regulation of ARHGAP31

Several modulatory mechanisms exist to control the activity of Rho GAPs to fine-tune and tightly regulate small GTPase activity in a spatial and temporal manner (Pertz and Fritz, 2016). These mechanisms include phosphorylation, protein-protein interactions and proteolytic degradation. Numerous binding partners have been identified in the regulation of ARHGAP31 activity (Figure 3) (Danek et al., 2007; McCormack et al., 2017; Ouadda et al., 2018; Tcherkezian et al., 2005). Namely, the proline-rich domain of ARHGAP31 contains several binding sites for proteins such as glycogen synthase kinase 3beta (GSK-3β), which upregulates ARHGAP31 protein levels through phosphorylation of its threonine 776 residue (Danek et al., 2007; Lamarche-Vane and Hall, 1998). The mitogen-activated protein kinase (MAPK) signalling pathway protein ERK1 binds to this same residue and to threonine 769, but negatively regulates ARHGAP31 activity (Tcherkezian et al., 2005). Interestingly, ERK1 is activated by increased ECM rigidity which has also been shown to impact ARHGAP31 regulation of Rac1 activity at the leading edge of the cell, whereby ARHGAP31 inhibits localised Rac1 activity in response to changes of matrix rigidity (Wormer et al., 2014). In the context of ARHGAP31, inhibition of Rac1 is hypothesised to suppress both lamellipodia formation and FA dynamics, impeding cell migration in an ECM rigidity-dependent manner (Wormer et al., 2014).

In addition to phosphorylation-mediated ARHGAP31 regulation, binding of the LIM-domain containing protein Ajuba to the ARHGAP31 C-terminus has been found to repress ARHGAP31 activity at cadherin adhesion sites (McCormack et al., 2017). Ajuba is critical for maintaining cell-cell contacts and stabilises cadherin adhesion. Accordingly, *ARHGAP31* mutant constructs lacking the C-terminus domain were unable to bind Ajuba and led to severe disruption of E-cadherin contacts in keratinocytes (McCormack et al., 2017). It is thought that the retention of ARHGAP31 at adherens junctions by binding to Ajuba allows for rapid regulation of Rac1 at cell-cell contacts (McCormack et al., 2017).

Alternatively, a mechanism of autoregulation for ARHGAP31 GAP activity has been proposed, whereby it is hypothesised that the interaction observed between the ARHGAP31 C-terminus and N-terminus is associated with overactivation of the RhoGAP domain (Southgate et al., 2011). Autoregulation is a common feature of many GEFs and GAPs, particularly by intramolecular interactions blocking protein activity (Colón-González et al., 2008; Southgate et al., 2011). Therefore, inactivation of the ARHGAP31 substrates Rac1 and Cdc42 through ARHGAP31 RhoGAP domain activity may be prevented by the loss of the C-terminus (Southgate et al., 2011). Gain-of-function of *ARHGAP31*-related AOS is thought to be induced by mutations causing protein truncation at the C-terminus domain. It is predicted that the truncated C-terminus can no longer bind to the N-terminus domain (Southgate et al., 2011). This would lead to constitutive activation of the GAP domain, as the protein would exhibit an open conformation and could bind to its target Rho GTPases (Southgate et al., 2011).

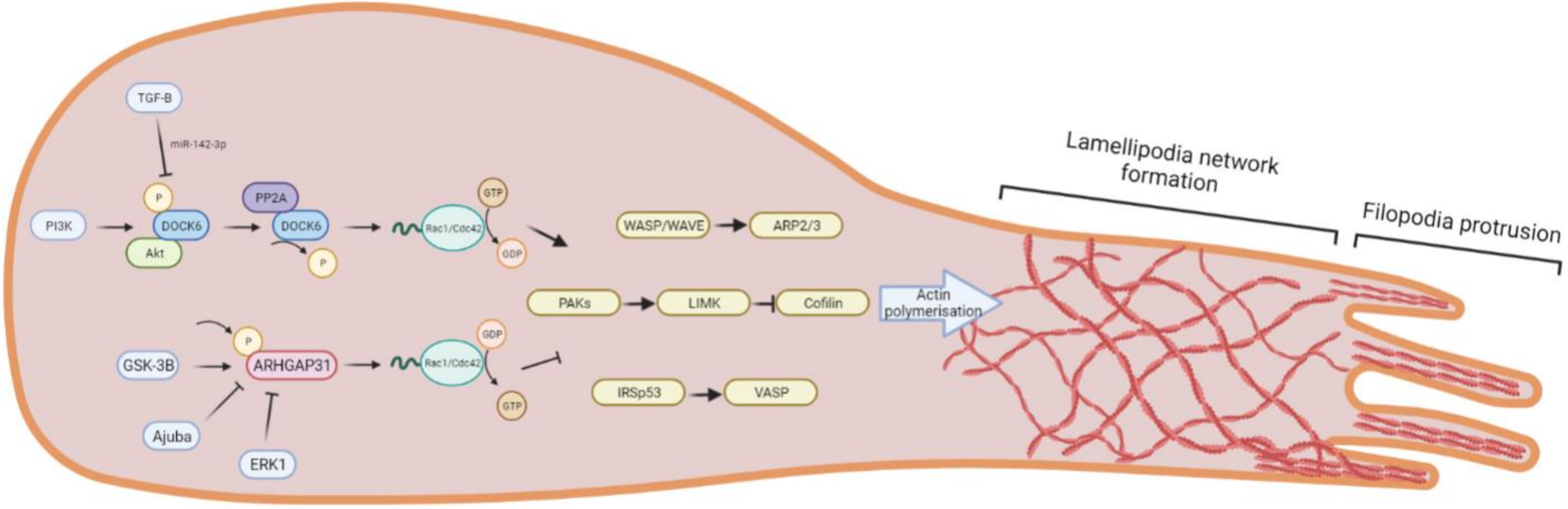

Figure 3: Schematic illustrating regulation of DOCK6 and ARHGAP31 and downstream events.

DOCK6 is regulated by miR-142-3p activity and phosphorylation and dephosphorylation by Akt ad PP2A, respectively (Miyamoto et al., 2013; Kim et al., 2015). Dephosphorylation leads to DOCK6 guanine exchange factor functions on Rac1 and Cdc42, increasing the active GTP-bound levels of these Rho GTPases. ARHGAP31 is regulated by GSK-3β, Ajuba and ERK1 (Tcherkezian et al., 2005; Danek et al., 2007; McCormack et al., 2017). GSK-3β-mediated phosphorylation upregulates the GTPase-activating activity of ARHGAP31, decreasing levels of active Rac1 and Cdc42. Several downstream signalling pathways, shown simplified here, are mediated by Rac1 and Cdc42 activity. The shown pathways are well established in the literature for stimulating actin polymerisation and formation of lamellipodia and filopodia in cell migration, one of the processes hypothesised to be implicated in AOS. Additionally, each included pathway has been linked to either the DOCK protein family, ARHGAP31, or both (Chi et al., 2020; Hernandez-Vasquez et al., 2017; Katoh and Negishi, 2003). Figure created with BioRender.com.

1.1.5.3 ARHGAP31 in the vasculature

Across model organisms, *ARHGAP31* expression during early embryogenesis appears localised to developing cardiac and vascular structures. In the mouse at E9.5, *Arhgap31* is most highly expressed in the heart, specifically in the ventral wall of the primitive ventricle and primitive atrium, remaining localised to this region as well as the surface ectoderm and developing limb buds until E12, where expression becomes negligible (Southgate et al., 2011). While displaying ubiquitous expression in humans, ARHGAP31 was also found to be highly expressed in human umbilical vein endothelial cells (HUVECs), implying a role in endothelial cells during development (Caron et al., 2016).

In an *Arhgap31*-null mouse model, complete removal of *Arhgap31* expression led to incomplete penetrance of embryonic lethality, with 44% of embryos deceased by post-natal day 21 (Caron et al., 2016). To investigate the causes underlying the high mortality rate, the vasculature and general features of the *Arhgap31*-deficient embryos were assessed. Hypovascularisation and subcutaneous oedema were key characteristics in these mutants, implying a critical role for ARHGAP31 in vascularisation during embryogenesis (Caron et al., 2016). Explanted aortic rings from *Arhgap31*-null mice were examined and found that VEGF stimulation in combination with *Arhgap31* depletion impaired the growth of capillary structures from the aortic rings, implying an essential role for ARHGAP31 in VEGF-mediated capillary formation (Caron et al., 2016). Additionally, this study aimed to elucidate the functional characteristics of ARHGAP31 in HUVECs, using siRNA to downregulate *ARHGAP31* and assessing cell migration and capillary formation (Caron et al., 2016). Their findings suggested that ARHGAP31 is required for migration, capillary network formation and capillary sprouting, which are all important processes in angiogenesis (Caron et al., 2016).

However, these results appear contradictory, as ARHGAP31 is a negative regulator of Rac1 and Cdc42 which are enforcers of migration, adhesion and proliferation among other important angiogenic processes. It might therefore be anticipated that knocking down ARHGAP31 should result in an increase in Rac1 and Cdc42 activation and enhanced angiogenesis-related cell functions. Accordingly, another study analysed endothelial cell tube and lumen formation upon siRNA-mediated *ARHGAP31* suppression and observed enhanced lumen and tube development upon reduced *ARHGAP31*, a finding consistent with increased Rac1 and Cdc42 activity (Norden et al., 2016). This observed discrepancy suggests that a more complex mechanism may be involved, perhaps implicating compensation whereby other GAPs

Characteristic	DOCK6-related AOS	ARHGAP31-related AOS
Percentage of AOS cases	17%	2%
Effect on gene function	Loss-of-function	Gain-of-function
Aplasia cutis congenital (ACC)	95%	32%
Terminal transverse limb defects (TTLD)	100%	82%
Congenital heart defect (CHD)	33%	0%
Cutis marmorata telangiectatica congenital (CMTC)	10%	0%
Other vascular anomalies	5%	0%
CNS abnormality	81%	0%
Microcephaly	57%	0%
Developmental delay	57%	0%
Seizures/epilepsy	57%	0%
Structural eye anomaly	57%	0%

Figure 4: Summary of Rho-related AOS clinical characteristics.

The clinical presentations of all Rho-related AOS patients reported to date with *DOCK6* or *ARHGAP31* mutations. (Figure adapted from Southgate, 2019).

specific for Rac1 and Cdc42 balance the equilibrium upon ARHGAP31 loss, however this remains to be investigated.

1.1.6 DOCK6

The DOCK family of GEFs is subdivided into four groups, dependent on their Rho GTPase specificity (Figure 5). The DOCK-A (DOCK1, 2 and 5) and –B (DOCK3 and 4) subfamilies are specific for Rac1 activation and the DOCK-D (DOCK9, 10 and 11) subfamily are specific for Cdc42 activation. DOCK6 is a member of the DOCK-C

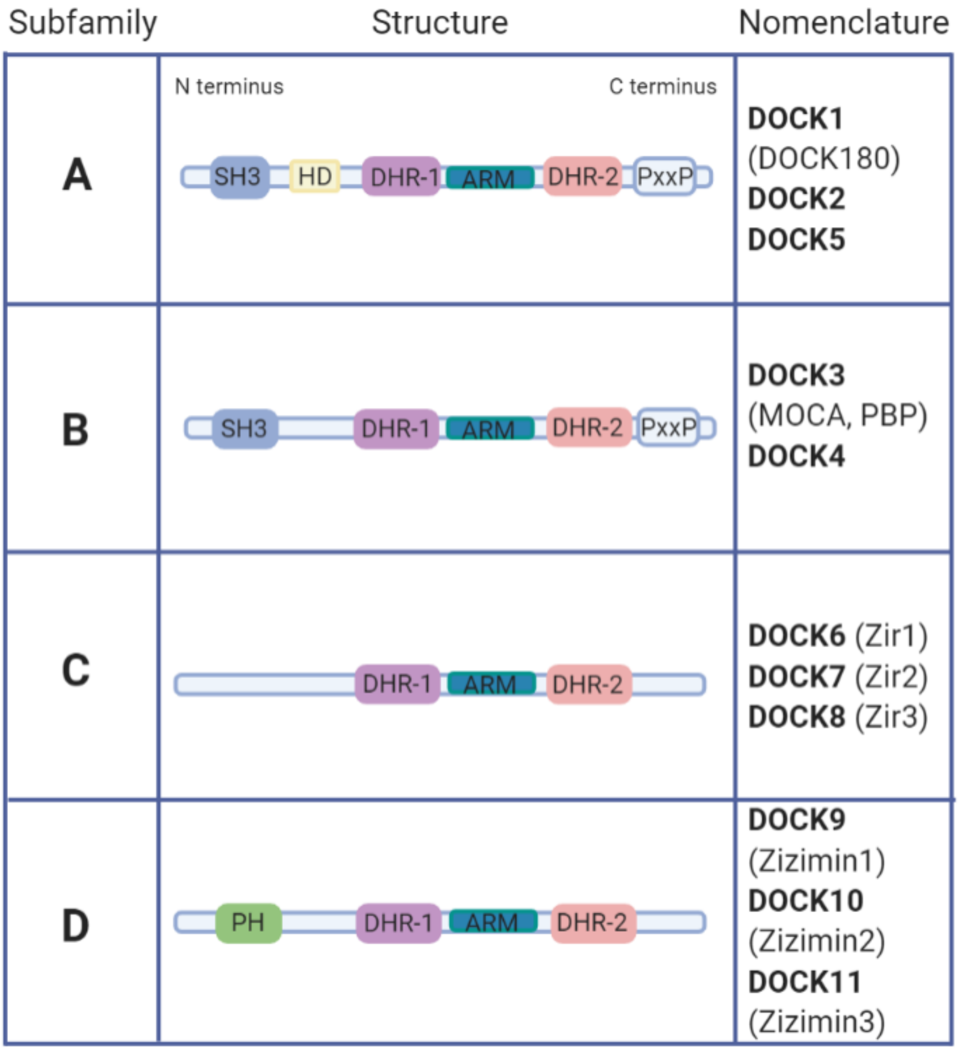

Figure 5: DOCK subfamily structures.

Structural domains of the four subfamilies of the DOCK protein family. ARM, armadillo repeat; DHR, DOCK homology region; DOCK, dedicator of cytokinesis; HD, helix domain; PxxP, proline-rich region; PH, pleckstrin homology domain; SH3, Src homology 3 domain (Benson and Southgate, 2021).

subgroup (DOCK6, 7 and 8) of DOCK proteins, which are characterised by their ability to upregulate the activity of both Rac1 and Cdc42 (Miyamoto et al., 2007). Unlike other GEFs, DOCK proteins do not contain the pleckstrin homology (PH) domains and Dbl homology (DH) domains required for GEF activity and membrane localisation (Miyamoto et al., 2007). Instead, they possess DOCK homology regions 1 and 2 (DHR1 and DHR2). DHR1 is responsible for the localisation of DOCK6 to the membrane via phosphatidylinositol 3,4,5-triphosphate (PIP3) interaction and is necessary for Rac1-dependent cell elongation and migration (Miyamoto et al., 2007). DHR2 has been shown to catalyse GTP-GDP exchange activity (Brugnera et al., 2002; Côté and Vuori, 2002; Yang et al., 2009).

1.1.6.1 DOCK6 in AOS

DOCK6 was identified as the second causal gene of AOS, determined by a combination of autozygosity mapping and exome sequence analysis of a patient presenting with the classic characteristics of AOS, with additional ocular and neurological complications (Shaheen et al., 2011). *DOCK6* mutations underlie an autosomal recessive form of AOS and, upon investigation, identified mutations were predicted to lead to protein truncation and a disruption of DOCK6 function, as the resulting protein lacks both functional domains. Since then, 41 independent *DOCK6* mutations have been described in association with AOS and account for ~17% of reported cases (Southgate, 2019). Predicted loss-of-function variants cover frameshift, missense and nonsense mutation types and are located across the length of the gene and have been shown in some cases to lead to nonsense-mediated decay or removal of the DHR1 domain, DHR2 domain or both (Figure 2) (Jones et al., 2017; Lehman et al., 2014; Pisciotta et al., 2018; Shaheen et al., 2011; Sukalo et al., 2015;

Wang et al., 2019). Loss of either of these domains impacts the function of DOCK6 as the DHR1 and DHR2 domains are essential in the localisation and GEF activity of the DOCK6 protein, respectively. Patients with *DOCK6* mutations show a broad range of clinical presentations in addition to the two major indicators, ACC and TTLD. Of significance, a large proportion of patients exhibit anomalies associated with the heart and/or vasculature, implicating AOS-related DOCK6 dysregulation in aberrant vascular development (Southgate, 2019). Loss-of-function *DOCK6* mutations are strongly associated with CNS and structural eye abnormalities (Alzahem et al., 2020; Sukalo et al., 2015). Additionally, developmental delay and seizures have been identified in >45% of patients with microcephaly and, even in the absence of microcephaly, demonstrate strong correlation with the presence of impaired intracranial vascularisation (Brancati et al., 2008; Southgate, 2019). A full summary of the characteristics seen in reported *DOCK6*-related AOS cases so far is displayed (Figure 4). In keeping with the known vascular involvement in AOS, several patients presenting with CNS abnormalities also displayed decreased perfusion, ischaemia and periventricular calcifications caused by microbleeds (Bilginer et al., 2008; Piazza et al., 2004). These findings are consistent with a role for disrupted cranial vascularisation in the manifestation of CNS defects. However, further investigations are required to provide clarity on the potential mechanism and impact of compromised vasculature on brain development.

Transient knockdown of *DOCK6* in HeLa cells exhibits a severe phenotype of cytoskeletal collapse and inhibited cell spreading, by comparison to patient-derived fibroblasts containing AOS-related *DOCK6* mutations which display blebbing and compromised lamellipodia formation (Cerikan et al., 2016; Cerikan and Schiebel, 2019; Shaheen et al., 2011). This discrepancy in results may be partly explained by overlaps in function between *DOCK* family genes. For example, *DOCK4, -5* and *-7* encode alternative regulators of Rac1 and repression of these genes by bone morphogenetic protein (BMP) is seen to induce the same variety of phenotypes (Kim et al., 2015). However, one study attempting to rescue the phenotype of *DOCK6*-depleted HeLa cells by overexpressing *DOCK2*, a GEF for Rac1, proved unsuccessful (Cerikan et al., 2016; Kang et al., 2011). While one further study has identified an increase in RhoA activity in *DOCK6*-negative patient-derived cells, thought to compensate for the loss of function seen in transient knockdown cells, the change of *DOCK* family gene expression upon stable *DOCK6* knockdown remains largely unexplored (Cerikan et al., 2016; Cerikan and Schiebel, 2019).

1.1.6.2 Regulation of DOCK6

In HEK293T cells, DOCK6 was found to be phosphorylated and dephosphorylated by Rac-alpha serine/threonine protein kinase 1 (Akt1) and protein phosphatase 2 (PP2A), respectively (Figure 3) (Miyamoto et al., 2013). Akt1 is the main downstream effector of phosphoinositide 3-kinase (PI3K), complete inhibition of which is known to severely disrupt angioblast cell fate determination (Hong et al., 2006). In addition, PI3K is a well-established mediator of VEGF signalling and appears to regulate the ERK pathway in angioblasts (Hong et al., 2006). While the ERK pathway was thought to trigger arterial cell fate specification, more recent work identified a role for ERK in sprouting endothelial cells during ISV angiogenesis (Shin et al., 2016). Contrary to earlier findings, inhibition of ERK activation by SL327 treatment did not impact expression of *ephrin-B2a*, a known arterial marker (Shin et al., 2016). Akt-mediated DOCK6 phosphorylation blocks binding of DOCK6 to Rac1, whereas PP2A-induced dephosphorylation leads to an increase in Rac1 activity as DOCK6 can bind and exert its functions as a GEF (Miyamoto et al., 2013). Thus far, the impact of PI3K/Akt-mediated DOCK6 phosphorylation has been assessed only in the dorsal root ganglia of mouse models (Miyamoto et al., 2013). These studies indicated that Rac1 and Cdc42 activation by dephosphorylated DOCK6 supports axonal elongation. Specifically, axon number and axonal branch point number are affected by Rac1 and Cdc42 activation, respectively (Miyamoto et al., 2013). Conversely, PI3K/Akt-mediated DOCK6 phosphorylation impairs axonal development through decreased Rac1 and Cdc42 activation (Miyamoto et al., 2013). Several comparisons can be drawn between the extension of neuronal axons and angiogenic sprouting, including the requirement for cytoskeletal rearrangement by active Rac1 and Cdc42 for filopodial formation and integrin-mediated cell-extracellular matrix (ECM) adhesion for branch advancement (Benson and Southgate, 2021). However, investigation of a role for DOCK6 in angiogenesis is yet to be explored.

1.1.6.3 DOCK6 in the vasculature

Though DOCK6 function during vascular development remains poorly examined, several studies point towards a mode of action in the vasculature. Whole-mount *in situ* hybridisation (WISH) in developing mouse embryos demonstrated localised *Dock6* expression to the developing heart and growing limb buds at E10.5 and E11.5 (Shaheen et al., 2011). Additionally, DOCK6 has been identified as highly expressed in endothelial cells (Hernández-García et al., 2015). Taken together, these findings suggest a role for Rho dysregulation in the development of cardiac defects and TTLD.

Interestingly, DOCK6 has also been implicated in the transforming growth factor beta (TGF-β) signalling pathway, which is critical for many cellular processes including vascular development and homeostasis (Kim et al., 2015). Importantly, TGF-β and BMP have roles in promoting VSMC differentiation and maintaining the contractile phenotype of VSMCs (Chen and Lechleider, 2004; Mack, 2011; Shah et al., 1996). TGF-β signalling induces the haematopoietic cell-specific microRNA *miR-142-3p*, which has been shown to down-regulate *DOCK6* expression and simultaneously decrease cell migration in VSMCs, providing preliminary evidence for a role for DOCK6 dysregulation in disrupted vascularisation (Kim et al., 2015). However, the mechanism underlying the impact of aberrant *DOCK6* expression on VSMC function is unclear.

1.2 Overview of the mammalian vascular system

As outlined above (see Section 1.1.1) the mechanisms underlying the characteristics observed in patients with AOS are currently unclear, but initial evidence suggests an origin in disrupted early vascularisation. A functioning vascular system is essential for limb and tissue development to transport oxygen and nutrients to their required locations via arterial, venous and capillary networks which connect to the heart (Semenza, 2007). The arterial system delivers nutrient- and oxygen-rich blood to all tissues, enabled by capillary networks which span between arteries and veins and play a dual role in blood distribution and facilitating the removal of metabolic products (Marziano et al., 2021). Capillaries collect deoxygenated blood and allow perfusion of carbon dioxide from the tissues through the vessel walls to feed into the venous system. Once depleted of oxygen and nutrients, veins transport blood pooled by the capillary network back to the heart and lungs.

1.2.1 Vasculogenesis

Vasculogenesis is the development of a closed circulatory system during early embryogenesis, via the *de novo* formation of blood vessels (Semenza, 2007). To initiate vessel development, multipotent progenitors known as haemangioblasts in the embryonic and extraembryonic mesoderm differentiate and aggregate to form blood islands. (Krah et al., 1994; Shalaby et al., 1995) Haemangioblasts give rise to both haematopoietic cells in the lumen and endothelial precursor cells (Charnock-Jones et al., 2004). These highly motile cells, known as angioblasts, migrate and assemble at sites of *de novo* vessel formation. The coalescence of angioblasts induces primitive construction of large vessels such as the dorsal aorta, ventral aorta and cardinal veins (Patel-Hett and D'Amore, 2011). Vasculogenesis continues by differentiation of angioblasts to endothelial cells, promoting vascular lumen formation and the development of a basal lamina in established vessels (Cox and Poole, 2000; Hong et al., 2006). Maturation of *de novo* vessels gives rise to the primary vascular plexus and mediates vascularisation of several organs, including the liver, spleen and lung (Patel-Hett and D'Amore, 2011). The rudimentary vessels formed by this process promote blood flow in the developing embryo (Marziano et al., 2021). However, these vessels are fragile and require further maturation via angiogenesis to support the transport of blood around the body (see Section 1.2.2). Therefore, vasculogenesis is the initial stage of vascularisation during embryogenesis and provides a framework for further development of the vascular system.

1.2.2 Angiogenesis

Following the establishment of a primitive vessel system and differentiation of angioblasts to endothelial cells in vasculogenesis, angiogenesis continues the process of blood vessel maturation to form a network which facilitates blood flow throughout the body (Drake, 2003). Though the transition from vasculogenesis to angiogenesis is loosely defined, it is considered to occur when angioblasts form endothelial junctions in conjunction with the onset of blood flow (Schmidt et al., 2007). In contrast to vasculogenesis, which is confined to early embryogenesis, angiogenic

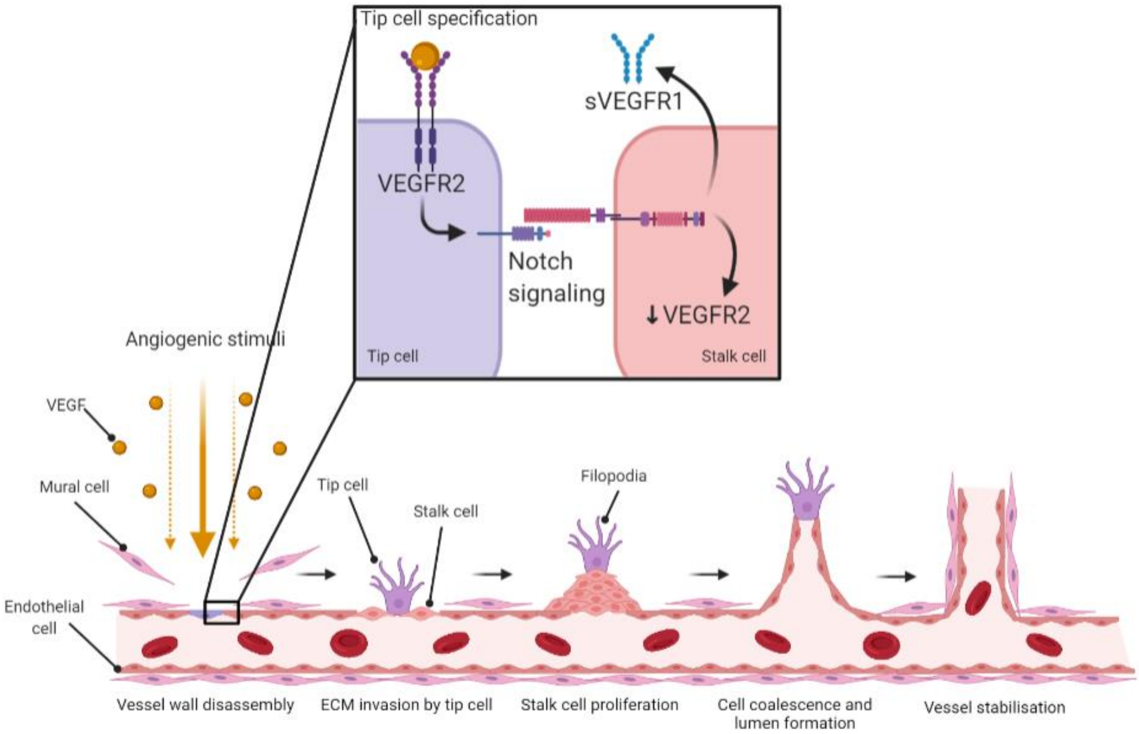

Figure 6: Process of sprouting angiogenesis and the role of VEGF signalling.

VEGF molecule production is stimulated by hypoxia in tissues. VEGF molecules are then released and interact with VEGFR2 receptors on endothelial cells. Cells with ligand-bound VEGFR2 become tip cells and Notch ligand expression is upregulated. Ligands interact with Notch receptors on adjacent cells to upregulate Notch signalling, leading to VEGFR2 downregulation and secretion of VEGFR1 to sequester VEGF in the surrounding tissues. The adjacent cells develop a stalk cell phenotype. The vessel extracellular matrix is degraded by enzymes in the basement membrane and the migratory tip cell can invade the surrounding tissue. The stalk cells proliferate and form the trailing body behind the tip cell, before coalescing and mediating lumen formation. The vessel is then stabilised by the recruitment of mural cells to the newly formed endothelial wall. Figure created with BioRender.com.

processes continue throughout life, primarily functioning to repair damaged blood vessels and promote branching of smaller blood vessels within the network (Persson and Buschmann, 2011; Poole and Coffin, 1989).

1.2.2.1 Process of sprouting angiogenesis

To begin the maturation of primary blood vessels into a more complex and complete vascular network, enzymatic degradation of the ECM and basal lamina takes place to disassemble the existing vessel wall (Davis et al., 2002). An initial chemotactic factor, such as VEGF, initiates the migration of endothelial tip cells into the perivascular layer (Figure 6) (Patan, 2000). These tip cells guide angiogenic sprouting and endothelial cell invasion of the ECM (Blanco and Gerhardt, 2013; Kubis and Levy, 2003a). The expansion of existing vessels is promoted through the proliferation of endothelial stalk cells, enabled by the loss of cell-to-cell contact (Kubis and Levy, 2003a). Vessels begin to form by stalk cell coalescence, followed by one of two lumenising processes: cell hollowing enables vessel lumenisation by the expansion of large vacuoles within endothelial cells; cord hollowing promotes the polarisation and separation of endothelial cells form a seamless blood vessel (Kubis and Levy, 2003a). Once fully expanded, anti-angiogenic factors in the vessels, such as transforming growth factor-beta (TGF-β), inhibit endothelial cell proliferation and migration (Gaengel et al., 2009). Re-stabilisation and maturation of the remodelled vessels occur by the recruitment of mural cells, which comprise pericytes and VSMCs (Figure 7) (Kubis and Levy, 2003a). Pericytes are solitary vascular smooth muscle-like cells that associate with and support microvasculature, such as arterioles, venules and capillaries (Gaengel et al., 2009). By contrast, VSMCs form concentric layers around larger blood vessels and are thought to maintain vessel integrity and prevent leakage caused by increases in blood pressure (Gaengel et al., 2009). The roles for mural cells in endothelial cell and ECM interaction and in supporting vessel integrity highlight the importance of both endothelial and mural cell migration and proliferation during development of functional vascular networks (Kubis and Levy, 2003b).

1.2.2.2 Endothelial cells in sprouting angiogenesis

Migrating endothelial tip cells direct sprouting angiogenesis whereas the expansion of vessels is promoted by the proliferation of endothelial stalk cells (Kubis and Levy, 2003a). Tip cells are distinct from endothelial stalk cells by their position, dynamic filopodia and migratory behaviour (see Section 1.2.2.1) (Blanco and Gerhardt, 2013). Tip cell migration defines the direction of new sprout growth (Blanco and Gerhardt, 2013). Endothelial cells respond to the surrounding environment by sensing extrinsic

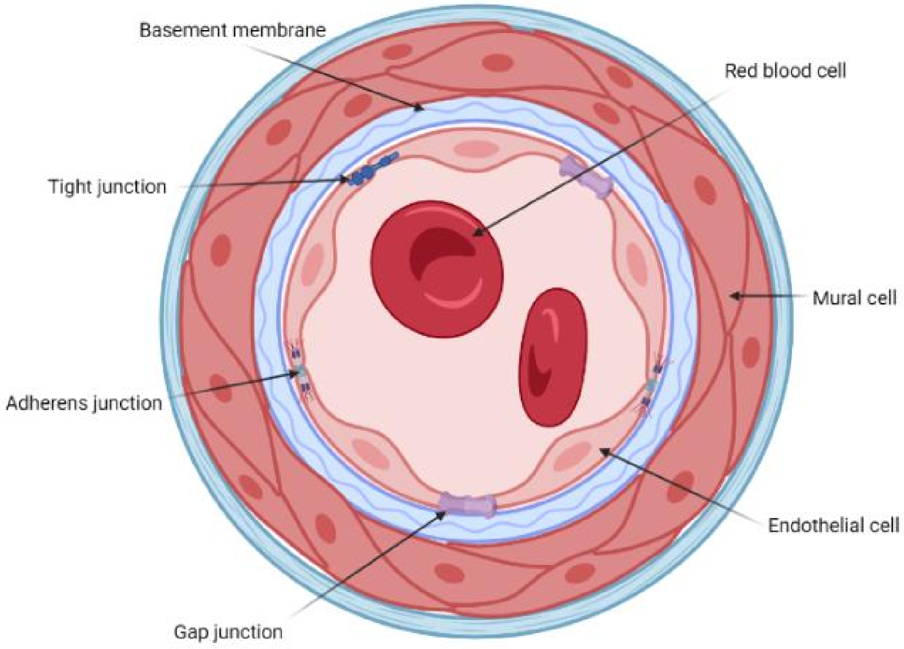

Figure 7: Cross-section of a blood vessel.

Schematic displaying the components constituting a blood vessel wall. Endothelial cells form the endothelial lining of the vessel lumen and interact by cell-cell contacts. A basement membrane surrounds the endothelial tube and in larger vessels forms a tunica media consisting of mural cells, which may be vascular smooth muscle cells or pericytes depending on the vessel type. Figure created with BioRender.com.

signals and demonstrate high levels of heterogeneity in gene expression dependent upon their localisation (Marziano et al., 2021). For example, capillary endothelial cells which are confined to tissues such as the brain and retina restrict passage of molecules through their membranes by expressing high densities of tight junctions (Bauer et al., 2014). By contrast, capillary endothelial cells which are required for extensive filtration, as in the kidney and liver, exhibit a vastly porous membrane (Bauer et al., 2014). These levels of specificity are required to enable endothelial cells to maintain tissue homeostasis.

1.3 Regulation of embryonic vascular development

Several pathways are involved in the regulation of early vascularisation, including but not limited to VEGF, Notch and fibroblast growth factor (FGF) signalling.

1.3.1 VEGF-mediated regulation

VEGF signalling coincides with the emergence of the first blood islands in the extra-embryonic visceral endoderm and in the extra-embryonic mesoderm (Fong et al., 1995). In mouse embryos, strong VEGF expression is found in endodermal cells at day E8.5 when the intra-embryonic vascular plexus begins to form. Vascular endothelial growth factor receptor 1 (*Vegfr1*) and *Vegfr2* deficiency in mice have shown critical functions in the development and organisation of blood islands, respectively, highlighting the importance of these receptors in vasculogenesis (Fong et al., 1995; Shalaby et al., 1995). Similarly, *Vegfr2* knockout mouse studies have also shown that *Vegfr2* is essential for endothelial cell development and that deletion of this gene is lethal by E9.5 (Shalaby et al., 1997). Graded VEGF signalling is stipulated to control arterial identity in part by regulating Notch signalling levels (Coultas et al., 2010).

Correspondingly, angiogenesis is largely controlled by VEGF and its specific binding to the integral membrane tyrosine kinases VEGF receptor 1 (VEGFR1, also known as FLT1) and VEGFR2 (also known as FLK1 or KDR) (Bryan and D'Amore, 2007; Gerhardt et al., 2003). Hypoxia in tissues indicates a need for improved perfusion by further vascularisation and stimulates VEGF production (Persson and Buschmann, 2011). VEGF molecules bind to VEGFR2 on the surface of endothelial cells and specifies a migratory tip cell phenotype (Patan, 2000). VEGFR2 signalling induces Dll4 secretion to the adjacent cells which upregulates Notch signalling in the adjacent cells, leading to downregulation of VEGFR2 and increased expression of secreted VEGFR1, which sequesters VEGF to prevent over-vascularisation (Nasevicius et al., 2000). With these lateral inhibition mechanisms in place, the adjacent cells differentiate to form stalk cells, which proliferate and form the trailing body of the new vessel.

This VEGF-mediated stimulation of its receptors also leads to the activation of other downstream signalling cascades. These include the MAPK and phosphoinositide 3-kinase (PI3K) pathways, which are critical in the management of angiogenic processes such as cell survival, proliferation and gene expression (Bryan and D'Amore, 2007). Additionally, the Rho family of GTPases is essential in transmitting signals downstream of VEGF and is required during *in vivo* angiogenesis (Bryan and D'Amore, 2007). This has been demonstrated through the use of angiogenic assays in Rho GTPase-depleted mice which demonstrated impaired vascular permeability, matrix metalloproteinases expression, migration, proliferation and survival when supplemented with VEGF (Bryan et al., 2010; Bryan and D'Amore, 2007). Further, VEGF signalling has been implicated in the differentiation of angioblasts to endothelial cells as VEGF-only media could facilitate this transition (Chen et al., 2021).

1.3.2 The Notch signalling pathway

The Notch signalling pathway is critical in early vascular development and has demonstrated a close interaction with both HH and VEGF signalling during vasculo- and angiogenesis (Coultas et al., 2010; Lawson et al., 2002). Notch signalling is a highly conserved and functionally essential pathway during organism development, mediating short-range cell interactions to specify cell fate (Le Borgne et al., 2005; Siekmann and Lawson, 2007a). The pathway utilises lateral inhibition via interactions between the asymmetrically expressed Notch receptor and its ligand to determine the fate of cells during the development of many organs and structures across numerous organisms including humans, mice, zebrafish and Drosophila (Chapouton et al., 2010; Itoh et al., 2003; Nikolaou et al., 2009). At the cell surface, the binding of a Delta/Serrate/Lag-2 (DSL) ligand to the Notch extracellular domain (NECD) leads to the sequential cleavage of the Notch receptor by two different protein families, namely the ADAM metalloprotease domain containing family and γ-secretase (Gupta-Rossi et al., 2004; Six et al., 2003). Cleavage by ADAMs release NECD from the receptor, leaving behind a membrane-tethered Notch intracellular domain (NICD), known as the Notch extracellular truncation (Lieber et al., 2002). Cleavage by γ-secretase leads to the release of NICD, which translocates to the nucleus where it can interact with the CBF1/Suppressor of Hairless/Lag-1 (CSL) family of transcription factors (Gupta-Rossi et al., 2004). CSL proteins (which include RBPJ) regulate the transcription of Notch target genes by acting with transcriptional co-repressors, which are then displaced by the NICD to form an NICD-CSL transcription-activating complex to regulate expression of downstream Notch effector genes (Gupta-Rossi et al., 2004; Lai, 2002; Pursglove and Mackay, 2005).

In the vasculature, Notch signalling is essential in numerous critical endothelial cell processes, such as arterial/venous specification, tip and stalk cell differentiation and the endothelial cell response to pro-angiogenic stimuli. During vasculogenesis, Notch signalling has a conserved role in arterial specification, as evidenced by the extensive angiogenic defects observed in mouse models lacking *Notch1* (Krebs et al., 2004). The essential role for Notch signalling in the vasculature continues through angiogenesis (Figure 6), whereby secretion of VEGF induces DLL4 expression by binding to VEGFR2 on the endothelial cell surface, which in turn promotes Notch signalling in the adjacent cell (Hellström et al., 2007). By lateral inhibition, a stalk cell phenotype is induced in the endothelial cell receiving the ligand, whereas the endothelial cell secreting the ligand will acquire a highly motile and migratory tip cell phenotype, to instigate angiogenic sprouting (See Section 1.2.2.2). Dysregulated Notch signalling results in excessive tip or stalk cell specification, leading to poor vascular development (Hellström et al., 2007; Krueger et al., 2011). As noted above, pathogenic variants in numerous members of the canonical Notch signalling pathway have been described in AOS (see Section 1.1.2).

1.3.3 FGF-mediated regulation

FGF signalling mediates upstream regulation of critical angiogenic signalling cascades, such as HH, VEGF and Notch. Although VEGF signalling is an essential regulator of angiogenic processes, VEGF alone cannot reconcile impaired endothelial cell formation in human induced pluripotent stem cells (iPSCs) (Poole et al., 2001). However, the addition of FGF stimulates the production of a high proportion of endothelial cells from iPSCs, implying a critical role for FGF signalling during embryonic vascularisation upstream of VEGF (Wu et al., 2015). Notably, numerous studies have implicated FGF signalling in early vascular development, a role supported by the endocardial localisation of fibroblast growth factor receptor (FGFR) (Parlow et al., 1991). In particular, FGF is required for the differentiation of mesodermal cells to angioblasts, as demonstrated by experiments whereby treatment with bovine FGF-only media was sufficient to form angioblasts from cultured mesodermal cells (Chen et al., 2021). Further, the use of mRNA flow cytometry has identified a role for the FGFR1/BRAF/MEK/ERK signalling pathway in angioblast formation (Chen et al., 2021).

Quail and chick experiments imply a key role for FGF2 in the induction of vasculogenesis, as observed in quail blastodisc-derived embryoid bodies following culturing with FGF2 (Krah et al., 1994). Chimeric transplantation of quail somitic mesoderm into chick embryo head or trunk promoted an increase in angioblast number in the head compared to the trunk, initiated by a much higher FGF2 concentration in the host head (Cox and Poole, 2000).

Taken together, these findings highlight the intricate network of regulatory pathways required for normal vascular development and emphasize the importance of spatial and temporal expression patterns in vascular patterning.

1.4 Models of disease

1.4.1 Zebrafish as a model organism

This project aimed to use zebrafish to generate disease models of Rho-related AOS. Previous studies using mouse models have been limited by the mid-gestation lethality of *Dock6*, *Rac1* and *Arhgap31* mutations, due to failed embryonic vascularisation (Caron et al., 2016; Miyamoto et al., 2013; Tan et al., 2008). For zebrafish, however, complete vasculature is non-essential for supplying nutrients and oxygen until 5 days after fertilisation, therefore they are an excellent model to examine any potentially lethal vascular defects caused by AOS-related mutations. Furthermore, zebrafish embryos can be made optically transparent through treatment with phenylthiourea (PTU), allowing for convenient investigation of internal phenotypes. In addition, zebrafish have a high fecundity, demonstrating an ability to lay approximately 200 eggs per week per mating pair. Though these embryos do not reach sexual maturity until they are around 3-4 months old, comparable to that of mice, the abundance of progeny presents an advantage over the use of mouse models (Kimmel et al., 1995). Finally, a wealth of genetic information of the zebrafish model has become available over the last 30 years and a comparison between zebrafish and human genomes demonstrates approximately 70% similarity between the two organisms, making zebrafish an attractive model for translational research. Many techniques for genetic manipulation and gene investigation have been developed, making the zebrafish an excellent model for unveiling gene function.

1.4.1.1 Morpholino technology to generate knockdown models

The use of morpholinos to generate zebrafish knockdown models is a well-established method. This technique requires the design of oligonucleotides with a phosphorodiamidate backbone to combat degradation, targeted to the translation start site of the gene of interest, or a splice acceptor/donor site (Summerton and Weller, 1997). These are developed with the aim of either blocking translation of the gene or preventing the spliceosome from correctly splicing introns (Heasman, 2002; Summerton and Weller, 1997). Blocking the spliceosome can lead to either intronic inclusion or exon skipping, resulting in disrupted splicing or a frameshift and failure of the spliceosome to generate a functional mRNA transcript, therefore creating a gene knockdown.

Historically, morpholinos are believed to be prone to off-target effects, therefore independent validation methods are required to verify morpholino-generated phenotypes (Bedell et al., 2011; Eisen and Smith, 2008). This can be achieved by use of a second, non-overlapping morpholino targeting the same gene; observation of an identical phenotype is considered reasonable evidence for the generation of a true knockdown model unencumbered by off-target effects (Eisen and Smith, 2008; Stainier et al., 2017). Alternatively, rescue experiments whereby the wild-type mRNA of the targeted gene is co-injected with the morpholino are considered to validate the morpholino if the wild-type phenotype is restored (Stainier et al., 2017). However, rescue experiments can be unreliable as over-expression phenotypes can be generated and the injected wild-type mRNA is not localised to the normal expression region of the embryo therefore generating unwanted effects.

Currently, the gold-standard independent validation technique for morphant knockdown models is the use of clustered regularly interspaced short palindromic repeats (CRISPR) technology. This method has been widely adopted to generate zebrafish disease models through targeted gene knockout (Stainier et al., 2017).

1.4.1.2 CRISPR-mediated knockdown models

The CRISPR-Cas9 technology is derived from the bacterial immune system and has been optimised to insert target site-specific edits into the genome (Figure 8) (Jinek et al., 2012). In this system, a single guide RNA (gRNA) constituted by a CRISPR RNA (crRNA) and a *trans*-CRISPR RNA (tracrRNA) contains a sequence of 17-20 nucleotides upstream of an NGG protospacer adjacent motif (PAM) site (Jinek et al., 2012). This

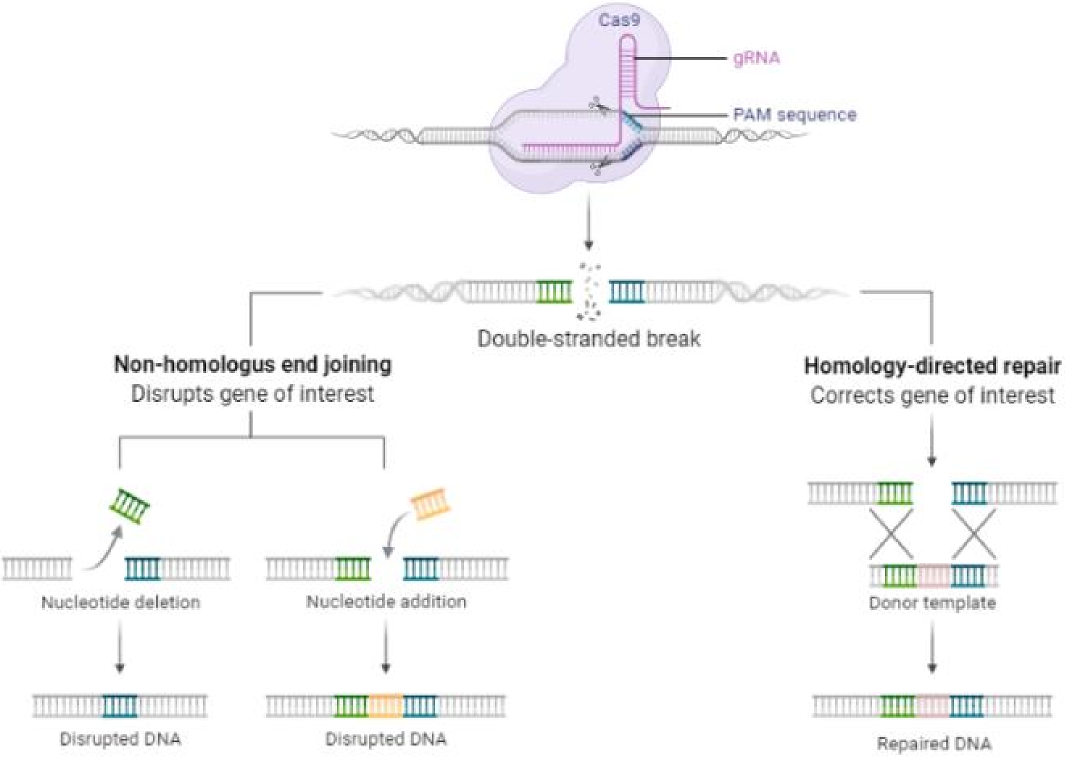

Figure 8: Mechanism of CRISPR-Cas9 genome editing.

A Cas9 nuclease complexed with a gRNA specific to a target site creates a double-stranded break three base pairs upstream of the PAM sequence. This break is repaired by either error-prone non-homologous end-joining or precise homology-directed repair. Figure created with BioRender.com.

sequence is specific to the target site of interest and guides a complexed Cas9 nuclease to create a double-stranded break (DSB) three nucleotides upstream of the NGG PAM site (Figure 8) (Jinek et al., 2012). The DSB is then reconstructed by either non-homologous end-joining (NHEJ) or homology-directed repair (HDR) (Jinek et al., 2012; Mao et al., 2008). NHEJ is an error-prone mechanism whereby random nucleotides are inserted or deleted at the breaks to join the strands, likely introducing frameshift mutations and impeding functional protein translation to generate a knockout model (Jinek et al., 2012; Mao et al., 2008). HDR on the other hand occurs when there is a homologous donor template present at the DSB site which can anneal to the broken strands and serve as a model to accurately repair the cut site (Chu et al., 2015; Liang et al., 2017; Zhang et al., 2017). However, by introducing an altered donor template, knock-in models can be generated wherein mutations are precisely inserted at the target site following generation of a DSB by Cas9 nuclease (Wu et al., 2013; Zhang et al., 2017).

Due to recent technological advancements, we have harnessed a technique which utilises CRISPR in the generation of F_0 embryo gene knockdown and phenotyping (Kroll et al., 2021; Wu et al., 2018). In zebrafish, CRISPR is typically used to complex a gRNA specific to the gene of interest with a Cas9 protein, which is then injected into the 1-cell stage zebrafish embryo (Kroll et al., 2021; Wu et al., 2018). Inside the embryo, the Cas9 nuclease is targeted to the gene of interest by the specific gRNA sequence and creates a double-stranded break in the DNA to disrupt gene function (Jinek et al., 2012). To create stable knockouts, injected embryos must be grown up and screened for mutations and then paired with another mutation-positive zebrafish create to give mutant F_1 progeny. These fish must also be screened and may then be used to generate knockout clutches of F_2 embryos which can be phenotyped. This is a long process which can take in excess of six months to generate the desired stable knockout line. Therefore, we adapted a protocol which uses three gRNAs targeted to the same gene and injected as a multiplex bound to Cas9 nuclease. This technique was proven to induce a 95% knockdown rate in the injected F_0 embryos and allows for the rapid generation of a knockdown phenotype which can be swiftly verified and assessed (Kroll et al., 2021). Therefore, this is a fast and convenient independent validation of phenotypes observed upon morpholino-mediated knockdown.

1.4.1.3 Transgenic reporter line

Another highly reliable genetic approach commonly used in zebrafish functional genomics is the generation of transgenic reporter lines to accurately visualise spatial gene expression. In this method, a transgenic construct is designed containing a transposable element, such as *Tol2*, which flanks a sequence comprising the promoter region of the gene of interest followed by a reporter gene, such as mCherry. This construct is then co-injected into the 1-cell stage embryo alongside *transposon* mRNA which mediates stable integration of the *Tol2*-flanked sequence into the genome. The reporter gene can then be expressed when the promoter sequence is in close proximity to an active enhance element of the gene of interest. Typically, F_0 embryos exhibit a mosaic expression of the transgene, providing limited information regarding localisation of the gene of interest. Therefore, breeding of transgene-positive zebrafish is required to generate a homozygous transgenic line, representative of the true gene expression localisation.

1.4.2 AOS-related Rho pathway in zebrafish

Currently, very limited data exist for *arhgap31* and *dock6* in zebrafish. Homologues for both genes have been identified, and display 59.27% and 70.49% homology of Arhgap31 and Dock6, respectively, compared to the human proteins (Figure 9, Figure 10). However there are no functional or expression data currently available for *dock6*. By contrast, *arhgap31* expression has been examined at 24 hpf by WISH and shows localisation to the developing vasculature in addition to the hypochord, hatching gland and spinal cord (Gomez et al., 2012). Overexpression of the major angiogenic transcription factor ETS-related protein (Etsrp) results in increased *arhgap31* expression levels and pattern, suggesting downstream regulation of Arhgap31 by Etsrp and further implying a vascular role for Arhgap31 in zebrafish (Gomez et al., 2012). However, the function of Arhgap31 during early zebrafish development is yet to be examined.

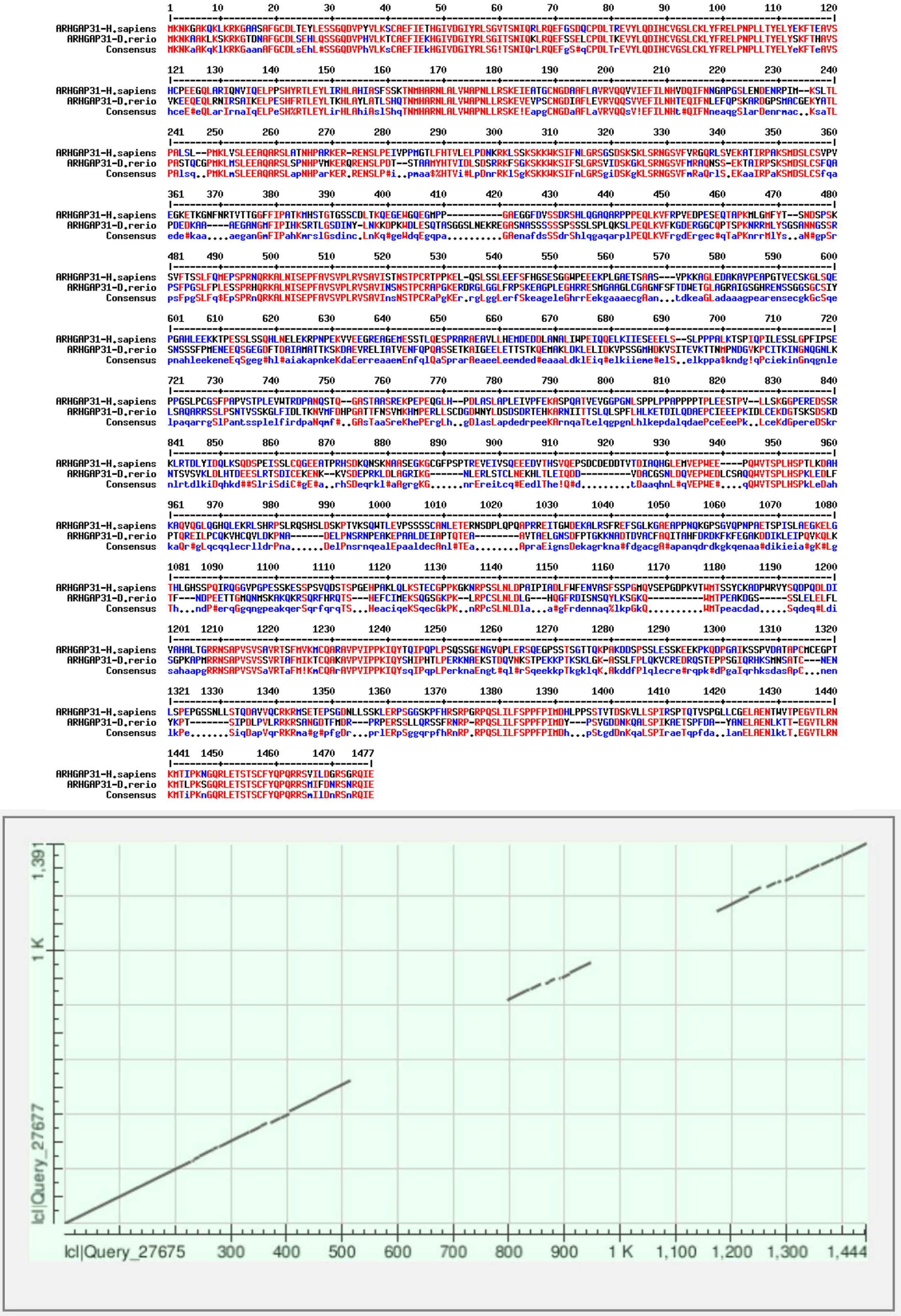

Figure 9: The degree of homology between the human and zebrafish ARHGAP31 proteins.

(**a**) Multiple alignment sequences generated by MultAlin and (**b**) dotplots made using Blast2Seq demonstrate 59.27% protein homology of ARHGAP31 between human and zebrafish.

Further, no studies have linked Arhgap31 and Dock6 to regulation of the zebrafish Rac1 and Cdc42 homologues Rac1a, Rac1b and Cdc42, respectively (Salas-Vidal et al., 2005). While there is limited information available for Rac1b, studies investigating Rac1a indicate ubiquitous expression throughout the zebrafish at all stages of development and during adulthood (Epting et al., 2015; Mikdache et al., 2020; Salas-Vidal et al., 2005). Knockdown of *rac1a* has been found to impact fast muscle myoblast fusion, heart bilateral symmetry and looping, as well as the development of neurons in the posterior lateral line ganglion (Epting et al., 2015; Mikdache et al., 2020; Srinivas et al., 2007). Expression studies of *cdc42* show similarly ubiquitous localisation throughout embryogenesis and in adulthood, consistent with mammalian expression (Hung et al., 2020; Morris et al., 2015; Salas-Vidal et al., 2005). Knockdown of *cdc42*, however, induces abnormal development of the caudal vein plexus (CVP), caudal fin, eye and brain (Choi et al., 2015, 2013; Wakayama et al., 2015). As known regulators of Rac1 and Cdc42 in mammals, it might be expected that knockdown of *arhgap31* and *dock6* would produce phenotypes expected of *rac1a* and *cdc42* knockdown, such as impaired fast muscle myoblast fusion, heart, vascular and neural development, however this remains to be elucidated.

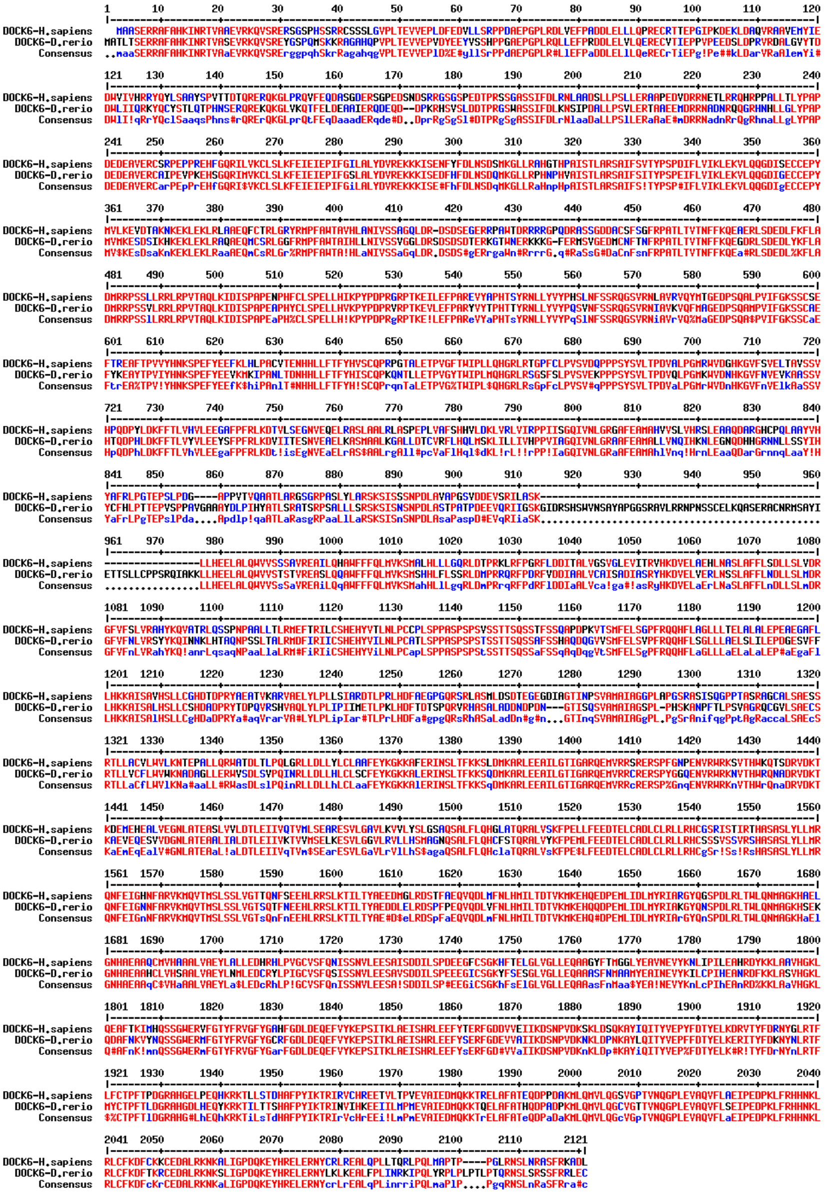

```
                1        10        20        30        40        50        60        70        80        90        100       110       120
                |--------+---------+---------+---------+---------+---------+---------+---------+---------+---------+---------+---------|
DOCK6-H.sapiens   MAASERRAFAHKINRTVAAEVRKQVSRERSGSPHSSRRCSSSLGVPLTEVVEPLDFEDVLLSRPPDAEPGPLRDLVEFPADDLELLLQPRECRTTEPGIPKDEKLDAQVRAAVEMYIE
  DOCK6-D.rerio MATLTSERRAFAHKINRTVASEVRKQVSREYGSPQMSKKRAGAHQPVPLTEVVEPVDYEEYVSSHPPGAEPGPLRQLLEFPRDDLELVLQERECVTIEPPVPEEDSLDPRVRDALGVYTD
      Consensus ..maaSERRAFAHKINRTVAaEVRKQVSREr ggpqhSkrRagahqgVPLTEVVEPlD%E#yllSrPPdAEPGPLR#LlEFPaDDLELlLQeRECrTiEPg!Pe##kLDarVRaAlemYi#

                121     130       140       150       160       170       180       190       200       210       220       230       240
                |--------+---------+---------+---------+---------+---------+---------+---------+---------+---------+---------+---------|
DOCK6-H.sapiens DWVIVHRRYQYLSAAYSPVTTDTQRERQKGLPRQVFEQDASGDERSGPEDSNDSRRGSGSPEDTPRSSGASSIFDLRNLAADSLLPSLLERAAPEDVDRRNETLRRQHRPPALLTLYPAP
  DOCK6-D.rerio DWLIIQRKYQCYSTLQTPHNSERQREKQKGLVKQTFELDEAAIERQDEQD--DPKRHSVSLDDTPRGSWASSIFDLKNSIPDALLPSVLERTAAEEMDRRNADNRQQGRHNHLLGLYPAP
      Consensus DWlI!qRrYQclSaaqsPhns#rQREr QKGLprQtFEqDaaadERqde#D..DprRgSgSl#DTPRgSgASSIFDLrNlaaDaLLPSlLERaAaE#mDRRNadnRrQgRhnaLLgLYPAP

                241     250       260       270       280       290       300       310       320       330       340       350       360
                |--------+---------+---------+---------+---------+---------+---------+---------+---------+---------+---------+---------|
DOCK6-H.sapiens DEDEAVERCSRPEPPREHFGQRILVKCLSLKFEIEIEPIFGILALYDVREKKKISENFYFDLNSDSMKGLLRAHGTHPAISTLARSAIFSVTYPSPDIFLVIKLEKVLQQGDISECCEPY
  DOCK6-D.rerio DEDEAVERCAIPEVPKEHSGQRIMVKCLSLKFEIEIEPIFGSLALYDVREKKKISEDFHFDLNSDQMKGLLRPHNPHVAISTLARSAIFSITYPSPEIFLVIKLEKVLQQGDIGECCEPY
      Consensus DEDEAVERCarPEpPrEHfGQRI$VKCLSLKFEIEIEPIFGiLALYDVREKKKISE#FhFDLNSDqMKGLLRaHnpHpAISTLARSAIFS!TYPSP#IFLVIKLEKVLQQGDIgECCEPY

                361     370       380       390       400       410       420       430       440       450       460       470       480
                |--------+---------+---------+---------+---------+---------+---------+---------+---------+---------+---------+---------|
DOCK6-H.sapiens MVLKEVDTAKNKEKLEKLRLAAEQFCTRLGRYRMPFAWTAVHLANIVSSAGQLDR-DSDSEGERRPAWTDRRRRGPQDRASSGDDACSFSGFRPATLTVTNFFKQEAERLSDEDLFKFLA
  DOCK6-D.rerio MVMKESDSIKHKEKLEKLRAQAEQMCSRLGGFRMPFAWTAIHLLNIVSSVGGLDRSDSDSDTERKGTWNERKKKG-FERMSVGEDMCNFTNFRPATLTVTNFFKQEGDRLSDEDLYKFLA
      Consensus MV$KEsDsaKnKEKLEKLRaaAEQmCsRLGr%RMPFAWTA!HLaNIVSSaGqLDR.DSDS#gERrgaWn#RrrrG.q#RaSsG#DaCnFsnFRPATLTVTNFFKQEa#RLSDEDL%KFLA

                481     490       500       510       520       530       540       550       560       570       580       590       600
                |--------+---------+---------+---------+---------+---------+---------+---------+---------+---------+---------+---------|
DOCK6-H.sapiens DMRRPSSLLRRLRPVTAQLKIDISPAPENPHFCLSPELLHIKPYPDPRGRPTKEILEFPAREVYAPHTSYRNLLYVYPHSLNFSSRQGSVRNLAVRVQYMTGEDPSQALPVIFGKSSCSE
  DOCK6-D.rerio DMRRPSSVLRRLRPVTAQLKIDISPAPEAPHYCLSPELLHVKPYPDPRVRPTKEVLEFPARYVYTPHTTYRNLLYVYPQSVNFSSRQGSVRNIAVKVQFMAGEDPSQAMPVIFGKSSCAE
      Consensus DMRRPSSlLRRLRPVTAQLKIDISPAPEaPH%CLSPELLH!KPYPDPRgRPTKE!LEFPAReVYaPHTsYRNLLYVYPqSlNFSSRQGSVRNiAVrVQ%MaGEDPSQA$PVIFGKSSCaE

                601     610       620       630       640       650       660       670       680       690       700       710       720
                |--------+---------+---------+---------+---------+---------+---------+---------+---------+---------+---------+---------|
DOCK6-H.sapiens FTREAFTPVVYHNKSPEFYEEFKLHLPACVTENHHLLFTFYHVSCQPRPGTALETPVGFTWIPLLQHGRLRTGPFCLPVSVDQPPPSYSVLTPDVALPGMRWVDGHKGVFSVELTAVSSV
  DOCK6-D.rerio FYKEAYTPVIYHNKSPEFYEEVKMKIPANLTDNHHLLFTFYHISCQPKQNTLLETPVGYTWIPLMQHGRLRSGSFSLPVSVEKPPPSYSVLTPDVQLPGMKWVDNHKGVFNVEVKAASSV
      Consensus FtrEA%TPV!YHNKSPEFYEEfK$hiPAnlT#NHHLLFTFYH!SCQPrqnTaLETPVG%TWIPL$QHGRLRsGpFcLPVSV#qPPPSYSVLTPDVaLPGMrWVDnHKGVFnVElkAaSSV

                721     730       740       750       760       770       780       790       800       810       820       830       840
                |--------+---------+---------+---------+---------+---------+---------+---------+---------+---------+---------+---------|
DOCK6-H.sapiens HPQDPYLDKFFTLVHVLEEGAFPFRLKDTVLSEGNVEQELRASLAALRLASPEPLVAFSHHVLDKLVRLVIRPPIISGQIVNLGRGAFEAMAHVVSLVHRSLEAAQDARGHCPQLAAYVH
  DOCK6-D.rerio HTQDPHLDKFFTLVYVLEEYSFPFRLKDVIITESNVEAELKASMAALKGALLDTCVRFLHQLMSKLILLIVHPPVIAGQIVNLGRAAFEAMALLVNQIHKNLEGNQDHHGRNNLLSSYIH
      Consensus HpQDPhLDKFFTLVhVLEEgaFPFRLKDt!isEgNVEaELrAS$AALrgAll#pcVaFlHql$dKL!rL!!rPP!IaGQIVNLGRaAFEAMAhlVnq!HrnLEaaQDarGrnnqLaaY!H

                841     850       860       870       880       890       900       910       920       930       940       950       960
                |--------+---------+---------+---------+---------+---------+---------+---------+---------+---------+---------+---------|
DOCK6-H.sapiens YAFRLPGTEPSLPDG----APPVTVQAATLARGSGRPASLYLARSKSISSSNPDLAVAPGSVDDEVSRILASK-----------------------------------------------
  DOCK6-D.rerio YCFHLPTTEPVSPPAVGAAAYDLPIHYATLSRATSRPSALLLSRSKSISNSNPDLASTPATPDEEVQRIIGSKGIDRSHSWVNSAYAPGGSRAVLRRNPNSSCELKQASERACNRMSAYI
      Consensus YaFrLPgTEPslPda....Apdlp!qaATLaRasgRPaaLlLaRSKSISnSNPDLAsaPaspD#EVqRIiaSK...............................................

                961     970       980       990       1000      1010      1020      1030      1040      1050      1060      1070      1080
                |--------+---------+---------+---------+---------+---------+---------+---------+---------+---------+---------+---------|
DOCK6-H.sapiens ---------------LLHEELALQWVVSSSAVREAILQHAWFFFQLMVKSMALHLLLGQRLDTPRKLRFPGRFLDDITALVGSVGLEVITRVHKDVELAEHLNASLAFFLSDLLSLVDR
  DOCK6-D.rerio ETTSLLCPPSRQIAKKLLHEELALQWVVSTSTVREASLQQAWFFFQLMVKSMSHHLFLSSRLDMPRRQRFPDRFVDDIAALVCAISADIASRYHKDVELVERLNSSLAFFLNDLLSLMDR
      Consensus ...............LLHEELALQWVVSsSaVREAiLQqAWFFFQLMVKSMahHLlLgqRLDmPRrqRFPdRFlDDIaALVca!ga#!asRyHKDVELaErLNaSLAFFLnDLLSLmDR

                1081 1090      1100      1110      1120      1130      1140      1150      1160      1170      1180      1190      1200
                |--------+---------+---------+---------+---------+---------+---------+---------+---------+---------+---------+---------|
DOCK6-H.sapiens GFVFSLVRAHYKQVATRLQSSPNPAALLTLRMEFTRILCSHEHYVTLNLPCCPLSPPASPSPSVSSTTSQSSTFSSQAPDPKVTSMFELSGPFRQQHFLAGLLLTELALALEPEAEGAFL
  DOCK6-D.rerio GFVFNLVRSYYKQINNKLHTAQNPSSLTALRMDFIRIICSHEHYVILNLPCATLSPPASPSPSTSSTTSQSSAFSSHAQDQGVVSMFELSVPFRQQHFLSGLLLAELSLILEPDGESVFF
      Consensus GFVFnLVRahYKQ!anrLqsaqNPaaLlaLRM#FiRIiCSHEHYViLNLPCapLSPPASPSPStSSTTSQSSaFSSqAqDqgVtSMFELSgPFRQQHFLaGLLLaELaLaLEP#aEgaFl

                1201 1210      1220      1230      1240      1250      1260      1270      1280      1290      1300      1310      1320
                |--------+---------+---------+---------+---------+---------+---------+---------+---------+---------+---------+---------|
DOCK6-H.sapiens LHKKAISAVHSLLCGHDTDPRYAEATVKARVAELYLPLLSIARDTLPRLHDFAEGPGQRSRLASMLDSDTEGEGDIAGTINPSVAMAIAGGPLAPGSRASISQGPPTASRAGCALSAESS
  DOCK6-D.rerio LHKKAISALHSLLCSHDADPRYTDPQVRSHVAQLYLPLIPIIMETLPKLHDFTDTSPQRVRHASALADDNDPDN---GTISQSVAMAIAGSPL-PHSKANPFTLPSVAGRQCGVLSAECS
      Consensus LHKKAISAlHSLLCgHDaDPRYa#aqVrarVA#LYLPLipIar#TLPrLHDFa#gpgQRsRhASaLadDn#g#n...GTInqSVAMAIAGgPL.PgSrAnifqgPptAgRaccaLSAEcS

                1321 1330      1340      1350      1360      1370      1380      1390      1400      1410      1420      1430      1440
                |--------+---------+---------+---------+---------+---------+---------+---------+---------+---------+---------+---------|
DOCK6-H.sapiens RTLLACVLWVLKNTEPALLQRWATDLTLPQLGRLLDLLYLCLAAFEYKGKKAFERINSLTFKKSLDMKARLEEAILGTIGARQEMVRRSRERSPFGNPENVRWRKSVTHWKQTSDRVDKT
  DOCK6-D.rerio RTLLVCFLWVWKNADAGLLERWVSDLSVPQINRLLDLLHLCLSCFEYKGKKALERINSLTFKKSQDMKARLEEAILGTIGARQEMVRRCRERSPYGGQENVRWRKNVTHWRQNADRVDKT
      Consensus RTLLaCfLWVlKNa#aaLL#RWasDLslPQinRLLDLLhLCLaaFEYKGKKAlERINSLTFKKSqDMKARLEEAILGTIGARQEMVRRcRERSP%GnqENVRWRKnVTHWrQnaDRVDKT

                1441 1450      1460      1470      1480      1490      1500      1510      1520      1530      1540      1550      1560
                |--------+---------+---------+---------+---------+---------+---------+---------+---------+---------+---------+---------|
DOCK6-H.sapiens KDEMEHEALVEGNLATEASLVVLDTLEIIVQTVMLSEARESVLGAVLKVVLYSLGSAQSALFLQHGLATQRALVSKFPELLFEEDTELCADLCLRLLRHCGSRISTIRTHASASLYLLMR
  DOCK6-D.rerio KAEVEQESVVDGNLATEAALIALDTLEIIVKTVVMSELKESVLGGVLRVLLHSMAGNQSALFLQHCFSTQRALVYKFPEMLFEEDTELCADLCLRLLRHCSSSVSSVRSHASASLYLLMR
      Consensus KaEmEqEalV#GNLATEAaL!aLDTLEIIVqTVm$SEarESVLGaVLrVlLhS$agaQSALFLQHclaTQRALVsKFPE$LFEEDTELCADLCLRLLRHCgSr!Ss!RsHASASLYLLMR

                1561 1570      1580      1590      1600      1610      1620      1630      1640      1650      1660      1670      1680
                |--------+---------+---------+---------+---------+---------+---------+---------+---------+---------+---------+---------|
DOCK6-H.sapiens QNFEIGHNFARVKMQVTMSLSSLVGTTQNFSEEHLRRSLKTILTYAEEDMGLRDSTFAEQVQDLMFNLHMILTDTVKMKEHQEDPEMLIDLMYRIARGYQGSPDLRLTWLQNMAGKHAEL
  DOCK6-D.rerio QNFEIGNNFARVKMQVTMSLSSLVGTSQTFNEEHLRRSLKTILTYAEDDLELRDSPFPEQVQDLVFNLHMILTDTVKMKEHQQDPEMLIDLMYRIAKGYQNSPDLRLTWLQNMAGKHSEK
      Consensus QNFEIGnNFARVKMQVTMSLSSLVGTsQnFnEEHLRRSLKTILTYAE#D$eLRDSpFaEQVQDLmFNLHMILTDTVKMKEHQ#DPEMLIDLMYRIArGYQnSPDLRLTWLQNMAGKHaEl

                1681 1690      1700      1710      1720      1730      1740      1750      1760      1770      1780      1790      1800
                |--------+---------+---------+---------+---------+---------+---------+---------+---------+---------+---------+---------|
DOCK6-H.sapiens GNHAEAAQCMVHAAALVAEYLALLEDHRHLPVGCVSFQNISSNVLEESAISDDILSPDEEGFCSGKHFTELGLVGLLEQAAGYFTMGGLYEAVNEVYKNLIPILEAHRDYKKLAAVHGKL
  DOCK6-D.rerio GNHAEAAHCLVHSAALVAEYLNMLEDCRYLPIGCVSFQSISSNVLEESAVSDDILSPEEEGICSGKYFSESGLVGLLEQAAASFNMAAMYEAINEVYKILCPIHEANRDFKKLASVHGKL
      Consensus GNHAEAAqC$VHaAALVAEYLa$LEDcRhLP!GCVSFQnISSNVLEESA!SDDILSP#EEGiCSGKhFsElGLVGLLEQAAasFnMaa$YEA!NEVYKnLcPIhEAnRD%KKLAaVHGKL

                1801 1810      1820      1830      1840      1850      1860      1870      1880      1890      1900      1910      1920
                |--------+---------+---------+---------+---------+---------+---------+---------+---------+---------+---------+---------|
DOCK6-H.sapiens QEAFTKIMHQSSGWERVFGTYFRVGFYGAHFGDLDEQEFVYKEPSITKLAEISHRLEEFYTERFGDDVVEIIKDSNPVDKSKLDSQKAYIQITYVEPYFDTYELKDRVTYFDRNYGLRTF
  DOCK6-D.rerio QDAFNKVYNQSSGWERMFGTYFRVGFYGCRFGDLDEQEFVYKEPSITKLAEISHRLEEFYSERFGDEVVAIIKDSNPVDKNKLDPNKAYLQITYVEPFFDTYELKERITYFDKNYNLRTF
      Consensus Q#AFnK!mnQSSGWERmFGTYFRVGFYGarFGDLDEQEFVYKEPSITKLAEISHRLEEFYsERFGD#VVaIIKDSNPVDKnKLDp#KAYiQITYVEP%FDTYELK#R!TYFDrNYnLRTF

                1921 1930      1940      1950      1960      1970      1980      1990      2000      2010      2020      2030      2040
                |--------+---------+---------+---------+---------+---------+---------+---------+---------+---------+---------+---------|
DOCK6-H.sapiens LFCTPFTPDGRAHGELPEQHKRKTLLSTDHAFPYIKTRIRVCHREETVLTPVEVAIEDMQKKTRELAFATEQDPPDAKMLQMVLQGSVGPTVNQGPLEVAQVFLAEIPEDPKLFRHHNKL
  DOCK6-D.rerio MYCTPFTLDGRAHGDLHEQYKRKTILTTSHAFPYIKTRINVIHKEEIILMPMEVAIEDMQKKTQELAFATHQDPADPKMLQMVLQGCVGTTVNQGPLEVAQVFLSEIPEDPKLFRHHNKL
      Consensus $%CTPFTlDGRAHG#LhEQhKRKTiLsTdHAFPYIKTRIrVcHrEEi!LmPmEVAIEDMQKKTrELAFATeQDPaDaKMLQMVLQGcVGpTVNQGPLEVAQVFLaEIPEDPKLFRHHNKL

                2041 2050      2060      2070      2080      2090      2100      2110      2121
                |--------+---------+---------+---------+---------+---------+---------+---------+|
DOCK6-H.sapiens RLCFKDFCKKCEDALRKNKALIGPDQKEYHRELERNYCRLREALQPLLTQRLPQLMAPTP----PGLRNSLNRASFRKADL
  DOCK6-D.rerio RLCFKDFTKRCEDALRKNKSLIGPDQKEYHRELERNYLKLKEALFPLINRKIPQLYRPLPLPTLPTQRNSLSRSSFRRLEC
      Consensus RLCFKDFcKrCEDALRKNKaLIGPDQKEYHRELERNYcrLrEALqPLinrriPQLmaPlP....PgqRNSLnRaSFRra#c
```

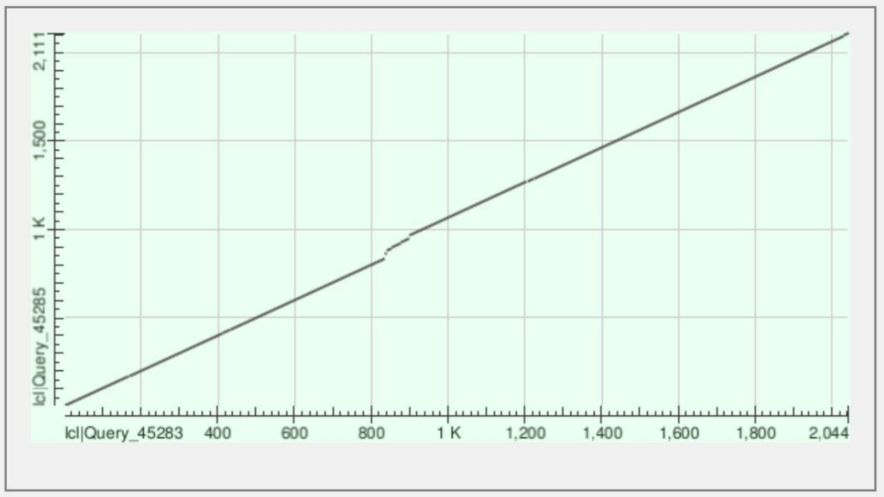

Figure 10: Conserved DOCK6 protein homology between humans and zebrafish.

(**a**) MultAlin and (**b**) Blast2Seq tools demonstrate 70.49% conservation of protein homology between human and zebrafish.

1.4.3 Zebrafish vascular development

To investigate vascular disruption in zebrafish models of AOS, it is critical to understand the various processes involved in early zebrafish vascularisation and the timeframe in which each event occurs.

1.4.3.1 Vasculogenesis

In zebrafish, vasculogenesis begins at around 14 hpf, when primitive haematopoiesis has taken place in the anterior and posterior lateral plate mesoderm (Lieschke et al., 2002; Proulx et al., 2010). By 22 hpf, zebrafish embryos have undergone vasculogenesis, whereby angioblasts from the posterior lateral plate mesoderm have migrated to the midline and assemble dorsal to the endodermal layer and ventral to the hypochord (Verma et al., 2010). Proper angioblastic migration to the midline is thought to be guided by hypochord-derived VEGF signalling (Gore et al., 2012). Once in position, these angioblasts begin to gain arterial and venous specification and form the two main axial vessels: the dorsal aorta (DA) and the posterior cardinal vein (PCV), which fully develop by the time of circulation onset at 24 hpf in the wild-type embryo (Hen et al., 2015). During vascular development, friend leukemia integration 1 (Fli1) works in combination with other ETS factors, namely Ets1 and Etsrp, to aid endothelial cell specification and differentiation (Liu et al., 2008). It can also induce the expression of other endothelial-specific genes, such as kinase insert domain receptor-like (*kdrl)*. The homolog of human VEGFR2, Kdrl has a conserved function in zebrafish and mammals in forming the endothelial and haematopoietic lineages during vasculogenesis (Ibrahim and Richardson, 2017). Vessel specification in zebrafish is also influenced by Notch signalling and displays high conservation between zebrafish and mammals (see Sections 1.2.2.2 and 1.3.1). Notch signalling in early zebrafish vessel specification is regulated by Shh and VEGF expression, through upregulation of VEGF signalling in the somites by Shh activity (Coultas et al., 2010; Lawson et al., 2002). Notch signalling is then promoted in the endothelial cells of the developing DA, leading to arterial cell specification (Lawson et al., 2001). Conversely, absence of Notch activity gives a venous cell fate.

1.4.3.2 Angiogenesis

Angiogenesis in zebrafish is defined as the point when intersegmental vessels begin to develop from the DA, at around 22 hpf. Following endothelial arterial/venous specification, endothelial cells attain either a migratory or proliferating phenotype, namely becoming tip or stalk cells, respectively (Lawson et al., 2001). Mechanistically, Kdrl activation promotes *dll4* expression which in turn up-regulates Notch activity in the neighbouring cells (Krueger et al., 2011). Cells expressing *dll4* gain a tip cell phenotype, whereas increased Notch signalling in the adjacent cells promotes stalk cell behaviour, exhibiting a conserved function between zebrafish and humans for the Notch pathway (see section 1.3.2). In zebrafish, loss of Notch signalling stimulates an increase in cells exhibiting tip cell behaviour, resulting in excess endothelial sprouting due to an abundance of migratory cells and filopodial formation (Siekmann and Lawson, 2007b). Conversely, excessive Notch signalling impairs angiogenic sprouting due to reduced tip cell specification. VEGF and Notch signalling are crucial in ISV formation (Figure 11b) as signalling Vegfa is secreted from the somites to guide the migrating endothelial sprouts and loss of *kdrl* impairs ISV development (Nasevicius et al., 2000). Endothelial tip cells initiate sprouting of new vessels from the DA and these sprouts migrate and proliferate dorsally, aided by filopodia emerging from the tip cells, mimicking the process for mammalian angiogenic sprouting (see 1.2.2.1). Upon reaching the neural tube (Figure 11a), the newly formed vessels migrate laterally to interconnect with their neighbouring ISVs to form the dorsal longitudinal anastomotic vessel (DLAV) (Figure 11b) (Isogai et al., 2003).

Once established, ISVs are believed to become lumenised via a cord-hollowing mechanism, whereby endothelial cells in the sprouting stalk overlap to form a multicellular tube by establishing cell-cell and cell-ECM contacts (Ellertsdóttir et al., 2010). The cells develop an apicobasal polarity by the aggregation of adhesive proteins to each side of the cell, which drive endothelial cell adhesion to adjacent cells and the ECM (Ellertsdóttir et al., 2010). The loss of adhesion molecules, such as VE-cadherin, leads to vascular leakage and in severe cases can cause luminal

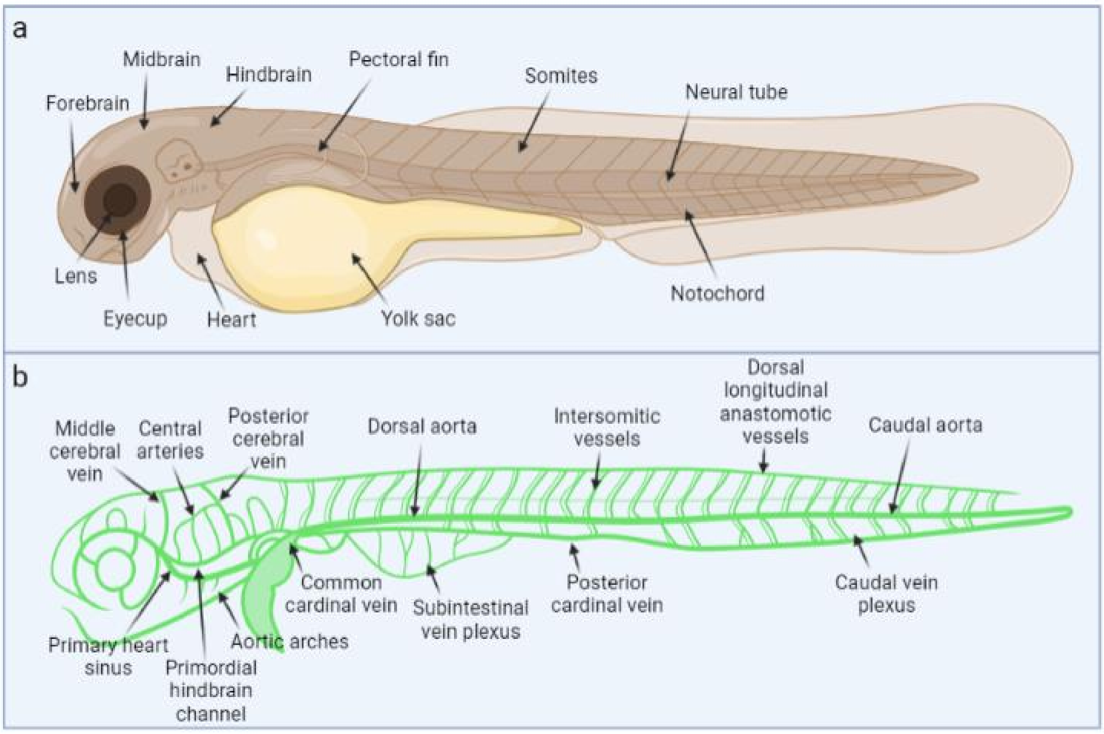

Figure 11: Schematic describing the general zebrafish anatomy and vasculature.

Labelled illustration denoting the general anatomical (**a**) and vascular (**b**) structures which have developed in the zebrafish embryo by 48 hpf.

occlusions, implying that correct formation of adherens junctions is crucial in effective lumen formation (Montero-Balaguer et al., 2009).

1.4.4 Cell models

Work using *in vitro* cell models is an informative and versatile tool which allows for the examination of basic scientific and translational research questions. Cell homogeneity in culture can be maintained through the use of selective media, mitigating the risk of cell contamination. Strict control of cell physiological conditions, such as the levels of hormones, nutrients, pH, temperature, osmolarity, contribute towards data reproducibility and provides a general insight towards molecular mechanisms in a given cell type (Miki et al., 2012). Additionally, the microenvironment of the cells can be controlled by regulating features such as the cell attachment substrate and the matrix (Katt et al., 2016).

The use of tissue culture is consistent with aims to replace, reduce and refine the use of animals in research, by providing an alternative method for investigating key research questions (Balls et al., 1995). Indeed, cell culture studies have provided a huge advancement in the knowledge of molecular pathways taking place inside of cell. Due to the sizeable interest in the use of cell culture to further research, a plethora of optimised characterisation techniques are available for use in cells, enabling fast and convenient functional investigation.

Despite the inexhaustible benefits to the use of cell culture in research, there are numerous disadvantages to consider. For example, the rapid growth of cells in cell culture leads to high chance of genetic variability in cells (Katt et al., 2016). This can lead to heterogeneity within a cell population which can be difficult to discern.

Additionally, cell culture techniques and assays are not necessarily standardised between research groups, therefore leading to lack of reproducibility of results. While primary cell cultures are the gold standard for use in research, primary cells usually have a limited number of passages, therefore the use of genetically manipulated cell lines is easier to maintain. However, due to the changes made to "immortalise" the cells, cell lines may not necessarily be representative of their original tissue type.

Further limitations apply, as cell culture mostly involves the growth of a single cell type in monolayers, whereas in the native state many cell types may be present and act upon the cell type of interest. While protocols been successfully developed to optimise three-dimensional cell culture, it is important to support findings derived from cell culture using *in vivo* methods.

1.4.4.1 In vitro functional analysis

In addition to the CRISPR-Cas9 system (see Section 1.4.1.2), gene function analysis *in vitro* can be carried out by generating knockdown models using short interfering RNA (siRNA) technology. By this mechanism, double-stranded RNA is cleaved by the RNase III family enzyme Dicer to form shorter double-stranded siRNAs (Dana et al., 2017; Xia et al., 2002). These siRNAs then bind to the RNA-induced silencing complex (RISC) and the two strands are separated, with the more stable siRNA strand becoming integrated into the RISC complex (Tang, 2005). The antisense siRNA strand guides the RISC complex to its complementary target sequence and directs cleavage of the target mRNA by the Argonaute-2 enzyme (Guang et al., 2009; Tang, 2005). This leads to mRNA degradation and therefore downregulation of the target gene. siRNA technology is used both *in vivo* and *in vitro* to target knockdown of the gene of interest by engineering double-stranded siRNA which is complementary to the target gene (Xia et al., 2002). While siRNA is widely considered an effective method for gene knockdown, off-target effects against partially complementary sites have been reported (Doench et al., 2007). Therefore, the use of controls while conducting siRNA-based experiments is essential. However, due to the versatility of models and modes of delivery, siRNA-mediated gene knockdown is a popular method for studying gene function.

1.4.4.2 In vitro expression analysis

In addition to functional analysis, many techniques have been optimised for *in vitro* expression analyses. This includes Western blot experiments which use SDS-polyacrylamide gel electrophoresis to determine protein expression levels in tissue or cell lysates. To investigate gene expression, quantitative polymers experiments can be performed to measure mRNA transcript levels, and RNA localisation within a cell can be identified by *in situ* hybridisation techniques. Further, highly specific antibodies and small molecules, such as phalloidin, are often used to examine protein localisation within a cell. High quality cell imaging can be carried out in most research facilities due the availability of equipment such as confocal microscopes, therefore enabling visualisation at a cellular and molecular level.

Due to the wide accessibility of optimised techniques to characterise molecular and cellular mechanisms *in vitro*, the development of cell models to investigate a research question is convenient and informative.

1.4.4.3 Using in vitro models to explore mechanisms of AOS pathology

As described (see Section 1.1.1), there is compelling evidence implicating disordered vascular development during embryogenesis in the pathogenesis of AOS. In particular, the role for mural cells in maintaining vascular integrity and vessel tone appears to be an important mechanism in the development of certain AOS characteristics, such as stenosis, pulmonary hypertension and TTLD (see Section 1.1.1). However, the impact of Rho dysregulation in mural cells has not yet been closely examined. Therefore, it is unclear how AOS-related mutations negatively affect mural cell function. Notably, the role for DOCK6 in maintaining the cell cytoskeleton remains largely unexplored, whereas the impact of ARHGAP31 dysregulation on cytoskeleton organisation has been investigated in several cell types (Southgate et al., 2011; Wormer et al., 2014).

1.5 Hypothesis

Adams-Oliver syndrome is hypothesised to derive from impaired vascularisation during early development. In patients with pathogenic variants in *DOCK6* or *ARHGAP31*, dysregulation of Rac1 and Cdc42 levels have been reported to disrupt cytoskeletal organisation. I therefore speculate that this leads to abnormal proliferation, migration and/or adhesion of vascular-derived cells and ultimately compromises the integrity of early embryonic blood vessels, disrupting blood flow to developing limb, scalp and cardiac structures.

1.6 Aims and objectives

Aim 1: To model Rho dysregulation in zebrafish as an investigation of impaired vascularisation in AOS.

a) Evaluate the levels and patterns of *dock6* and *arhgap31* gene expression throughout early embryogenesis and in relation to vascular development.

b) Use morpholinos to generate *dock6* and *arhgap31* knockdown models to define potential roles for these genes during early zebrafish development.

c) Independently validate gene knockdown models using CRISPR/Cas9 knockout technology in zebrafish embryos.

d) Assess and quantify the phenotypic impacts of *dock6* and *arhgap31* depletion and compare these to the vascular defects seen in AOS patients.

Aim 2: To characterise the impact of *DOCK6* knockdown on vascular and keratinocyte cell lines and examine the cellular functions contributing to AOS-related congenital abnormalities.

a. Optimise *DOCK6* knockdown models in a human aortic vascular smooth muscle cell line and a human adult keratinocyte cell line.

b. Examine the impact of *DOCK6* depletion on cytoskeletal organisation, migration, proliferation and adhesion of these cell lines.

Chapter 2: Materials and Methods

2.1 Materials

2.1.1 General reagents.

Material	**Supplier**
Aqueous Mounting Media	R&D systems
Chloroform	Merck
Dextran	Merck
Eco*RI*	New England Biolabs
Isopropanol	Merck
Methanol	Merck
Paraformaldehyde (PFA)	Merck
Phenylthiourea (PTU)	Merck
Phosphate Buffered Saline tablets (PBS)	Merck
Proteinase K	Thermo Fisher Scientific
Sodium Chloride (NaCl)	VWR
TRIzol	Invitrogen
Trypsin-EDTA	Merck
TWEEN20	Merck
Virkon Disinfectant Tablets (50 x 5g)	Camlab

2.1.2 Electrophoresis and Western blotting components

Component	**Supplier**
Ammonium persulfate	Thermo Fisher Scientific
Anti-Actin antibody [EPR16769] (ab179467)	Abcam
Anti-beta I Tubulin antibody [EPR16778] (ab179511)	Abcam
Anti-DOCK6 Rabbit Polyclonal Antibody	Proteintech
Goat Anti-Rabbit IgG H&L (HRP) preadsorbed (ab7090)	Abcam

Halt Protease Inhibitor Cocktails	Thermo Fisher Scientific
Pierce ECL Western Blotting Substrate	Thermo Fisher Scientific
Pierce BCA Protein Assay	Thermo Fisher Scientific
N,N,N′,N′-Tetramethyl Ethylenediamine (Temed), Re-distilled	Geneflow
Nonfat dried milk powder	VWR International
Novex NuPAGE LDS Sample Buffer (4X)	Thermo Fisher Scientific
Novex NuPAGE Sample Reducing Agent (10X)	Thermo Fisher Scientific
Novex NuPAGE Transfer Buffer (20X)	Thermo Fisher Scientific
Odyssey® Protein Molecular Weight Marker	Antibodies-Online
ProtoGel, 30% Solution at 37.5:1 Ratio	Geneflow
REVERT total protein staining kit	LI-COR
Sodium Dodecyl Sulfate (SDS), Lauryl	Thermo Fisher Scientific

2.1.3 Bacterial culture components

Component	**Supplier**
5-Bromo-4-chloro-3-indolyl-β-D-galactoside (X-Gal)	Thermo Fisher Scientific
Ampicillin Sodium Salt	Merck
Bacto Agar	Appleton Woods
Bacto Yeast Extract	Appleton Woods
Glycerol, 98+%, Extra Pure	Thermo Fisher Scientific
Isopropylthio-β-galactoside (IPTG)	Thermo Fisher Scientific
Kanamycin sulfate	Merck

2.1.4 Tissue culture reagents

Reagent	**Supplier**
CytoSelect™ 48-well Cell Adhesion Assay (ECM Array, Fluorometric)	Cell BioLabs

DMEM (With High 4500 mg/L Glucose)	Merck
DOCK6 siRNA (siRNA ID 2133244)	Thermo Fisher Scientific
F-10 Ham nutrient	Merck
Fetal bovine serum	Merck
L-glutamine	Merck
3-(4,5-Dimethylthiazol-2-yl)-2,5-Diphenyltetrazolium Bromide (MTT)	Biotechne Ltd (R&D Systems)
Penicillin/streptomycin (P/S)	Merck
Phalloidin-iFluor 555 Reagent (ab176756)	Abcam
Silencer™ Negative Control No. 1 siRNA	Invitrogen
Viromer® CRISPR	Cambridge Bioscience

2.1.5 Molecular biology reagents

Reagent	**Supplier**
Turbo DNase	Invitrogen
2 × PWO Mastermix	Merck
4 × RT buffer	PrimerDesign
10 mM dNTP mix	PrimerDesign
10 × Transcription buffer	Merck
ACTB probe (Assay ID: Hs00357333_g1)	Life Technologies
AllPrep DNA/RNA Mini Kit	Qiagen
Alt-R CRISPR-Cas9 crRNA	Integrated DNA Technologies
Alt-R CRISPR-Cas9 tracrRNA	Integrated DNA Technologies
Alt-R® S.p. Cas9 Nuclease V3	Integrated DNA Technologies
10 × CutSmart buffer	New England Biolabs
ARHGAP31 probe (Assay ID: Hs00393361_m1)	Life Technologies

DOCK6 probe (Assay ID: Hs01092545_m1)	Life Technologies
Duplex buffer	Integrated DNA Technologies
Electroporation Enhancer	Integrated DNA Technologies
ExoSAP-IT PCR Product Cleanup Reagent	Thermo Fisher Scientific
GAPDH probe (Assay ID: Hs02758991_g1)	Life Technologies
Gencrispr NLS-Cas9-EGFP Nuclease protein	GenScript
High Capacity cDNA Reverse Transcription kit	Thermo Fisher Scientific
HiSpeed Maxiprep kit	Qiagen
LunaScript RT SuperMix Kit	New England Biolabs
Luna Universal qPCR Master Mix	New England Biolabs
Miniprep kit	Qiagen
10 × NEBuffer 3.1	New England Biolabs
*Not*I restriction enzyme	New England Biolabs
Precision nanoScript2 RT enzyme	PrimerDesign
QuickExtract™ DNA Extraction Solution 1.0	Epicentre
Random nonamer primers	PrimerDesign
RNeasy AllPrep	Qiagen
SP6 mMessage mMachine	Thermo Fisher Scientific
SP6 polymerase	Merck
SYBR™ Safe DNA Gel Stain	Invitrogen
T7 polymerase	Merck
TaqMan Universal Master Mix II, no UNG	Thermo Fisher Scientific

2.1.6 In situ hybridisation reagents

Reagent	**Supplier**
10 × DIG labelling mix	Merck
UltraPure™ SSC, 20 ×	Invitrogen

Anti-Digoxigenin-AP, Fab fragments	Merck
P-Nitroblue tetrazolium chloride/ 5-bromo-4-chloro-3-indolyl phosphate (NBT/BCIP) Stock Solution	Merck
Roche Blocking Reagent	Merck

2.1.7 Stock solutions

Solution	**Components**
1 × PBS	1 × Phosphate Buffered Saline tablet in 200 ml distilled H_2O
20% PBTw	1 × PBS, 20% (v/v) Tween20
0.2% PBTw	1 × PBS, 0.2% (v/v) Tween20
1 × Hybe buffer	50% (v/v) Formamide, 20x SSC (25% v/v), citric acid (0.01 M final conc.), 20% PBTw (0.005% v/v), 1:150 probe
1 × Luria-Bertani (LB) agar	1.5% (w/v) Bacto Agar in 1x LB broth
1 × Luria-Bertani (LB) broth	1% (w/v) Bacto-Tryptone, 1% (w/v) NaCl, 0.5% (w/v) Yeast extract, pH 7.4
1 × MabTw	Maleic acid (0.1 M final conc.), NaCl (0.15 M final conc.), 0.2% (v/v) Tween20, pH 7.5
1× MTT solvent	4 mM HCl, 0.1% (v/v) Nonidet P-40 in isopropanol
1× Pre-Hybe buffer	Formamide (50% v/v), 20 × SSC (25% v/v), citric acid (0.01 M final conc.), 20% PBTw (0.005% v/v)
1 × RIPA buffer	150 mM NaCl, 1.0% (v/v) Nonidet P-40, 0.5% (w/v) sodium deoxycholate, 0.1% (w/v) SDS, 50 mM Tris (pH 8.0)
1 × Novex running buffer	5% (v/v) 20 × Novex NuPAGE MOPS SDS Running Buffer in distilled H_2O

1 × Novex transfer buffer	5% (v/v) 20 × Novex NuPAGE Transfer Buffer, 10% (v/v) methanol in distilled H_2O
20 × Novex NuPAGE MOPS SDS Running Buffer	50 mM MOPS, 50 mM Tris Base, 0.1% SDS, 1 mM EDTA, pH 7.7 in distilled H_2O
20 x Novex NuPAGE Transfer Buffer	25 mM Bicine, 25 mM Bis-Tris (free base), 1 mM EDTA, pH 7.2 in distilled H_2O
UltraPure™ SSC, 20 ×	3.0 M NaCl and 0.3 M sodium citrate, at pH 7.0

2.1.8 Oligonucleotides

Type	**Name**	**Sequence (5' – 3')**
Forward primer	zfActb2 sybr_Ex2Fa	CTT CCC ATC CAT CGT GGG TC
Forward primer	zfActb2 sybr_Ex2Fb	AAT TGC CGC ACT GGT TGT TG
Reverse primer	zfActb2 sybr_Ex3R	CAA TAC CGT GCT CGA TGG GG
Reverse primer	zfActb2 sybr_Ex4R	GGG GGT GTT GAA GGT CTC G
Forward primer	zfActb2 sybr_Ex5F	GCA GAA GGA GAT CAC ATC CCT GGC
Reverse primer	zfActb2 sybr_Ex6R	CAT TGC CGT CAC CTT CAC CGT TC
Forward primer	zfArhgap31_Ex2F	ACC TGT GCA GAG TTC ATC GAG
Forward primer	zfArhgap31_Ex2F_T7	TAA TAC GAC TCA CTA TAG GGA CCT GTG CAG AGT TCA TCG AG
Forward primer	zfArhgap31 sybr_Ex2F	AAC ATG GGA TTG TGG ACG GAA
Reverse primer	zfArhgap31 sybr_Ex2R	AAG TGA GAA GCG GGT TGG G
Forward primer	zfArhgap31 E2MO_Ex2F	CAG AGT TCA TCG AGA AAC ATG GG
Reverse primer	zfArhgap31 E2MO_Int2R	CCC CCA TTT CTC AGT GCT CC
Forward primer	zfArhgap31 E3MO_Ex3F	GAA CTC TGT CCT GAC CTC AC
Reverse primer	zfArhgap31 E3MO_Int3R	CAC TCC TTT TCC CCA CTC ACA
Reverse primer	zfArhgap31_Ex8R	TGA CAG ATC GCC CGA GAC T
Reverse primer	zfArhgap31_Ex8R_SP6	ATT TAG GTG ACA CTA TAG ATG ACA GAT CGC CCG AGA CT
Forward primer	zfArhgap31_Ex9F	AAA GAC TGC TAT CCG GCC AT
Forward primer	zfArhgap31 sybr_Ex9F	CTG CTA TCC GGC CAT CCA AA
Reverse primer	zfArhgap31 sybr_Ex9R	CGC TCC TTC TCG TTT CTC GT
Reverse primer	zfArhgap31_Ex10R	CCC CAC TCT GCT CCT CAT TTT
Forward primer	zfArhgap31 sybr_Ex11F	GGG GAA GAA CTG GAA ACC ACA
Reverse primer	zfArhgap31 sybr_Ex12R	AAC TAC TTC GCC GTG CTT GA
Forward primer	zfArhgap31_Ex12F	ATT GCA CCA ACT CAA ACC GAA G
Reverse primer	zfArhgap31_Ex12R	ACG TCG CAC TAT TCA TGG ACT

Forward primer	zfDll4 sybr_ex1F	GCT CTT TCT GGG AAT ATA ATC GTG G
Reverse primer	zfDll4 sybr_ex2R	AGG CGT GCA CGA ATT GC
Forward primer	zfDll4 sybr_ex8F	AAG GAC AAT GGA CGC AGC TA
Reverse primer	zfDll4 sybr_ex9R	AGT CGT TAA TGT TGA TCT CAC AGC
Forward primer	zfdock6 E2 MO_Ex1F	ACT TTA ACC AGC GAA CGG AGA
Forward primer	zfdock6 WISH_Ex2F	ATA TGG CTC CCC ACA GAT GTC
Forward primer	zfdock6 WISH_Ex2F_T7	TAA TAC GAC TCA CTA TAG GGA TAT GGC TCC CCA CAG ATG TC
Reverse primer	zfdock6 E2 MO_Int1R	AAA AGA CTG GCC CTA CGC AA
Reverse primer	zfdock6 E2 MO_Ex3R	CTG GGA CAG GTG GCT CTA TG
Reverse primer	zfdock6 E2 MO_Ex4R	TGG ATG ATA AGC CAG TCA TCA GT
Forward primer	zfDock6 sybr_Ex5F	CCT CAT CCA GCT CAA ACG TC
Reverse primer	zfDock6 sybr_Ex6R	GCA TCC GGA ATG GAG TTT T
Reverse primer	zfdock6 WISH_Ex9R	TCA GGT CAA AGT GGA AAT CCT CA
Reverse primer	zfdock6 WISH_Ex9R_SP6	ATT TAG GTG ACA CTA TAG ATC AGG TCA AAG TGG AAA TCC TCA
Forward primer	zfDock6 sybr_Ex20F	GGA CAC CTG TGT TCG CTT TT
Reverse primer	zfDock6 sybr_Ex21R	TGA TGG TCC TGG TTT CCT TC
Forward primer	zfdock6 WISH_Ex24F	CCG CCT ACA TCG AGA CTA CC
Reverse primer	zfdock6 WISH_Ex30R	CTG CAT CGT GAC TGC ATA GC
Forward primer	zfDock6 sybr_Ex41F	GAG GGC ATC TGT TCA GGA AA
Reverse primer	zfDock6 sybr_Ex42R	ACC GAG GCC AGC TTC TTA AA
Forward primer	zfdock6 WISH_Ex46F	ACG TCA TCC ACA AAG AGG AGA TT
Reverse primer	zfdock6 WISH_Ex50R	TCG TTT GCC CTC TTT CTC ACA
Forward primer	zfEef1a1 sybr_Ex2F	TCT GAT CTA CAA ATG CGG TGG AA

Reverse primer	zfEef1a1 sybr_Ex3R	GCA CAG TCA GCC TGA GAA GTA
Forward primer	zfEef1a1 sybr_Ex4F	CAG CTC AAA CAT GGG CTG G
Reverse primer	zfEef1a1 sybr_Ex6Rb	GGA TGA TGA CCT GAG CGT TG
Forward primer	zfEef1a1 sybr_Ex5F	GTA CTA CTC TTC TTG ATG CCC
Reverse primer	zfEef1a1 sybr_Ex6Ra	GTA CAG TTC CAA TAC CTC CA
Forward primer	zfFli1 sybr _Ex4F	CCG AGG TCC TGC TCT CAC AT
Reverse primer	zfFli1 sybr _Ex5R	GGG ACT GGT CAG CGT GAG AT
Forward primer	zfFli1 sybr _Ex7F	GTC CAA AAA CCC GGA TCA GC
Reverse primer	zfFli1 sybr _Ex9R	GTC TGG GTC CGT CAT CTT GA
Forward primer	zfFli1 sybr _Ex7bF	AGC GGA AAA GGC TCT CCA AC
Reverse primer	zfFli1 sybr _Ex9bR	AAC TCT CCG TTG GTT CCT TCC
Forward primer	zfKdrl sybr _Ex2F	CCT TCA GCA TGT TGG TGG GA
Reverse primer	zfKdrl sybr _Ex3R	TCG CTG GAC TTC TTG TGA CTG
Forward primer	zfKdrl sybr _Ex10F	CCA TGT GAC CCC AGT GCT AA
Reverse primer	zfKdrl sybr _Ex12R	CCG GTT GCC AAG TTC ATT CC
Forward primer	zfKdrl sybr _Ex22F	AAG TGG CTA AAG GCA TGG AGT
Reverse primer	zfKdrl sybr _Ex24R	CTT GTC AAA AAT GGC CTC TGG C
Forward primer	zfNotch1a sybr_ex4F	GAG GTG GGC TCT TAC CTG TG
Reverse primer	zfNotch1a sybr_ex5R	TAG GTG TTG ATG CCG TCG AT
Forward primer	zfNotch1a sybr_ex14F	TGG CTG GAT TCA AGT GCA AC
Reverse primer	zfNotch1a sybr_ex16R	ATT AGT GCA CGG GTT CCT CA
Forward primer	zfNotch1a_Ex3F	GAT GCA GGG CAA TGA AGT GG
Reverse primer	zfNotch1a_Ex6R	GCA GTC GTC GAT GTT TTC GC
Forward primer	zfNotch1a_Ex15F	CTC CTG TAA CTG TCC GGC TG
Reverse primer	zfNotch1a_Ex20R	AGA CAC ACC TTG CTG TCT GG
Forward primer	zfNotch1a_Ex22F	CAG CGG ATC CTA CAA CTG TGT
Reverse primer	zfNotch1a_Ex25R	AGT GAC CGT CCG CAT AGT GA
Reverse primer	huDOCK6cDNA_Ex5Int_seq_5’R	GCT GTA TGC TGC ACT CAG GT
Forward primer	Human_DOCK6Ex3F	CCC TCA GGG ACC TGG TAG AA
Reverse primer	Human_DOCK6Ex7R	CAC GGC TTC ATC CTC GTC A

Forward primer	Human_DOCK6Ex6F	CAG AAG ATG TGG ACC GGC G
Reverse primer	Human_DOCK6Ex11R	CTT CTC TTT GTT CTT GGC TGT GTC
Forward primer	Human_DOCK6Ex9F	TTC CTG GTC ATC AAG TTG GAG AAG
Reverse primer	Human_DOCK6Ex14R	TTG ATA TGA AGC AGC TCA GGG G
Forward primer	Human_DOCK6Ex13F	GAC TAC GTC CTG TGA CTG CC
Reverse primer	Human_DOCK6Ex18R	AAG TAA AGC CCA CGG GTG TC
Forward primer	Human_DOCK6Ex17F	TTC TAC GAG GAG TTC AAG CTG C
Reverse primer	Human_DOCK6Ex21R	ACG GCC CAG GTT CAC AAT C
Forward primer	Human_DOCK6Ex20F	TGG ACA AGC TCG TGC GTC
Reverse primer	Human_DOCK6Ex24R	CAG CGC CAT ACT CTT CAC CAT
Forward primer	Human_DOCK6Ex22F	CAG CAA GCT GCT TCA CGA G
Reverse primer	Human_DOCK6Ex26R	ACG TAG TGC TCG TGG CTG
Forward primer	Human_DOCK6Ex25F	GGT CCG GGC CCA CTA CA
Reverse primer	Human_DOCK6Ex29R	CCT TCT GTG TCT GAG TCA AGC AT
Forward primer	Human_DOCK6Ex28F	CTA TCG ATT GCA CGG GAT ACC T
Reverse primer	Human_DOCK6Ex31R	CGA CTT CGC CGA ACC ATT TC
Forward primer	Human_DOCK6Ex31F	GAA CGC ATC AAC AGC CTC AC
Reverse primer	Human_DOCK6Ex35R	TGT CGC ATG AGC AGG TAC AG
Forward primer	Human_DOCK6Ex34F	CCC TTG TGT CCA AGT TCC CG
Reverse primer	Human_DOCK6Ex38R	TGT TCT GCA ACC AGG TCA GC
Forward primer	Human_DOCK6Ex37F	CCC TGA GAT GCT CAT CGA CC
Reverse primer	Human_DOCK6Ex42R	GAA ATA CGT CCC GAA CAC GC
Forward primer	Human_DOCK6Ex39F	CTA CTT CAC CAT GGG CGG G
Reverse primer	Human_DOCK6Ex44R	CTT ACG CTT GTG TTG CTC GG
Forward primer	Human_DOCK6Ex44F	GGT GAC CTA CTT TGA CCG CA
Reverse primer	Human_DOCK6Ex47R	GCT CAC GGT GGT ACT CCT TC
Reverse primer	huDOCK6cDNA_Ex45Int_seq_3’F	TAC AGA TGG TGC TTC AGG GC
crRNA	IDT gRNA1_zfdock6_Ex3	AGAGCCACCTGTCCCAGAAG

crRNA	IDT gRNA2_zfdock6_Ex6	GGA TGA CCC AAA GAG GCA CT
crRNA	IDT gRNA3_zfdock6_Ex17	CCG AGT TCT ATG AGG AGG TG
Morpholino	Dock6_Ex1 (*dock6*-E1)	CTC GCC AAA CTT CTC CTA CCT GTT A
Morpholino	Dock6_Ex2 (*dock6*-E2)	ACC GTC CTG AGA AAG ACA AAA CAC A
Morpholino	Arhgap31_Ex2 (*arhgap31*-E2)	TCA AAC AAA ACT GTC CGA CCT GAG T
Morpholino	Arhgap31_Ex3 (*arhgap31*-E3)	TCC CCA CTC ACA CAA CTT ACT GTA A

2.2 General molecular biology methods

2.2.1 Plasmids

Plasmid name	**Description**	**Antibiotic resistance**	**Source**
pFli1 plasmid	Contains fli1-specific riboprobe for ISH use	Kanamycin	Addgene (Lawson et al., 2001)
Tol2(*dock6:*mCherry)	Contains mCherry transcript expressed under the dock6 promoter, to report dock6 expression localisation	Ampicillin	VectorBuilder
pcDNA3-EGFP	Contains EGFP transcript to report transfection efficiency	Ampicillin	Addgene
Human DOCK6 ORF clone (DYKDDDDK Tag)	Full DOCK6 transcript fused to DYKDDDDK Tag	Ampicillin	Genscript
HuDOCK6_c.3154G-A	Contains DOCK6 transcript with c.3154G>A missense mutation	Ampicillin	Genscript
HuDOCK6_c.4786C-T	Contains DOCK6 transcript with c.4786C>T missense mutation	Ampicillin	Genscript
HuDOCK6_WT	Contains DOCK6 transcript	Ampicillin	Genscript
pCS2FA CO Tol2 TPase	Expression vector for codon optimized Tol2 transposase	Ampicillin	Addgene

2.2.1.1 Bacterial culture

To generate plasmid stocks, each bacterial stab/glycerol stock was streaked, using a sterile inoculation loop, onto IPTG/X-gal Luria-Bertani (LB) agar plates containing 100 µg/ml ampicillin or 50 µg/ml kanamycin, according to the antibiotic resistance of the plasmid. The agar plates were incubated at 37 °C for 16 hr to grow bacterial colonies. Individual white colonies were picked to inoculate 5 ml of LB media, containing 100 µg/ml ampicillin or 50 µg/ml kanamycin, to grow a starter colony overnight at 37 °C in a shaking incubator. From this starter colony, 1 ml was used in a miniprep and sequencing experiment, as described in Sections 2.2.1.2 and 2.2.1.3, to verify the plasmid sequence. The remaining 4 ml was used to inoculate 200 ml of antibiotic-containing LB media, which was incubated overnight at 37 °C with shaking at 225 rpm to culture enough bacteria to perform a maxiprep, as described in Section 2.2.1.2.

2.2.1.2 Plasmid DNA isolation

Bacterial cells were harvested from 1 ml or 200 ml of bacterial culture, prepared as described in Section 2.2.1.1, by centrifuging at 6,800 × *g* for 3 min or 6,000 × *g* for 15 min at room temperature for use in miniprep or maxiprep, respectively. The supernatant was discarded into Virkon and the bacterial pellet resuspended in 250 µl or 10 ml of buffer P1 with RNase A (Qiagen), respectively. The plasmid was then isolated from the bacterial cells according to manufacturer's instructions. The extracted plasmid DNA was quantified by measuring UV absorbance using a NanoDrop 2000 spectrophotometer (Thermo Fisher Scientific). Sample purity was verified by obtaining a 260/280 ratio of 1.7-2.0 and a 230/260 ratio of ≥2.0.

2.2.1.3 Plasmid sequence verification

To sequence validate purified plasmid DNA, a 1.5 ml microcentrifuge tube was prepared for each reaction for sequence analysis using the GATC LightRun Tube Sanger sequencing service (Eurofins Genomics). In each tube, 80-100 ng/µl (final concentration) of plasmid, 2.5 µl of primer (10 µM) and water to a total volume of 10 µl per reaction were combined. The tubes were individually barcoded for identification. Sequence results were received in a fasta format, which were analysed by an alignment with the reference genome using Benchling software. Sequence chromatograms (.ab1 files) were visualised using FinchTV software. Validated plasmids containing sequences identical to the reference genome were used in a maxiprep to isolate high-quality plasmid DNA. Primer sets huDOCK6cDNA_Ex5Int_seq_5’R – huDOCK6cDNA_Ex45Int_seq_3’F (see Section 2.1.8) were used to verify plasmids HuDOCK6_WT, HuDOCK6_c.3154G>A and HuDOCK6_c.4786C>T.

2.2.1.4 Making glycerol stocks

Glycerol stocks of the plasmids were made by combining 750 µl of starter culture (see Section 2.2.1.1) with 250 µl of sterile 80% glycerol. The mixture was homogenised and stored at -80 °C.

2.2.1.5 Plasmid linearisation

Plasmids were linearised by incubation with the appropriate restriction enzyme and buffer, according to Section 2.2.1.5. Plasmid linearisation was verified by gel electrophoresis (see Section 2.2.5) and band visualisation of the digested plasmid against the uncut plasmid.

Table 1: Plasmid linearisation assembly

Reagent	**Volume (µl)**
10 × NEBuffer 3.1	2
*Not*I restriction enzyme	2
Plasmid	~1 µg
Nuclease-free H_2O	To 20 µl

2.2.2 Zebrafish RNA extraction

RNA was extracted from 50 wildtype embryos using TRIzol (Invitrogen). First, the embryos were homogenised in a 1.5 ml microcentrifuge tube in 50 µl TRIzol and incubated at room temperature for 5 min. After addition of 10 µl chloroform, the tube was incubated at room temperature for a further 3 min. The sample was then centrifuged at 12,000 × *g*, 4 °C for 15 min and the colourless upper aqueous phase containing RNA was collected. Following precipitation with 25 µl isopropanol, RNA samples were incubated for 10 min at room temperature and then centrifuged at 12,000 × *g*, 4 °C for 10 min. The supernatant was removed and the residual gel-like pellet washed with 50 µl 70% ethanol and centrifuged at 12,000 × *g*, 4 °C for 5 min. After air-drying, the RNA pellet was dissolved in 10 µl nuclease-free water. The extracted RNA was quantified using a NanoDrop 2000 spectrophotometer. Sample purity was verified by obtaining a 260/280 ratio of ≥1.8 and a 230/260 ratio of ≥2.0.

2.2.3 Reverse transcription

Extracted RNA was DNase-treated to remove residual genomic DNA, using ~7,000 ng of RNA, 1 µl of 10 × Turbo DNase buffer (Invitrogen), 1 µl of Turbo DNase (Invitrogen) and nuclease-free H_2O to 10 µl total volume. This reaction was incubated at 37 °C for 15 min. After RNA quantification and purity verification by NanoDrop (see Section 2.2.1.2), complementary DNA (cDNA) was synthesised using the LunaScript RT SuperMix Kit (New England Biolabs) with 1 µg of RNA as per manufacturer's instructions.

2.2.4 Polymerase chain reaction

Polymerase chain reaction (PCR) components were assembled as detailed in Table 2 and amplified according to the cycling parameters in Table 3.

Table 2: PCR reaction assembly

Component	**Volume (µl)**
2 × PWO Mastermix	25
10 µM forward primer	2
10 µM reverse primer	2
cDNA (100-500 ng/µl)	1
Nuclease-free H_2O	To 50 µl

Table 3: General PCR program parameters

Temperature (°C)	**Time**	**Cycles**

94	2 min	1
94	30 s	35
Variable (56-60)	30 s	
72	Variable (1 min/kb)	
72	5 min	1

2.2.5 Gel electrophoresis

Following amplification, 8 µl PCR products and 2 µl of 5 × loading dye were loaded onto a 1% (w/v) agarose gel containing SYBR Safe (7 µl per 100 ml) and electrophoresed for 30 min at 125 V, before visualisation on a UV transilluminator. Primer pairs generating a single band at the correct size were chosen for use in *in situ* hybridisation probe synthesis.

2.3 Experimental models

2.3.1 Fish husbandry

All zebrafish studies were conducted in accordance with Home Office regulations, under appropriate establishment, project and personal licences as required by the Animals (Scientific Procedures) Act 1986 (ASPA). Embryos were collected via breeding tanks under a light-conditioned system and injections took place at the one-cell stage where possible. Collected embryos were incubated at 28 °C and, when grown to adulthood, added to the main aquaria at 5 days post fertilisation (dpf).

2.3.2 Zebrafish lines

Experiments from Sections 2.4.2-2.4.7.5 were performed on embryos with a King's wild-type background. Vascular reporter *tg(fli1*:EGFP) zebrafish embryos kindly gifted by Dr Paul Frankel (UCL) were used for experiments from Sections 2.4.7.6 and 2.4.7.8. A *dock6*:mCherry transgenic zebrafish line was used for the experiments described in Section 2.4.

2.3.3 Human cell lines

Mammalian cell culture was conducted using either an in-house vascular smooth muscle cell (VSMC) line, derived from primary human aorta smooth muscle cells transfected with a pSV3ne plasmid (Harris et al., 2006), or HaCaT keratinocytes (Arcidiacono et al., 2018).

2.3.4 Cell maintenance

VSMCs were incubated at 37 °C and 5% CO_2 and maintained with F-10 Ham nutrient media containing 1% P/S (penicillin (10,000 U/ml)/streptomycin (10 mg/ml)), 1% L-glutamine and 10% fetal bovine serum, replaced every two days. HaCaT cells were maintained similarly in Dulbecco's Modified Eagle Medium (DMEM) with high glucose, supplemented with 1% P/S, 1% L-glutamine and 5% FBS. The cells were routinely passaged at ~80% confluency by aspirating the media from the 75 cm^2 culture flask and washing the cells with 3 ml of 1 × PBS to remove residual media. To detach the cells, 3 ml Trypsin-EDTA solution (0.25% trypsin) was added and the flask was incubated at 37 °C for 3-5 min, or until the majority of cells were detached. To neutralise the trypsin-EDTA, 3 ml of serum-containing media was added to the flask and the entire volume was transferred to a 15 ml tube for centrifugation at 200 × *g* for 5 min. After aspiration of the supernatant, the cell pellet was resuspended in complete media, dispensed into fresh culture flasks and incubated at 37 °C.

2.4 Zebrafish studies

2.4.1 Primer design

To quantify *dock6* and *arhgap31* gene expression during zebrafish development, three sets of primers per gene were designed to amplify 200 bp amplicons in the *actb2* (primer sets zfActb2 sybr_Ex2Fb – Ex3R, zfActb2 sybr_Ex2Fa – Ex4R, zfActb2 sybr_Ex5F – Ex6R), *eef1a1* (primer sets zfEef1a1 zfEef1a1 sybr_Ex2F – Ex3R, zfEef1a1 sybr_Ex4F – Ex6Rb, sybr_Ex5F – Ex6Ra), *dock6* (primer set zfDock6 sybr_Ex5F – Ex6R, zfDock6 sybr_Ex20F – Ex21R, zfDock6 sybr_Ex41F – Ex42R), *arhgap31* (primer sets zfArhgap31 sybr_Ex2F – Ex2R, zfArhgap31 sybr_Ex9F – Ex9R, zfArhgap31 sybr_Ex11F – Ex12R), *fli1* (primer sets zfFli1 sybr – Ex5R, zfFli1 sybr_Ex7F – Ex9R, zfFli1 sybr_Ex7bF – Ex9bR), *kdrl* (primer sets zfKdrl sybr_Ex2F – Ex3R, zfKdrl sybr_Ex10F – Ex12R, zfKdrl sybr_Ex22F – Ex24R), *dll4* (primer sets zfDll4 sybr_Ex1F – Ex2R, zfDll4 sybr_Ex8F – Ex9R) and *notch1a* (primer sets zfNotch1a sybr_Ex4F – Ex5R, zfNotch1a sybr_Ex14F – Ex16R) genes in a 2-step Sybr-based qPCR. The reference genes *actb2* and *eef1a1* were chosen due to previous independent experiments which demonstrated stability in their gene expression (Hu et al., 2016; Papasani et al., 2006). Reverse transcriptase-PCR (RT-PCR) followed by gel electrophoresis of the amplified fragment confirmed that the expected product sizes of approximately 200 bp were generated, with no non-specific bands present (Figure 63). The *dock6* primer pair amplifying exons 5-6 showed only a band marking primer-dimer formation, as in the negative control lane, indicating that PCR amplification was not successful for these primers.

2.4.2 Analysis of gene expression in early zebrafish embryogenesis

To quantify *dock6* and *arhgap31* gene expression, C_q values generated by qPCR were normalised against the reference genes *actb2* and *eef1a1*. For the *arhgap31*, *actb2* and *eef1a1* genes, melt curve analysis confirmed the suitability of using the primer pairs generating the strongest bands by gel electrophoresis, as these pairs gave rise to consistent, single-peak melt curves (Figure 64). However, the strongest-performing primers, targeting *dock6* exons 20-21, were found to give inconsistent, poor melt curves (Figure 64).

To optimise qPCR conditions, 2-fold serial dilutions (200 ng, 100 ng, 50 ng, 25 ng) of cDNA were prepared to determine the most effective concentration and best primer efficiency for cDNA quantification. Primers with 100% efficiency were used for all subsequent experiments and the most effective cDNA quantity (200 ng) was selected. Based on primer efficiency, melt curve analyses and RT-PCR results, *actb2* set zfActb2 sybr_Ex2Fa – Ex4R, *eef1a1* set zfEef1a1 sybr_Ex2F – Ex3R, *dock6* set zfDock6 sybr_Ex41F – Ex42R *arhgap31* set zfArhgap31 sybr_Ex2F – Ex2R, *fli1* set zfFli1 sybr_Ex7F – Ex9R and *kdrl* set zfKdrl sybr_Ex2F – Ex3R were used for all subsequent qPCR experiments.

2.4.2.1 Quantitative PCR

To measure *dock6* and *arhgap31* transcript levels, zebrafish embryos were collected, treated with methylene blue to prevent infection and incubated at 28.5 °C until the fish reached the desired developmental stage. Approximately 50 embryos were collected from each of developmental stages 14 hpf, 24 hpf, 48 hpf, 72 hpf and 4 dpf. RNA was extracted with TRIzol and reverse-transcribed as previously described (see

Section 2.2.3). Experiments were repeated across three independent RNA samples per developmental time point.

Table 4: qPCR reaction assembly

Components	**Volume (µl)**
2 × Universal qPCR Master Mix	10
10 µM forward primer	0.5
10 µM reverse primer	0.5
cDNA (200 ng/µl)	1
Nuclease-free H_2O	To 20 µl

The Luna Universal qPCR Master Mix (New England Biolabs) was used for the qPCR experiments in 20 µl reactions (Table 4). Each reaction was performed in experimental triplicate. To confirm there was no genomic contamination, no-reverse transcriptase (NO-RT) controls used DNase-treated RNA instead of cDNA. To test for contamination or primer-dimer formation, no-template controls (NTC) were set up, using nuclease-free water in place of the cDNA sample.

Table 5: qPCR parameters to measure gene expression using Luna Universal qPCR Master Mix.

Stage	Temperature (°C)	Time	No. of cycles
Initial denaturation	95	60 s	1
Denaturation	95	15 s	40
Amplification	60	30 s	
Melt curve	60-95	Variable	1

The qPCR cycle parameters are detailed in *Table 5*. The melt curve final step was used to detect any non-specific amplification which could skew the gene expression results.

2.4.2.2 *Reference gene validation*

To verify the suitability of the chosen reference genes to normalise target gene expression, BestKeeper software (Pfaffl et al., 2004) was used to assess the stability of reference gene expression across zebrafish embryogenesis. This software calculated the Pearson correlation coefficient using the Cq values generated by eight samples from stage 14 hpf to 4 dpf, amplified using *actb2* or *eef1a1* primer sets. A regression analysis was performed to generate a *p* value for each primer set. Genes with a *p* value ≤0.05 were considered stable across zebrafish embryogenesis, therefore representing a suitable reference.

2.4.3 *In situ* hybridisation

Three sets of primers per gene were designed to isolate 800 bp amplicons of *dock6* (primer sets zfdock6 WISH_Ex2F – Ex9R, zfdock6 WISH_Ex24F – Ex30R, zfdock6 WISH_Ex46F – Ex50R), *arhgap31* (primer sets zfArhgap31_Ex2F – Ex8R, zfArhgap31_Ex9F – Ex10R, zfArhgap31_Ex12F – Ex12R), *kdrl* (primer sets zfKdrl_Ex10F – Ex15R, zfKdrl_Ex17F – Ex25R, zfKdrl_Ex18F – Ex26R) and *notch1a* (primer sets zfNotch1a_Ex3F – Ex6R, zfNotch1a _Ex15F – Ex20R, zfNotch1a _Ex22F – Ex25R) with the dual purpose of assessing expression of these transcripts during early embryogenesis and generating *in situ* hybridisation probes. The primers were designed by inputting the fasta sequence for each gene, extracted from zebrafish genome assembly GRCz11 (Ensembl), into Primer-BLAST (NCBI). Primer parameters were set as default to the Danio rerio (taxid:7955) genome, with the exceptions of the primer melting temperatures (Tm), which were amended to a range of 59-61 °C with a maximum Tm difference of 1 °C, and the PCR product size which was set to between 700 bp and 900 bp. Primer pairs with the fewest potential nonspecific products and a GC% content between 40-60% for each gene were manufactured by Integrated DNA Technologies (IDT) as unmodified 25 nm desalted oligonucleotides.

2.4.3.1 Probe template preparation

The optimal primer sets for *dock6, arhgap31, kdrl* and *notch1a* were zfdock6 WISH_Ex2F – zfdock6 WISH_Ex9R, zfArhgap31_Ex2F – zfArhgap31_Ex8R, zfKdrl_Ex17F – zfKdrl_Ex25R and zfNotch1a_Ex3F – zfNotch1a_Ex6R respectively, each of which generated amplicons of ~800 bp in length (Figure 66) using the previously described PCR procedure (see Section 2.2.4). To facilitate sense and antisense transcription, the T7 promoter sequence (5′ TAATACGACTCACTATAG 3′) was added to the 5′ of each forward primer and the SP6 promoter sequence (5′ ATTTAGGTGACACTATAG 3′) added to the 5′ of each reverse primer. PCR reactions generating bacterial promoter-flanked templates used primer sets zfdock6 WISH_Ex2F_T7 – zfdock6 WISH_Ex9R_SP6 and zfArhgap31_Ex2F_T7 – zfArhgap31_Ex8R_SP6. Following gel electrophoresis and visualisation, fragments of the correct size were excised, and cDNA amplicons extracted using a Monarch Gel Extraction kit (New England Biolabs), according to manufacturer's instructions. The PCR products were then quantified using NanoDrop according to Section 2.2.1.2. *In situ* hybridisation (ISH) riboprobes for the *fli1* gene were synthesised from a pFli1 plasmid prepared as described in Section 2.2.1.2. The plasmid was linearised by incubation with Eco*RI* restriction enzyme and CutSmart buffer at 37 °C for 30 min according to Section 2.2.1.5. To verify that the correct templates were amplified, all excised and purified bands for *dock6*, *arhgap31*, *fli1* and *kdrl* were sequenced as described in Section 2.2.1.3.

2.4.4 PCR amplification of vascular marker *in situ* hybridisation fragments

To compare *dock6* and *arhgap31* gene expression localisation to that of vascular markers during early development, primers targeting intron-spanning regions of each gene were designed. PCR and gel electrophoresis of the resulting fragment was used to confirm that the expected product size was being generated (Figure 66). Based on visualisation of the amplified fragments, primer pairs targeting exons 17-25 of *kdrl* were used to amplify a ~800 bp partial template for the synthesis of a DIG-labelled RNA WISH probe for each gene.

2.4.4.1 RNA probe transcription

To transcribe the sense and antisense digoxigenin (DIG)-labelled RNA probes, a DIG-labelling mix (Sigma-Aldrich) was used according to manufacturer's instructions, with T7 or SP6 polymerase to transcribe the sense or antisense strand of the template, respectively. The products were then treated with 1 µl of Turbo DNase and incubated at 37 °C for 15 min. After addition of 30 µl of nuclease-free H_2O to each probe, the resulting 50 µl of DIG-labelled probes were purified using Probequant G-50 microcolumns (Merck), according to the manufacturer's protocol. Gel electrophoresis was used to verify RNA probe product size and stability, as previously described (see Section 2.2.5).

2.4.4.2 In situ hybridisation across developmental stages

2.4.4.2.1 Fixation

Fifty phenylthiourea (PTU)-treated wildtype embryos were selected from each developmental stage (12 hpf, 16 hpf, 24 hpf, 48 hpf, 72 hpf) and fixed overnight in 4% paraformaldehyde (PFA) at 4 °C. The embryos were then dehydrated, undergoing 3 × 10 min washes at room temperature on a shaker (**Table *6***).

Table 6: Embryo fixation in paraformaldehyde.

Reagent	Time	Conditions
4% (v/v) paraformaldehyde	Overnight	4 °C
0.2% PBTw	10 min	Room temperature on a shaker
PBTw:100% MeOH	10 min	
100% MeOH	10 min	
100% MeOH	N/A	Storage at -20 °C

2.4.4.2.2 Hybridisation

When required, the embryos were rehydrated in 0.2% PBTw using sequential washes (Table 7). For each gene (*arhgap31*, *dock6*, *fli1, kdrl*), embryos were selected for staining: 10 per developmental stage needed for positive control (*myf5*), 20 per negative control (sense probes) and 20 per experiment (antisense probes).

Table 7: Embryo rehydration for WISH

Reagent	**Time**	**Conditions**
0.2% PBTw:100% MeOH	10 min	Shaking at RT
0.2% PBTw	10 min	Shaking at RT

0.2% PBTw: pre-Hybe buffer	10 min	Shaking at RT
Pre-Hybe buffer	10 min	65 °C
Pre-Hybe buffer	> 1 h	Shaking at 65 °C

Following pre-hybridisation, pre-Hybe buffer was then replaced with Hybe buffer containing a 1:150 dilution of probe and left overnight on the shaker at 65 °C. The next day, the probe-containing Hybe was removed and the embryos further washed for 10 min per solution at 65 °C (Table 8).

Table 8: WISH continued

Reagent	Time	Conditions
Hybe buffer	10 min	65 °C
Hybe buffer: 2 × SSC	10 min	65 °C
2 × SSC	10 min	65 °C
0.2 × SSC	10 min	65 °C
0.2 × SSC:MabTw	10 min	RT
MabTw	10 min	RT
Blocking reagent	>1 h	Shaking at RT
Anti-DIG antibody (1:2000 in Blocking reagent)	10 min	Shaking at RT
	Overnight	4 °C
	1 h	Shaking at RT

2.4.4.2.3 Stain development

Following hybridisation, embryos were washed in fresh MabTw for 4 × 10 min with shaking at room temperature, followed by 2 × 10 min washes with BCL III buffer to equilibrate the embryos. The BCL III buffer was replaced with a developing BCL III buffer, containing 20 µl/ml of NBT/BCIP, then the embryos were incubated at room temperature with shaking and protected from light to develop colour staining. After 2 hr of incubation, the developing BCL III buffer was replaced with 100% MeOH for 10 min at room temperature with shaking. The MeOH was then replaced with 0.2% PBTw, and the stained embryos were incubated at 4 °C in the dark until imaging the next day using a Nikon Digital Sight DS-L3 camera.

2.4.5 Dock6:mCherry transgenic

2.4.5.1 Plasmid design

To visualise *dock6* gene expression during early zebrafish development and support observations from the WISH experiments, a transgenic construct was designed using VectorBuilder to express mCherry under the *dock6* promoter. The promoter was chosen as the 1.5 kbp of sequence immediately upstream of the *dock6* gene. The resulting construct was 5,085 bp in length and contained the transposon Tol2 sequence, flanking the *dock6* promoter and mCherry sequence (Figure 12, Table 9).

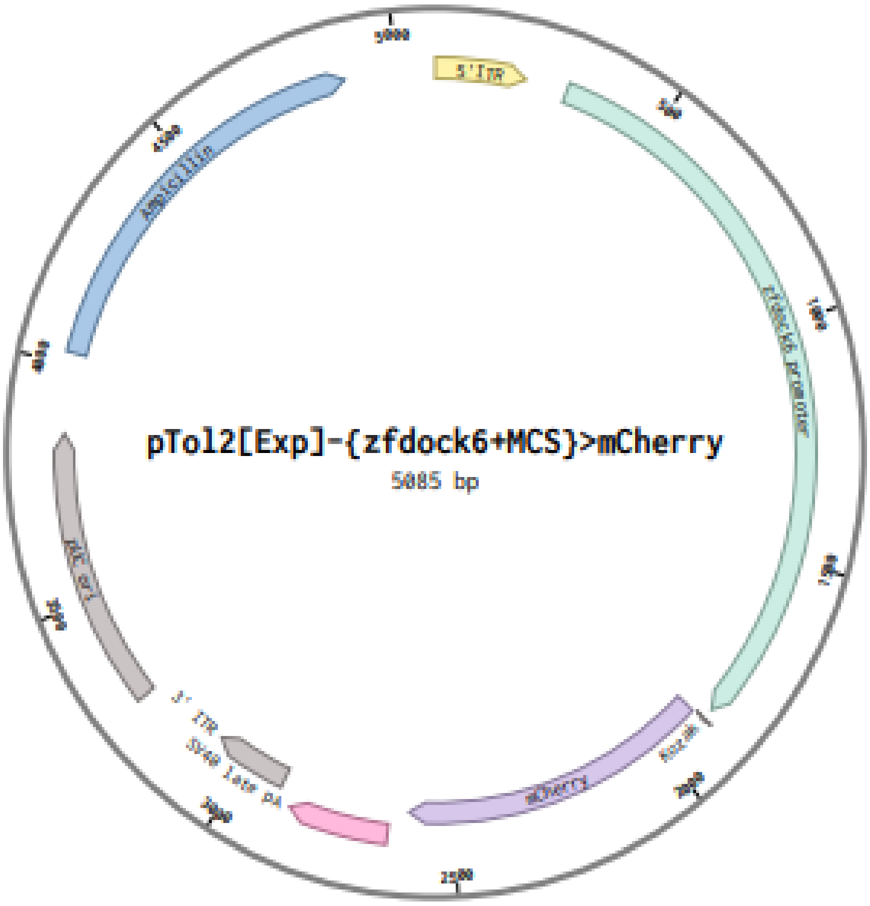

Figure 12: Tol2(*dock6*:mCherry) plasmid map.

Table 9: Tol2(*dock6*:mCherry) plasmid properties.

Component	Position	Type	Description
Tol2 5′ inverted terminal repeat	1-200	ITR	Recognised by Tol2. Allows genomic insertion of DNA flanked by the Tol2 5′ and 3′ ITRs
dock6 promoter sequence + MCS	293-1862	Sequence 1500 bp upstream of *dock6* 5′ MCS: *Pac*I, *Asc*I, *Mfe*I, *Bbs*I, *Eco*RV, *Xma*I 3′ MCS: *Bsa*I, *Bsg*I, *Sal*I, *Xba*I, *Xho*I	To promote the expression of mCherry at sites of *dock6* localisation
Kozak	1887-1892	Kozak translation initiation sequence	Facilitates transcription initiation of ATG start codon
mCherry	1893-2603	Transcript of RFP variant mCherry	To be expressed in vivo under the *dock6* promoter
Simian virus 40 late polyadenylation signal	2648-2869	PolyA signal	Transcription termination and polyadenylation of transcribed mRNA
Tol2 3′ inverted terminal repeat	2904-3078	ITR	Recognised by Tol2. Allows genomic insertion of DNA flanked by the Tol2 5′ and 3′ ITRs
pUC origin of replication	3266-3854	Replication origin	Facilitates plasmid replication in E. coli
Ampicillin	4025-4885	Ampicillin resistance gene	Confers bacterial resistance to ampicillin, as a selective marker

2.4.5.2 Transposase generation

2.4.5.2.1 mMessage Machine mRNA transcription

Transposase mRNA was generated from a transposase plasmid (pCS2FA CO Tol2 TPase). The plasmid was linearised by *Not*I digestion in 3.1 buffer for 30 min at 37 °C (see Section 2.2.1.5).

The linearised plasmid was transcribed using the mMessage Machine SP6 kit (Thermo Fisher Scientific) as detailed in Table 10.

Table 10: SP6 mMessage mMachine reaction assembly.

Reagent	**Volume (µl)**
GTP	1
2 × NTP/CAP	10
10 × reaction buffer	2
Linear template DNA (0.5 µg)	1
Enzyme mix	2
Nuclease-free H_2O	To 20 µl

Lithium chloride (LiCl)-based RNA precipitation, included in the mMessage Machine SP6 kit, was performed as per manufacturer's instructions and the RNA pellet resuspended in 20 µl of RNase-free H_2O. The extracted RNA was quantified by NanoDrop (see Section 2.2.1.2).

2.4.6 Microinjection and confocal microscopy analysis

Co-injections of 250 pg of the Tol2(*dock6*:mCherry) construct and 125 pg of transposase mRNA were performed on 1-cell stage embryos, to catalyse genomic integration of the *dock6* promoter-mCherry insert. The resulting transgenic zebrafish line enables accurate visualisation of *dock6* expression throughout embryogenesis. Preliminary analysis of the F_0 zebrafish was undertaken using a Nikon A1R inverted confocal microscope to capture *dock6* expression during embryogenesis at stages 24 - 72 hpf. Fish were prepared as in Section 2.4.7.8.

2.4.7 Transient morpholino knockdown studies

2.4.7.1 Morpholino design

Antisense morpholino (MO) oligonucleotides (Genetools, LLC) were designed against the exon 1-intron 1 (*dock6*-E1) donor splice site and the intron 1-exon 2 (*dock6*-E2) acceptor splice site of the zebrafish *dock6* gene (Ensembl(GRCz11): ENSDARG00000035706). MOs to target *arhgap31* splicing were designed against the exon 2-intron 2 (*arhgap31*-E2) and exon 3-intron 3 (*arhgap31*-E3) donor splice sites.

2.4.7.2 Optimising morpholino injections: assessing mortality and control

To optimise morphant generation, 1-6 ng of each MO were injected into the yolk sacs of ~20 × 1-cell stage embryos per amount and type of MO. To confirm successful injection and uptake into the cells, every MO included 10% of 500 kilodalton (kDa) dextran which could then be identified under a green fluorescent protein (GFP)-detecting microscope. The mortality rate was optimised by injection of 1-8 ng of each MO. The quantities that did not produce a phenotype were discounted; the amounts generating a phenotype were monitored to determine the concentration inducing the least lethality. Survival was counted as the percentage of injected embryos which survived 24 hr after injection.

To give rise to morphant embryos, MOs were injected into the yolk sacs of wildtype 1-cell stage embryos. The *arhgap31*-E2 and *arhgap31*-E3 morphants were generated using 3 ng and 4 ng of each MO respectively; 3 ng and 1 ng of each MO was used to produce *dock6*-E1 and *dock6*-E2 morphants.

2.4.7.3 Validating morpholino interference of splicing by RT-PCR

To evaluate splicing defects in the morphants, RNA was extracted (see Section 2.2.2) from ~20 × 4 dpf zebrafish injected with *dock6*-E1 or *dock6*-E2. A forward primer (*zfdock6* E2 MO_Ex1F) was designed to target *dock6* exon 1, paired with reverse primers targeting exon 3 (*zfdock6* E2 MO_Ex3R), exon 4 (*zfdock6* E2 MO_Ex4R) or intron 1 (*zfdock6* E2 MO_Int1R). Following cDNA synthesis (see Section 2.2.3), PCR was performed (see Section 2.2.4) and the fragments were separated by gel electrophoresis (see Section 2.2.5) to check for any size differences between the wildtype and morphant amplicons. Bands displaying expected intronic inclusions upon *dock6*-E1, *dock6*-E2, *arhgap31*-E2 or *arhgap31*-E3 injection were extracted from the gel using a Monarch Gel extraction kit and sequenced as per Section 2.2.1.3.

2.4.7.4 Validating morphant specificity by rescue experiment

2.4.7.4.1 Synthesising wildtype DOCK6 mRNA

Wildtype *DOCK6* mRNA was custom designed and generated by Genscript using a pCS2+ mammalian/xenopus/avian/zebrafish expression vector, expressed under the Simian CMV IE94 promoter and containing the wildtype human *DOCK6* sequence. The plasmid was linearised by incubation at 37 °C for 30 min with N*ot*I digestion in 3.1 buffer (see Section 2.2.1.5). Wildtype human *DOCK6* mRNA was transcribed, precipitated and quantified as described in Section 2.4.4.1.

2.4.7.4.2 Optimising rescue injections

To optimise rescue experiments, 50-100 pg of wildtype *DOCK6* mRNA was injected into the cells of ~50 × 1-cell stage embryos per amount of mRNA. The amounts of mRNA which induced lethality were not investigated further. Non-lethal quantities were then co-injected with each *dock6* MO; mRNA was first injected into the cells of mRNA only and mRNA + MO cohorts followed by MO injection into the yolk sac of MO only and mRNA + MO cohorts. Mortality at 24 hr post-injection was assessed and the mRNA quantity showing the lowest mortality when co-injected with the MOs was used in all rescue experiments.

2.4.7.5 Assessing morphant phenotype

Images of the morphants were taken at 2.5 × magnification using a Nikon Digital Sight DS-L3 camera at 48 hpf, 72 hpf and 4 dpf by dechorionating the embryo if necessary and immobilising, by placing the morphant in 3% methylcellulose. Phenotypes caused by gene knockdown and their frequencies in the injected population were noted and the flow of blood throughout injected embryos was captured by video using a Canon camera.

2.4.7.6 Use of a kdrl:EGFP/fli1:GFP line to assess vascular function

Microinjections of *dock6* MOs were then performed in an in-house *Tg*(*kdrl-EGFP*) zebrafish line, where EGFP is expressed under the *kdrl* promoter and allows visualisation of the developing vasculature. After MO injection, embryos were kept until age 48 hpf, at which point vascularisation progression was captured using a Nikon A1R inverted confocal microscope.

Following confirmation of abnormal vascular development in *kdrl*:EGFP embryos upon morpholino-mediated *dock6* knockdown, *arhgap31* and *dock6* morpholino- and *dock6*-CRISPR-mediated knockdown was induced in 1-cell stage *fli1*:GFP embryos. These larvae were brought to 72 hpf and 5 dpf and used in microangiography experiments (see Section 2.4.7.7).

2.4.7.7 Microangiography

To further assess vascular function, wild-type, *arhgap31* and *dock6* knockdown embryos (*fli1*:GFP) aged 72 hpf and 5 dpf were used in microangiography experiments. Embryos were anaesthetised using a 1:25 dilution of tricaine (pH 7) in embryo media. Embryos were applied to a 1% agarose gel mould and positioned to expose the sinus venosus to the glass capillary needle. To visualise the vasculature, 2 nl or 3 nl of a 1 mg/ml 2000 kDa tetrarhodamine dextran solution was injected into the sinus venosus of 72 hpf and 5 dpf embryos, respectively. Following injection, embryos were extracted from the 1:25 tricaine solution and left to recover for 1 hr in fresh embryo media before preparation for confocal imaging (see Section 2.4.7.8).

2.4.7.8 Confocal microscopy

To prepare the MO-injected *kdrl:EGFP* embryos for imaging, 1% low melt agarose was heated until in solution and then aliquoted into microcentrifuge tubes and maintained at 37 °C until use. Each embryo to be imaged was placed into the liquid agarose and then rapidly retrieved using a glass Pasteur pipette. Embryos were placed on a glass cover slipped petri dish and rapidly positioned before the agarose set. The glass surface of the dish was filled with agarose to secure the embryo in place. Once set, fish water containing 1:25 tricaine, to anaesthetise the embryo, was poured over the top of the agarose. The prepared embryos were then imaged at 10 × magnification and 20 × magnification, to obtain images of the whole embryo and the head, respectively.

2.4.8 Multiplexed guide RNA gene knockout

2.4.8.1 Designing CRISPR RNAs

To knockout *dock6* expression in zebrafish embryos, three CRISPR RNAs (crRNAs) were designed, according to published recommendations (Kroll et al., 2021). Two crRNAs were chosen by inputting the first 1,000 bp of the *dock6* transcript into a gRNA designing tool (IDT) and selecting '*Danio rerio*' for the species choice. A third gRNA was similarly selected by using bases 1,000-2,000 of the *dock6* transcript. The crRNAs estimated to have the highest cutting efficiency and lowest off-target capacity were chosen as part of the crRNA design set. The chosen crRNA sequences

(Alt-R CRISPR-Cas9 crRNA), IDT gRNA1_zfdock6_Ex3, IDT gRNA2_zfdock6_Ex6 and IDT gRNA3_zfdock6_Ex17 (see Section 2.1.8), were synthesised by IDT.

2.4.8.2 Synthetic guide RNA synthesis

Lyophilised crRNA and tracrRNA were resuspended in Duplex buffer (IDT) to a final stock concentration of 200 µM and stored at -80˚C. To form the sgRNA, each crRNA was individually annealed with the tracrRNA, by combining equal molar amounts of crRNA and tracrRNA (Table 11). These reactions were heated to 95 ˚C for 5 min, then cooled on ice, generating a sgRNA solution of 57 µM.

Table 11: sgRNA assembly.

Component	**Volume**
200 µM crRNA	1 µl
200 µM tracrRNA	1 µl
Duplex buffer	1.5 µl

2.4.8.3 Ribonucleoprotein complex formation

Ribonucleoprotein (RNP) complexes were assembled for delivery into the embryos from the prepared sgRNAs and Alt-R® S.p. Cas9 Nuclease V3. The Cas9 protein was diluted to 9.34 µg/µl (57 µM) in the supplied 1 × storage buffer for use in RNP complex assembly.

For each crRNA RNP, sgRNA and Cas9 solutions were mixed and incubated at 37 °C for 10 min and then cooled on ice. To test the efficiencies of different ratios of Cas9 to gRNA, the Cas9 protein was diluted to give solutions of 1:3.5 and 1:7 molar ratios of Cas9:sgRNA. For each of the three sgRNAs (see Section 2.4.8.2), RNP complexes were assembled (Table 12) and pooled by combining equal amounts of each RNP to form the multiplexed sgRNA solution, which was then stored at -20 °C until use.

Table 12: RNP assembly.

Molar ratio (Cas9:sgRNA)	**Component**	**Volume**
1:1	Alt-R® S.p. Cas9 Nuclease V3 (57 µM)	1 µl
	sgRNA (57 µM)	1 µl
1:3.5	Alt-R® S.p. Cas9 Nuclease V3 (57 µM)	1 µl
	sgRNA (57 µM)	3.5 µl
1:7	Alt-R® S.p. Cas9 Nuclease V3 (57 µM)	0.5 µl
	sgRNA (57 µM)	3.5 µl

2.4.8.4 Knockout verification

Multiplexed CRISPR injections were verified by Sybr-based quantitative PCR (Figure 63), reverse-transcription PCR (see Section 2.2.4) and Sanger sequencing of the RT-PCR products (see Section 2.2.1.3).

2.4.8.4.1 PCR and sequencing

Each PCR product was treated with ExoSAP-IT solution, by dispensing 2 µl of ExoSAP-IT solution with 5 µl of undiluted PCR product. The reactions were then heated at 37 °C for 30 min, then at 80 °C for 15 min. To prepare the samples for sequence analysis, a 1.5 ml microcentrifuge tube was prepared for each sequencing reaction for outsourced sequencing using the Eurofins Mix2Seq service. In each tube, 2.5 µl ExoSAP-cleaned PCR product, 2.5 µl of primer (10 µM) and 5 µl water per reaction were combined. The tubes were individually barcoded and delivered to Eurofins for sequencing. Sequencing results were analysed as in Section 2.2.1.3 by comparison to the wild-type reference genome (Ensembl(GRCz11):ENSDARG00000035706) to identify potentially mutated sequences. Chromatograms were examined using FinchTV software, to identify alterations in peaks which may indicate a heterozygous or homozygous genome edit. Upon target edit identification, ICE analysis was used to determine the mutation efficiency.

2.5 Cell culture studies

2.5.1 RNA extraction, cDNA synthesis, qPCR

RNA was extracted from VSMC pellets of ~1 × 10^6 cells using the AllPrep DNA/RNA Mini Kit according to manufacturer's instructions and quantified by NanoDrop (see Section 2.2.1.2). The resulting RNA was reverse-transcribed according to Section 2.2.3, using ~2 µg of RNA per sample. To confirm the expression of *DOCK6* in the VSMC line, a TaqMan qPCR approach was employed. TaqMan probes for *ACTB* (Assay ID: Hs00357333_g1) and *GAPDH* (Assay ID: Hs02758991_g1) were used to detect reference genes and the *DOCK6* probe (Assay ID: Hs01092545_m1) was used to detect *DOCK6* gene expression. To perform qPCRs, cDNA was diluted using nuclease-free H_2O to 100 ng of cDNA in each reaction. TaqMan Universal Master Mix II, no UNG was used to make 20 µl reactions. The qPCRs were carried out as per manufacturer's instructions, using clear 96-well low-profile PCR plates in a CFX Connect Real-Time PCR Detection System.

2.5.2 Protein extraction

Cells prepared in a 12- or 6-well plate were washed 3 times in pre-chilled PBS and kept on ice to prevent proteolytic degradation. To each well, 100 or 200 µl of standard RIPA buffer and 1 or 2 µl of 100 × Halt Protease Inhibitor Cocktail were added, respectively. Cells were incubated at room temperature for 10 min. The wells were scraped using a cell scraper and entire volume transferred to a microcentrifuge tube.

The samples were vortexed once every 10 min for 30 min and finally centrifuged at 2500 × *g* for 5 min at 4 °C to pellet any unlysed cells. The supernatant cell lysate was then transferred to a fresh tube and stored at -20 °C until the protein concentration could be determined.

2.5.3 BCA assay and analysis

From a Pierce BCA kit, 10 µl of 9 protein standards (0, 1.25, 6.25, 12.5, 25, 37.5, 50, 75, 100 µg/well) were distributed in duplicate into a 96-well microplate alongside duplicates of 10 µl of cell lysate per sample. Following this, 200 µl of reagent A and 5 µl of reagent B were added to each well, according to manufacturer’s instructions, and the plate protected from light and incubated for 30 min at 37 °C. Following incubation, absorbance of each well was measured using a colorimetric plate reader at OD=560 nm.

To calculate the protein concentration of each lysate, the duplicate readings for each sample were averaged and the mean absorbance value from the standard containing 0 µg/µl of protein was subtracted from each assay reading to give the corrected absorbance. The amount of absorbance is proportional to protein concentration, which was calculated using the linear equation derived from the trendline produced by plotting the known protein standards on a scatter graph.

2.5.4 Western blotting experiments

2.5.4.1 SDS-PAGE

To resolve the 230 kDa DOCK6 protein, a 4-8% gradient SDS-PAGE gel was made for each experiment with the components listed in Table 13:

Table 13: SDS-PAGE recipe.

Component	**4% stacking gel**	**8% resolving gel**
ProtoGel	1.33 ml	2.7 ml
Tris-HCl	2.5 ml (pH 6.8, 0.5M)	2.5 ml (pH 8.8, 1.5M)
10% (w/v) SDS	100 µl	100 µl
H_2O	6.01 ml	4.65 ml
10% (w/v) Ammonium persulfate	50 µl	50 µl
TEMED	10 µl	5 µl
Total	**10 ml**	**10 ml**

Ammonium persulfate and TEMED were added immediately prior to setting the gel. The resolving gel was set first in a 1 mm gel cast and coated with water to decrease exposure to oxygen, allowing the gel to set within 20 min. Once set, the stacking gel was prepared and gently decanted onto the resolving gel and a gel comb inserted. Once set, the prepared SDS-PAGE gel was placed into the electrophoresis chamber immediately and the wells rinsed with running buffer. Before performing electrophoretic protein separation, each 16 µl protein sample was diluted to the least concentrated sample in the experiment and denatured by boiling at 72 °C with 6 µl of loading buffer and 3 µl of reducing agent.

Once denatured, each sample was applied to the gel alongside a Prestained PageRuler molecular weight marker, to distinguish each protein band by size upon visualisation. The electrophoretic chamber and tank were filled appropriately with running buffer, and the samples separated on a Mini-PROTEAN Tetra Buffer Tank system (BioRad) by running the gel at 120 V for 100 min.

2.5.4.2 Protein transfer

Following protein separation by electrophoresis, the protein samples were transferred to a PVDF membrane by wet transfer. Filter paper and transfer sponges were soaked in transfer buffer and the PVDF membrane re-hydrated by soaking for 10 min in methanol, followed by 10 min of equilibration in transfer buffer. Once the gel run was complete, each gel was equilibrated in transfer buffer for 10 min. The transfer sandwich was then assembled for the BioRad Mini-transblot transfer system according to manufacturer's instructions. Bubbles between the membrane and gel were removed by rolling a sterile stripette over the assembly. The transfer took place overnight at 30 volts, with a cool block present to prevent the system from overheating.

2.5.4.3 REVERT total protein staining

Upon completion of the protein transfer, the membrane was fully dried for 1 hr and rehydrated in methanol, then rinsed in deionised water for REVERT total protein staining. Each membrane was incubated in REVERT staining solution at room temperature on a shaker. This was followed by two washes in fresh REVERT wash solution for 30 s each under agitation. The membrane was finally rinsed in deionised water before visualisation of the total protein in the 700 nm channel on the Odyssey imaging system (LI-COR). The staining and washing process was performed under protection from light. To quantify total protein, the intensity of each stained sample lane was measured using the LI-COR Image Studio software.

2.5.4.4 Primary antibody incubation

Following total protein staining, the membrane was rinsed in water and then blocked in 5% milk in PBTw (0.1%) for 1 hr at room temperature with shaking. The membranes were incubated for 1 hr at room temperature with shaking in each primary antibody sequentially, diluted as appropriate in 5% milk in PBTw (0.1%).

2.5.4.5 Secondary antibody incubation

After incubation of the membrane in all appropriate primary antibodies, the membrane was washed 5 times for 5 min in PBTw (0.1%) to remove all primary antibody before addition of the secondary antibody diluted optimally in 5% milk in PBTw (0.1%). The membrane was incubated in the secondary antibody at room temperature for 1 hr with shaking. Following secondary antibody incubation, the membrane was washed 5 times for 5 min in PBTw (0.1%) and then once for 5 min in PBS only.

2.5.4.6 HRP-based enhanced chemiluminescent protein visualisation

To visualise the housekeeping genes and genes of interest, Pierce ECL Western blotting substrate was applied to the membrane according to manufacturer’s instructions. The HRP substrate was visualised by chemiluminescent exposure using a ChemiDoc MP Imaging system. The molecular weight marker was visualised using the 700 nm channel on the system.

2.5.4.7 *Protein quantification analysis*

Protein bands were quantified by inverting the raw .tiff image of the exposed membrane on ImageJ and measuring the intensity of each protein band. To normalise the protein of interest, the housekeeping protein intensity values were used to calculate a normalisation factor for each sample. The housekeeping protein intensity value for each sample was divided by the sample with the highest value, to calculate the normalisation factor for each sample. This was then used to normalise the protein of interest, by dividing the intensity value for the protein of interest by the normalisation factor.

2.5.5 Transient *in vitro* DOCK6 knockdown studies

2.5.5.1 *Optimising transfection conditions*

To test electroporation efficiency, a pcDNA3-EGFP plasmid (Addgene) was transfected into the VSMC line using a Neon Transfection system (Thermo Fisher Scientific). Three electroporation programs (Table 14) were chosen for testing, according to the manufacturer's recommendations for this cell type.

Table 14: Electroporation programs used to optimise transfection of VSMC line.

Program	**Voltage of pulse (V)**	**Width of pulse (ms)**	**Number of pulses**
A	1100	40	1
B	1200	40	1

C	1100	20	2

A 10 µl Neon Transfection kit (Thermo Fisher Scientific) was used to transfect the cells. To prepare the cells for electroporation, cells from 75 cm^2 flasks were detached with trypsin when they reached 70-80% confluency and 10 µl of cells from each flask was counted using a haemocytometer. The remaining cell suspension was transferred to a 15 ml Falcon tube and centrifuged at 200 × g for 5 min. Buffer R (Thermo Fisher Scientific) was used to resuspend the resulting cell pellet, to give a final concentration of 1×10^7 cells/ml. For each well, a 10 µl reaction containing 100,000 cells and 500 ng of pcDNA3-EGFP plasmid was electroporated. In total, 9 wells in a 24-well plate were seeded with electroporated cells, using 3 different electroporation programs in technical triplicate. At 24 hr post-transfection, the total number of cells and the number of cells expressing EGFP were counted and the transfection efficiency calculated. This was confirmed by fluorescence-activated cell sorting (FACS) following pcDNA3-EGFP transfection.

2.5.5.2 *Optimising siRNA concentration*

Following optimisation of electroporation parameters for the VSMC line, program B (Table 14) was selected for use in all subsequent electroporation experiments.

To knock down *DOCK6* in the VSMCs for functional analysis, a gene-specific siRNA (Thermo Fisher Scientific, siRNA ID 2133244) targeting exon 7 of *DOCK6* was used. As negative controls, Silencer™ Negative Control siRNAs No. 1 and 2 (Invitrogen) were used initially, in addition to electroporation of cells using H_2O only.

Cells were prepared and plated as described (see Section 2.3.4) and harvested for electroporation. For optimal knockdown, transfections were performed using the 10 µl Neon Electroporation kit according to manufacturer's recommendations with different cell densities: 1 × 10^5, 1.5 × 10^5, 2 × 10^5, 3 × 10^5, 4 × 10^5. To optimise the concentration of siRNAs for effective DOCK6 knockdown, cells were transfected with either 5, 10, 20, 40, 50 or 100 nM of siRNA. A density of 1.5 × 10^5 cells per 10 µl electroporation, performed twice for each well (6/12-well plate), and an siRNA concentration of 20 nM were considered to be the optimal conditions for knockdown and were used for all subsequent *DOCK6* knockdown experiments. After electroporation, cells were seeded into 6- or 12-well plates (Thermo Fisher Scientific) containing pre-warmed, pre-prepared F-10 Ham nutrient mixture without antibiotic and gentle shook to spread the cells evenly. To find the timepoint post-electroporation with the most comprehensive knockdown, the electroporated cells were grown for 5 days, and every 24 hr protein and RNA were extracted for Western blot and qPCR experiments as previously described (see Sections 2.5.1, 2.5.2, 2.5.4). cDNA was synthesised and TaqMan-based qPCR performed to quantify *DOCK6* gene expression in siRNA-electroporated and negative control cells.

2.5.6 *In vitro* angiogenic assays

2.5.6.1 Cell rounding quantification

Following transfection, cells were seeded into 12-well plates at a density of 2 × 10^5 cells per well in P/S-free media. At 24 hr and 48 hr, media was replaced with complete media. Cells were imaged at 10 × magnification using a digital Nikon microscope at 24 hr and 48 hr, following 3 washes with PBS to remove any dead cells. Three images per well were taken, and the number of rounded cells and normal cells were counted using the Cell Counter plugin on ImageJ. To determine the proportion of rounded cells, the number of rounded cells was divided by the total number of cells. The average proportion of rounded cells per well was calculated using the three images taken of each well, which was classed as a biological replicate.

2.5.6.2 *Manual cell counting*

Following transfection, cells were seeded into 12-well plates at a density of 2 × 10^5 cells per well in P/S-free media. The media was replaced with complete media at 24 hr and subsequently changed every 24 hr. At 24 hr, 48 hr, 72 hr and 96 hr, cells were detached by trypsinisation (see Section 2.3.4), centrifuged and the supernatant removed. 100 µl of complete media and 100 ul of trypan blue were added to the cell pellet and this was incubated at room temperature for 1 min before 10 µl of cells were applied to a haemocytometer and viable cells were counted. Three technical replicates per timepoint were counted and the number of viable cells averaged to give the number of cells per timepoint per biological replicate.

2.5.6.3 *MTT assay*

The MTT (3-(4,5-dimethylthiazol-2-yl)-2,5-diphenyltetrazolium bromide) assay uses NAD(P)H-dependent cellular oxidoreductase enzymes present in the cell to reduce the tetrazolium dye MTT to purple formazan. The absorbance of purple formazan measured in a well of cells by a colorimetric spectrophotometer indicates the number of viable cells present in the well, which can be calculated by curating a calibration curve of different cell densities which each produce an absorbance reading in proportion to the number of viable cells present. Traditionally, the MTT assay is used for measuring cell metabolism and viability. However by using a calibration curve this technique can also be used to quantify cell proliferation as an indirect readout, by treating wells of cells with MTT at each timepoint of interest and plotting a graph to show the number of viable cells per well over time (Verma et al., 2010). The MTT assay was used in the context of measuring the number of viable cells over time throughout chapter 6 as an independent validation of my manual cell counting assays.

2.5.6.3.1 Procedure

Cell cultures were prepared in 96-well plates 24 hr before addition of MTT (5 mg/ml of PBS) at a density of 5 × 10^4 cells/well in 150 µl medium. After 24 hr, the media was aspirated and 50 µl of serum-free media and 50 µl of MTT solution were dispensed into each well, including a control set of wells containing no cells. The plate was incubated at 37 °C for 2 hr.

After incubation, the MTT/serum-free media solution was removed and 150 µl of MTT solvent (4 mM HCl, 0.1% NP40 in isopropanol) was added into each well. The plate was protected from light and the solution gently pipetted in each well to encourage cell lysis and dissolving of the MTT formazan. The plate was then agitated on an orbital shaker at room temperature for 15 min. The absorbance of each well was measured on a Promega GloMax Multiplus Plate Reader at OD=590 nm within 1 hr of MTT solvent addition.

To calculate cell proliferation, the duplicate reading for each sample was averaged and the absorbance value from the control wells was subtracted from each assay reading to give the corrected absorbance. The amount of absorbance is proportional to cell number, which was calculated using the linear equation derived from an MTT calibration curve (see Section 2.5.6.3.2).

2.5.6.3.2 Calibration

To estimate the resulting cell number using the absorbance value obtained from the plate reader, a calibration curve was produced. To prevent cell proliferation, cells were seeded in serum-free media in a 96-well plate from a density of 3.33×10^5 cells/well and serially diluted two-fold to 1.3×10^3 plus no-cell containing wells as a control. These cell densities were plated in technical duplicate. Cells were allowed to attach to the plate surface for 90 min, or until the majority of the cells were attached. At this point, the serum-free media was replaced with the MTT reagent/serum-free media solution as before and the MTT assay performed. The absorbance values obtained from the plate reader were averaged for each cell dilution duplicate and plotted on a scatter graph against the known cell numbers in each well. The linear equation derived from the trendline was then used to calculate cell number in all further MTT proliferation assays.

2.5.6.4 Wound-healing migration assays

2.5.6.4.1 Optimisation

To identify the optimal cell density in a 6 well-plate to reach confluence in 24 hr, cell densities of 2×10^5, 4×10^5, 6×10^5, 8×10^5 and 1×10^6 were dispensed into each well and the total well volume made up to 2 ml with complete media. A cell density of 1×10^6 cells per well was identified as optimal and was used for all further experiments.

2.5.6.4.2 Procedure

Cell suspensions of 1×10^6 cells were seeded into a 6-well plate and left to grow to confluence in complete media for 24 hr. Once fully confluent, a scratch was made across each plate using a P200 pipette tip, guided in a straight line by a ruler. For consistency in imaging between timepoints, marks were made on the base of each well using a scalpel. This ensured identical positioning of the plate under the microscope when obtaining images.

2.5.6.5 *Ibidi migration assays*

Forceps were used to place 2-chamber culture inserts on the empty well surface in a 6-well plate. To ensure confluency in each chamber before removal, optimisation experiments were performed whereby cell densities of 2.45×10^4, 4.9×10^4, 5.25×10^4 and 7×10^4 cells were pipetted into both chambers of 4 different culture inserts. A seeding density of 7×10^4 cells per chamber was identified as reaching confluence after 24 hr.

At 24 hr post-transfection, 70 µl of the optimal cell density resuspended in complete media was pipetted into each well of the chamber and left to grow to confluence for 24 hr. Upon cell confluency, the chamber was removed by gripping the centre barrier of the chamber with forceps and 2ml of media was added to each well. Marks were made on the base of each well using a scalpel to aid accurate imaging between timepoints. Images of the cell-free gaps were taken immediately following chamber removal. The media was replaced 24 hr after chamber removal and images taken of the cell-free gaps to capture cell migration over a 24 hr period.

2.5.6.6 *Phalloidin staining*

Cells were applied to coverslips in a 12-well plate at a density of 2×10^5 cells per treatment 24 hr before fixing, to give timepoints of 24 hr, 48 hr and 72 hr following transfection. Cells were fixed by washing with PBS and incubating with 500 µl of 4%

PFA at room temperature for 30 min. Following incubation, cells were washed 3 times with PBS and stored at 4 °C until required.

When ready to stain, coverslips were washed 3 times in PBS for 30 s each, followed by incubation in PBS Triton X-100 (0.1%) for 3 min to permeabilise the cells. The coverslips were then washed in PBS twice for 30 s before incubation in a 1:1000 phalloidin in 1 × PBS dilution for 1 hr at room temperature in a humidity chamber. The phalloidin-stained cells were briefly washed in PBS once, before undergoing 3 PBS washes for 5 min each.

Coverslips were then incubated at room temperature in a 1:1000 DAPI (5 mg/ml) in 1 × PBS dilution for 1 min. The DAPI-stained cells were then washed 4 times in distilled water for 1 min each before being mounted onto glass slides using Aqueous Mounting Media. Slides were stored at 4 °C wrapped in foil for 72 hr until confocal imaging.

2.5.6.7 In vitro confocal imaging

After mounting (see Section 2.5.6.6), cell Z-stacks were imaged at 60 × magnification on a Nikon A1R Inverted confocal microscope by settings of 1/2 frames/sec and sized 1024 pixels using Galvano scanning. Z-stacks were taken from the bottom of the cell where the cell attaches to the coverslip, to the top of the cell.

2.6 Statistical analysis

Statistical analyses were conducted using GraphPad Prism version 7.03. Details of each analysis are given in each results chapter.

Chapter 3: Expression analysis of *arhgap31* and *dock6* in zebrafish embryogenesis

3.1 Introduction

To provide a framework for evaluating the molecular mechanisms underpinning vascular development in AOS, it was necessary to elucidate the normal expression of *arhgap31* and *dock6* over early zebrafish embryogenesis. As previously established (see Sections 1.1.5.3 and 1.1.6.3), mouse models investigating *Arhgap31* and *Dock6* knockdown have been reported in the literature (Caron et al., 2016; Miyamoto et al., 2013). However, loss of *Arhgap31* induced early lethality in many embryos and invasive techniques are required to investigate the impact of gene knockdown in the developing vasculature (Caron et al., 2016). Therefore, zebrafish were chosen as an alternative model to examine the vascular origins for Rho-related AOS. As the roles and expression patterns of *arhgap31* and *dock6* during early zebrafish development remain poorly elucidated, qPCR and whole-mount *in situ* hybridisation were used to evaluate the transcript levels and tissue localisation of *arhgap31* and *dock6* in zebrafish embryos aged 14 hpf to 5 dpf. A transgenic zebrafish line was generated to visualise *dock6* gene expression by using the *dock6* promoter to express mCherry. This timeframe encompasses all stages of vascular development including vasculogenesis, beginning at 14 hpf, the vasculogenesis to angiogenesis transition at 24 hpf and the continuation of vascularisation by angiogenesis until 5 dpf.

To investigate the impact of Rho dysregulation in AOS and address the vascular hypothesis of disease, these experiments were designed to provide a comparison between gene expression in zebrafish and humans and to determine whether *arhgap31* and *dock6* are expressed in relevant vascular structures. Therefore, the results were compared to the expression levels of two known vascular markers, *kdrl* and *fli1*. As a homologue of the human *VEFGR2* gene, *kdrl* is known for its involvement in angiogenesis, primarily in VEGF-induced sprouting of new blood vessels during early development (Gore et al., 2012). Conversely, *fli1* is homologous to the human Fli-1 proto-oncogene, ETS transcription factor (*FLI1*) and is expressed throughout the majority of early vascular structures including in angioblastic mesenchymal cells, the cardiovascular and hematopoietic systems, as well as the mesoderm and the pharyngeal arches (PA) (Brown et al., 2000; Liu et al., 2008).

3.2 Assessing transcript levels of *arhgap31* and *dock6* over embryogenesis

Initially, mRNA expression levels of *arhgap31* and *dock6* were examined by SYBR Green-based qPCR in zebrafish embryos from 14 hpf to 4 dpf (Figure 13). Following statistical analysis, transcript levels of *arhgap31* were significantly increased at all timepoints from 48 hpf to 4 dpf (Figure 13a). At 24 and 48 hpf, expression increased ~5-fold and ~12-fold respectively (*p*=0.0298). Following a notable peak of expression at 72 hpf, where *arhgap31* gene expression showed ~20-fold levels compared to 14 hpf (*p*=0.0014), *arhgap31* transcript abundance decreased at 4 dpf (*p*=0.0284). Conversely, *dock6* mRNA expression revealed a significant decrease at 48 hpf and 4 dpf by comparison to expression levels at 14 hpf (Figure 13b). A general trend of reduced *dock6* expression was observed from 24 hpf onwards, displaying a final abundance of ~0.6-fold levels at 4 dpf by comparison to 14 hpf. Thus, qPCR data showed that *arhgap31* was expressed highly from 24 hpf, reaching a peak at 72 hpf. Conversely, *dock6* was expressed at relatively low levels over embryogenesis.

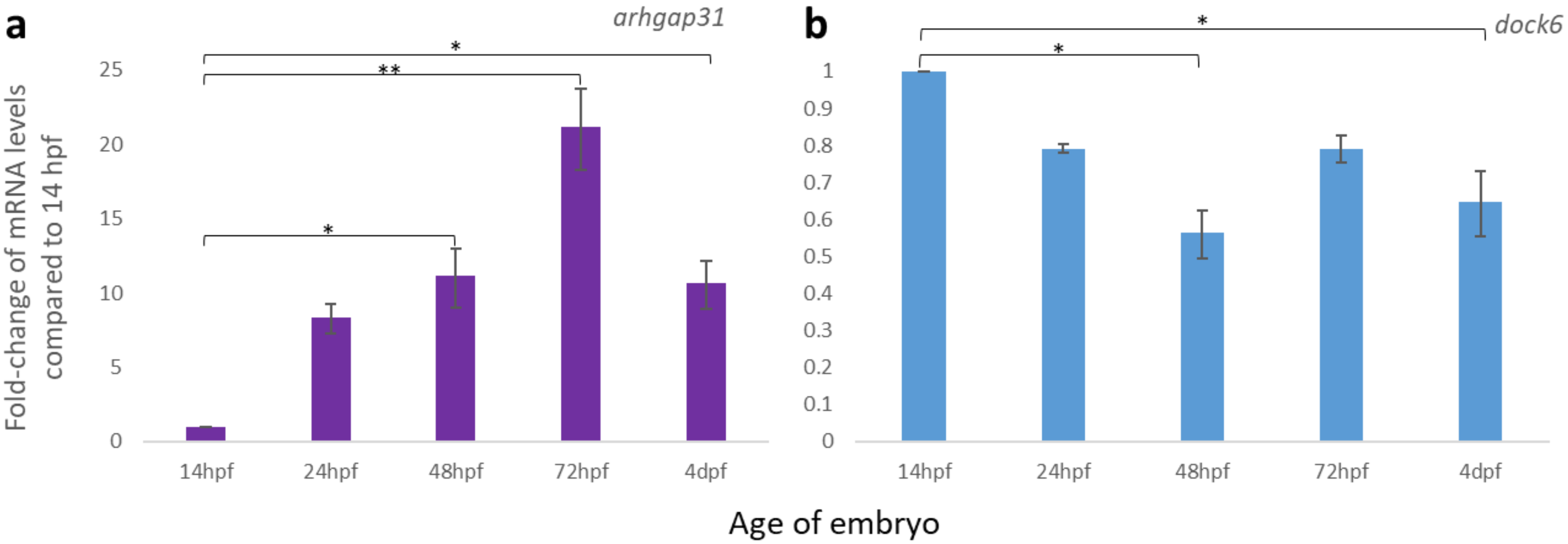

Figure 13: *arhgap31* and *dock6* transcript levels throughout early zebrafish development.

Fold-change of **(a)** *arhgap31* and (**b**) *dock6* gene expression from 14 hpf to 4 dpf, normalised to *actb2* and *eef1a1*. Expression was measured in triplicate (n= 3 cohorts of 50 embryos/target gene/timepoint) and all timepoints were normalised against target gene expression at 14 hpf. Error bars denote standard deviation. Statistical analysis was performed by one-way ANOVA and a Dunnett's test for multiple comparisons. Asterisks represent a significant difference in gene expression by comparison to 14 hpf (*p<0.05, **p<0.001).

3.2.1 Expression of *arhgap31* and *dock6* compared to known vascular markers

To examine the relevance of *arhgap31* and *dock6* to vascular development, qPCR experiments measuring the transcript levels of early vascular marker genes *kdrl* and *fli1* were performed (Figure 14a) and analysed against previously generated *arhgap31* and *dock6* expression data (Figure 13). In Figure 14, the C_q values generated by qPCR were normalised against the averaged C_q values of *fli1* at 14 hpf so that expression fold-change could be directly compared between each gene and each timepoint. This enabled us to identify temporal changes in mRNA expression of each gene over early zebrafish development in addition to determining the abundance of each gene across embryogenesis. At 14 hpf, which is shortly after the initiation of zebrafish vasculogenesis at 12 hpf, *arhgap31* expression was significantly reduced by comparison to *dock6* (p=0.0136) and *kdrl* (p=0.0053), while there was no significant difference in C_q values between *dock6* and *kdrl* at this timepoint. At 24 hpf, 48 hpf and 4 dpf, expression levels of *arhgap31*, *fli1* and *kdrl* were comparable, demonstrating no significant difference from one another within a timepoint. However, *dock6* transcript levels were significantly lower when statistically compared to *kdrl* (p=0.0195, p=0.0217, p=0.0005), *fli1* (p=0.0065, p=0.0091, p=0.0008) and *arhgap31* (p=0.0263, p=0.0117, p=0.0002) at 24 hpf, 48 hpf and 4 dpf, respectively (Figure 14b). At 72 hpf, conversely, there were no significant differences between *kdrl*, *fli1* and *dock6* expression, but *arhgap31* transcript levels showed a significant increase by comparison to *kdrl* (p=0.0192),

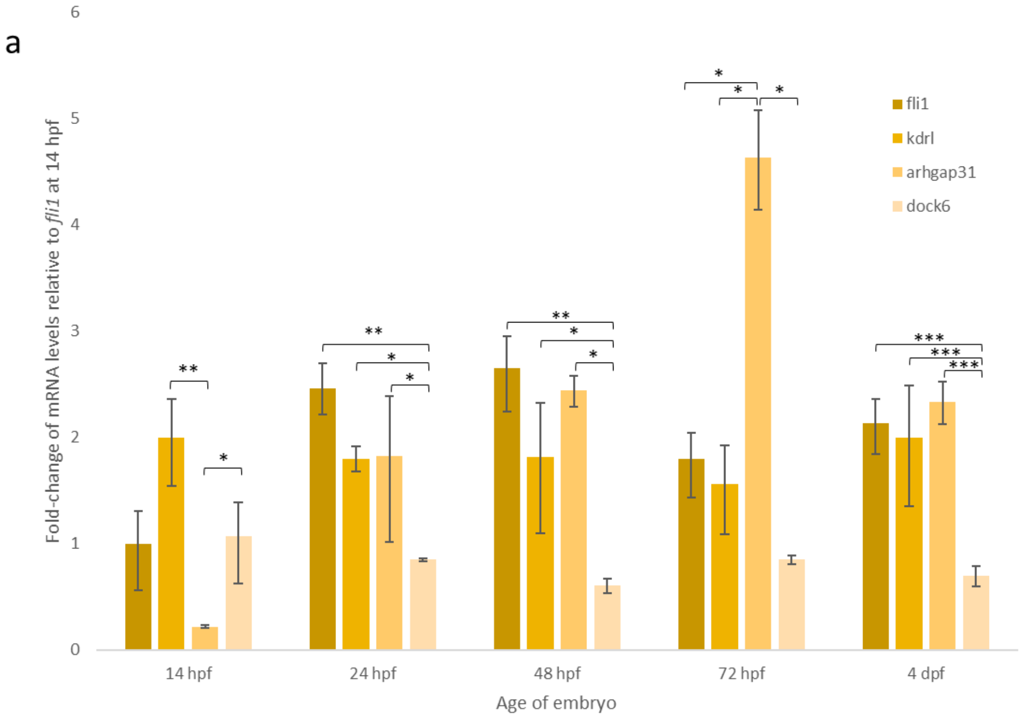

b

	fli1	***kdrl***	***arhgap31***	***dock6***
14 hpf	1	1.993267	**0.218565**	1.0751
24 hpf	2.46387	1.800491	1.823829	**0.850868**
48 hpf	2.652114	1.812731	2.437334	**0.605416**
72 hpf	1.795978	1.560136	**4.630402**	0.850355
4 dpf	2.13639	1.997599	2.332203	**0.696747**

Figure 14: Expression of *arhgap31* and *dock6* throughout embryogenesis compared to vascular endothelial markers.

(**a**) Transcript levels of *fli1*, *kdrl*, *arhgap31* and *dock6* from 14 hpf to 4 dpf, normalised to *fli1* expression at 14 hpf. Statistical significance between C_q values within a timepoint was determined by one-way ANOVA followed by a Dunnett's multiple comparisons test. *, *p*<0.05, **, *p*<0.01, ***, *p*<0.001. n=4 cohorts of ~50 embryos/time point. (**b**) The fold-changes of *fli1*, *kdrl*, *arhgap31* and *dock6* transcript levels from 14 hpf to 4 dpf relative to transcript levels of *fli1* at 14 hpf are displayed. Fold-changes which were significantly different are highlighted in **bold**.

fli1 (*p*=0.047) and *dock6* (*p*=0.0042). These data suggest that *arhgap31* and *dock6* have opposing expression, with the latter fluctuating at different timepoints, whereas the expression of known vascular markers remains relatively stable across this time period.

3.3 Embryonic expression localisation of *arhgap31* and *dock6*

Following confirmation of *arhgap31* and *dock6* expression over embryogenesis, I next sought to determine the localisation of gene expression within the embryo. Whole-mount *in situ* hybridisation experiments were used to examine the expression of *arhgap31* and *dock6* from 16 hpf and 72 hpf. To evaluate the expression patterns of *arhgap31* and *dock6* in the developing vasculature, WISH experiments in embryos from 16 hpf to 72 hpf were compared to the localisation of the vascular marker *fli1*.

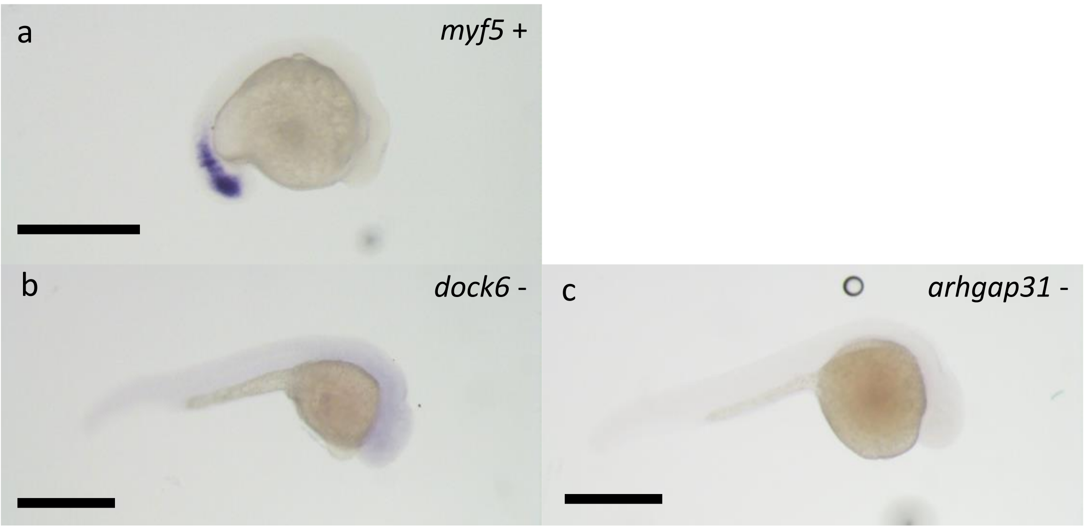

Figure 15: *in situ* hybridisation control experiments.

(**a**) Positive control experiment of a *myf5* probe in a 16 hpf embryo, taken at 6.3x magnification. Negative control experiments using (**b**) *dock6* and (**c**) *arhgap31* sense probes in 24 hpf embryos, taken at 5x magnification. Approximately 10 embryos were stained per condition and representative images of a single embryo per probe are shown. All scale bars represent 500 µm.

Positive control WISH experiments displayed the expected staining of *myf5* (Figure 15a). Negative control sense probes for *dock6* showed transparent embryos at 24 hpf, indicating specificity of the *dock6* antisense probe to dock6 mRNA (Figure 15b). Similarly, all *arhgap31* sense-stained embryos were transparent (Figure 15c). No negative control experiment was conducted for *fli1*, as this was derived from a previously validated probe (Lawson et al., 2001).

At 16 hpf, the *fli1* WISH probe demarcates migrating angioblasts from the anterior lateral plate mesoderm (ALM), cells which will make up the presumptive vasculature (Figure 16a, b). These cells were also faintly highlighted in the posterior and anterior

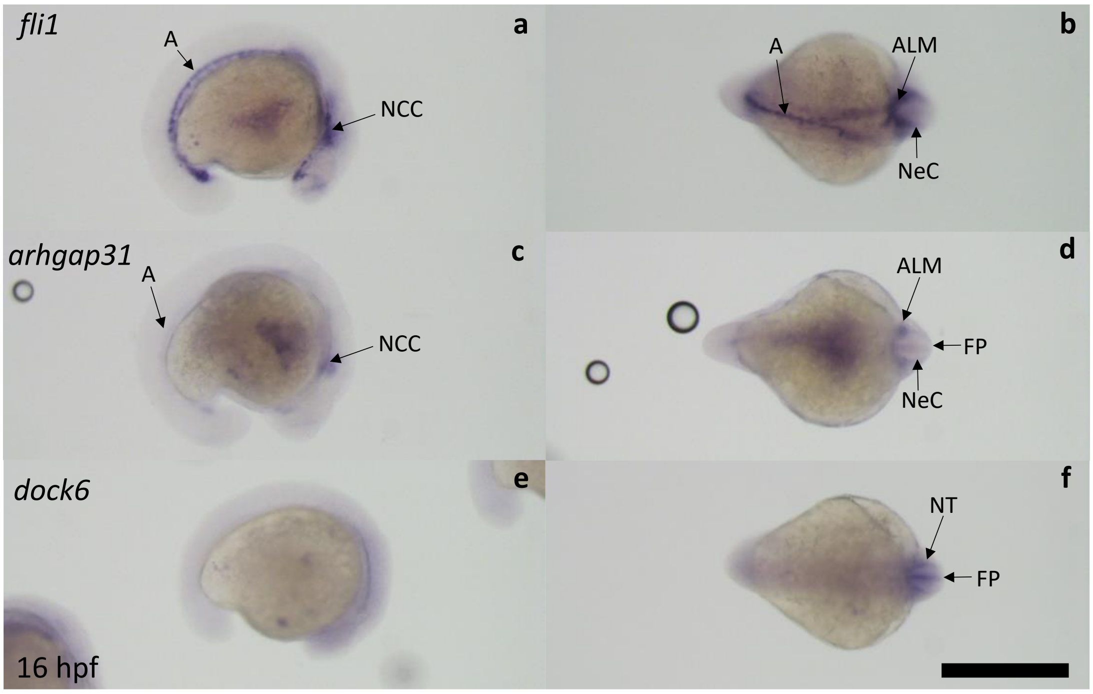

Figure 16: Whole-mount *in situ* hybridisation of *fli1*, *arhgap31* and *dock6*.

Expression of (**a, b**) *fli1*, (**c, d**) *arhgap31* and (**e, f**) *dock6* at 16 hpf. *fli1* expression outlines the developing vasculature. WISH for each probe was performed on 20-25 embryos per timepoint; representative results from a single embryo per timepoint are shown. Abbreviations: A: angioblast, AA: aortic arches, ALM: anterior lateral plate mesoderm, CVP: caudal vein plexus, CaV: cardinal vein, DA: dorsal aorta, CV: cranial vasculature, DLAV: dorsal lateral anastomotic vessels, ISV: intersegmental vessels, MCeV: middle cerebral vein, NC: notochord, NeC: neural crest, NT: neural tube, PA: pharyngeal arches, PCeV: posterior cerebral vein, PHBC: primordial hindbrain channel, PHS: primary heart sinus, PMBC: primordial midbrain channel, SB: somite boundary. Scale bar, 500 µm.

of the embryo by *arhgap31* expression at 16 hpf (Figure 16c, d). Expression of *arhgap31* at 16 hpf was also demonstrated in the floor plate and migrating neural crest cells (NCCs) (Figure 16c, d). At 16 hpf, *dock6* staining was most localised to the anterior of the embryo and appeared prominent in the neural tube and floor plate (Figure 16e, f). Expression of *dock6* showed limited vascular specificity at 16 hpf and 24 hpf, demonstrating expression only in the aortic arches (AA) region at 24 hpf.

At 24 hpf, *fli1* demarcates developing vascular structures, namely the CVP, cardinal vein (CaV), ISVs, DA, posterior cerebral vein (PCeV), primordial midbrain channel (PMBC), posterior hindbrain channel (PHBC) and AA (Figure 17a, b). Similarly, expression of *arhgap31* at 24 hpf was observed in the PCeV, PMBC, DA, CVP, CaV and AA. Additionally, expression of *arhgap31* was observed in the developing PA at 24 hpf (Figure 17c, d). Embryos at 24 hpf demonstrated strong localisation of *dock6* mRNA expression to the ocular, forebrain, midbrain and hindbrain regions (Figure 17e). Specificity of *dock6* localisation was also observed in the developing PA at 24 hpf, overlapping with *arhgap31* expression, and to the midbrain-hindbrain boundary, somite boundaries and skeletal muscle (Figure 17e, f).

Expression of *fli1* stayed localised to the DLAV, PCV, DA, AA, PMBC and PHBC at 48 and 72 hpf (Figure 18a, b, Figure 18a, c). At 48 and 72 hpf, *arhgap31* expression remained evident in the PCeV, PMBC, AA, as well as in the middle cerebral vein (MCeV), primary heart sinus (PHS) and PHBC (Figure 18a, b, Figure 18a, c). Localisation of *arhgap31* to the floor plate was observed at 48 hpf, which was also seen in *dock6* expression at 48 and 72 hpf (Figure 18c, e, Figure 18e). Additionally, at 48 and 72 hpf, *dock6* expression was observed in the PHS, PCeV, MCeV, PHBC, PMBC and AA and specific expression of *dock6* in the heart was seen at 72 hpf (Figure 18e*i*). Moreover, *dock6* gene expression at 72 hpf outlined the somite boundaries (Figure 18e).

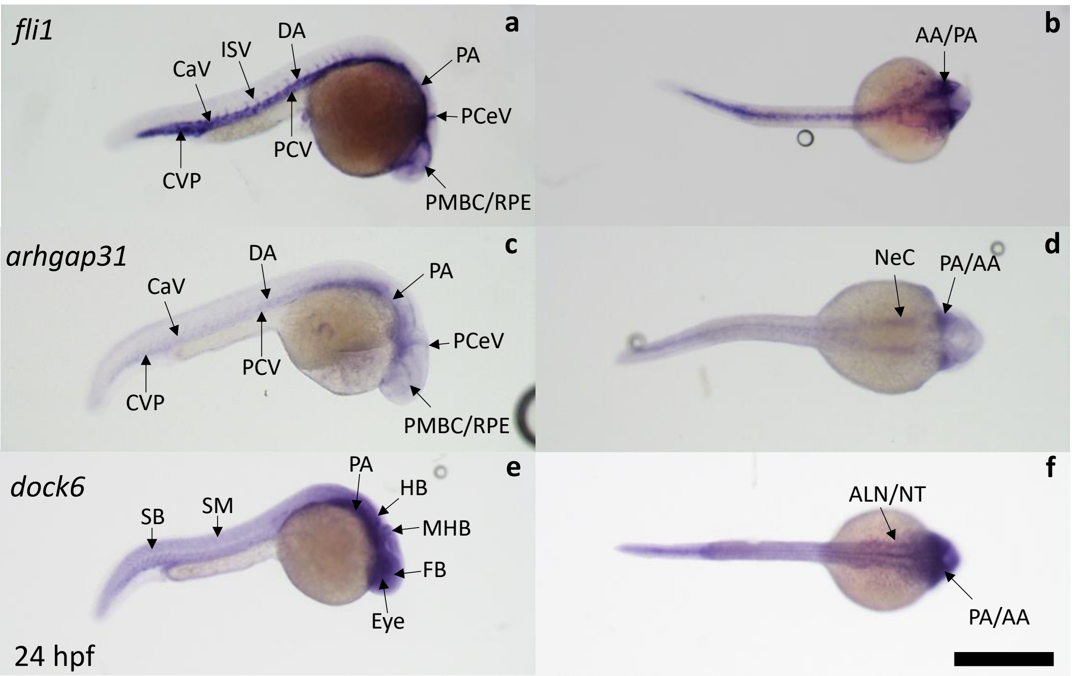

Figure 17: Expression of *fli1*, *arhgap31* and *dock6* at 24 hpf.

WISH showing expression of (**a, b**) *fli1*, (**c, d**) *arhgap31* and (**e, f**) *dock6* in 24 hpf zebrafish. WISH for each probe was performed on 20-25 embryos; representative results from a single embryo are shown. Abbreviations: AA, aortic arches; ALN, anterior lateral line neuromast; CVP, caudal vein plexus; CaV, caudal vein; DA, dorsal aorta; HB, hindbrain; ISV, intersegmental vessels; MHB, midbrain-hindbrain boundary; NeC, neural crest; NT, neural tube; PA, pharyngeal arches; PCV, posterior cardinal vein; PCeV, posterior cerebral vein; PHBC, primordial hindbrain channel; PHS, primary heart sinus; PMBC, primordial midbrain channel; RPE, retinal pigmented epithelium; SB, somite boundary. Scale bar, 500 µm.

Localisation of *fli1* is also known to demarcate cranial NCC expression (Coles et al., 2008). Therefore, expression in the AA region may not be vascular-specific, hence expression here has also been marked as potentially PA-specific. Interestingly, *arhgap31* and *dock6* expression in this region appears to mimic *fli1* expression at 48 and 72 hpf. Together, these data display evidence for the expression of *arhgap31* and *dock6* in developing vascular structures, as well as expression of *dock6* to areas associated with *DOCK6*-related AOS characteristics. Additionally, use of a *fli1* marker enabled the identification of *arhgap31* and *dock6* to some NCC-associated structures, such as the PA.

3.3.1 Use of a *dock6* transgenic reporter line tg(*dock6*:mCherry)

WISH experiments provided convincing evidence for *arhgap31* expression association with the developing vasculature and corresponded with the existing literature for expression at 24 hpf (Gomez et al., 2012). However, specific *dock6* localisation was less conclusive as there is currently no published literature to independently validate early *dock6* localisation results in zebrafish. Therefore, a *dock6*:mCherry transgenic reporter fish line was generated to confirm the specific structures which express *dock6* during early development.

At the one-cell stage, embryos were co-injected with transposase RNA and a plasmid containing the 1.5 Kb *dock6* promoter sequence upstream of mCherry flanked by Tol2 sequences. This induced genomic integration of mCherry expression under the *dock6* promoter. Merged Z-stack images taken of embryos aged 24 hpf to 5 dpf showed mCherry expression under the *dock6* promoter throughout the embryo for the duration of early embryogenesis (Figure 19). Though stable *dock6*:mCherry transgenic embryos were unavailable for imaging, preliminary examination of the

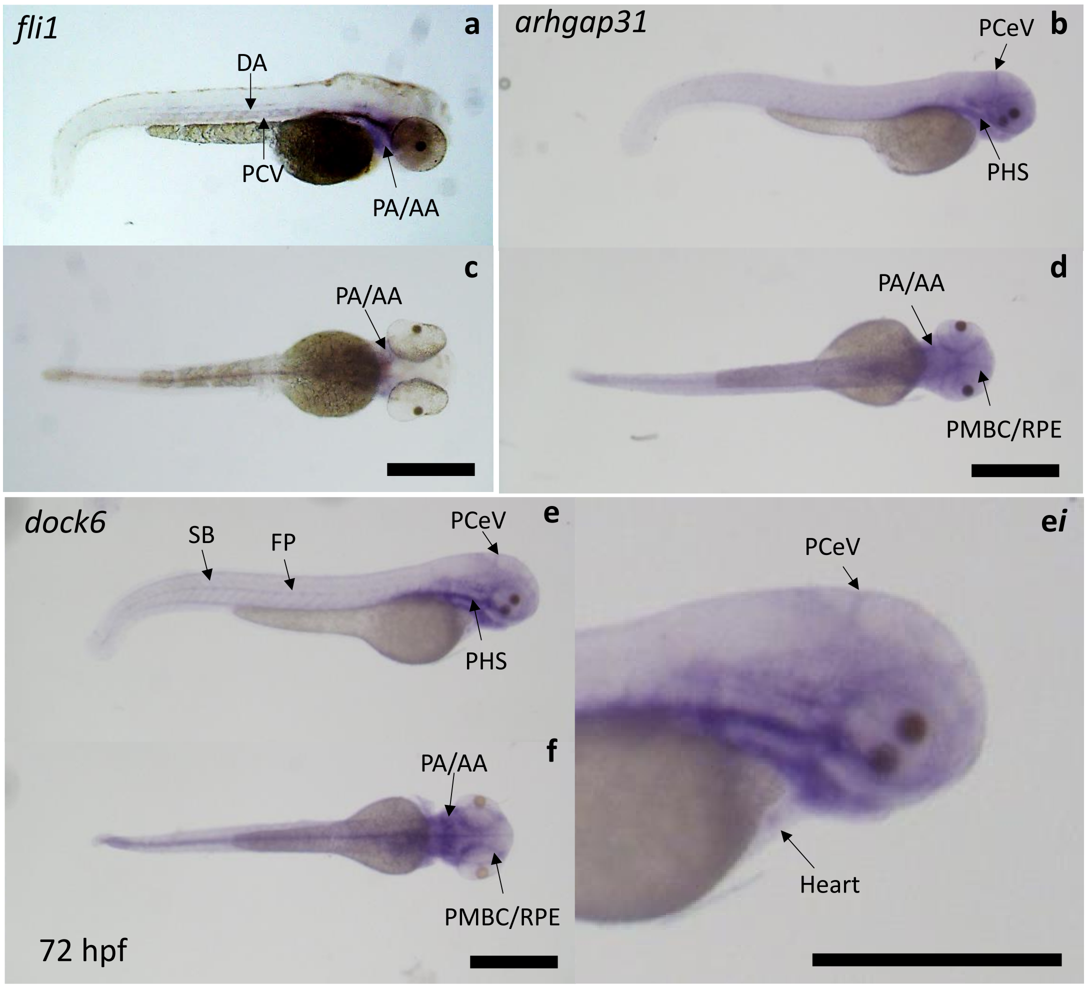

Figure 18: Expression localisation of *fli1*, *arhgap31* and *dock6* at 72 hpf.

(**a, c**) *fli1*, (**b, d**) *arhgap31* and (**e, f**) *dock6* expression at 72 hpf as shown by WISH experiments using 20-25 embryos per probe. Representative images are shown here. A magnified inset of *dock6* expression in the heart is displayed in ***ei***. Abbreviations: AA, aortic arches; DA, dorsal aorta; FP, floor plate; PA, pharyngeal arches; PCeV, posterior cerebral vein; PHS, primary heart sinus; PMBC, primordial midbrain channel; RPE, retinal pigmented epithelium; SB, somite boundary. Scale bar, 500 µm.

mosaic F_0 generation by confocal microscopy facilitated evaluation of likely *dock6* expression localisation. At 24 hpf, mCherry was expressed non-specifically throughout the embryo as a punctate expression pattern likely to demarcate epithelial cells or macrophages and did not appear localised to any particular structure (Figure 19a). The punctate distribution of *dock6* expression persisted throughout early embryogenesis and was seen at the surface of the cranium at each imaged timepoint, indicating potential localisation of *dock6* to the cranial epidermis. At 48 hpf to 4 dpf, *dock6* expression was observed throughout the cranium and appeared localised to the optic lens, common cardinal vein (CCV), AA, as well as in the developing heart at 72 hpf and 4 dpf. In the trunk, *dock6* was expressed in the developing slow muscle fibres from 48 hpf to 72 hpf and was present in both the slow and fast-twitch muscle fibres by 4 dpf (Figure 19d*ii*, e*ii*).

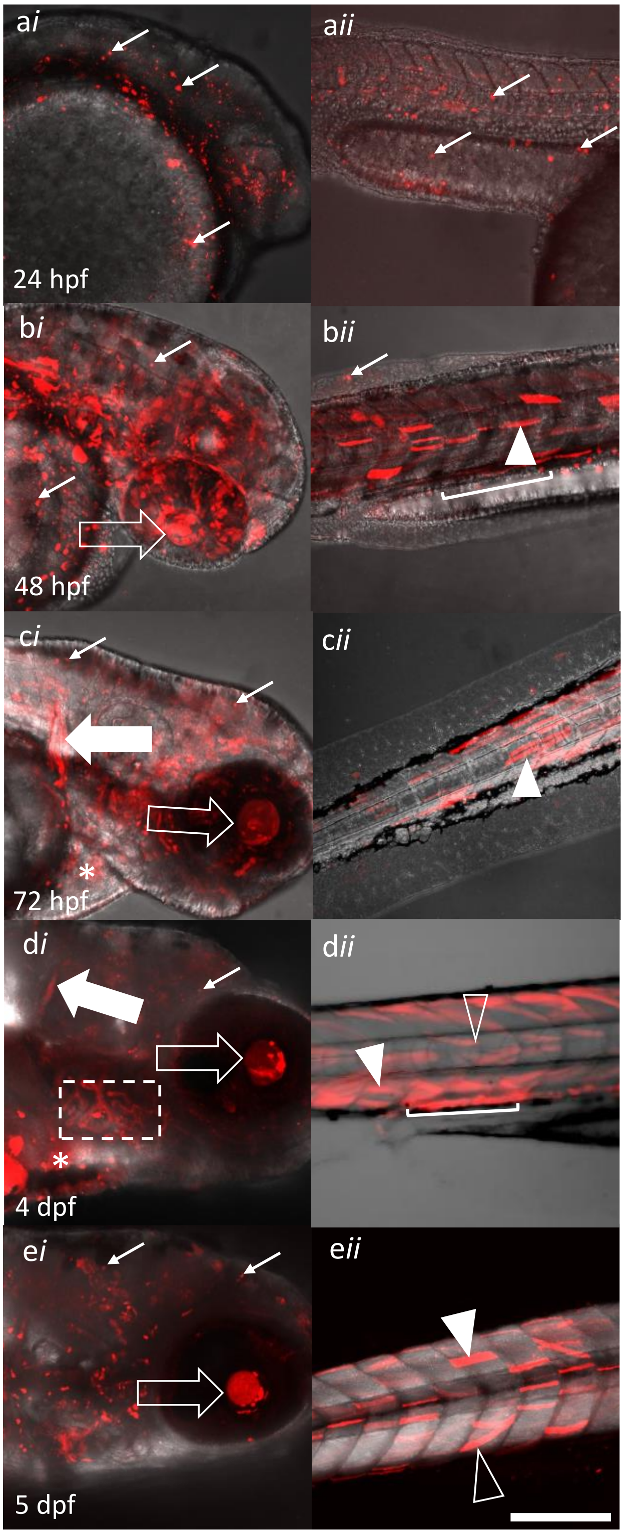

Figure 19: mCherry expression under the *dock6* promoter from 24 hpf to 5 dpf.

Expression of *dock6* in representative embryos (n≈50/timepoint) at (**a**) 24 hpf, (**b**) 48 hpf, (**c**) 72 hpf, (**d)** 4 dpf and (**e**) 5 dpf in the head (***i***) and trunk (***ii***) at 20x magnification. Thin white arrows demarcate potential macrophage expression. An unfilled white arrow indicates lens expression. The posterior and common cardinal veins are marked by a white bracket and a filled white arrow, respectively. The heart is indicated by an asterisk. A dashed white box encloses expression in the aortic arches. Slow and fast muscle fibres are denoted by filled and unfilled arrowheads, respectively. Scale bar, 200 µm.

3.3.1.1 Expression of dock6 in the developing cranial vasculature

Following identification of *dock6* localisation to general muscular and cranial structures, cranial vascular structures were further analysed by separating the Z-stacked images to determine the surface and internal structures bearing *dock6* expression (Figure 20). From 48 to 72 hpf, *dock6* is expressed in the CCV and lens (Figure 20a, b). Additionally, *dock6* expression was observed in the PCeV at 48 hpf and throughout the developing heart at 72 hpf, in accordance with the *dock6* WISH experiments. From 72 hpf to 5 dpf, *dock6* was expressed in the maturing AA (Figure 20b, d, e).

Figure 20f shows a merged Z-stack of *dock6* expression in the cranium of a 72 hpf embryo, which exhibits *dock6*-positive cells travelling through the cranial vascular network. In particular, the central cerebellar arteries and optic vessels are outlined by *dock6* expression within the lumen. Of interest due to the clinical phenotype of TTLD seen in AOS, *dock6* expression is also apparent in the pectoral fin vasculature at 72 hpf (Figure 20f). Together, these data confirm localisation of *dock6* to the cranial vasculature, slow and fast muscle fibres and the lens from 48 hpf to 5 dpf (Figure 19,

Figure 20).

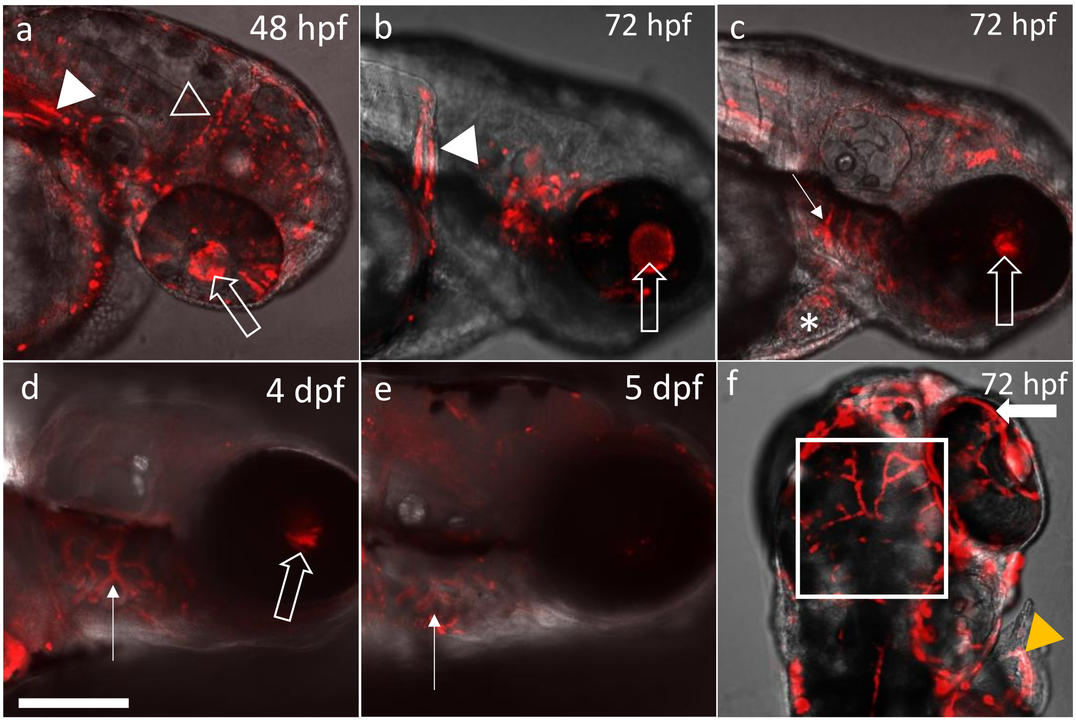

Figure 20: Visualisation of *dock6*:mCherry expression in cranial vascular structures.

Confocal microscopy at 20x magnification shows internal expression of *dock6* in representative (**a**) 48 hpf, (**b**) 72 hpf, (**d**) 4 dpf and (**e**) 5 dpf embryos (n≈50 embryos/timepoint). Surface expression and merged Z-stack at 72 hpf are displayed in **c** and **f**, respectively. mCherry is expressed under the *dock6* promoter in the common cardinal vein (filled arrowhead), posterior cerebral vein (unfilled arrowhead), fin vasculature (yellow arrowhead), lens (unfilled arrow), optic vessel (filled arrow), aortic arches (thin arrow) and central cerebellar vessels (white box). The heart is denoted by an asterisk. Scale bar, 200 µm.

3.4 Discussion

3.4.1 Transcript levels of *arhgap31* and *dock6* show opposing patterns over embryogenesis

To establish the temporal expression levels of *arhgap31* and *dock6* and determine the suitability of using zebrafish as a model for Rho-related AOS, transcript levels were measured from 14 hpf to 4 dpf, a critical developmental period encompassing both vasculo- and angiogenic processes. Quantitative PCR experiments revealed the highest expression levels of *dock6* at 14 hpf and displayed a general decrease in transcript abundance until 4 dpf. Conversely, *arhgap31* gene expression was negligible at 14 hpf and significantly increased by 20-fold in transcript levels at 72 hpf. These opposing patterns of expression reflect the known antagonistic functions of ARHGAP31 and DOCK6 in the context of regulating Cdc42 and Rac1 activity in humans, although experiments measuring the activity of Rac1 and Cdc42 over this period are required to determine whether Arhgap31 and Dock6 maintain an evolutionarily conserved role during zebrafish development (Tcherkezian et al., 2006; Van Buul et al., 2014). Overlapping expression of *arhgap31* and *dock6* seen in WISH experiments between *arhgap31* and *dock6* from 48 hpf to 72 hpf may suggest that the two genes co-localise. To investigate this further, it would be useful to examine Arhgap31 and Dock6 expression under the loss of either *arhgap31* or *dock6*. To examine the functions of *arhgap31* and *dock6* during early zebrafish embryogenesis, Rho GTPase pulldown assays could be performed in *arhgap31* and *dock6* knockdown embryos to quantify Rho-mediated regulation of Cdc42 and Rac1. This could identify potential conserved functions between zebrafish and mammals and discern the tissues in which *arhgap31* and *dock6* display activity.

3.4.2 Early *arhgap31* expression correlates to vascular development events

To relate *arhgap31* and *dock6* expression levels to the stages of early vascularisation, the mRNA abundance of vascular markers *fli1* and *kdrl* was measured and all four genes quantified relative to *fli1* transcript levels at 14 hpf to generate data which conveyed the expression patterns and quantities of each gene by comparison to each other (Figure 16). Expression levels of *arhgap31* at 24 hpf, 48 hpf and 4 dpf increased to levels comparable to *kdrl* and *fli1*; conversely, *dock6* levels at these timepoints decreased and became significantly lower than that of *arhgap31*, *kdrl* and *fli1*. *kdrl* is known for its role in ISV formation at 24 hpf and another ETS family protein, Etsrp, is known to positively regulate *arhgap31* expression in early zebrafish development (Gerhardt et al., 2003; Lawson et al., 2002). This information, coupled with previous work that has identified a role for ARHGAP31 upstream of VEGFR2 in mice, suggest a potential role for Arhgap31 in early zebrafish vascular development, however vascular function experiments are required to investigate this further (Caron et al., 2016).

By comparing *fli1* and *arhgap31* localisation from 16 hpf to 72 hpf, notable correlation of *arhgap31* expression to the vasculature was displayed, including localisation to the migrating angioblasts at 16 hpf and the PCeV, DA, CVP and PCV at 24 hpf. This closely corresponds with previous *arhgap31* WISH experiments performed in 24 hpf zebrafish embryos which identified *arhgap31* localisation to the cranial vasculature, DA, CVP, PCV, hypochord, hatching gland, and the spinal cord (Gomez et al., 2012). Alone, these data do not conclude that *arhgap31* promotes vascular development; indeed, previous studies have suggested a function for *arhgap31* in negative regulation of angiogenesis (Engelse et al., 2008; Norden et al., 2016). However, the observed expression patterns do support a likely contribution of *arhgap31* during the early stages of vascularisation, however functional studies are required to determine the role of *arhgap31* in development. Additionally, gene expression studies in mice identified strong localisation of *Arhgap31* to the cardiovascular system, surface ectoderm and limbs, consistent with the clinical features observed in AOS (Southgate et al., 2011). The conserved association of *arhgap31* to the vasculature between vertebrate models suggests that the use of zebrafish to investigate *arhgap31* function be a suitable model for AOS.

3.4.2.1 A potential role for arhgap31 in angioblast migration

Low expression levels of *arhgap31* at 14 hpf appear to correspond with identified *arhgap31* localisation to migrating angioblasts at 16 hpf. Vasculogenic caudal angioblasts begin migration at around 14 hpf before differentiating into endothelial cells, initiating angiogenesis at approximately 24 hpf (Gore et al., 2012). Tight regulation of Rac1 and Cdc42 is a well-established mechanism for controlling the actin cytoskeleton during processes such as migration, therefore low level *arhgap31* expression may participate in regulating Rac1 and Cdc42 activity in migrating angioblasts at this timepoint.

Angioblast migration is a key vasculogenic process in establishing the DA and PCV before angiogenesis (Poole et al., 2001). Therefore, *arhgap31* overexpression leading to reduced Rac1 and Cdc42 activity, as seen in AOS, may compromise early vascular organisation through impaired angioblast migration. It has been hypothesised that the major characteristics in AOS arise from a vascular event occurring between 29 and 36 days gestation (Swartz et al., 1999). This equates to approximately 14 and 18 hpf in zebrafish development, corresponding with the low *arhgap31* expression observed in migrating angioblasts (Kimmel et al., 1995). To further understand the impact of ARHGAP31 gain-of-function on angioblast migration in the context of AOS, *arhgap31* could be overexpressed in *kdrl* transgenic reporter embryos, and angioblast migration and differentiation monitored over early development by lightsheet microscopy.

3.4.2.2 A potential role for *arhgap31* in the neural crest

The significant increase in *arhgap31* expression at 72 hpf may imply a role in development for *arhgap31* at this timepoint, perhaps in the reduction of Rac1 and Cdc42 activity in tissues expressing *arhgap31*. WISH experiments investigating *arhgap31* at 72 hpf displayed localisation confined to specific cranial vascular structures including the AA, MCeV and PCeV. As described in Section 3.3, *arhgap31* localisation to *fli1*-specific regions near the AA may not correlate with vascular structures due to the additional expression of *fli1* in cranial NCCs and the PA. To further determine whether *arhgap31* is indeed confined to the vasculature or is expressed in neural crest- and neural crest-derived cells, future experiments using transgenic reporter lines for the neural crest-specific gene *crestin*, the endothelial cell-specific gene *kdrl* and for *arhgap31* could be used and assessed for any overlapping expression patterns.

Interestingly, at 72 hpf when *arhgap31* is most highly expressed, cartilage cells derived from the neural crest begin to differentiate to form pharyngeal arches 1 and 2 and the first visible bone in the zebrafish, the cleithrum (Kimmel et al., 1995). Accordingly, AA 3-6 are known to develop in parallel to their corresponding pharyngeal cartilages at age 4 dpf, however defects in these arches and cartilages may arise synonymously or independently (Anderson et al., 2008). This suggests that while neither is critical for the others development, defects in their common cell type of origin, the cranial NCC population, can lead to malformation of both the aortic and cartilage arches (Anderson et al., 2008). This is significant in the context of AOS as this is typically a disorder characterised by scalp ACC and TTLD, among other phenotypes. These manifestations are often associated with abnormal development of bony structures such as the skull and digits, respectively, which are derived from cartilage formation.

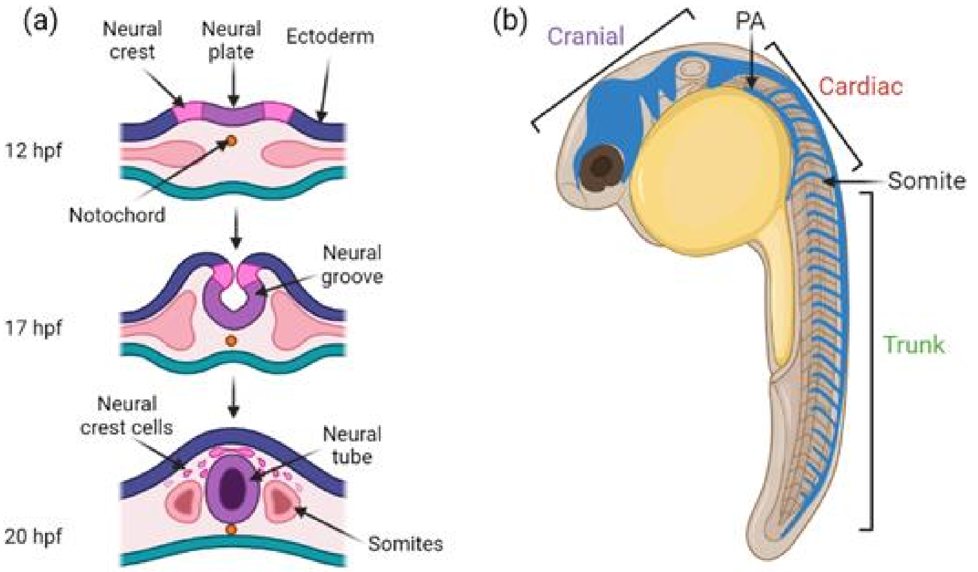

(c)

Cranial neural crest:	Cardiac neural crest:	Trunk neural crest:
Chondrocytes	Aorticopulmonary septum	Chromaffin cells
Osteocytes	Smooth muscle cells	Dorsal root ganglia
Cranial sensory ganglia	Pericytes	Sympathetic ganglia
Odontoblasts	Melanocytes	Schwann cells
Melanocytes	Cardiac ganglia	Melanocytes
Ciliary ganglia	Cardiomyocytes	

Figure 21: Neural crest migration and its derivative cell types.

The dynamic process of (**a**) neural tube formation and the onset of neural crest cell (NCC) migration until 20 hpf. By 24 hpf, (**b**) NCCs have migrated across the anteroposterior axis of the developing embryo to form distinct populations of cranial, cardiac and trunk NCCs which (**c**) differentiate to form many different cell types (Rocha et al., 2020). PA, pharyngeal arches. Figure created using Biorender.com.

3.4.3 *dock6* expression during early development

WISH experiments and supporting transgenic *dock6*:mCherry line data revealed *dock6* expression in the developing vasculature and neural crest. No transgenic *arhgap31* reporter line was generated as observed expression patterns corresponded precisely with published WISH data for *arhgap31* at 24 hpf (Gomez et al., 2012). The *dock6*:mCherry confocal images unveiled *dock6* expression in the developing slow and fast muscle fibres. In the context of AOS, one report describes hypotonia caused by *DOCK6*-related mutations, suggesting that there may be potential conservation for DOCK6 between human and zebrafish development, although further experiments are required to determine if *dock6*-depleted zebrafish also exhibit hypotonia (Shaheen et al., 2011). Interestingly, another member of the DOCK family, *dock1,* is similarly expressed in zebrafish muscle fibres during early development before becoming specified to the DA and PCV during later development (Benson and Southgate, 2021; Epting et al., 2010). Expression of *dock1* is known to mediate myoblast fusion in the early embryo. However when *dock1* is knocked down by morpholino, a strong vascular phenotype is produced, indicating a role for *dock1* in the developing vasculature (Epting et al., 2010). Due to the close relation and similar expression patterns between *dock1* and *dock6*, there may be scope for these genes share a similar mechanism of action during vascularisation. Alternatively, the similar expression patterns between *dock1* and *dock6* may support a potential compensatory mechanism between these two DOCK family members, however these avenues are yet to be explored.

3.4.3.1 Localisation of dock6 to the developing vasculature

My WISH data and transgenic studies revealed specific localisation of *dock6* to numerous cranial vascular structures from 48 hpf to 5 dpf, including the heart and developing CCV, as well as expression in cells passing through the cranial vasculature. Expression of *dock6* in the heart is of particular interest in the context of AOS, as congenital heart defects have been reported in 33% of *DOCK6*-related AOS cases (Southgate, 2019). WISH experiments performed by Shaheen *et al*. in mouse embryos aged E9.5 to E13.5 demonstrate *Dock6* localisation to the developing limb buds, and more importantly, to the developing heart (Shaheen et al., 2011). Further investigation of these findings may suggest an evolutionarily conserved function across vertebrate models and support the use of zebrafish models for *DOCK6* dysregulation in AOS.

Further, *dock6* expression is found in the AA from 72 hpf to 5 dpf, corresponding with *arhgap31* expression at 72 hpf. However, additional work is required to determine how *arhgap31* expression localisation progresses from 72 hpf onwards. Development of the AA is known to begin from around 34 hpf, where the arches appear as angioblast islands from which sprouts emerge and form bilateral ventral aortae by 48 hpf (Linnerz and Bertrand, 2021). These aortae fuse to form a single midline vessel by 72 hpf and the developed AA turn beneath the primary head sinus (Weinstein et al., 1995). AA 3 and 4 connect independently to the lateral dorsal aortae, whereas AA 5 and 6 merge and extend to the lateral dorsal aortae as a single vessel (Anderson et al., 2008). Expression of both *arhgap31* and *dock6* in the AA at 72 hpf may suggest a role for these genes in regulating Rac1a/b and Cdc42 in these structures. However, as expression does not infer functionality, further experiments investigating Rac1a/b and Cdc42 activity upon depleted *arhgap31* and *dock6* expression are required. As described above (see Section 3.4.2.2), AA formation is closely related to development of the pharyngeal arches, both of which originate from the cranial NCC population (Kirby and Waldo, 1995).

To detect overlap between *arhgap31* and *dock6* expression and early vascular development, combined transgenic reporter lines of *arhgap31*, *dock6* and *kdrl* could be generated and analysed. Functional studies are required to specify the contributions of *arhgap31* and *dock6* towards zebrafish vascular development and to determine their molecular mechanisms by identifying any potential interactions with genes involved in early vascularisation. Assessing *arhgap31* and *dock6* transcript levels in isolated vascular and cranial tissues across different developmental stages will determine the spatial and temporal expression patterns that appear most important.

3.4.3.2 dock6 expression localisation correlates with AOS-associated regions

WISH and transgenic experiments indicate increased *dock6* expression in the regions affected in *DOCK6* mutation-positive AOS patients, such as the brain and optic structures. As noted, biallelic *DOCK6* mutations in AOS are highly correlated with intellectual disability, structural brain abnormalities and ocular anomalies including microphthalmia (Sukalo et al., 2015). In the zebrafish, eye morphogenesis commences at 11.5 hpf and leads to the development of the primary optic structures, such as the eyecup, by 24 hpf. Accordingly, morpholino-mediated knockdown of *cdc42* has been shown to give rise to a decrease in eye size and loss of photoreceptor cilia (Choi et al., 2015). This information, coupled with the relatively high *dock6* expression at 14 hpf and localisation to the eye, may implicate *dock6* in the regulation of Cdc42 during early eye development. The zebrafish brain begins development at around 16 hpf, generating a simple network comprising of neuromeres to coordinate larval behaviour (Kimmel et al., 1995). Further neurogenesis continues to define the subregions of the mature brain by 72 hpf. Therefore, localisation of *dock6* to both the developing brain and eye structures supports further investigations into determining the function for *dock6* as a comparison between zebrafish and mammals, to determine a potential conserved function.

3.4.4 Early localisation of Rho regulators to the neural crest

The high and low expression levels of *arhgap31* and *dock6*, respectively, at 14 hpf suggest a net effect of increasing active Rac1 and Cdc42 levels at this timepoint. Interestingly, 14 hpf marks the onset of NCC migration (Figure 21), a process which requires the formation of lamellipodia and filopodia for which active Rac1 and Cdc42 are essential (Ridley, 2015). Accordingly, WISH data describe *arhgap31* and *dock6* localisation to migrating NCCs and neural tube, respectively, at 16 hpf. As described, it is currently unclear whether *arhgap31* and *dock6* are specific to the developing PA or the AA, and further experimentation is required to delineate this. Of interest, cranial NCCs are known to give rise to cells in the peripheral nervous system, such as the dorsal root ganglia (Fuchs et al., 2009). In mice, the majority of DOCK6-related research has been conducted in dorsal root ganglia and has identified a role for DOCK6 in axon sprouting and elongation, supporting a critical function for DOCK in NCC-derived structures (Miyamoto et al., 2013). In zebrafish, NCCs give rise to the most anterior cartilages which form the upper part of the skull, consistent with the underlying skull defects seen in AOS patients exhibiting ACC (Minoux and Rijli, 2010). Furthermore, zebrafish studies examining the cell fate of the neural crest have identified a role for NCCs in the development of the myocardium. In particular, the mutant *lef1*, which impairs several NCC lineages, exhibits defective cardiomyocyte differentiation in the atrial-ventricular valve, consistent with valve and septal defects identified in some AOS patients (Sato and Yost, 2003). AOS is highly heterogenous, therefore the potential involvement of *arhgap31* and *dock6* in the function of a cell type which gives rise to many structures provides insight towards how dysfunction of one gene may impact several different systems of the body.

3.4.5 Conclusions

The overlapping localisation of *arhgap31* and *dock6* tissue expression and opposing transcript levels of *arhgap31* and *dock6* from 14 hpf to 4 dpf may indicate that these two genes may cooperate in regulating the activity of Rac1 and Cdc42. These novel data support an potential evolutionarily conserved function for ARHGAP31 and DOCK6 in the tight regulation of Rac1 and Cdc42 activity.

This work has uncovered an association for *arhgap31* and *dock6* to developing vascular structures at critical points of vascular development. These data suggest a potential role for *arhgap31* and *dock6* during vasculogenesis and angiogenesis and highlight angioblast migration at 14 hpf as an event of interest. These data further implicate *arhgap31* and *dock6* expression with migrating NCCs and both genes exhibited potential localisation to cranial NCC-derived structures later in embryogenesis. These data provide preliminary evidence to suggest that AOS-related characteristics may derive from impaired NCC function. Gene knockdown studies will identify which structures are impacted by reduced *arhgap31* and *dock6* expression and begin to elucidate whether AOS is a disorder of vasculogenic or a neural crest origin.

Together, these findings correspond with known expression of *arhgap31* and *dock6* studied in other animal models and support the suitability of using a zebrafish model to study the roles of these two genes in the context of AOS.

Chapter 4: Gene function analysis in early zebrafish development

4.1 Introduction

Following investigation of healthy *dock6* and *arhgap31* expression throughout early development, I next aimed to elucidate the phenotypic effects of *dock6* and *arhgap31* depletion during embryogenesis. By identifying affected structures and functions upon the reduction of *dock6* or *arhgap31*, this work sought to draw comparisons regarding the functions of these genes between zebrafish and mammals, in order to further our understanding of the mechanisms underpinning Rho-related AOS.

Transient morpholino- and CRISPR-based techniques were used to knock down the two genes of interest. Morpholinos oligonucleotides designed to block the canonical splice regions of a target gene typically result in mis-splicing of the mRNA, therefore preventing production of the target protein (Summerton and Weller, 1997). In this study, morpholinos targeting the donor and acceptor splice sites of *dock6* intron 1 and the donor sites of *arhgap31* introns 2 and 3 were optimised and the general phenotypes in morphant embryos were evaluated and quantified.

To independently validate my *dock6* morphant observations, I used the CRISPR/Cas9 system to generate another knockdown model. This system generates genome edits by using a Cas9 nuclease complexed with a gRNA complementary to the target gene (Jinek et al., 2012). The gRNA guides the Cas9 nuclease to cleave the target site, creating a DSB. These are most commonly repaired by NHEJ, an error-prone process which randomly inserts or deletes nucleotides leading to frameshift mutations, resulting in a non-functional protein (Zhang et al., 2017). Our CRISPR-based method harnessed a protocol whereby three gRNAs were designed to target sequences within *dock6* to increase knockdown efficiency (Kroll et al., 2021; Wu et al., 2018). Following knockdown verification, crispant embryos were closely examined to assess the impact of diminished *dock6* expression.

4.2 Optimising morpholino-mediated *dock6* and *arhgap31* knockdown models

To optimise morpholino experiments, a balance between lethality and phenotype was established by injecting increasing amounts of each morpholino. Phenotypes were defined as characteristics differing from the wild-type and induced by gene knockdown. Embryos were evaluated after each injection to identify any phenotypes generated, and injection dose increased according to embryo mortality and strength of phenotype (Figure 22). Upon optimisation of *arhgap31*-E2 and *arhgap31*-E3 injections, no phenotypic effects were observed at concentrations of 1 to 3 ng and 1 to 2 ng, respectively. Increasing doses of each *arhgap31* morpholino were administered to produce phenotypes, showing optimal results at 4 ng and 3 ng for *arhgap31*-E2 and *arhgap31*-E3, respectively (Figure 22a and b). Similar optimisation of *dock6* morpholino injections noted that 3 ng and 1 ng were the optimal injection doses for *dock6*-E1 and *dock6*-E2, respectively, based on the increased lethality at higher doses (Figure 22c, d). The optimised concentrations for each *arhgap31* and *dock6* morpholino were used in all future knockdown experiments.

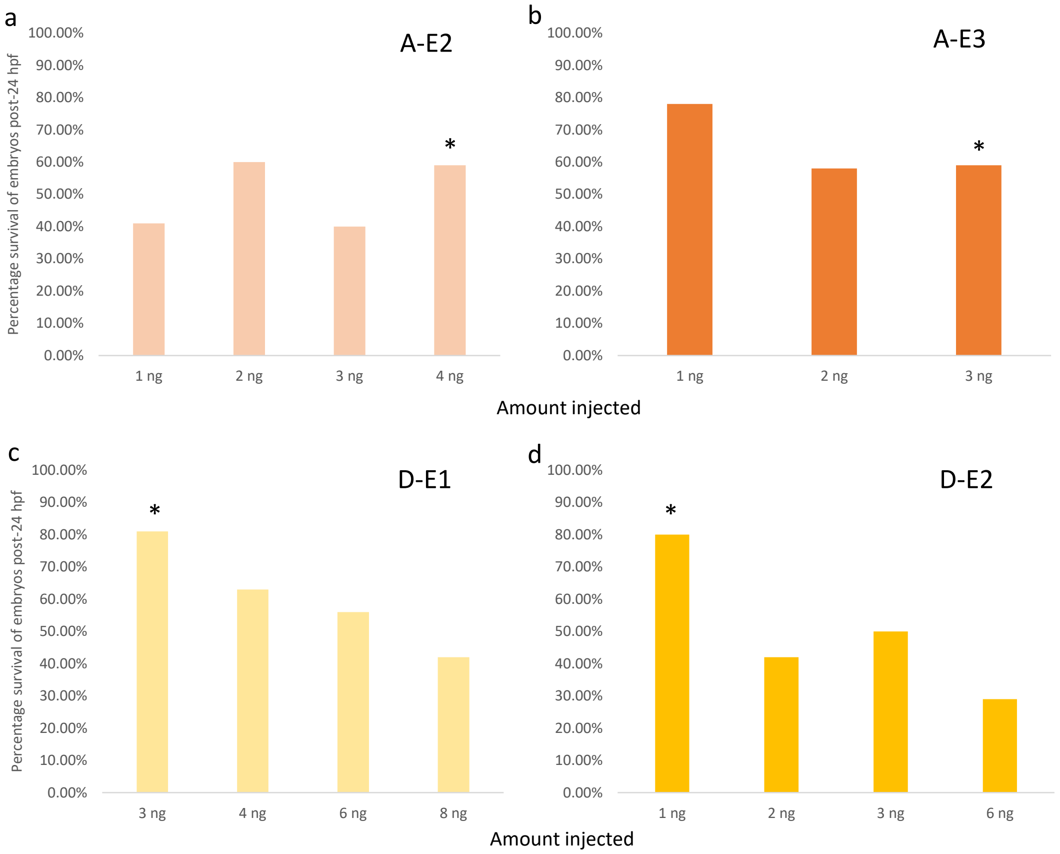

Figure 22: Percentage of viable injected embryos post-24 hpf.

Graphs **a-d** represent survival rates of embryos injected with varying amounts of (**a**) *arhgap31*-E2 (A-E2), (**b**) *arhgap31*-E3 (A-E3), (**c**) *dock6*-E1 (D-E1) and (**d**) *dock6*-E2 (D-E2). N=2-4 cohorts of 20-88 embryos/condition. Optimal injection amounts chosen for future experiments are signified by asterisks.

4.2.1 Identifying splicing defects in morphants

To further validate the *dock6* and *arhgap31* morpholinos, primers were designed to amplify the regions encompassing the targeted splice sites and determine any splicing disruptions produced by morpholino injection (Figure 23). RT-PCRs using cDNA from wild-type, *arhgap31*-E2, *arhgap31*-E3, *dock6*-E1 and d*ock6*-E2 embryo cohorts showed that morpholino injection gave rise to splicing defects in each condition by comparison to the wild-type. Each sample displayed a band generated by the positive control reactions, ensuring successful cDNA synthesis in each experiment (Figure 23).

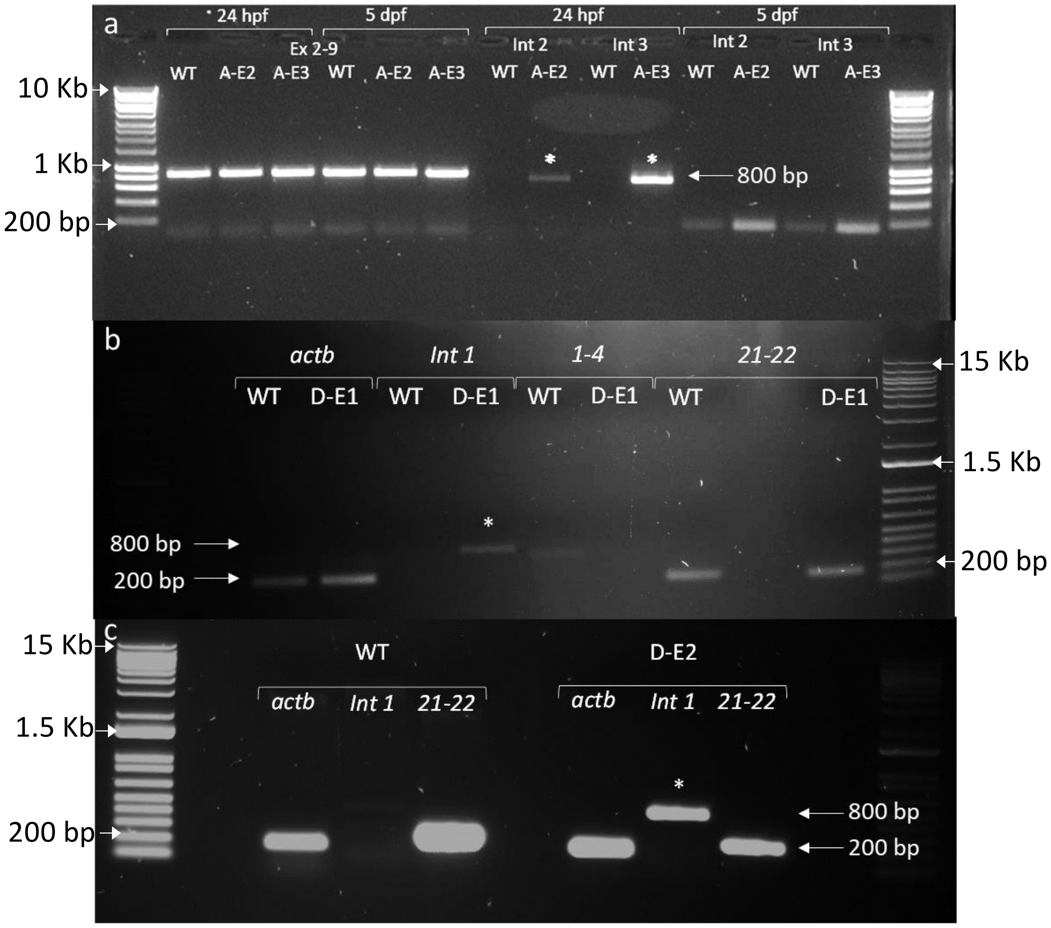

Figure 23: Morpholino-mediated intronic inclusions shown by RT-PCR.

Gel electrophoreses displaying RT-PCRs amplifying intronic inclusions generated by injection of (**a**) *arhgap31*-E2 and -E3 (A-E2, A-E3), (**b**) *dock6*-E1 (D-E1) and (**c**) *dock6*-E2 (D-E2). Bands representing intronic inclusions are marked with an asterisk. Meridian BioScience HyperLadder 1 Kb (**a**) and Invitrogen 1 Kb Plus DNA Ladder (**b, c**) were used as molecular weight markers.

RT-PCR across the splice junctions spanning *arhgap31* exon 2-intron 2 and exon 3-intron 3 generated the expected 800 bp product in *arhgap31*-E2 and *arhgap31*-E3 morphant cohorts, respectively (Figure 23a). The positions of these primer pairs are indicated in Figure 24a and b with the expected product size. A positive control using an *arhgap31* primer pair previously validated by RT-PCR (Appendix: Figure 66) verified successful cDNA synthesis from each cohort. At both 24 hpf and 5 dpf, no intron 2 or intron 3 band was generated in the wild-type (Figure 23a). However, in cDNA synthesised from *arhgap31*-E2 and *arhgap31*-E3 embryos, a band was generated at 24 hpf but not at 5 dpf. This is in accordance with the known transiency of morpholino-mediated knockdown experiments.

The amplification of *arhgap31* introns 2 or 3 upon *arhgap31*-E2 or -E3 injection, respectively, implies that both morpholinos disrupt splicing. While intronic amplification may be a sign of genomic contamination, all RNA samples were treated with DNase and the absence of a band in the wild-type sample suggests no genomic DNA is present. Sanger sequencing of these bands confirmed intronic inclusion of introns 2 and 3 in *arhgap31*-E2 and -E3 samples, respectively. Although the amplified band of *arhgap31* exons 2-9 appears similar between the wild-type and *arhgap31*-E2 and -E3 samples, this may be due to an insufficient PCR extension time to generate the large products expected upon inclusion of *arhgap31* intron 2 or 3.

To test for intronic inclusion under *dock6*-E1 or -E2 injection, primers were designed to amplify the 800 bp region encompassing the exon 1-intron 1 splice site (Figure 24c). cDNA synthesised from RNA extracted from *dock6*-E1 and *dock6*-E2 embryos but not wild-type embryos displayed a PCR product when targeted with primers amplifying exon 1-intron 1 (Figure 23b, c). This indicated mis-splicing due to the *dock6*-E1 and -E2 morpholinos binding to the acceptor and donor sites of intron 1, respectively. Intronic inclusion in both morphant cohorts was verified by Sanger sequencing. The presence of a band in the wild-type but not *dock6*-E1 when exons 1-4 are amplified implies disruption to this region in the morphants, potentially due to the targeting of a region too large to be amplified under an extension time of 1

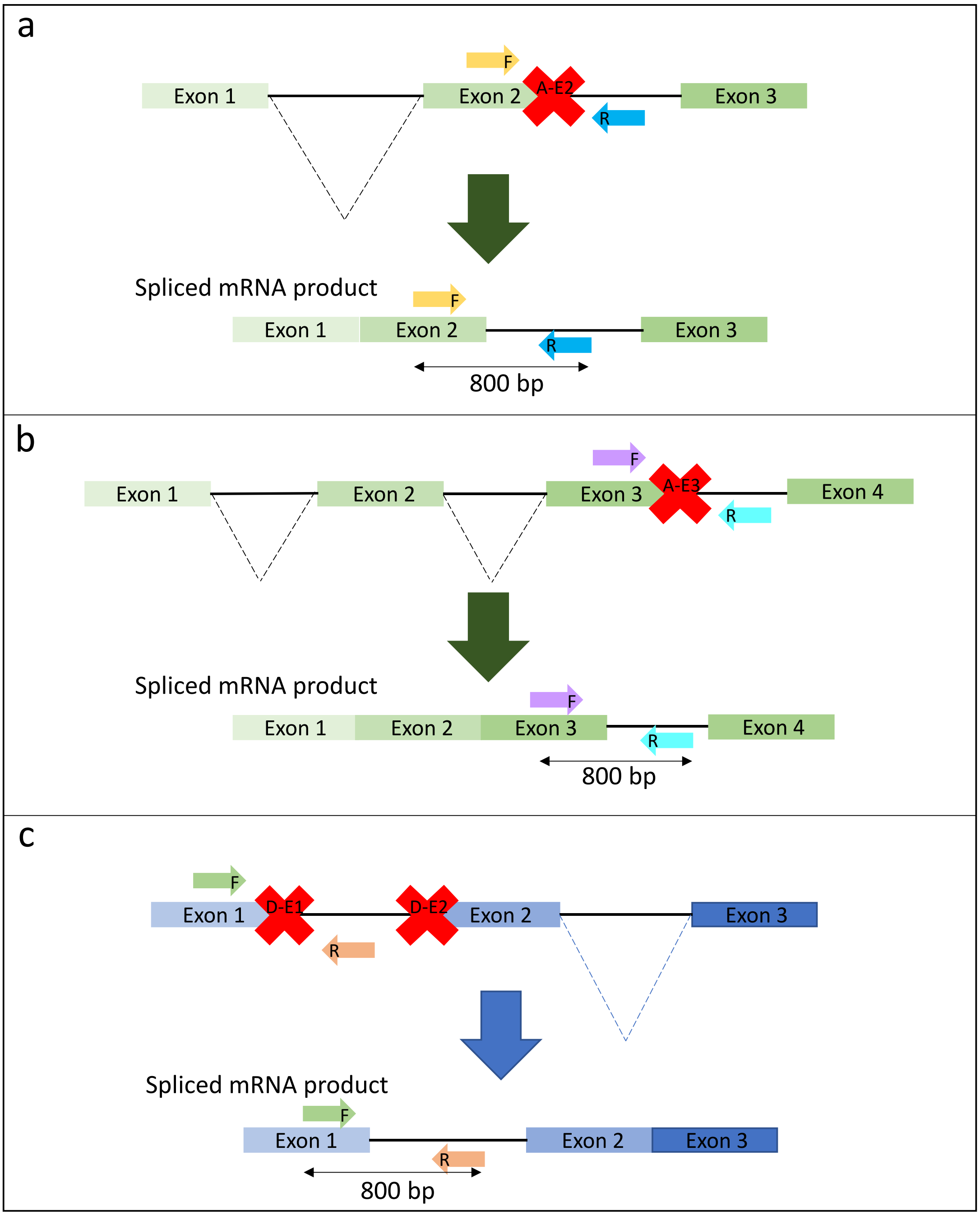

Figure 24: Predicted splicing defects in *dock6* and *arhgap31* due to morpholino interference.

(**a**) The arhgap31-E2 (A-E2) and (**b**) arhgap31-E3 (A-E3) morpholinos target the splice donor sites of intron 2 and 3, respectively. (**c**) The dock6-E1 (D-E1) and dock6-E2 (D-E2) morpholinos target the splice donor and acceptor sites of dock6 intron 1, respectively. F and R arrows represent forward and reverse primers to PCR amplify across the dock6 intron-exon junctions. The size of the region amplified by each primer set confirming intronic inclusion is indicated in each panel. The dashed lines indicate splicing of introns. The predicted spliced mRNA product is displayed for each morpholino.

minute. Primers targeting exons 2-3 of *actb* were used as a positive control and were amplified in all samples. Upon amplification of the dock6 exons 21-22, the band generated from the *dock6*-E1 morphant embryos was comparable to the wild-type, suggesting that morpholino injection does not result in an unstable mRNA transcript (Figure 23b). However, the exon 21-22 band generated in *dock6*-E2 morphants appears much less intense than in the wild-type (Figure 23c). Although this could have resulted from overloading the wild-type sample, it may imply that inclusion of intron 1 has led to the transcription of an early stop codon, resulting in nonsense-mediated mRNA decay.

The phenotypic impact of morpholino-mediated *arhgap31* and *dock6* knockdown are described in Sections 4.4 and 4.5.

4.3 Independent validation of *dock6* knockdown using CRISPR/Cas9

To further verify the validity of phenotypic effects seen under morpholino-mediated *dock6* knockdown, CRISPR/Cas9 experiments were optimised to cut the gene at exons 3, 6 and 17 and develop an independent *dock6* knockdown model. As with the morpholino-based knockdown experiments, different volumes of the CRISPR-gRNA complex were injected to determine the best embryonic survival rate (Figure 25a). The optimal dose was established as 1 nl of *dock6*-ribonucleoprotein complex (RNP) for minimal lethality with a phenotype.

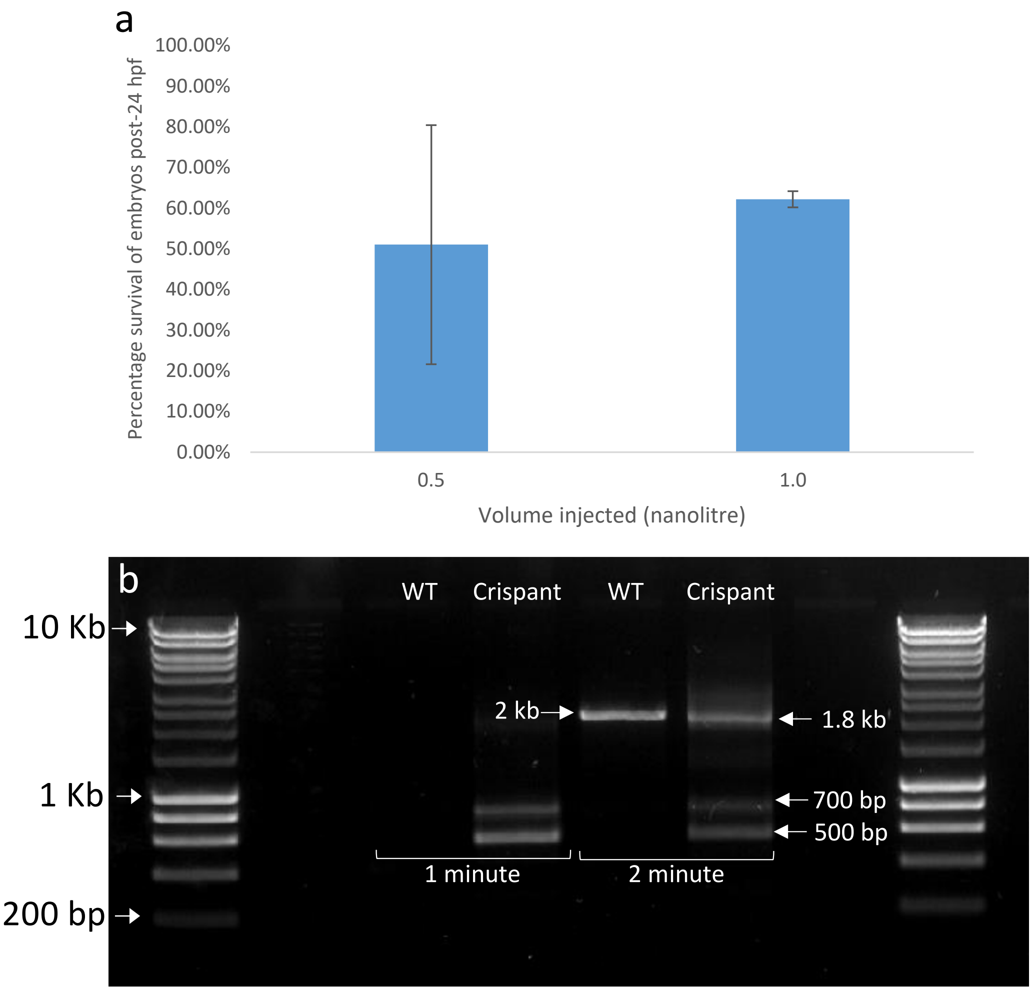

Figure 25: Optimised multiplexed CRISPR injections result in exonic base pair deletions.

(**a**) The embryonic mortality rates upon injection of different volumes of the CRISPR-gRNA complex. Conditions were statistically compared by unpaired t-test, n=4 cohorts of ~50 24 hpf embryos (**b**) Primers targeting *dock6* exon 2 to exon 20 were used to identify deletions in *dock6*-crispants. Bands generated by a 1- or 2-minute extension time are indicated. Meridian BioScience HyperLadder 1 Kb was used as a molecular weight marker.

PCR experiments amplified a 2 kb region across exons 2-20, encompassing the target sequences of all three injected gRNAs (Figure 25b). Two PCR extension times were used, to accommodate the varying sizes of PCR products expected following CRISPR-mediated cleavage of *dock6*. The longer extension time amplified the expected 2 kb product in the wildtype cohort, whereas in the *dock6*-crispant cohort, additional products were generated at sizes 1.8 kb, 700 bp and 500 bp (Figure 25b). The 1.8 kb band indicates deletion of 200 bp between gRNA 1 and gRNA 2, at exons 3 to 6. The

700 bp product represents deletion of the region between gRNAs targeting exon 6 to exon 17. The 500 bp product has been generated by CRISPR-mediated deletion of exon 3 to exon 17 (Figure 26b). Using a 1-minute extension time, the expected 2 kb band was not amplified in either the wild-type or the *dock6*-crispant, but the 700 bp and 500 bp bands were more intensely amplified in the crispant. This confirmed that the 500 and 700 bp products were specific bands and are likely to be truncated amplicons of *dock6* exons 3-17. Sanger sequencing confirmed disruption of each sequence from gRNA 1 onwards (Figure 26c).

To confirm that the observed nucleotide deletions gave rise to *dock6* depletion, qPCR experiments displayed an average *dock6* expression fold-change of 0.34 ± 0.12 (SD) in CRISPR-treated embryos by comparison to wildtype cohorts (Figure 27). Statistical analysis by unpaired t-test with Welch's correction confirmed a significant reduction of *dock6* transcript levels in *dock6*-crispants when compared to wild-type levels (p=0.003). Therefore, the injection of a multiplexed *dock6*-CRISPR/Cas9 complex effciently produced a *dock6* knockdown model in the F_0 generation.

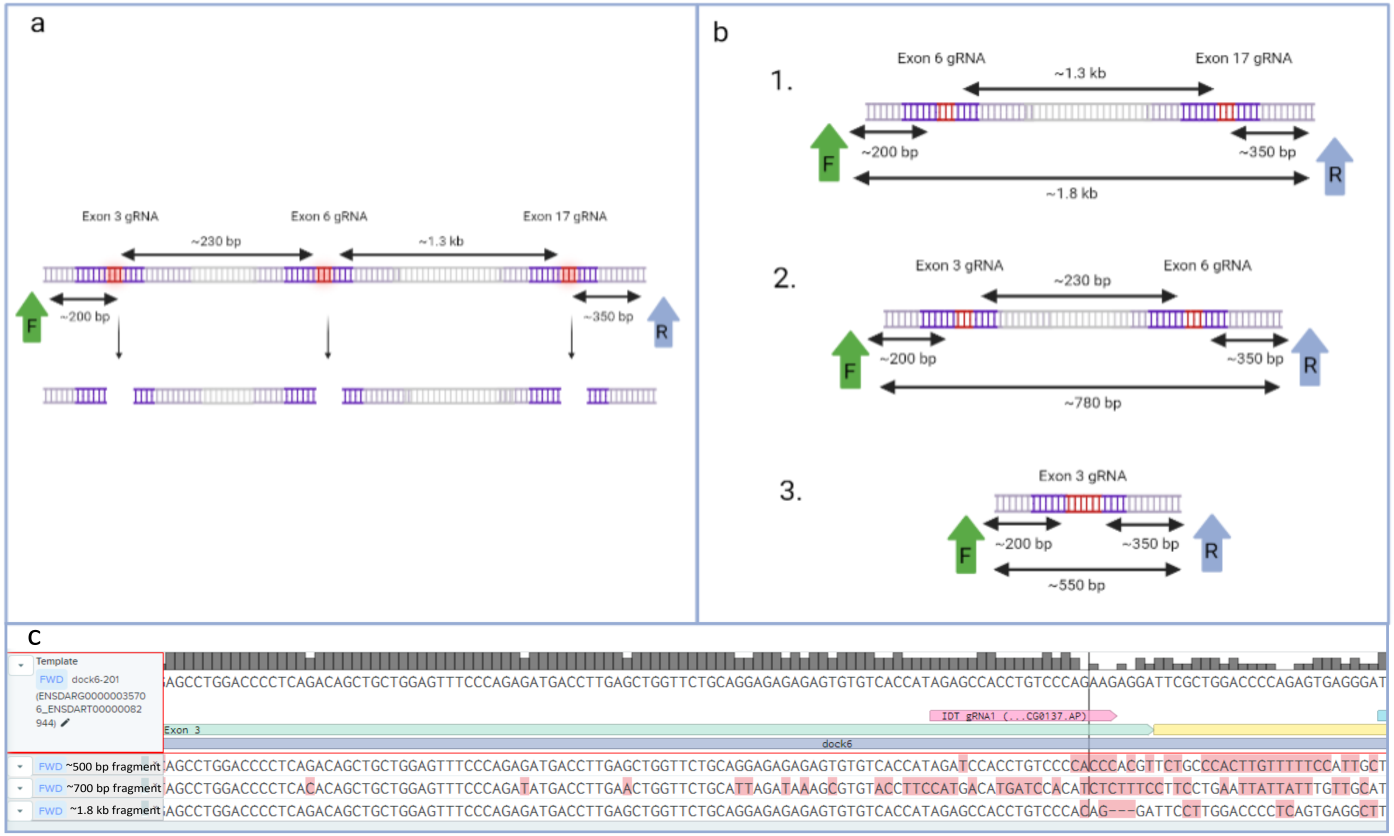

Figure 26: Schematic illustrating the genetic consequences of *dock6*-crispant injections in zebrafish embryos.

(**a**) The three *dock6*-specific gRNAs targeted exons 3, 6 and 17. To assess cutting of these sites by Cas9, forward (**F**) and reverse (**R**) primers were used to amplify the target region for sequencing. (**b**) After Cas9 cleavage, gene deletions were expected between each of the three target sites: **1.**, **2.** and **3.** (**c**) Following amplification of the target region, three fragments were sequenced. Each displayed disruption around the expected cut site of the gRNA targeting exon 3 (vertical line), implying a high efficiency of gene deletion following injection of the Cas9-gRNA complexes targeting exons 3, 6 and 17.

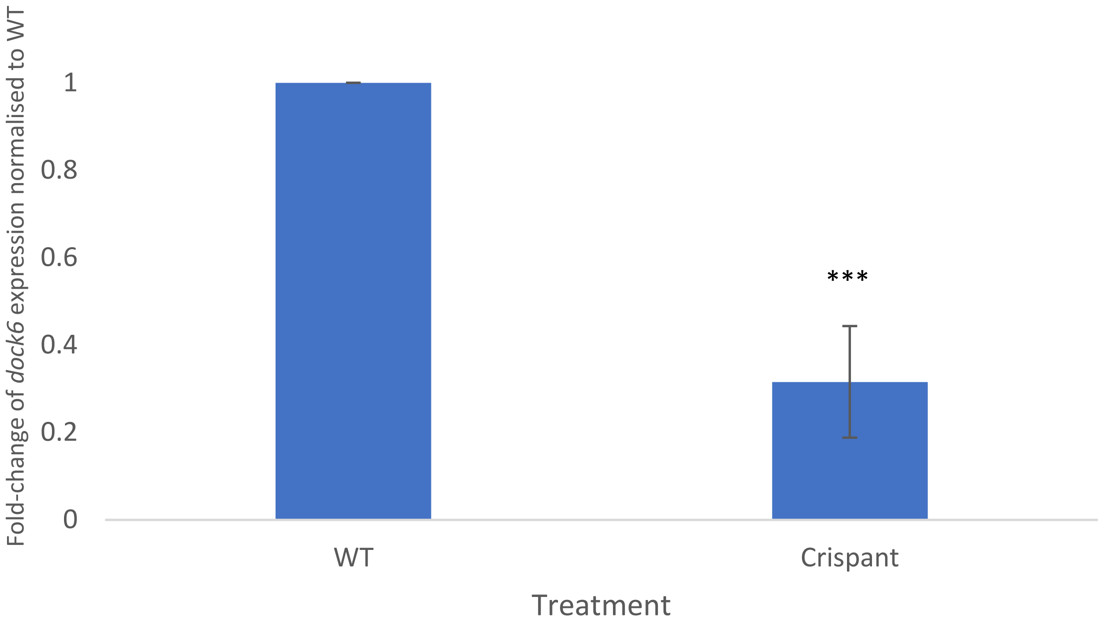

Figure 27: *dock6* mRNA level fold-change of 5 dpf *dock6* CRISPR-treated embryos.

qPCR experiments measured *dock6* mRNA level in wild-type and *dock6*-crispant embryos. Transcript levels were calculated relative to wild-type *dock6* expression. N=5 (N represents 50 embryos). ****p*=0.0003. Error bars represent standard deviation.

4.4 Phenotypic effects of *arhgap31* knockdown

Following validation of *arhgap31* knockdown upon injection of *arhgap31*-E2 or E3, *arhgap31* morphants were assessed for phenotypes induced by reduced *arhgap31* expression during embryogenesis. A dextran-injected control was included to verify that the injection method was not causing any phenotypic effect (Figure 28). Morphological changes upon *arhgap31* knockdown did not become apparent until around 48 hpf (Figure 29a*ii*, a*iii*). Depletion of *arhgap31* displayed a phenotype of blood accumulation in the pericardium and heart chamber from 48 hpf to 4 dpf. By 4 dpf, a visibly enlarged PCV was also observed, likely due to accumulation of blood in this vessel (Figure 29d*ii*, d*iii*).

Phenotype frequencies were calculated in wild-type, *arhgap31*-E2 and *arhgap31*-E3 embryos aged 72 hpf and 4 dpf (Figure 30). No abnormalities were detected in wild-type embryos aged 72 hpf and 4 dpf, however all counted embryos treated with *arhgap31*-E2 and *arhgap31*-E3 showed pericardial oedema, blood accumulation and an enlarged PCV at 72 hpf (Figure 30a). This reduced to 75% of *arhgap31*-E2 embryos showing all three phenotypes at 4 dpf (Figure 30b). Under *arhgap31*-E3 injection, 66.67% of 4 dpf embryos showed pericardial oedema, and 100% of *arhgap31*-E3 embryos displayed blood accumulation and enlarged PCV. Thus, the phenotypic consistency between morphant models implies that reduced *arhgap31* expression induces pericardial oedema, blood accumulation and enlargement of the PCV.

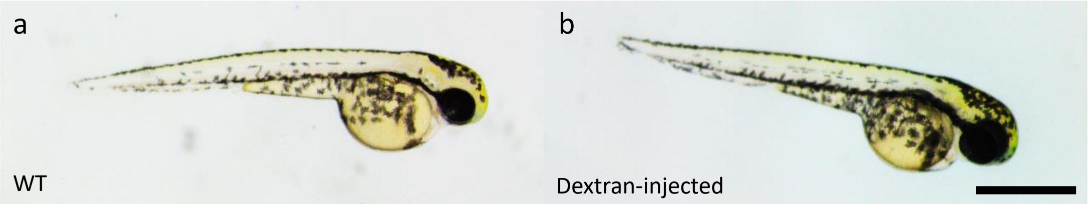

Figure 28: Comparison between wild-type and injected control embryo at 48 hpf.

a. Wild-type (WT) and **b.** dextran-injected control embryos show no morphological differences and are indistinguishable. N=3 cohorts of 50 embryos, representative images are shown. Scale bar, 500 µm.

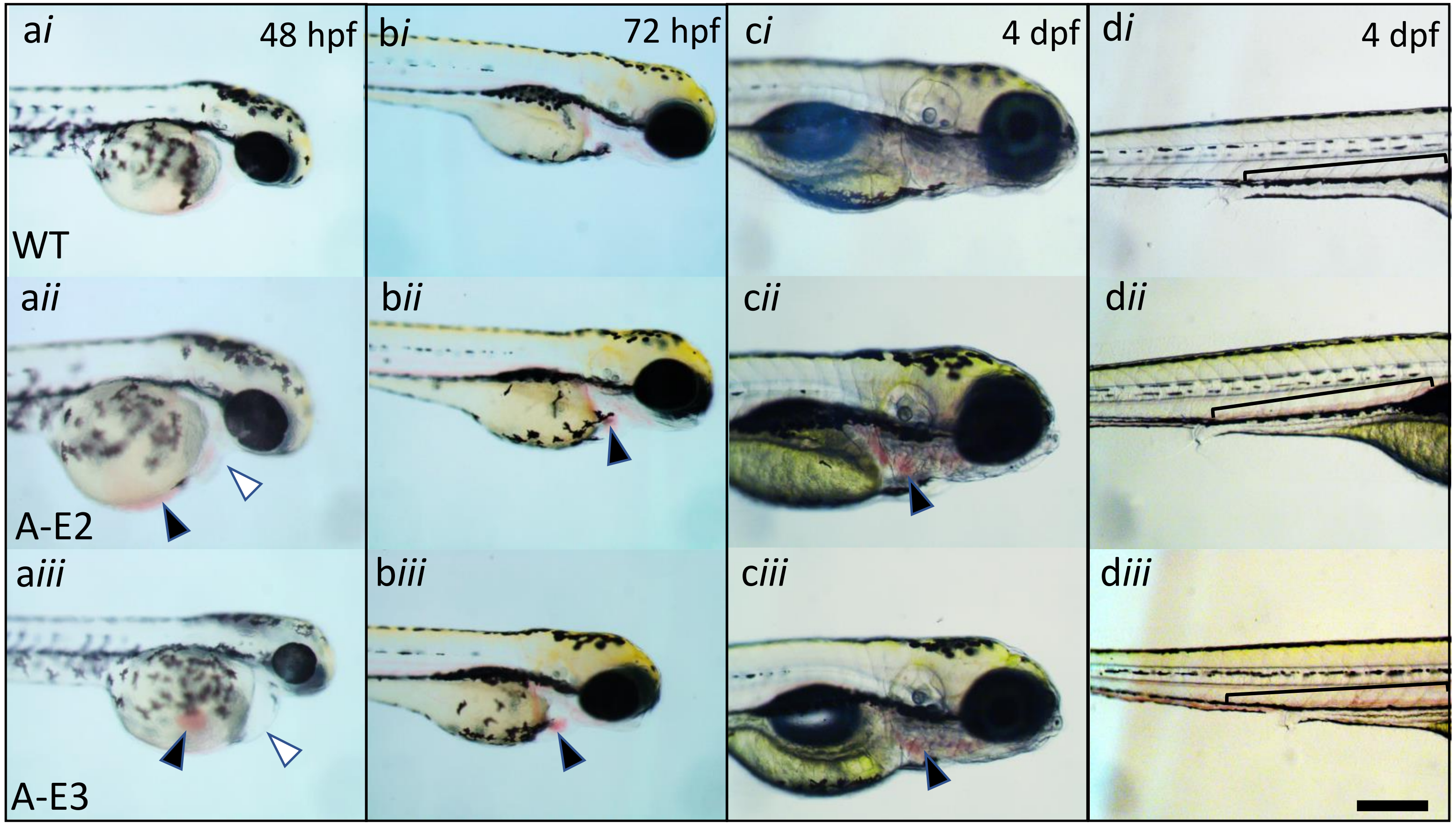

Figure 29: Phenotypic effects of *arhgap31* knockdown.

Phenotyping of *arhgap31* morphant embryos at (**a**) 48 hpf, (**b**) 72 hpf and (**c, d**) 4 dpf by comparison to wild-type (WT) embryos. Pericardial oedema (white arrowheads) is present in *arhgap31* morphants from 48 hpf. Blood accumulation in the heart chamber (black arrowheads) throughout development and enlarged posterior cardinal vein (black bracket) at 4 dpf were observed in the morphant embryos. N=4-6 cohorts of 30-88 embryos, representative images are shown. Scale bar, 300 µm.

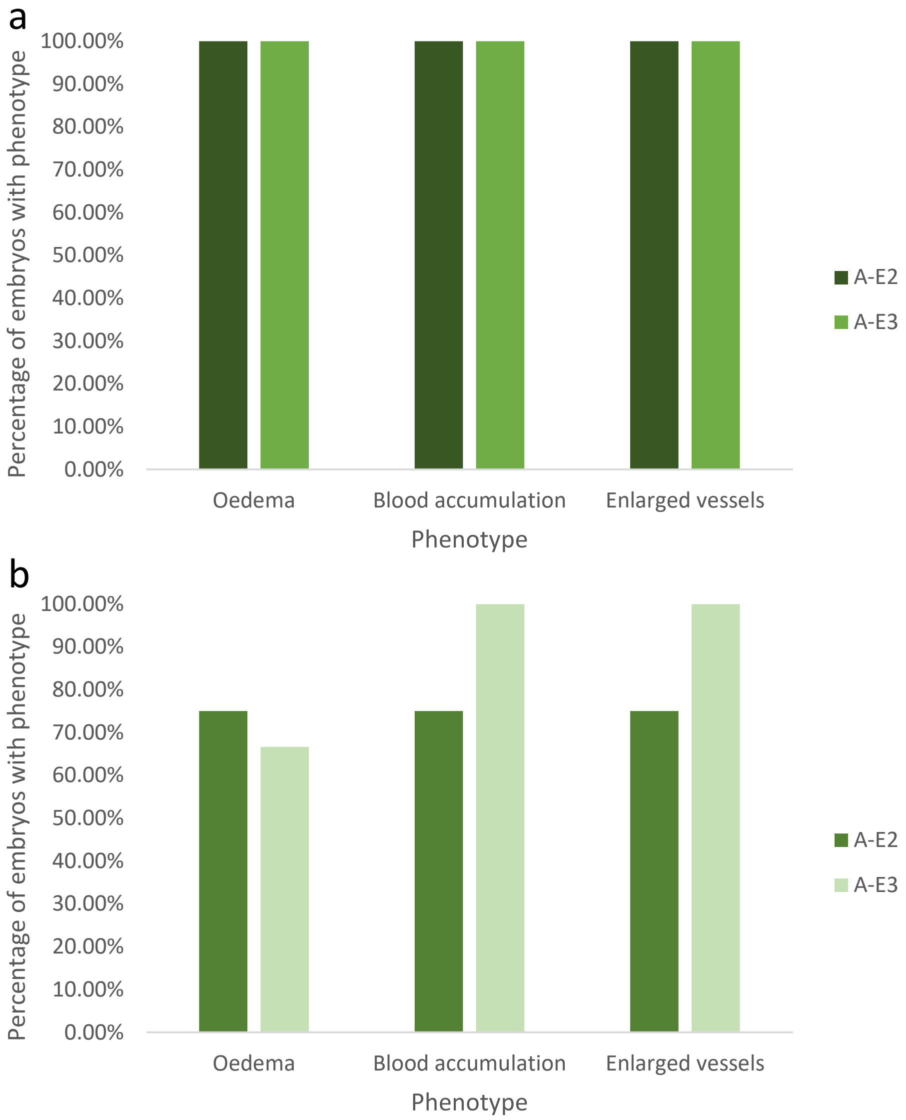

Figure 30: Phenotype frequency upon *arhgap31* depletion.

Quantification of oedema, blood and vessel phenotypes observed in *arhgap31*-E2 (A-E2) and *arhgap31*-E3 (A-E3) at (**a**) 72 hpf and (**b**) 4 dpf. N= 12 embryos/condition. 20 wild-type embryos were assessed and displayed no phenotypic abnormalities. Statistics were not performed as these data represent cumulative results rather than averages over multiple experiments.

4.5 Phenotypic effects of *dock6* knockdown

Following verification of morpholino- and CRISPR/Cas9-mediated *dock6* knockdown models, embryos were phenotypically assessed over embryogenesis. Embryos injected with multiplexed *dock6*-CRISPR/Cas9 or morpholinos targeting the splice donor and acceptor sites of *dock6* intron 1 were imaged from age 48 hpf to 4 dpf (Figure 31). Embryos depleted of *dock6* showed no distinguishable phenotype by comparison to wild-type embryos at 24 hpf. By 48 hpf, all *dock6* knockdown embryos displayed microphthalmia but otherwise appeared morphologically healthy (Figure 31a*i*-d*i*). At 72 hpf and 4 dpf, however, pericardial oedema combined with impaired cardiac looping presented in *dock6*-depleted embryos, in addition to increased pigmentation and absent blood flow (Figure 31a*ii*-d*ii*, a*iii*-d*iii*).

Wild-type, dextran-injected control and *dock6* knockdown embryos were scored for each observed phenotype at 72 hpf and 4 dpf (Figure 32). For each phenotype, no abnormalities were observed in the wild-type or the dextran-injected control embryos at either 72 hpf or 4 dpf. Timepoint 48 hpf was not scored as microphthalmia was the only phenotype displayed and was present in all treated embryos. At 72 hpf, the most prominent phenotypes include pericardial oedema and microphthalmia, which each displayed a 100% frequency in both *dock6* morphants. A 90% and 95% frequency of pericardial oedema and microphthalmia, respectively, was observed in the *dock6*-crispants (Figure 32a). Representative movies demonstrating blood circulation in wild-type and *dock6*-depleted embryos are provided (Movie 1). While all wild-type embryos displayed blood circulation at 72 hpf (Movie 1a), this was absent in 100% of *dock6*-E2 morphant embryos (Movie 1c) and

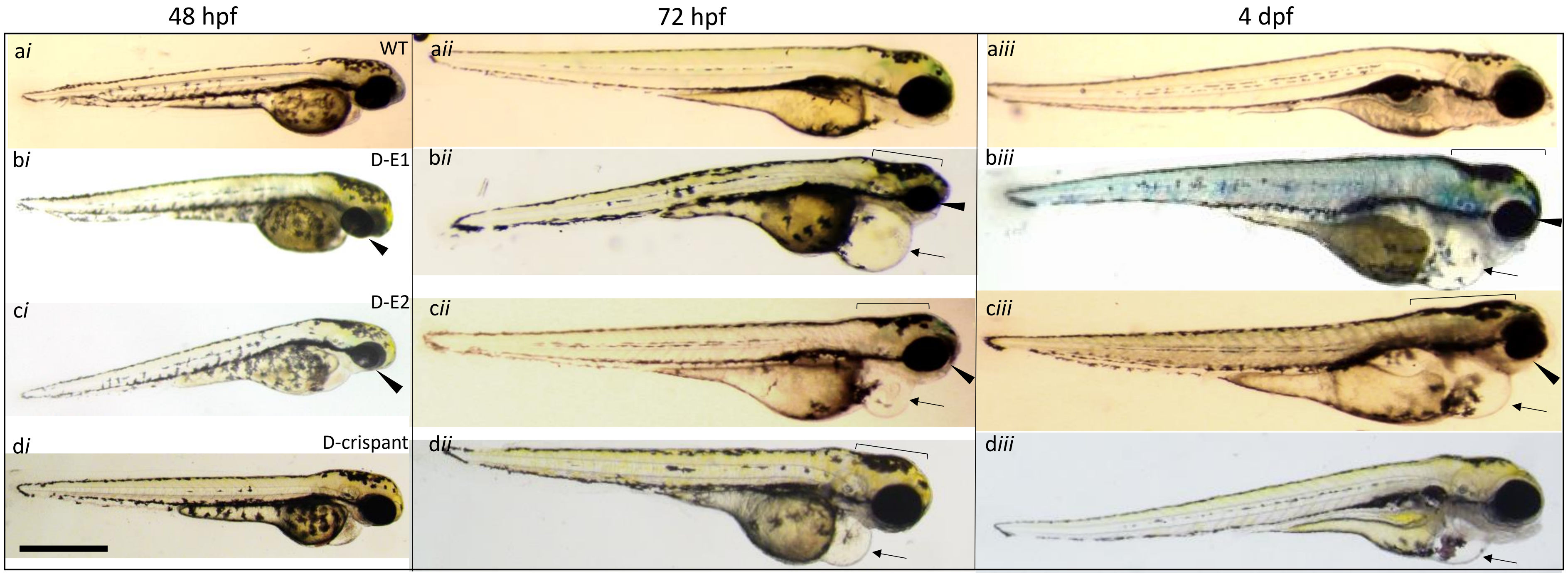

Figure 31: Phenotypic effects of *dock6* depletion.

Images taken from a lateral view of (*i*) 48 hpf, (*ii*) 72 hpf and (*iii*) 4 dpf embryos representing (**a**) uninjected wild-type zebrafish (WT) and fish injected with (**b**) *dock6*-E1 (D-E1), (**c**) *dock6*-E2 (D-E2) morpholinos or (**d**) *dock6*-crispant (D-crispant) complex. Pericardial oedema (arrow), microphthalmia (arrowhead) and increased pigmentation (brackets) are demarcated. N=5-7 cohorts of 40-100 embryos per condition. Scale bar, 500 µm.

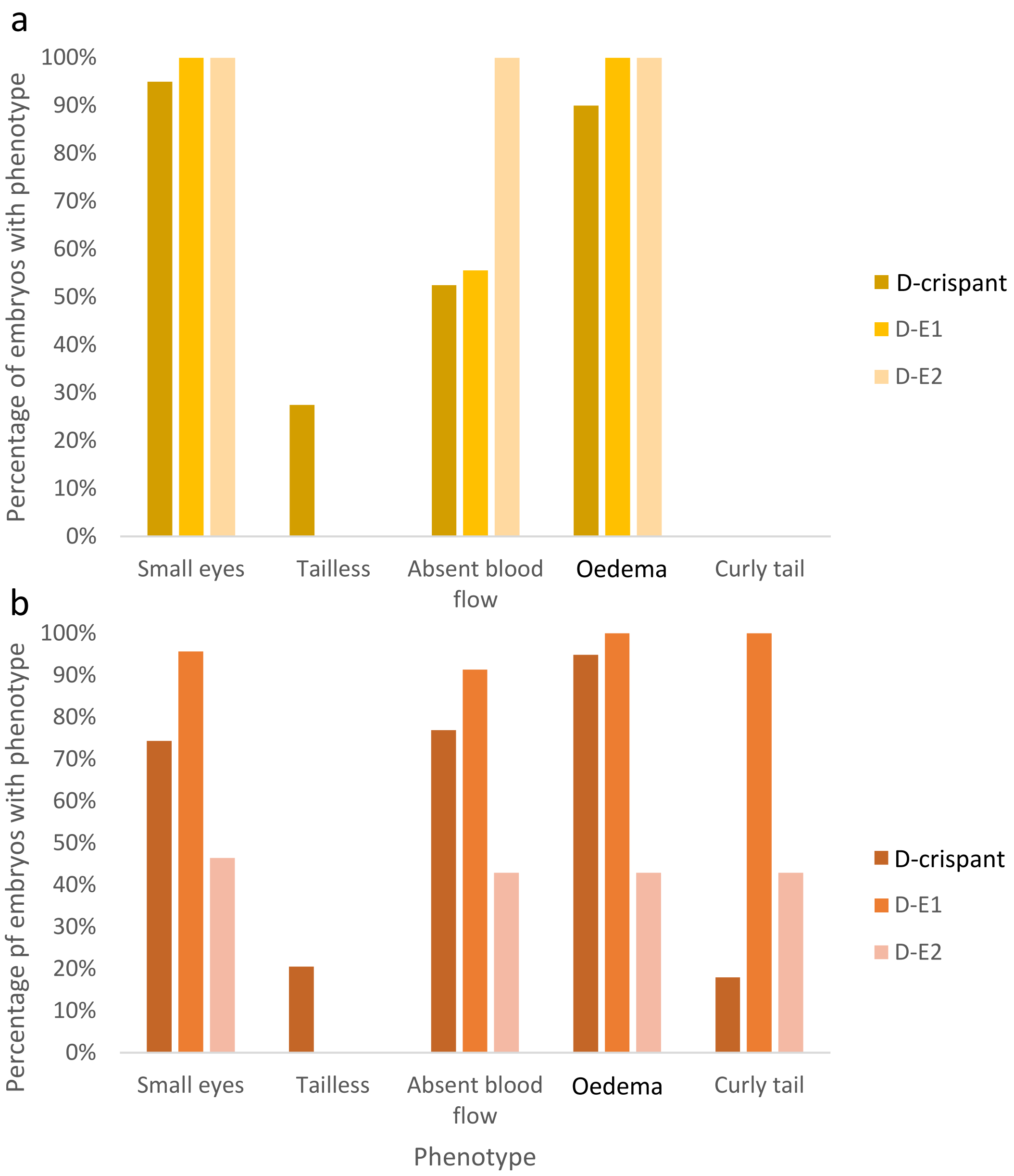

Figure 32: Phenotypic frequency upon *dock6* depletion.

Quantification of phenotypes observed in *dock6*-crispant (D-crispant), *dock6*-E1 (D-E1) and *dock6*-E2 (D-E2) embryos at (**a**) 72 hpf (n=40, 18, 17, respectively) and (**b**) 4 dpf (n=39, 23, 28, respectively). A total of 55 wild-type control embryos were assessed at 72 hpf and 4 dpf and displayed no phenotypic abnormalities. Statistics were not performed as these data represent cumulative results rather than averages over multiple experiments.

in 56% and 53% of *dock6*-E1 (Movie 1b) and *dock6*-crispant morphants (Movie 1d), respectively. At 72 hpf, 28% of *dock6*-crispant embryos were tailless, however a tail phenotype was not established in either *dock6* morphant. The tailless and curly tail phenotypes are demonstrated in Figure 33c and d, respectively, but not included in Figure 31 as this figure demonstrates representative images of the typical phenotype seen in the *dock6*-crispant embryos. Due to the low frequency of the phenotype, as shown in Figure 31, the tailless and curly tail phenotypes was not considered typical and therefore not included in Figure 31. However, due to the association of abnormal tail development with embryonic patterning defects and the parallels to AOS-related phenotype TTLD, a potential link between *dock6* knockdown and early tail development will be further discussed (Section 4.6.3.2).

By 4 dpf, the microphthalmia and oedema phenotypes were slightly attenuated (Figure 32b). At this timepoint, microphthalmia presented in 74%, 95.65% and 46.43% of *dock6*-crispant, *dock6*-E1 and *dock6*-E2 embryos, respectively. Pericardial oedema was apparent in 95%, 100% and 42.86% of *dock6*-crispant, *dock6*-E1 and *dock6*-E2 embryos, respectively (Figure 32b). The proportion of embryos lacking

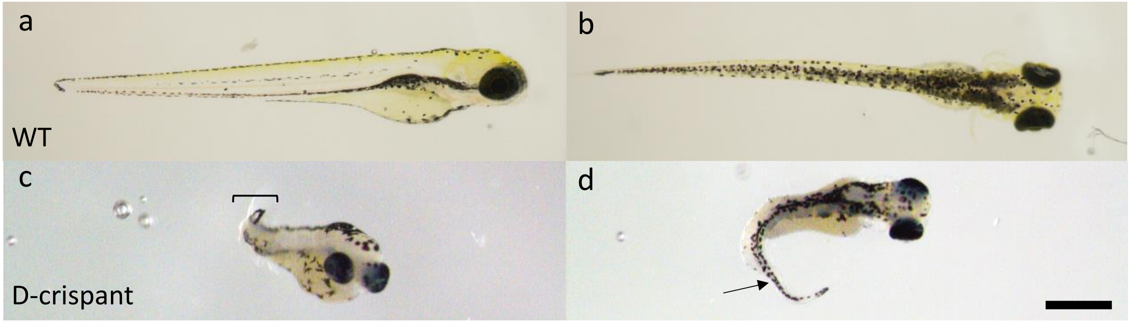

Figure 33: Tail phenotypes observed in *dock6*-crispant embryos at 72 hpf.

A lateral and dorsal view of (**a, b**) wild-type (WT) and (**c, d**) *dock6*-crispant (D-crispant) embryos are displayed. The (**c**) short tailless (bracket) and (**d**) curly tail (arrow) phenotypes are indicated in two different embryos injected with the *dock6*-crispant complex. N= 2 cohorts of 17-39 embryos/condition. Scale bar, 500 µm.

blood flow was largely maintained, found in 77%, 91.3% and 42.86% of *dock6*-crispant, *dock6*-E1 and *dock6*-E2 embryos, respectively. By 4 dpf, the number of tailless *dock6*-crispant embryos decreased to 21% and remained unobserved in the *dock6*-E1 and -E2 embryos. However, the proportion of embryos exhibiting a curly-tailed phenotype rose from 0% to 18%, 91.3% and 42.86% of *dock6*-crispant *dock6*-E1 and *dock6*-E2 embryos, respectively (Figure 32b). Together, these data show that the absent blood flow, pericardial oedema and microphthalmia knockdown phenotypes are consistent between *dock6* knockdown models, with an additional tail phenotype observed in some embryos across the three treatments.

4.5.1 *dock6* knockdown induces microphthalmia

Following the observation of microphthalmia in developing embryos depleted of *dock6*, ImageJ was used to measure the head and eye areas of 48 hpf treated and untreated embryos (n=9/treatment). These measurements were then used to quantify the eye-to-head size ratio (Figure 34). After normalisation to the wild-type, the eye sizes of *dock6*-E1, *dock6*-E2 and *dock6*-crispant embryos at 48 hpf showed a fold-change of 0.85, 0.83 and 0.69 by comparison to the wild-type. Therefore, reduction of *dock6* expression leads to decreased eye size in zebrafish over embryogenesis.

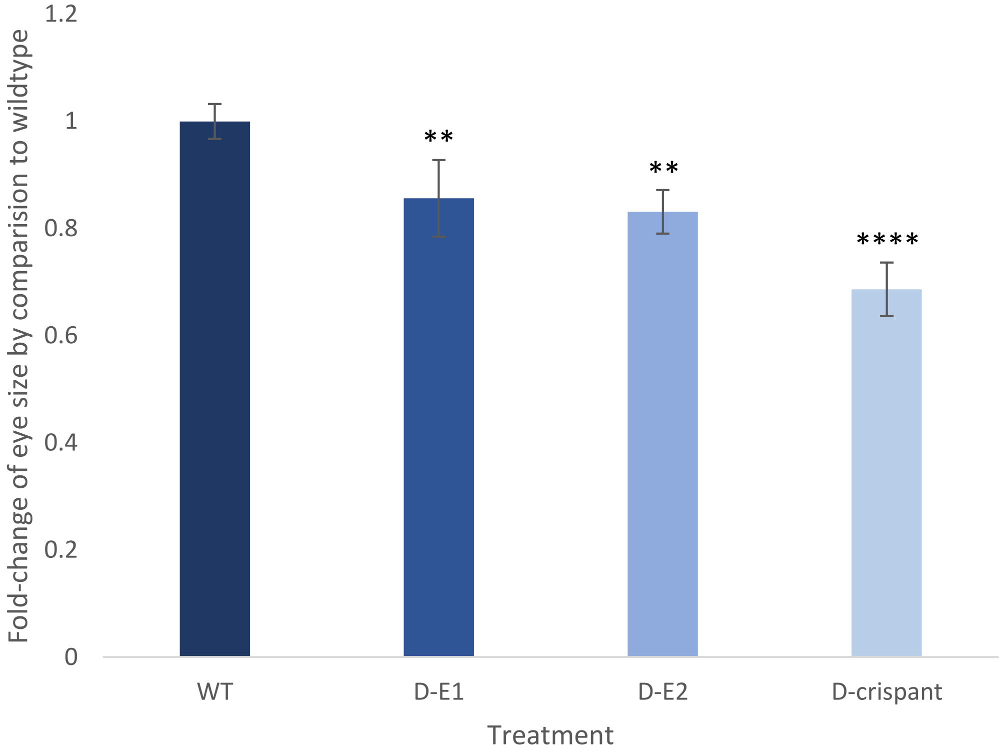

Figure 34: Decreased eye size in *dock6* morphants compared to wild-type embryos.

Measurement of eye:head size ratio in wildtype (1 ± 0.033), *dock6*-E1 (0.85 ± 0.072), *dock6*-E2 (0.83 ± 0.041) and *dock6*-crispant (0.69 ± 0.050) embryos aged 48 hpf. **p>0.005, ****p<0.0001. Statistical analysis was performed by one-way ANOVA with a Dunnett's test for multiple comparisons. Error bars represent standard deviation. N = 9 embryos/condition.

4.6 Discussion

4.6.1 Validating knockdown models

Morpholino- and CRISPR/Cas9-mediated knockdown techniques were implemented to assess the phenotypic impact of reduced *arhgap31* and *dock6* expression during embryogenesis. RT-PCR and Sanger sequencing indicated inclusion of intron 2 and intron 3 in *arhgap31*-E2 and *arhgap31*-E3, respectively, and of intron 1 in both *dock6* models. Therefore, it is likely that the morpholinos disrupt splicing by binding to splice acceptor sites within the genes *arhgap31* and *dock6* to generate knockdown models. Although a knockdown model may not be truly representative of *ARHGAP31*-linked AOS, which has been shown to produce a gain-of-function phenotype, the disruption of *arhgap31* in zebrafish will provide important insights into the normal function of this gene during vascular development.

Due to a history of morpholinos being liable to off-target effects, in particular affecting *p53* expression, two non-overlapping morpholinos per gene were used to generate *arhgap31* and *dock6* knockdown models. It is generally accepted that if two different morpholinos target the same gene and show identical phenotypes, observations are considered as a true representation of specific gene knockdown and not an off-target effect. In preliminary *arhgap31* and *dock6* morphant experiments, consistent phenotypes were seen between the two morphants for each gene, suggesting that the effects seen are representative of a gene-specific loss-of-function.

4.6.1.1 Knockdown model limitations

For completeness, experiments to rescue the phenotypes generated by *dock6* and *arhgap31* reduction were attempted, however injection of the wild-type mRNA alongside morpholinos mediated lethality by 24 hpf.

A drawback of morpholino technology is that the knockdown is transient and, hence, not representative of the clinical state. Evidence in both HeLa cells and patient-derived fibroblasts suggest that genetic compensation, in the form of active Rho GTPase equilibration, can develop following stable disruption of *DOCK6* (Cerikan et al., 2016; Cerikan and Schiebel, 2019; Shaheen et al., 2011). This does not occur with transient knockdown; therefore, it will be necessary to generate a stable knockout of *dock6* to assess the effect of *dock6* loss-of-function in a more representative zebrafish model of AOS. The DOCK family contains 11 proteins, each known to regulate Rac1, Cdc42 or both, leaving much scope for genetic compensation upon the knockdown of *DOCK6*. In this case, it may be useful to measure the gene expression of other Rac1/Cdc42-specific GAPs and GEFs and GDIs following *dock6* knockdown.

4.6.1.2 Confirmation of CRISPR-mediated dock6 knockdown

Wildtype and *dock6*-CRISPR/Cas9 injected embryos were assessed for evidence of base pair deletions by RT-PCR. In the wild-type, the expected product of 2 kb was generated. However, in the *dock6*-crispant, three separate bands were generated at 1.8 kb, 700 bp and 500 bp, indicating CRISPR-mediated nucleotide deletion. Sanger sequencing confirmed that each band contained sequence disruption at the *dock6* gRNA 1 (exon 3) site. Due to the nature of CRISPR/Cas9 technology, it is likely that other changes were introduced to the genome, which can be detected by techniques such as MiSeq (Ran et al., 2013). However it was not within the scope of this study to perform further validation experiments. Quantitative PCR experiments confirmed a significant knockdown in the injected F_0 embryos. Taken together, the RT-PCR, sequencing and qPCR data strongly support the use of multiplexed gRNAs to generate crispants as an efficient method of gene knockdown in zebrafish and a reliable independent validation of morpholino-mediated phenotypes.

4.6.2 Phenotypic observations following *arhgap31* knockdown

Reduced *arhgap31* expression gave rise to pericardial oedema, similarly to the *dock6* knockdown models. While pericardial oedema can be associated with morpholino off-target effects, the presence of pericardial oedema to the same degree in both *arhgap31* knockdown models implies that this observation is specific to reduced gene expression. Pericardial oedema is indicative of cardiac malformation, particularly defective cardiac left-right patterning (Tessadori et al., 2021). By contrast to the *dock6* knockdown models, a 'stringy heart' defect was not observed, and heart looping appeared normal. This may be due to the relatively mild oedema caused by *arhgap31* which appears to recover over time, as the frequency of oedema decreases by 4 dpf. Therefore, the mechanical pressures which may impact heart looping during *dock6* knockdown may be less severe upon *arhgap31* reduction and so do not physically impair healthy cardiac looping. Other causes of pericardial oedema include altered kidney development caused by impaired cardiac function, leading to defective kidney filtration and hypertension (Hill et al., 2004; Zennaro et al., 2014). Consequently, zebrafish embryos develop pericardial and yolk sac oedema due to the compromised ability of the kidneys to excrete excess water. A functional cardiovascular system is required for healthy kidney development, in addition to Notch signalling which is known to have a critical role in the developing pronephros as Notch-specific ligands are expressed and restricted to the proximal intermediate mesoderm (Outtandy et al., 2019). Therefore, the presence of pericardial oedema upon *arhgap31* knockdown may be due to impaired cardiac development, resulting in poor kidney function and a build-up of excess fluid.

4.6.2.1 Blood accumulation and enlarged vessels under arhgap31 depletion

The observation of blood accumulation in the heart upon *arhgap31* knockdown appears to correlate with an enlarged PCV. Typically, blood accumulation is associated with thrombosis, whereby the blood vessels are occluded and there is a build-up of red blood cells. However, it is unlikely that the *arhgap31* knockdown embryos suffered from blood vessel blockage as each embryo displayed circulating red blood cells. There are several possible explanations: firstly, a partial blockage or narrowing of the PCV, also known as stenosis, which causes red blood cells to exit the PCV more slowly than they arrive (Lu et al., 2020). Alternatively, PCV enlargement and blood accumulation has been associated with dorsal-ventral patterning defects. A specific example of this includes the Twisted gastrulation (*tsg*) gene which causes ventralisation upon overexpression and when depleted in zebrafish leads to blood accumulation and oedema of the PCV (Little and Mullins, 2004). Additionally, disordered endothelia have been noted to cause blood accumulation during zebrafish development (Chen et al., 1996). Therefore, it is likely that blood accumulation induced by *arhgap31* knockdown is caused by vessel stenosis, patterning defects, or both. To investigate the possibility of stenosis or vessel occlusion underlying blood accumulation, microangiography experiments could be performed to determine the efficiency of vessel perfusion and detect the presence of occlusions.

4.6.3 Phenotypic observations following *dock6* knockdown

Upon phenotypic assessment of both *dock6* morphant groups, the larvae appear relatively healthy until reaching 72 hpf, with the exception of microphthalmia which becomes prominent by 48 hpf. By 72 hpf, morphant development appears quite distinct from the wild-type. This coincides with the expression of *dock6* in the cranial vasculature, fast and slow muscle fibres, optic vessels and heart previously seen at this stage. Morphant larvae develop pericardial oedema, display a lack of blood circulation and a higher intensity of pigmentation on the cranium, in addition to the microphthalmia phenotype.

However, inconsistencies in the frequencies of the phenotypes between *dock6*-E1, *dock6*-E2 and *dock6*-crispant embryos were observed. This is likely due to the morphants knocking down dock6 at different efficiencies and potential recovery of the phenotype at contrasting rates between the treatments, due to the transient nature of morpholinos. Differences between phenotypes in the morphants and crispant embryos can be explained by the crispant treatment likely giving a more efficient knockdown of the gene which does not attenuate over time, as CRISPR gene editing is not transient. Despite these discrepancies, the observation of similar phenotypes at a high frequency between each treatment means that the phenotypes observed are likely true and reflect the function of dock6 in zebrafish.

4.6.3.1 Depleted dock6 expression causes cardiac and vascular defects

The presence of pericardial oedema and lack of blood flow is indicative of malformations in the development of the heart or vasculature. Previous studies have identified altered heart looping, compact ventricles and elongated atria as causal factors of pericardial oedema (Antkiewicz et al., 2005). This is in accordance with our findings whereby pericardial oedema occurs in embryos that have not successfully undergone heart looping, resulting in a ‘stringy heart’ phenotype. The developing heart is the first organ in zebrafish embryogenesis to break left-right symmetry (Tessadori et al., 2021). Consequently, cardiac looping is known to become randomised in zebrafish mutants where midline structure development is affected (Bisgrove and Yost, 2001; Tessadori et al., 2021). Interestingly, cardiac looping defects in humans are known to cause severe congenital heart defects, including those found in *DOCK6*-related AOS patients, such as tetralogy of Fallot and arterio-venous malformations (Hassed et al., 2017; Lehman et al., 2014; Sukalo et al., 2015). However, it is unclear whether the ‘stringy heart’ defect is a secondary effect caused by mechanical stretching of the heart due to the pericardial oedema.

In zebrafish, a lack of blood flow is typically associated with defective cardiac contractility due to impaired cardiomyocyte function (Kochhan et al., 2013; Xu et al., 2002). As previously noted (see Section 3.3.1), *dock6* expression corresponds with both the heart and slow and fast muscle fibres from 48 hpf to 5 dpf, suggesting a potential role for *dock6* in skeletal and cardiac muscle development and function. Interestingly, during early zebrafish development a healthy blood flow is required for the formation of the vascular system (Kochhan et al., 2013; Kugler et al., 2021). This is apparent in the midbrain vasculature, where a combination of angiogenesis and blood vessel perfusion drives extensive vessel pruning to generate a simplified network for efficient blood flow (Chen et al., 2012). Similarly, a study which inhibited developmental pruning of the retinal vasculature by suppressing Dll4/Notch1 investigated the role of this pathway on vasoconstriction (Lobov et al., 2011). Modulation of blood flow had a direct impact on vessel pruning whereby loss of blood flow, maintained by Dll4/Notch1 signalling, immediately preceded blood vessel regression (Lobov et al., 2011). Therefore, the lack of blood flow that was observed in *dock6*-depleted embryos may impact the refinement and expansion of the developing vasculature due to the loss of haemodynamic-mediated vessel pruning, resulting in further vascular abnormalities.

4.6.3.2 Abnormal tail development upon dock6 knockdown

Defective tail development was observed in all three *dock6* knockdown models. The *dock6*-crispant displayed a tailless phenotype at a low frequency at both 72 hpf and 4 dpf, however no tailless phenotype was seen in *dock6* morphant embryos. Instead, a curly-tail phenotype became apparent at varying frequencies by 4 dpf in all *dock6* knockdown models. The lower frequency of curly-tailed *dock6*-crispant embryos may be due to the number of embryos that did not develop a tail. Typically, curly-tailed embryos correspond with mutations of genes associated with midline development, such as *cyclops* and *chameleon* (Brand et al., 1996). These mutants commonly display median brain defects, disorganised motor neuron development and a reduced or absent floor plate and demonstrate an interaction with the Hedgehog pathway. In this pathway, *Shh* is essential for floor plate cell differentiation in addition to its known roles in vasculo- and angiogenesis (Albert et al., 2003; Brand et al., 1996).

Therefore, knockdown of *dock6* may impair development of the midline, leading to the tail defects in zebrafish embryos.

4.6.3.3 Neural crest-associated abnormalities upon dock6 knockdown

The increased pigmentation observed in *dock6*-E1 and -E2 embryos is of interest in the context of the neurological abnormalities associated with *DOCK6*-related AOS. Pigmented cells in zebrafish are derived from the neural crest, along with neurons and glia of the peripheral and enteric nervous system, and head and neck cartilage (Figure 21) (Furutani-Seiki et al., 1996). Therefore, variation of morphant pigmentation patterns is commonly due to a disruption in the functions of cells derived from the neural crest. Interestingly, the neural crest plays a critical role in the formation of the dorsal and ventral midline of the neural tube including the development and differentiation of the notochord and floor plate, strengthening the association of *dock6* with healthy midline establishment (Sedykh et al., 2017).

Increased *dock6* and decreased *arhgap31* transcript levels at 14 hpf seen in Section 3.4 suggest a net increase in active Rac1 and Cdc42 at this timepoint. This corresponds with the onset of NCC migration, for which active Rac1 and Cdc42 are essential for lamellipodia and filopodia formation (Minoux and Rijli, 2010). The combination of the observed pigmentation phenotype and likely Rac1 and Cdc42 activation by Dock6 at this timepoint support a novel association of *dock6* with early neural crest development. Accordingly, studies have found that mutations affecting the neural crest-associated *mitfa* gene in zebrafish result in microphthalmia and defective pigmentation resulting from a loss of melanophores, as well as impaired osteoclast and mast cell function (Lister et al., 1999). Therefore, *dock6*-related neural crest abnormalities could account for the observation of microphthalmia and pigmentation changes in *dock6*-depleted embryos. Alternatively, the small eye phenotype observed may be a result of defective retinal vascularisation. Under normal conditions, at age 48 hpf the zebrafish eye is vascularised by an intraocular hyaloid system and a superficial system which vascularises the eye surface (Kaufman et al., 2015). However, abnormal formation of the ocular vasculature in the embryo and abnormal vascularisation in the mature eye is known to impair eye development and has been implicated in blinding diseases (Kaufman et al., 2015). This is important in the context of AOS whereby 57% of *DOCK6*-related AOS patients display structural eye anomalies, such as vitreoretinopathy, retinal detachment, microphthalmia and retinal avascularisation (Alzahem et al., 2020; Hassed et al., 2017; Jones et al., 2017; Southgate, 2019; Tao et al., 2021). Experiments using microangiography and transgenic vascular reporter lines could be used to investigate the progress of ocular vascularisation in *dock6* knockdown models and determine the origins of microphthalmia observed under reduced *dock6* expression.

4.6.3.4 Comparing phenotypes between dock6 and cdc42 knockdown models

Notably, the abnormalities observed upon *dock6* knockdown are concordant with the phenotypes seen in a *cdc42* morphant (Choi et al., 2013). Similar to the *dock6* morphants and crispant, at 72 hpf the *cdc42* morphant displays pericardial oedema and microphthalmia, with an additional hydrocephaly phenotype (Choi et al., 2013). The comparable phenotypes between *dock6* and *cdc42* knockdown models support the likelihood that the *dock6*-related phenotypes are associated with Cdc42 inactivation (Choi et al., 2013). Additionally, the phenotypes from both the *dock6* and *cdc42* morphants increase in severity with age. Whilst the 5 dpf *cdc42* morphant phenotype appears more severe than the 4 dpf *dock6* morphants, this may be due to an increased phenotype severity with age, or due to global loss of *cdc42* as opposed to reduced Cdc42 activity in *dock6*-localised regions. These parallel phenotypes support the upstream role of *dock6* in regulating Cdc42 activity during embryogenesis. Therefore, future experiments to rescue the *dock6* phenotype with wild-type *cdc42* mRNA injections may support a conserved pathway between mammals and zebrafish and may reveal if reduced *cdc42* activity is key in inducing *dock6* knockdown phenotypes.

4.6.4 Conclusions

The combined defects observed upon *dock6* depletion are indicative of a role for *dock6* in early developmental patterning and segmentation. The presence of pericardial oedema with a ‘stringy heart’ phenotype implies abnormal cardiac looping during early development, impacting circulation of blood around the embryo. Combined with the findings of *dock6* localisation to the floorplate, these data suggest a critical role for *dock6* in normal midline development, potentially in the migration of NCCs to establish correct organ patterning and embryo segmentation.

By contrast, knockdown of *arhgap31* causes a milder phenotype, including pericardial oedema and accumulation of blood in the heart and PCV leading to enlargement of the PCV. This is likely due to *arhgap31*-induced patterning abnormalities giving rise to malformations in the vascular network, although this has yet to be confirmed.

The current work aimed to further our understanding of *arhgap31* and *dock6* involvement during vascular development, therefore future work will largely investigate the vascular consequences following knockdown of these genes. However, given the evidence for a potential role for *dock6* in the neural crest, it would be useful to examine the impact of loss of *dock6* and *arhgap31* in a transgenic *sox10* reporter line and assess cartilage and bone development by Alcian Blue and Alizarin Red staining. A role for *arhgap31* or *dock6* in NCC function may help to elucidate the origins of ACC and TTLD in Rho-related AOS.

Chapter 5: Vascular analysis of Rho dysregulation models

5.1 Introduction

To further analyse the vascular disruption phenotypes identified in zebrafish models of Rho dysregulation (see Sections 4.4, 4.5), expression of the Notch pathway genes *dll4* and *notch1a* were examined following *arhgap31* and *dock6* depletion by qPCR and WISH. Similarly, the gene expression of known vascular markers *kdrl* and *fli1* was assessed. These experiments aimed to examine the effects of decreased *arhgap31* and *dock6* expression on the patterning of vascular structures, in addition to identifying potential regulatory roles for *arhgap31* and *dock6* within established molecular pathways for vascular development. Mutations in *DLL4* and *NOTCH1,* a ligand and receptor of the Notch signalling pathway, are known to cause autosomal dominant AOS. Expression analyses of these two genes under Rho dysregulation therefore aimed to investigate potential crosstalk between the Rho and Notch signalling pathways that might explain the overlapping clinical phenotype. Moreover, as the Notch signalling pathway is strongly associated with developmental vascularisation, these experiments were designed to explore the impact of reduced *arhgap31* and *dock6* expression on early vascular patterning.

To visualise vascular malformations under *arhgap31* and *dock6* depletion in further detail, a combined approach was undertaken using a transgenic vascular reporter line (tg[*fli1*:GFP]) and microangiography in embryos aged 72 hpf and 5 dpf. These experiments aimed to quantify the compromised vasculature observed following genetic disruption of *arhgap31* and *dock6* by comparison to the wild-type and indicate how cellular movements may be affected to produce a diminished vascular network under reduced *arhgap31* and *dock6* expression.

5.2 Impact of Rho dysregulation on Notch signalling pathway

To examine a potential link between the Notch and Rho signalling pathways, *notch1a* expression patterns were examined in *arhgap31* and *dock6* knockdown models at 24 hpf (Figure 35). Wild-type expression at this timepoint was observed strongly in the forebrain, midbrain and hindbrain ventricles, and to a lesser extent in the otic vesicle and the general forebrain, midbrain and hindbrain regions, consistent with *notch1a* patterns reported in the literature (Figure 35a). The expected endothelial expression of *notch1a* was not observed, likely because of weak staining due to inadequate stain development time. Expression of *notch1a* also highlighted an open conformation of the neural tube in the midbrain-hindbrain boundary.

Expression of *notch1a* following *arhgap31* reduction was no longer confined to the brain ventricles (Figure 35b*iii*, c*iii*). Instead, *notch1a* exhibited low level expression throughout the embryo and was expressed more strongly in the general forebrain, midbrain and hindbrain regions than seen in the wild-type. Specific expression to the otic vesicles also appeared lost. Upon *dock6* knockdown however, expression in the otic vesicle and midbrain ventricle appeared diminished with restricted extension of expression to the forebrain ventricle (Figure 35d*ii*, e*ii*). Moreover, absent *notch1a* expression in the midbrain-hindbrain boundary indicated constriction of the neural tube upon reduced *dock6* expression.

Therefore, reduced *arhgap31* or *dock6* expression altered the expression pattern of *notch1a*, although it is currently unclear whether this is due to structural or genetic changes in the developing zebrafish brain.

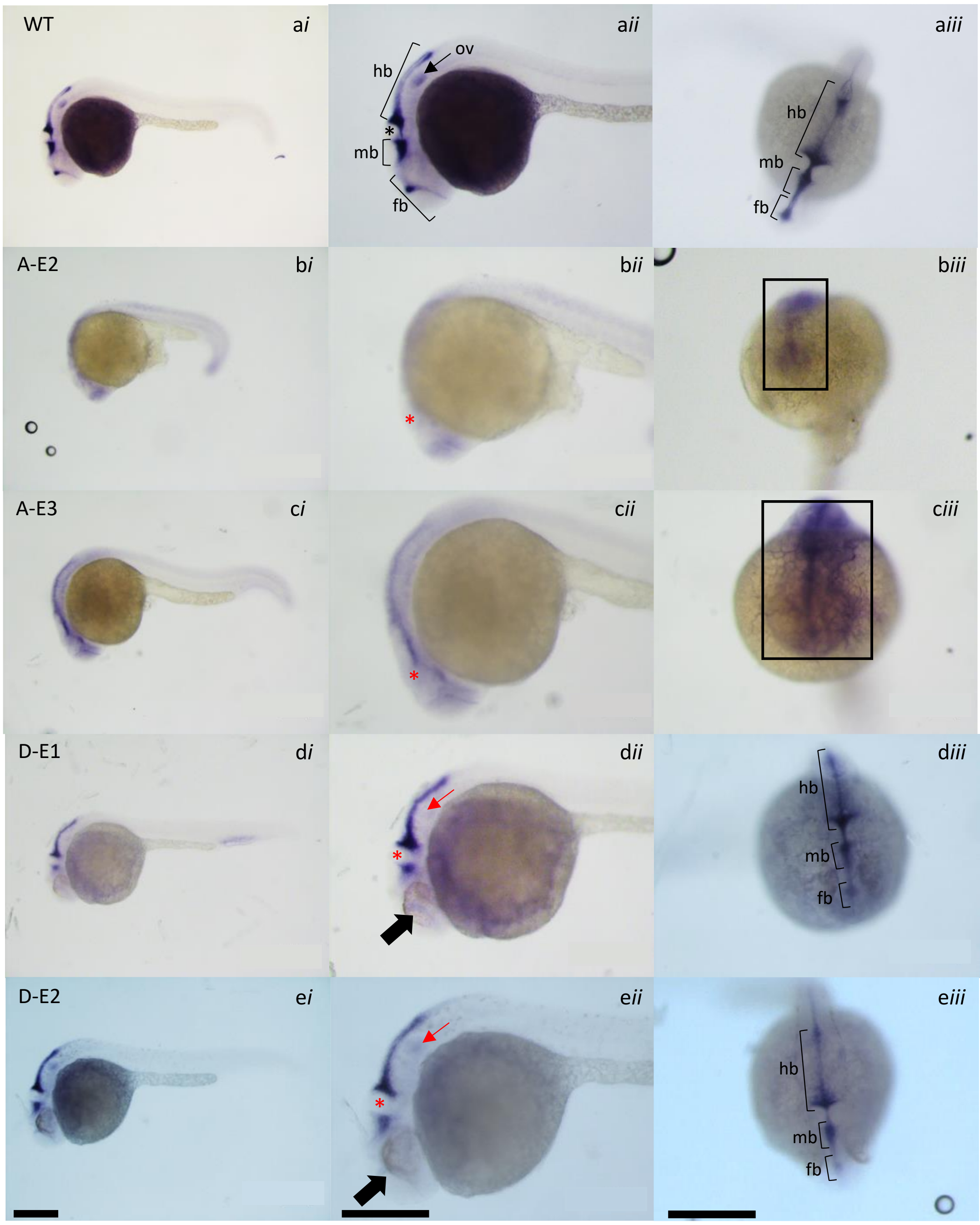

Figure 35: *notch1a* expression pattern upon *arhgap31* and *dock6* depletion.

Expression of *notch1a* in (**a**) wild-type and (**b**) *arhgap31*-E2 (A-E2), (**c**) *arhgap31*-E3 (A-E3), (**d**) *dock6*-E1 (D-E1) and (**e**) *dock6*-E2 (D-E2) morphant embryos at 24 hpf. Embryos were imaged laterally (*i*, *ii*) and dorsally (*iii*). Brackets indicate expression in the midbrain (mb), hindbrain (hb) and forebrain (fb) ventricles and the otic vesicle is marked (ov). Healthy and aberrant midbrain-hindbrain boundary formation is denoted by a black and red asterisk, respectively. Absent *notch1a* expression in the otic vesicles is illustrated by a red arrow. Missing forebrain expression is indicated by a thick black arrow. A black box encases widened *notch1a* expression in the cranium. N=2 cohorts of 20-25 embryos. Scale bar, 200 µm.

5.2.1 Notch pathway transcript levels under genetic disruption of *arhgap31* and *dock6*

To investigate the levels of *notch1a* and *dll4* expression under *arhgap31* and *dock6* depletion, qPCR experiments were performed. Both *notch1a* and *dll4* showed a general increase in expression in *arhgap31*-E2 (mean: 1.73, SD: 0.21 and mean: 1.87, SD: 0.08) and *arhgap31*-E3 (mean: 1.25, SD: 0.15 and mean: 2.22, SD: 0.001) samples at 24 hpf. However, these were not found to be significantly different by comparison to the wild-type, likely due to the limited biological replicates of morphant embryos available fo analysis. The observation of increased *notch1a* and *dll4* transcript levels under *arhgap31* knockdown (Figure 36a) is in contrast with WISH experiments which displayed less intense *notch1a* staining upon *arhgap31* knockdown (Figure 35). As *notch1a* expression was primarily observed in the brain, this discrepancy could be caused by the qPCR experiments being performed on whole organism RNA rather than tissue-specific analysis. By contrast, *notch1a* and *dll4* expression in *dock6*-crispant and *dock6*-E1 embryos were similar to wild-type transcript levels and show no significant difference (Figure 36a). Unfortunately, qPCR data for *dock6*-E2 embryos at this timepoint were not available.

By 5 dpf, *notch1a* and *dll4* expression levels in *arhgap31*-E3, *dock6*-crispant and *dock6*-E1 embryos remained similar to the levels measured in the wild-type embryo (Figure 36b). Unfortunately, qPCR data for *arhgap31*-E2 and *dock6*-E2 embryos at this timepoint were not available. It is likely that the decrease in *notch1a* and *dll4* expression in *arhgap31* morphants from 24 hpf to 5 dpf is due to degradation of morpholinos and recovery of correct protein splicing, therefore removing the impact of *arhgap31* knockdown on *notch1a* and *dll4* expression. Alternatively, as Notch signalling is known to self-regulate, this may represent a feedback mechanism to maintain stable *notch1a* levels in response to the elevated gene expression at 24 hpf.

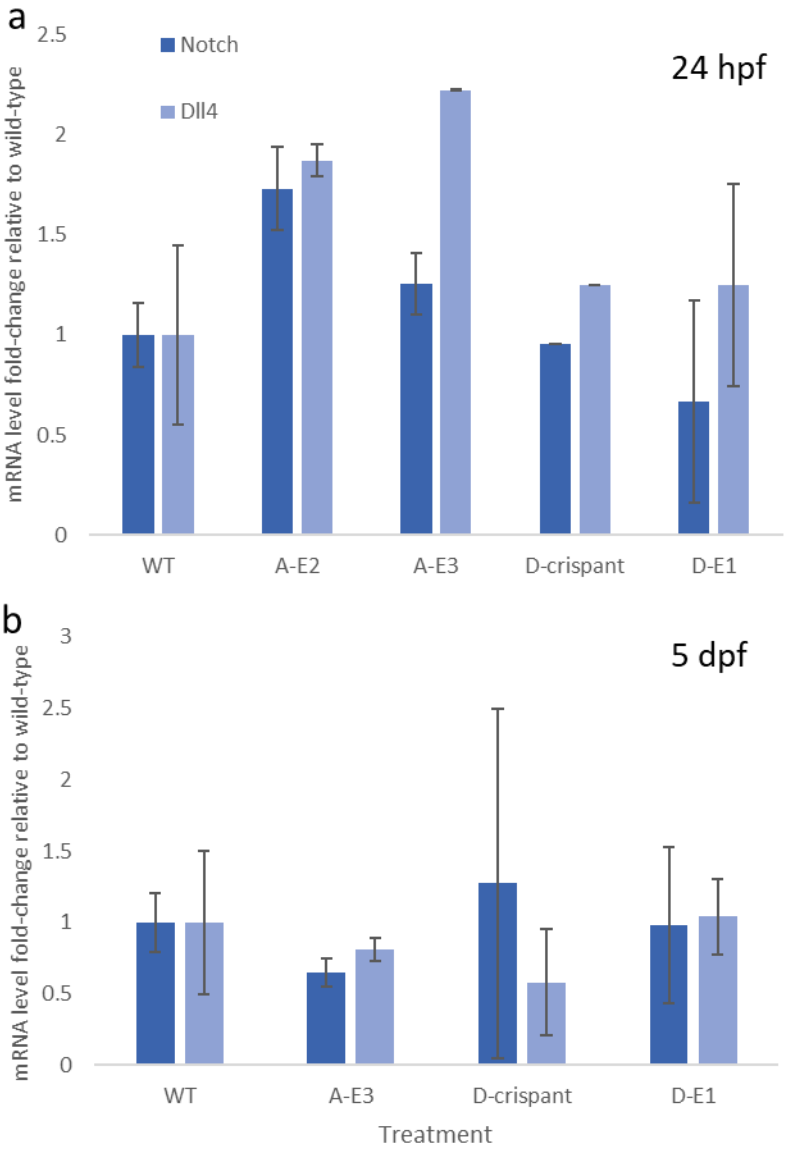

Figure 36: *dll4* and *notch1a* mRNA levels under *arhgap31* and *dock6* depletion.

Relative expression levels of *dll4* and *notch1a* measured by qPCR in (**a**) 24 hpf and (**b**) 5 dpf embryos treated with *arhgap31*-E2 (A-E2), *arhgap31*-E3 (A-E3), *dock6*-E1 (D-E1), *dock6*-E2 (D-E2) or *dock6*-crispant (D-crispant). Transcript levels were normalised to the wild-type. Statistical analyses were conducted using a two-way ANOVA and a Tukey's test for multiple comparison. At 24 hpf, n = 2-4 cohorts of 50 embryos. At 5 dpf, n = 2-6 cohorts of 50 embryos. Error bars display standard deviation.

5.3 Analysis of known vascular markers under Rho dysregulation

To investigate vascular development at 24 hpf and a potential link between the Rho pathway and critical vascular molecular pathways, WISH for *fli1* and *kdrl* were performed in *arhgap31* and *dock6* knockdown models at 24 hpf.

5.3.1 Expression patterns of *fli1* and *kdrl under* arhgap31 *and* dock6 *depletion*

Both *kdrl* and *fli1* expression were confined to the DA, PCV, caudal aorta, CaV and ISVs in the 24 hpf-stage wild-type embryo (Figure 37a*i* and a*ii*). As in Figure 35, weak staining of the *fli1* and *kdrl* probes are observed likely due to an inadequate staining time, however in this case enough staining was present to infer a potential effect of *arhgap31* and *dock6* knockdown on endothelial patterning. In both *arhgap31* morphants, *fli1* and *kdrl* expression was present in these structures but at a reduced level, however the patterning of these structures did not appear to differ from that of the wild-type (Figure 37b*i* and c*ii).* By contrast, staining in the *dock6* knockdown models showed no apparent overall reduction in the levels of *kdrl* and *fli1* present at 24 hpf (Figure 37d*i* and d*ii)*, instead displaying aberrant patterning of the trunk vasculature, most notably a marked absence of *kdrl* and *fli1* expression within the caudal vein plexus (CVP).

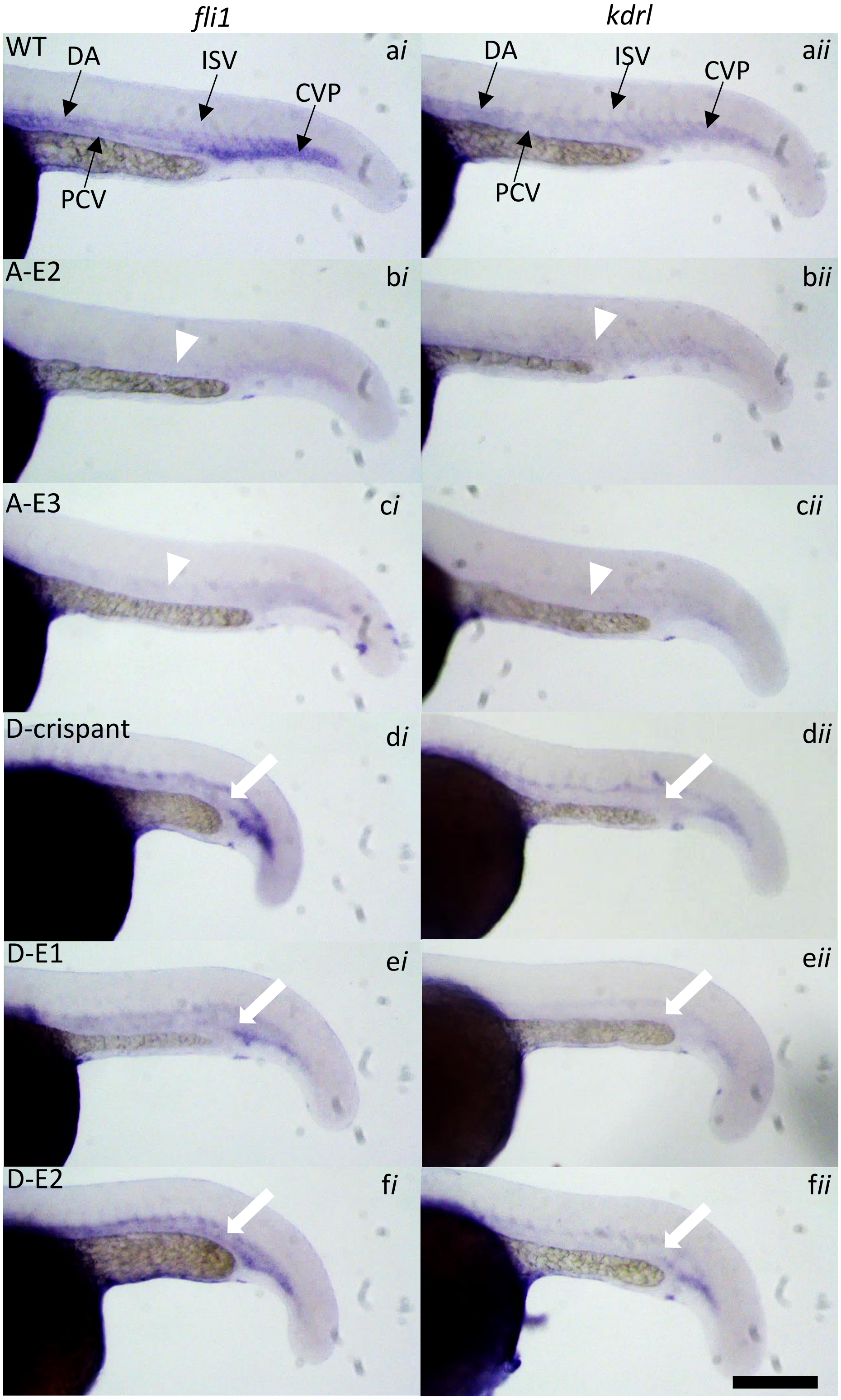

Figure 37: Impact of reduced *arhgap31* and *dock6* expression on vascular marker patterning.

i. *fli1* and ***ii.*** *kdrl* expression at 24 hpf in (**a**) wild-type (WT), (**b**) *arhgap31*-E2 (A-E2) and (**c**) *arhgap31*-E3 (A-E3) morphants, (**d**) *dock6*-crispants (D-crispant), (**e**) *dock6*-E1 (D-E1) and (**f**) -E2 (D-E2) morphants. Dorsal aorta (DA), posterior cardinal vein (PCV), caudal vein plexus (CVP) and intersegmental vessel (ISV) patterning are displayed in the (**a**) wild-type (WT). Reduced *fli1* and *kdrl* expression is denoted by a white arrowhead, abnormal CVP patterning is signified by a white arrow. N= 2 cohorts of 20-25 embryos. Scale bar, 250 µm.

5.3.2 Quantifying *fli1* and *kdrl* transcript level changes under Rho dysregulation

Following the differences in *fli1* and *kdrl* expression patterns observed in *arhgap31* and *dock6* knockdown embryos aged 24 hpf (Figure 37), qPCR experiments were conducted to identify quantified transcript levels in these genes under *arhgap31* or *dock6* knockdown (Figure 38). Unfortunately, data for *dock6*-E2 embryos were

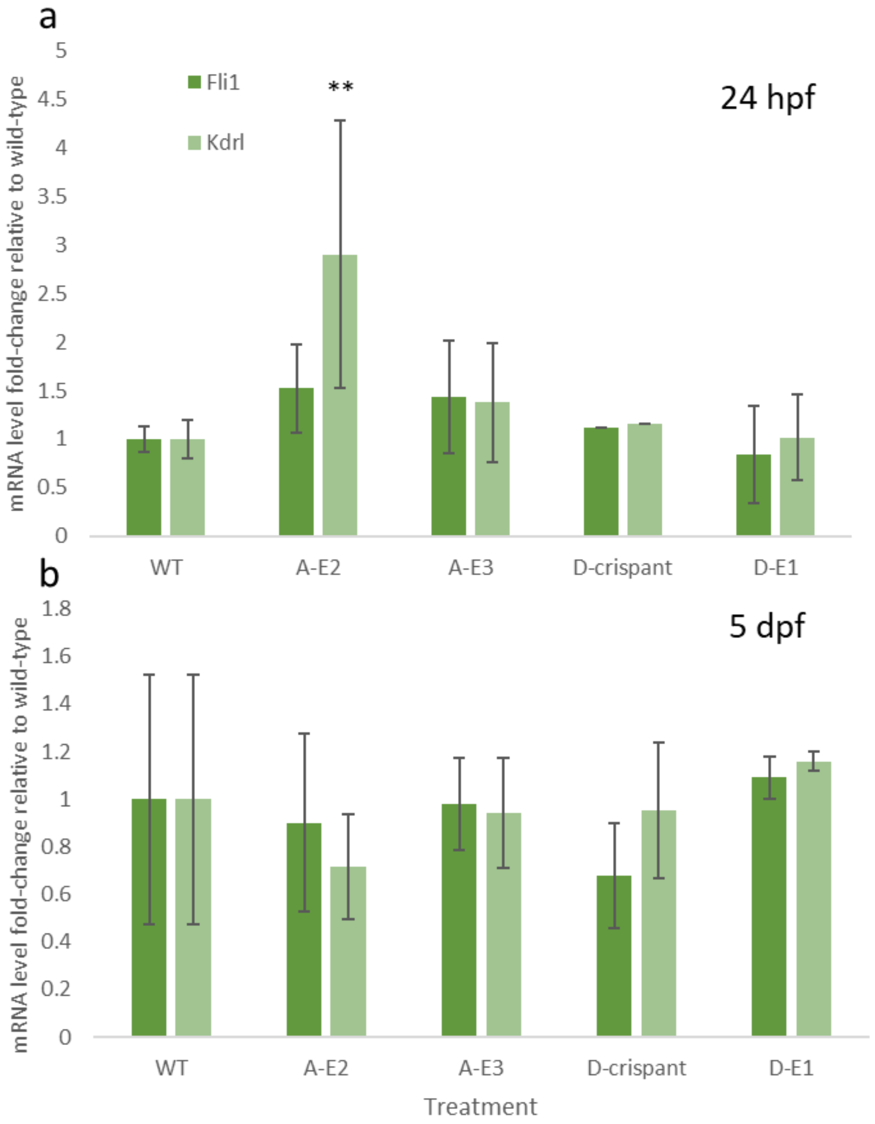

Figure 38: Transcript levels of *fli1* and *kdrl* under *arhgap31* or *dock6* depletion.

Relative expression levels of *fli1* and *kdrl* quantified by qPCR in embryos aged (**a**) 24 hpf and (**b**) 5 dpf. Embryos were injected with *arhgap31* E2 (A-E2), *arhgap31* E3 (A-E3), *dock6*-crispant (D-crispant) and *dock6*-E1 (D-E1) knockdown reagents. Transcript levels were normalised to the wild-type. At 24 hpf, n = 2-4 cohorts of 50 embryos. At 5 dpf, n=2-6 cohorts of 50 embryos. Statistical analyses were conducted using a two-way ANOVA and a Tukey's test for multiple comparison against wildtype expression. Error bars display standard deviation. **, p=0.0013.

unavailable. At 24 hpf and 5 dpf, fold-changes of *fli1* expression in *arhgap31* and *dock6* knockdown models did not display a significant difference by comparison to the wild-type. Transcript levels of *fli1* in *arhgap31*-E2 and *arhgap31* E3 morphants at 24 hpf showed a general trend of increased expression, displaying *fli1* expression fold-changes of 1.53±0.455 (SD) and 1.43±0.57 (SD), respectively. However, this was not significant.

Expression levels of *kdrl* at 24 hpf remained stable in *dock6*-crispant and *dock6*-E1 embryos and showed no significant difference by comparison to the WT (Figure 38a). In the *arhgap31* morphants however, a significant increase in *kdrl* transcript levels was seen in *arhgap31*-E2 samples, with a fold-change of 2.91 ± 1.38 (SD) by comparison to wild-type (*p*=0.0013). There was also a general increase in *kdrl* expression following *arhgap31*-E3 morpholino injection (1.38 ± 0.61 (SD) fold-change) but this was not statistically significant. At 5 dpf however, *kdrl* expression in all treated embryo types remained at a similar level to the wild-type and displayed no significant difference (Figure 38b). It is likely that the increased *kdrl* expression levels observed in *arhgap31* morphants are lost by 5 dpf due to the transient nature of morpholinos.

The ostensibly conflicting results observed between WISH (Figure 37) and qPCR data under *arhgap31* knockdown at 24 hpf (Figure 38a) potentially indicate a more complex expression pattern for *fli1* and *kdrl*. The higher expression levels detected by qPCR may be due to the use of whole organism RNA rather than measuring tissue-specific expression. Alternatively, the WISH probes may not have hybridised optimally in the *arhgap31* morphants, resulting in a weak signal across the whole embryo.

5.4 Microangiographic imaging of aberrant vascular development

Following the observation of compromised blood flow in *arhgap31*- and *dock6*-depleted embryos (see Sections 4.4 and 4.5), microangiography was used to assess the extent of vascular disruption in mildly affected embryos.

5.4.1 Cranial vascular analysis

The cranial vasculature at 72 hpf was examined from the dorsal and lateral perspective in *arhgap31*-E2, *arhgap31*-E3, *dock6*-E1, *dock6*-E2 and *dock6*-crispant embryos and compared to the wild-type (Figure 39). Under each condition, fluorescein-labelled dextran was absent from one or more of the three main optic vessels, namely the nasal ciliary artery (NCA), dorsal ciliary vein (DCV) and optic vein (OV) (Figure 39b*i*-f*i*). In addition, no dye was observed in the aortic arches, indicating either truncation or poor development of these vessels. In *arhgap31*-reduced embryos the cerebellar central artery structures were not visible (Figure 39b*ii*, c*ii*), implying that the dye was unable to perfuse these vessels or the vessels themselves are under-developed. By contrast, in the three *dock6*-depleted embryos however, cerebellar central artery development was merely reduced by comparison to the wild-type (Figure 39d*ii*, e*ii*, f*ii*). Given the consistent phenotypes displayed in *arhgap31*-E2 and *arhgap31*-E3 embryos and between *dock6*-crispant, *dock6*-E1 and *dock6*-E2 embryos, these treatments provide independent validation for each other in support of a specific knockdown effect induced by reduction of either *arhgap31* or *dock6*.

Similarly, a dorsal view revealed that the fluorescein-dextran showed limited permeability in *arhgap31*-E3 (Figure 39b*iv*) and *dock6*-E2 (Figure 39f*iv*) embryos and could not permeate the cerebral vasculature of the *dock6*-E1 (Figure 39e*iv*) embryos. In addition, the anterior cerebral vein (ACev), mesencephalic vein (MsV), dorsal latitudinal vein (DLV), metencephalic artery (MtA), MceV and PCeV appeared poorly perfused in the 72 hpf *arhgap31*-E3 embryos, *dock6*-E1 and *dock6*-E2 by comparison to the wild-type. Dorsal views of the *arhgap31*-E2 morphant and *dock6* crispant embryos were not available for analysis.

Non-vascular dextran-fluorescein in the morpholino- and crispant-treated embryos, seen most clearly in Figure 39b*iii*, indicated potential loss of vessel integrity upon reduction of *arhgap31* and *dock6* leading to leakage of fluorescent dye from the injected vessels.

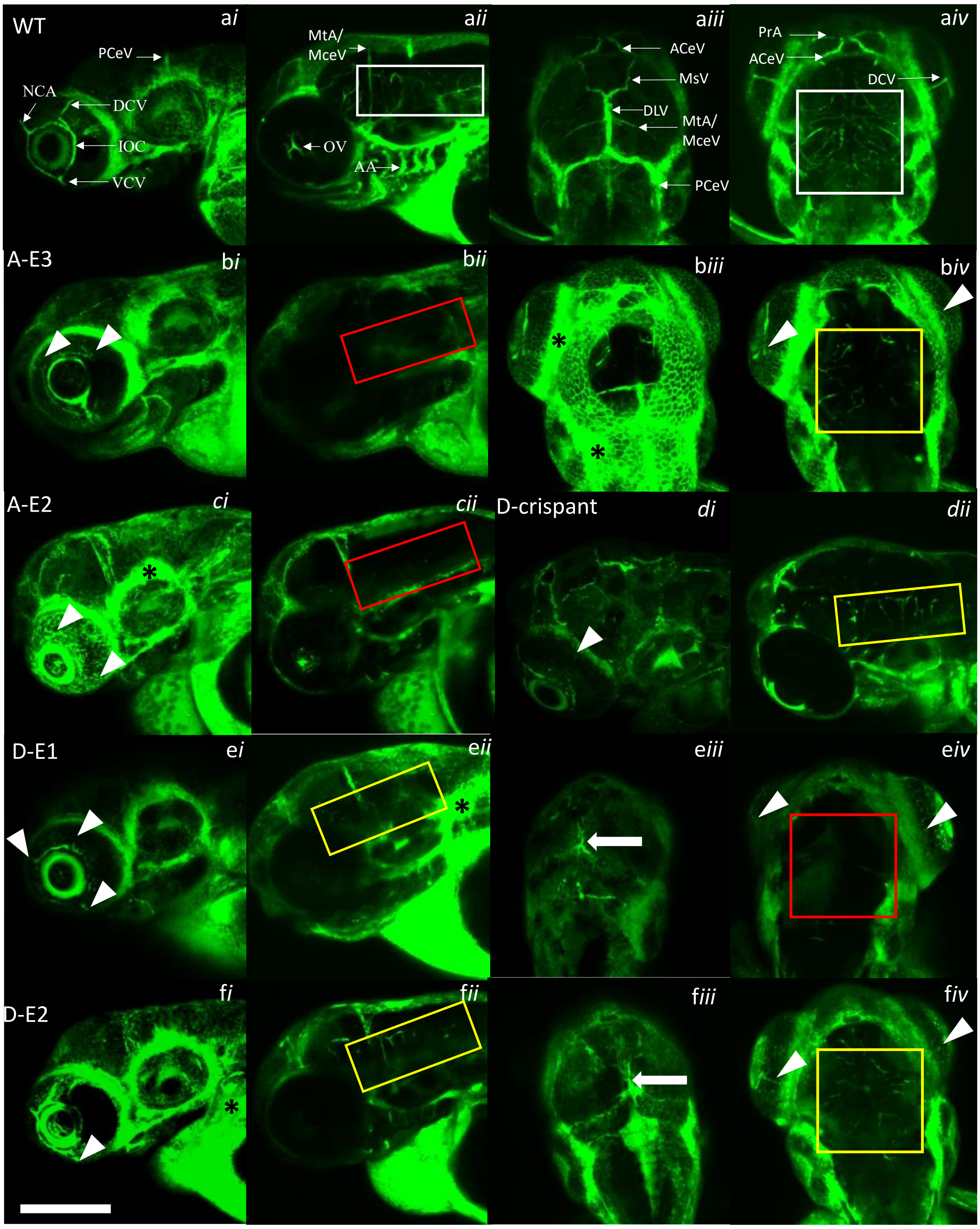

Figure 39: Effects of Rho dysregulation on cranial vascular perfusion at 72 hpf.

Views of the **i.** lateral exterior, **ii.** lateral interior, **iii.** dorsal exterior and **iv.** dorsal interior cranial vasculature in (**a**) wild-type and (**b**-**f**) knockdown embryos at 10x magnification. Absent optic vessels and cranial structures are marked by the white arrowheads and thick white arrows, respectively. Examples of dextran leakage are denoted by an asterisk. Rectangular and square boxes enclose the cerebellar central artery and cerebral vasculature, with colours indicating normal (white), reduced (yellow) and negligible (red) development. N=6-9 embryos/condition. **Key:** A-E2, A-E3, *arhgap31* morphants; AA, aortic arches; ACeV, anterior cerebral vein; DCV, dorsal ciliary vein; D-crispant, *dock6*-crispant; D-E1, D-E2, *dock6* morphants; IOC, inner optic circle; MceV, middle cerebral vein; MsV, mesencephalic vein; MtA, metencephalic artery; NCA, nasal ciliary artery; PCeV, posterior cerebral vein; PrA, prosencephalic artery; VCV, ventral ciliary vein; WT, wild-type. Scale bar, 200 µm.

To determine whether the observed phenotypes were due to developmental delay and may recover over time, embryos were grown to 5 dpf and examined again by microangiography (Figure 40). Similar to 72 hpf, several embryos exhibited compromised vessel integrity at 5 dpf as evidenced by leakage of the dextran-conjugate into non-vascular structures. In each embryo condition, at least one optic vessel was not visible (Figure 40b*i*-f*i*). Further, cerebral vasculature in the *arhgap31*-E3 and *dock6*-E1 embryos displayed limited permeability of the dextran-conjugate (Figure 40b*ii*, e*ii*), and the uptake in *dock6*-E2 and *dock6*-crispant embryos was imperceptible (Figure 40c*ii*, d*ii*), implying that the restricted cranial vascular development observed at 72 hpf does not recover by 5 dpf. In addition, numerous vascular structures (ACeV, prosencephalic artery (PrA), MsV, DCV, MtA, MCeV, DLV and PceV) were found to be either incomplete or absent in the *dock6*-E2, *dock6*-crispant and *arhgap31*-E3 embryos (Figure 40c*iii*-e*iii*). The cranial vasculature in the *dock6*-E1 embryos appeared affected to a lesser extent, where only the DLV, MtA and MCeV were not visible (Figure 40b*iii*). Unfortunately, images displaying the dorsal and lateral cranial vasculature were not available for the *arhgap31*-E2 morphants.

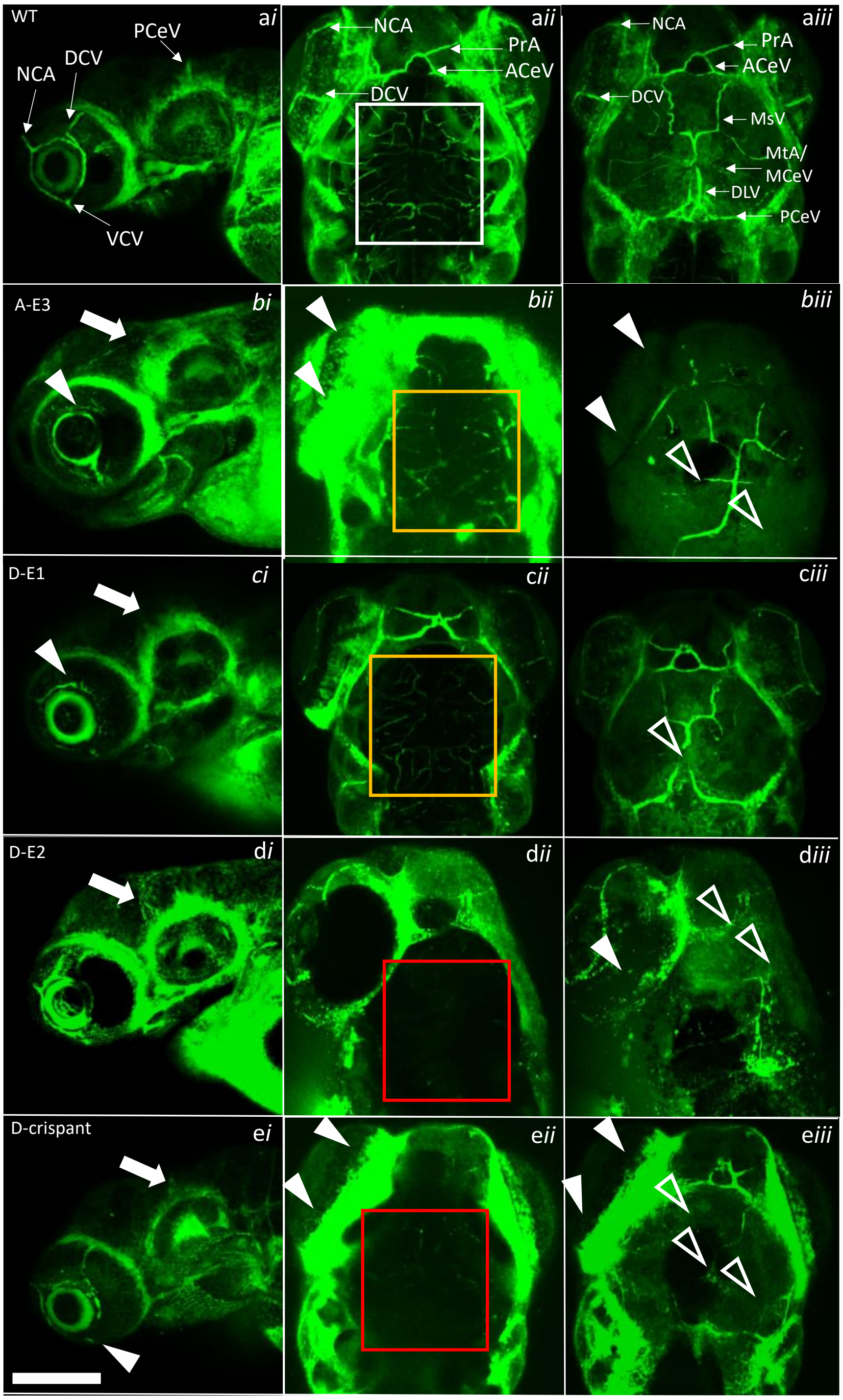

Figure 40: Cranial vascular development under Rho dysregulation at 5 dpf.

Microangiograms displaying cranial vasculature in *arhgap31* and *dock6* knockdown models. Images of the lateral, interior dorsal and exterior dorsal cranial vasculature were taken at 10x magnification. Absent optic vessels are marked by white arrowheads. White arrows demarcate an absent PCeV. Unfilled arrowheads indicate missing cranial vessels. White, yellow and red boxes encase normal, reduced or absent cerebral vasculature, respectively. N=6-9 embryos/condition. **Key:** AA, aortic arches; ACeV, anterior cerebral vein; DCV, dorsal ciliary vein; MceV, middle cerebral vein; MsV, mesencephalic vein; MtA, metencephalic artery; NCA, nasal ciliary artery; PCeV, posterior cerebral vein; PrA, prosencephalic artery; VCV, ventral ciliary vein. Scale bar, 200 µm.

5.4.2 Trunk vascular analysis

To examine the impact of gene disruption on non-cranial vasculature, microangiography was also used to visualise the trunk region at 5dpf. Microangiography at 5 dpf displayed expected perfusion of the CVP in the wildtype mid-trunk and tip-trunk, as well as complete infiltration of the ISVs (Figure 41a*i* and a*ii*). Upon reduced *arhgap31* and *dock6* expression, incomplete or asymmetrical ISVs were observed throughout the trunk (Figure 41b*i*-e*i*). However, it is unclear from these data whether the vessels themselves are truncated, asymmetric or merely occluded, restricting the flow of dextran-conjugate throughout the vasculature. Similarly, the CVP of *arhgap31*-E2 (Figure 41b*ii*), *arhgap31*-E3 (Figure 41c*ii*), *dock6*-E2 (Figure 41d*ii*) and *dock6*-crispant (Figure 41e*ii*) embryos exhibit decreased perfusion, indicating either incomplete or sub-optimal development of the CVP upon *arhgap31* or *dock6* depletion.

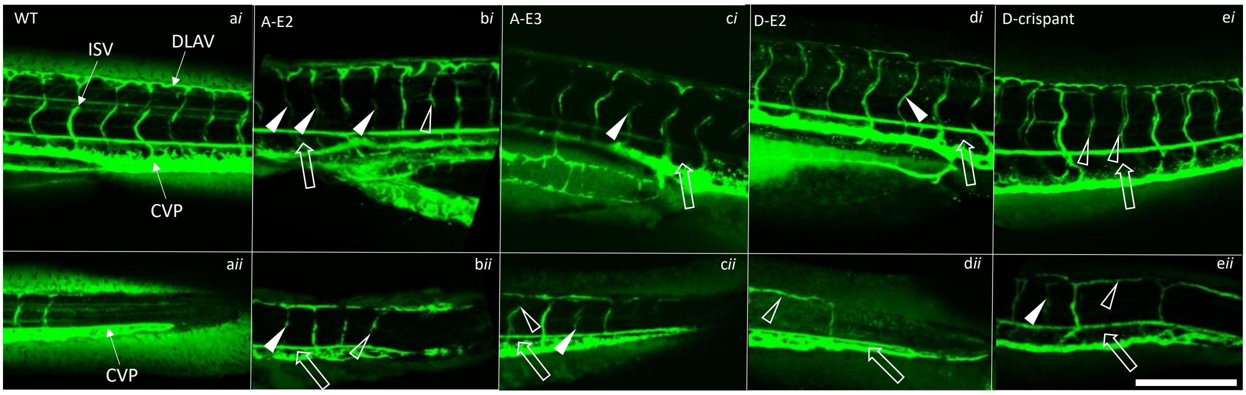

Figure 41: Microangiography displaying the trunk vasculature at 5 dpf.

Vascular structures highlighted by microangiography in the mid-trunk (***i***) and trunk tip (***ii***) in (**a**) wild-type (WT), (**b**) *arhgap31*-E2 (A-E2), (**c**) *arhgap31*-E3 (A-E3), (**d**) *dock6*-E2 (D-E2), (**e**) *dock6*-crispant (D-crispant), embryos. Unfilled white arrows demarcate decreased CVP perfusion. Truncated and asymmetric ISVs are indicated by unfilled and filled arrowheads in the Rho dysregulation models. Key: CVP, caudal vein plexus; DLAV, dorsal lateral anastomotic vessels; ISV, intersegmental vessel. N=3-6 embryos/condition. Scale bar, 300 µm.

5.4.3 Frequency of vascular abnormalities under Rho dysregulation

Embryos used in microangiography studies were phenotypically analysed to quantify the proportion of fish displaying absent optic vessels or defective ISV development.

5.4.3.1 Ocular avascularisation is seen upon arhgap31 and dock6 depletion

All *arhgap31* knockdown embryos at both 72 hpf and 5 dpf showed at least one absent optic vessel (Figure 42a). In the *dock6* knockdown embryos however, only *dock6*-E2-injected embryos showed complete penetrance of the absent optic vessel phenotype at both 72 hpf and 5 dpf (Figure 42a). At 72 hpf, all *dock6*-E1 embryos showed an absent optic vessel, however by 5 dpf this reduced to 75% of embryos, perhaps indicating recovery due to morpholino degradation. This milder phenotype by comparison to the *dock6*-E2 morphants may be caused by the decreased knockdown efficiency of *dock6*-E1 stipulated in Chapter 4 (see Section 4.2). In *dock6*-crispant embryos, only 50% of 72 hpf embryos displayed an absent optic vessel, which was maintained at 5 dpf. Maintenance of this phenotype is consistent with a stable CRISPR-mediated knockdown. Thus, these data imply that *arhgap31* or *dock6* depletion impairs ocular vascularisation in early development.

5.4.3.2 Reduced arhgap31 and dock6 expression induces asymmetric ISV development

At 72 hpf, 44.44% ± 4.44% (SD) and 38.81% ± 10.89% (SD) of ISVs in *arhgap31*-E2 and E3 embryos, respectively, displayed asymmetry (Figure 42b). In *arhgap31*-E2 embryos, ISV asymmetry was maintained at 5 dpf and displayed a frequency of 37.5% ± 2.5% (SD). However, recovery was observed in *arhgap31*-E3 embryos by 5 dpf, with a decreased asymmetric ISV frequency to 15.87% ± 16.72% (SD). Again, this may indicate recovery due to the transient nature of morpholinos

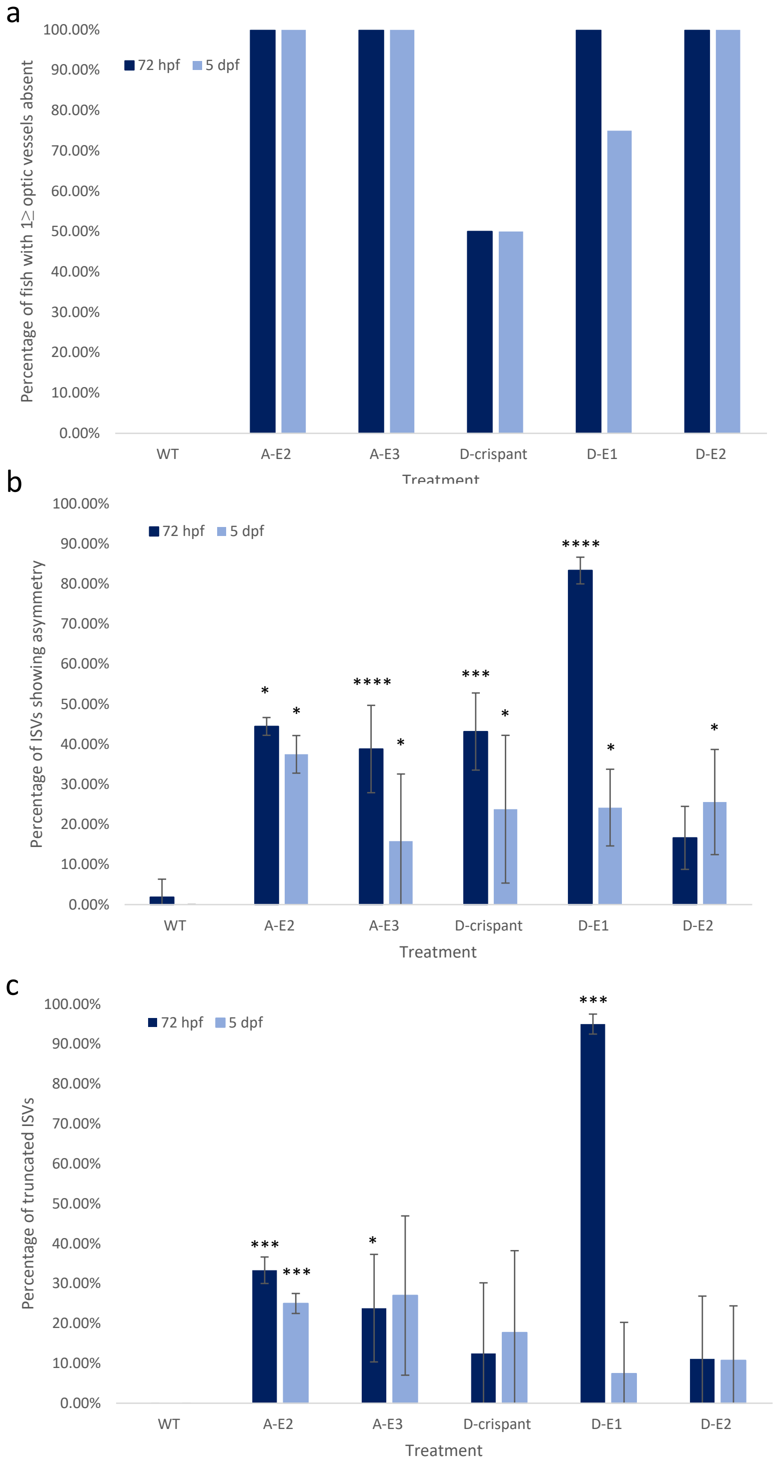

Figure 42: Frequency of vascular abnormalities under *arhgap31* and *dock6* depletion.

Frequencies of optic vessel defects (**a**), asymmetric vessels (**b**) and truncated vessels (**c**) in wild-type (WT), *arhgap31*-E2 (A-E2), *arhgap31*-E3 (A-E3), *dock6*-crispant (D-crispant), *dock6*-E1 (D-E1) and *dock6*-E2 (D-E2) embryos at 72 hpf and 5 dpf. Vessel analysis was conducted on 3-6 randomly imaged embryos per condition. Statistical analyses were performed by one-way ANOVA combined with a Dunnett's test for multiple comparisons. Significant differences by comparison to the wild-type are displayed. *, $p<0.05$, ***, $p<0.001$, ****, $p<0.0001$.

or suggest that *arhgap31*-E3-mediated knockdown may have been less efficient than that of *arhgap31*-E2. Asymmetry in *dock6* knockdown ISVs was prevalent in *dock6*-crispant and *dock6*-E1 embryos at 72 hpf, displaying a frequency of 43.18% ± 9.64% (SD) and 83.33% ± 3.33% (SD), respectively. In *dock6*-E2 embryos, asymmetric ISVs presented at a lower frequency of 16.67% ± 7.86% (SD) at 72 hpf (Figure 42b), contrasting with the strong optic vessel phenotype previously observed (Figure 42a). By 5 dpf, ISV asymmetry frequency was reduced in both the *dock6*-crispant and *dock6*-E1 embryos, which displayed asymmetry in 23.81% ± 18.42% (SD) and 24.21% ± 9.55% (SD) of ISVs, respectively. However, this was not seen in *dock6*-E2 embryos which maintained asymmetry in 25.6% ± 13.1% (SD) of ISVs (Figure 42b). In every *arhgap31* and *dock6* knockdown model, the frequency of asymmetrical ISVs was significantly increased by comparison to the wild-type, aside from that seen in *dock6*-E2 at 72 hpf. Therefore, it can be concluded that reduced expression of *arhgap31* and *dock6* induces asymmetrical ISV development.

5.4.3.3 *Truncated ISVs observed under arhgap31 and dock6 knockdown*

Truncations were observed in 33.33% ± 3.33% (SD) and 23.81% ± 13.47% (SD) of ISVs in 72 hpf *arhgap31*-E2 and -E3 embryos (Figure 42c). These values were found to be significantly higher by comparison to the wild-type (Figure 42c). This was largely maintained at 5 dpf, where 25% ± 2.5% (SD) and 26.98% ± 19.97% (SD) of ISVs displayed truncations in embryos injected with *arhgap31*-E2 and -E3, respectively. At 72 hpf, an average of 12.5% ± 17.68% (SD), 95% ± 5.0% (SD) and 11.11% ± 15.71% (SD) of ISVs in *dock6*-crispant, *dock6*-E1 and *dock6*-E2-injected embryos were truncated (Figure 42c). By 5 dpf, this phenotype was maintained in the *dock6*-crispant and *dock6*-E2 embryos, where 17.71% ± 20.52% (SD) and 10.71% ± 13.68% (SD) of

ISVs displayed truncation, respectively. By contrast, the *dock6*-E1 embryos demonstrated recovery of the phenotype, showing a frequency of 7.41%±12.83% (SD) truncated ISVs. This is in line with the phenotypic recovery seen in asymmetric ISV frequency upon *dock6*-E1 injection (Figure 42b). As there appears to be recovery only in embryos with more severe phenotypes at 72 hpf, this may be due to potentially lethal impairment caused by poor ISV development, which may not be seen in embryos displaying milder phenotypes. Together, these data imply that *arhgap31* and *dock6* depletion leads to ISV truncation, although to a lesser extent than ISV asymmetry.

5.5 Vascular analysis using a transgenic reporter line

Though informative, microangiography enabled visualisation of the vasculature only in mildly affected *arhgap31* and *dock6* knockdown models, which had sufficient blood flow to facilitate transport of the dextran-conjugate around the embryo. A more comprehensive method was required to examine embryos with severe phenotypes of defective vascular development, therefore gene knockdown in a tg(*fli1*:GFP) zebrafish reporter line was used to visualise the vasculature. As *fli1* is also expressed in cranial NCCs and therefore does not display vascular-specific fluorescence in the head, microangiography was performed in parallel to facilitate visualisation of cranial structures such as the aortic arches and optic vessels where possible.

To counter the leaking vessel phenotype observed in Figure 39, the molecular weight of the dextran conjugate used was increased from 500 kDa to 2000 kDa. While this did indeed minimise vessel leakage and provide clearer images, smaller cranial vessels could not support the flow of the larger dextran molecules and therefore are only visible by transgenic reporter line.

5.5.1 Intersegmental vessel development at 24 hpf

By 24 hpf, wild-type embryos developed an average of 13 ± 1.41 (SD) ISVs. By contrast, the *arhgap31*-E2, *arhgap31*-E3, *dock6*-crispant and *dock6*-E1 embryos displayed a highly significant reduction in ISV number, with averages of 0.33 ± 0.51 (SD), 1 ± 1.82 (SD), 0.38 ± 0.74 (SD) and 0 ± 0 (SD) ISVs per embryo, respectively (Figure 43b). The PCeV had developed in the wild-type by 24 hpf but was not present in any of the genetic models examined (Figure 43a). Development of the CVP was apparent in the wild-type and in the *arhgap31* morphants to a lesser extent. This may be due to the smaller size of the morphant embryos by comparison to the wild-type, possibly caused by morpholino-induced developmental delay. However, despite the comparable sizing between the *arhgap31* and *dock6* knockdown embryos, the CVP appeared thinner in the *dock6*-crispant and *dock6*-E1 embryos than under *arhgap31* depletion. This indicates that additional *dock6*-induced CVP abnormalities may be an effect of the gene disruption rather than due to a developmental delay causing an overall decrease in the size of developing structures.

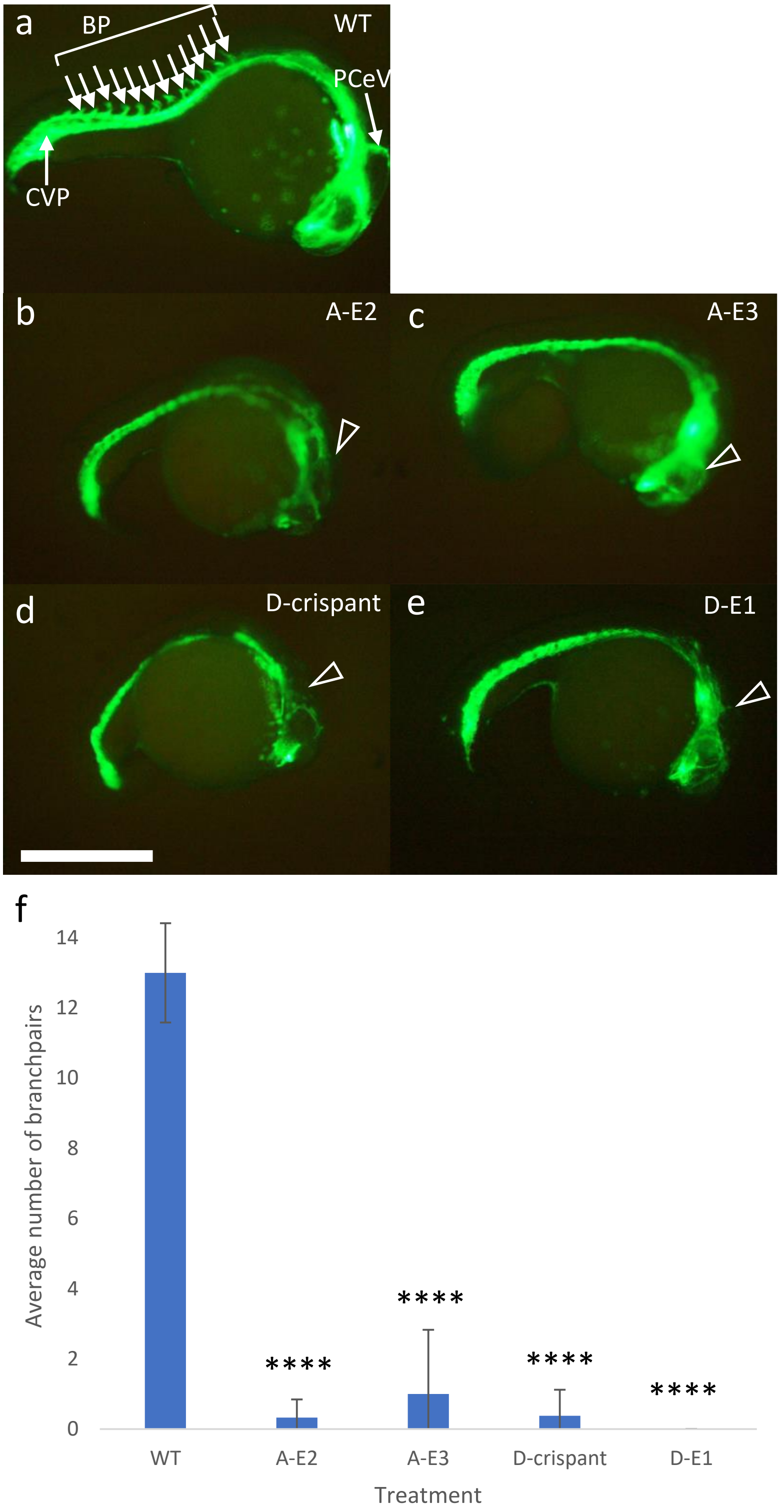

Figure ~~43~~: Intersegmental vessel development under Rho dysregulation.

Representative images of (**a**) wild-type, (**b**) *arhgap31*-E2 (A-E2), (**c**) *arhgap31*-E3 (A-E3), (**d**) *dock6*-crispant (D-crispant) and (**e**) *dock6*-E1 (D-E1) at 24 hpf. Unfilled arrowheads denote absent PCeV formation. (**f**) The average number of intersegmental vessels developed by 24 hpf in wild-type and knockdown models (n=6 embryos). **Key:** BP, intersegmental vessel; CVP, caudal vein plexus; PCeV, posterior cerebral vein. Statistical analysis was performed by one-way ANOVA with a Tukey's test for multiple comparisons. ****, $p<0.0001$. Scale bar, 500 µm.

5.5.2 Trunk vascular analysis under reduced *arhgap31* and *dock6* expression

Visualisation of wild-type trunk vasculature using a *fli1:*GFP reporter line and microangiography highlighted the completed and uniform ISVs, which are able to circulate the injected dextran-conjugate throughout the embryo (Figure 44a). In the *arhgap31*-E2-, *arhgap31*-E3, *dock6*-E1 and *dock6*-E2-injected embryos however, truncated and asymmetric ISVs were observed upon transgenic visualisation (Figure 44b*ii*-e*ii*). In *arhgap31*-E2, *dock6*-E1 and *dock6*-E2, an equal distribution of truncated and asymmetric vessels was observed. These are indicated in the microangiography-only images as loss of dextran-conjugate perfusion entirely in the asymmetric vessels and stunted perfusion in the truncated vessels. In contrast, the imaged *arhgap31*-E3 embryo displayed primarily asymmetric ISVs. Consequently, transport of dextran-conjugate through the ISVs was inhibited and can only be visualised in the DLAV of the embryo. As embryos were chosen at random for imaging, this example may demonstrate the varying severity of phenotypes promoted by morpholino-mediated *arhgap31* reduction. Therefore, a stable knockout model would be more suitable and would likely engender a more consistent phenotype than the transient knockdown approach employed in these experiments.

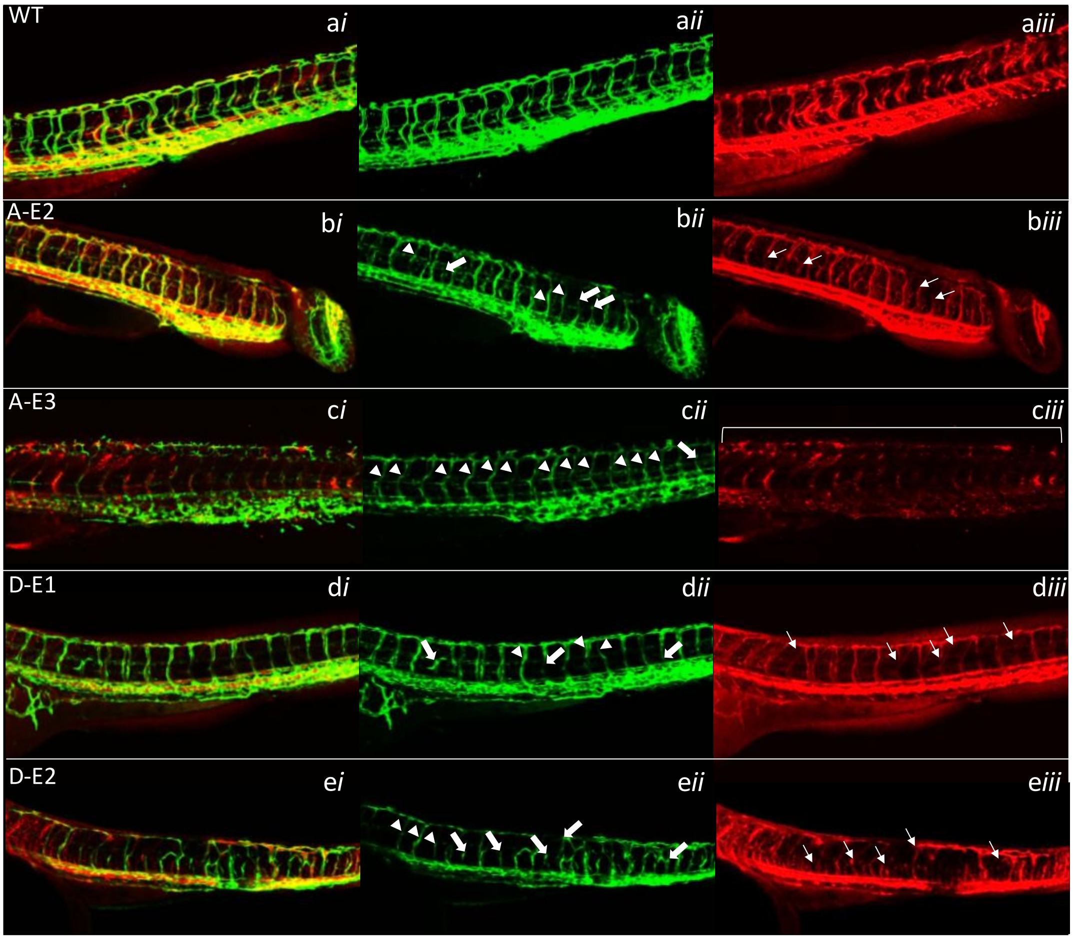

Figure 44: Visualisation of trunk vasculature by microangiography in a transgenic line.

Confocal microscopy of microangiography experiments in 72 hpf tg(*fli1*:GFP) embryos of uninjected wild-types (**a**) or embryos injected with A-E2 (**b**), A-E3 (**c**), D-E1 (**d**) or D-E2 (**e**). Images are shown of the composite transgenic and microangiography vasculature (*i*), transgenic (GFP) expression alone (*ii*) and microangiography (dextran-rhodamine) alone (*iii*). Truncated (thick arrow) and asymmetric (arrowhead) intersegmental vessels are demarcated in the transgenic images, whereas non-perfused vessels (thin arrow) are denoted in the microangiography images. Brackets indicate where dextran-conjugate is only seen in the dorsal longitudinal anastomotic vessels. N=3-6 embryos/condition. Scale bar, 300 μm.

5.5.3 Cranial vascular development following *arhgap31* and *dock6* knockdown

The combination of microangiography and the use of a tg(*fli1*:GFP) reporter line in 72 hpf wild-type embryos permitted the identification of complete cranial vascular structures (Figure 45, Figure 46). As previously described (see Section 5.5), the increased molecular weight of the dextran-conjugate used in these experiments impaired the ability of the microangiography technique to permeate the small cerebral vessels. However, while previous cranial microangiography experiments (Figure 39) examined only the perfusion of the cranial vasculature, the use of a transgenic line determined whether impaired perfusion was due to vessel blockage or vessel truncation.

The completed cerebellar central artery (CCtA) and middle mesencephalic central artery (MMCtA) networks, subintestinal vein plexus (SVP) and the MceV are outlined by the tg(*fli1*:GFP) reporter line (Figure 45a*ii*-f*ii*). Reduced cerebral vascularisation was seen in both *arhgap31* morphants, *dock6*-E1 and *dock6*-crispant (Figure 45b*ii*-f*ii*), whereas absent cerebral vascularisation was observed in the *dock6*-E2 embryos (Figure 45e*ii*). Where the wild-type displayed a fully formed and perfused MceV, each knockdown model displayed either a thin or absent vessel (Figure 45b*ii*-f*ii*). The ‘stringy-heart’ phenotype described in *dock6* knockdown models (see Section 4.5) became clear upon microangiography and co-occurred with a large pericardial edema (Figure 45d*i*-f*i*). This was not seen in the *arhgap31*-E2 and *arhgap31*-E3 models, which appeared to show normal heart development by comparison to the wild-type (Figure 45b*i*, c*i*). However, less obvious heart phenotypes cannot be

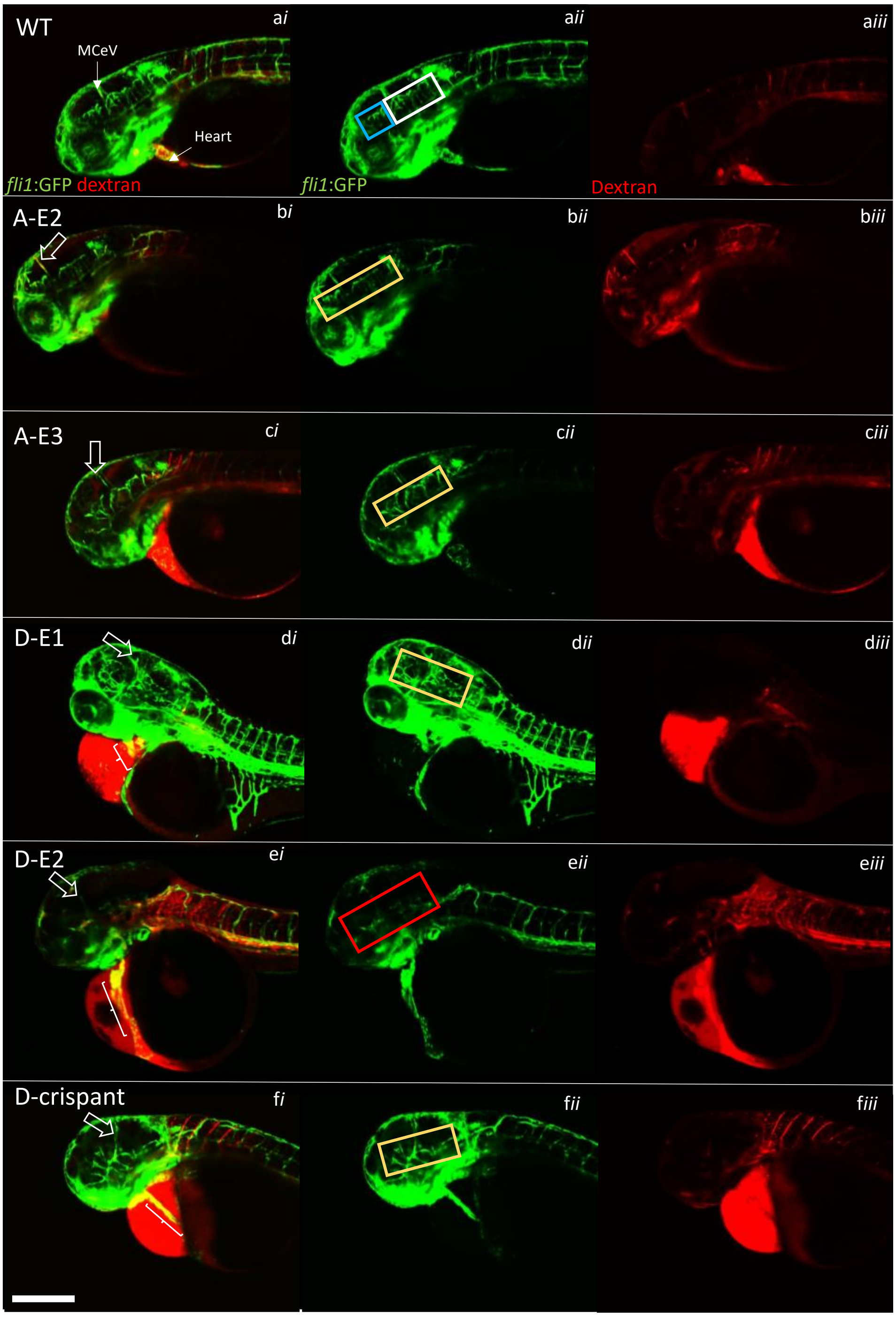

Figure 45: Analysis of internal cranial vasculature in Rho dysregulation models at 72 hpf.

Microangiography in a tg(*fli1*:GFP) line displaying the internal cranial vasculature in (**a**) wild-type (WT), (**b**) *arhgap31*-E2 (A-E2), (**c**) *arhgap31*-E3 (A-E3), (**d**) *dock6*-E1 (D-E1), (**e**) *dock6*-E2 (D-E2) and (**f**) *dock6*-crispant (D-crispant). Images are shown of **i.** the composite transgenic and microangiography vasculature, **ii.** transgenic (GFP) expression alone and **iii.** microangiography (dextran-rhodamine) alone. Truncated (thick arrow) and asymmetric (arrowhead) intersegmental vessels are demarcated in the transgenic images, whereas non-perfused vessels (thin arrow) are denoted in the microangiography images. Brackets indicate where dextran-conjugate is only seen in the dorsal longitudinal anastomotic vessels. N=3-7 embryos/condition. Scale bar, 300 µm.

identified using the current magnification and visualisation technique.

When examining the surface cranial vasculature, the tg(*fli1*:GFP) line was unable to demarcate many cranial vascular structures due to its specificity to NCCs and NCC-derived structures. Nonetheless, the SVP, CCV and heart were clearly visible. Microangiography delineated all other surface cranial vasculature (Figure 46a*iii*-f*iii*). At least one optic vessel was absent under each knockdown condition aside from *arhgap31*-E2 (Figure 46c*iii*-f*iii*). The SVP displayed malformation in *arhgap31*-E2 and *dock6*-E1 embryos (Figure 46b*ii*, d*ii*) and had not developed in *arhgap31*-E3, *dock6*-E2 and *dock6*-crispant embryos (Figure 46c*ii*, e*ii,* f*ii*). Additionally, *arhgap31*-E3 and all *dock6* knockdown models showed unperfused AA (Figure 46c*iii*-f*iii*), although it is unclear from the transgenic images if this is due to aberrant formation of the AA (Figure 46c*ii*-f*ii*).

Due to the observation of absent or poorly formed vascular structures in the tg(*fli1*:GFP) line (Figure 45, Figure 46), these data indicate that the poor vessel perfusion with reduced expression of *arhgap31* or *dock6* is caused by under development of cranial vascular structures rather than by vessel occlusion.

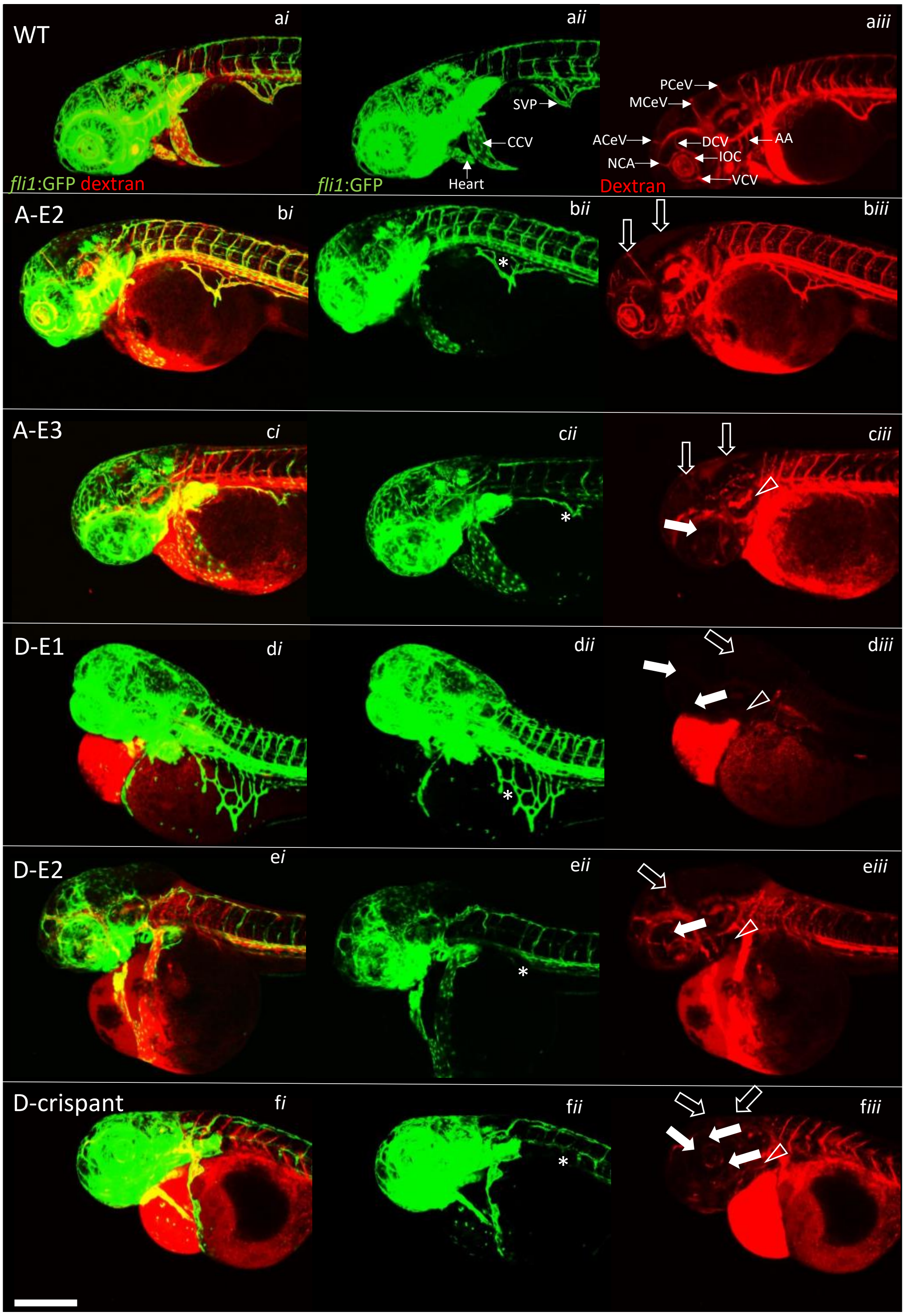

Figure 46: Analysis of surface cranial vasculature in Rho dysregulation models at 72 hpf.

Microangiography in a tg(*fli1*:GFP) line displaying the surface cranial vasculature in (**a**) wild-type (WT), (**b**) *arhgap31*-E2 (A-E2), (**c**) *arhgap31*-E3 (A-E3), (**d**) *dock6*-E1 (D-E1), (**e**) *dock6*-E2 (D-E2) and (**f**) *dock6*-crispant (D-crispant). Composite, transgenic and microangiography images are labelled ***i***, ***ii*** and ***iii***, respectively. Absent cranial and otic vessels are indicated by unfilled and filled white arrows, respectively. Absent aortic arches are marked with an arrowhead, and abnormal SVP development is denoted by an asterisk. **Key:** AA, aortic arches; ACeV, anterior cerebral vein; CCV, common cardinal vein; DCV, dorsal ciliary vein; IOC, inner optic circle; MCeV, middle cerebral vein; NCA, nasal ciliary artery; PCeV, posterior cerebal vein; SVP, subintestinal vessel plexus VCV, ventral ciliary vein. N=3-7 embryos/condition. Scale bar, 300 µm**.**

5.5.4 Vascular phenotype quantification in tg(*fli1*:GFP) line

Having identified poor vascular development and blood flow as a consequence of *arhgap31* and *dock6* knockdown, I next sought to quantify the extent of vascular malformation. Using the tg(*fli1*:GFP) reporter line to visualise the ISVs, the ImageJ Single Neurite Tracer (SNT) plugin was used to determine the average length and width of ISVs upon *arhgap31* or *dock6* knockdown (Figure 47a). Quantification of vessel width and length found that at 72 hpf, the mean lengths of ISVs injected with *dock6*-E1 (mean: 137.7 µm, SD: 28.1 µm), *dock6*-E2 (mean: 141.4 µm, SD: 46.1 µm), *arhgap31*-E2 (mean: 143.2 µm, SD: 25.7 µm) and *arhgap31*-E3 (mean: 165.3 µm, SD: 34.3 µm) were all significantly shorter than that of the wild-type (mean: 231.5 µm, SD: 63 µm) (Figure 47c). Similarly, in each of these conditions the width of the ISVs was significant shorter than the wild-type (mean: 54.09 µm, SD: 23 µm), with *dock6*-E1, *dock6*-E2, *arhgap31*-E2 and *arhgap31*-E3 displaying average ISV widths of 27.1±14.5 µm (SD), 32.2±18.3 µm (SD), 41.9±16 µm (SD) and 30.4 µm±10.4 µm (SD), respectively (Figure 47d).

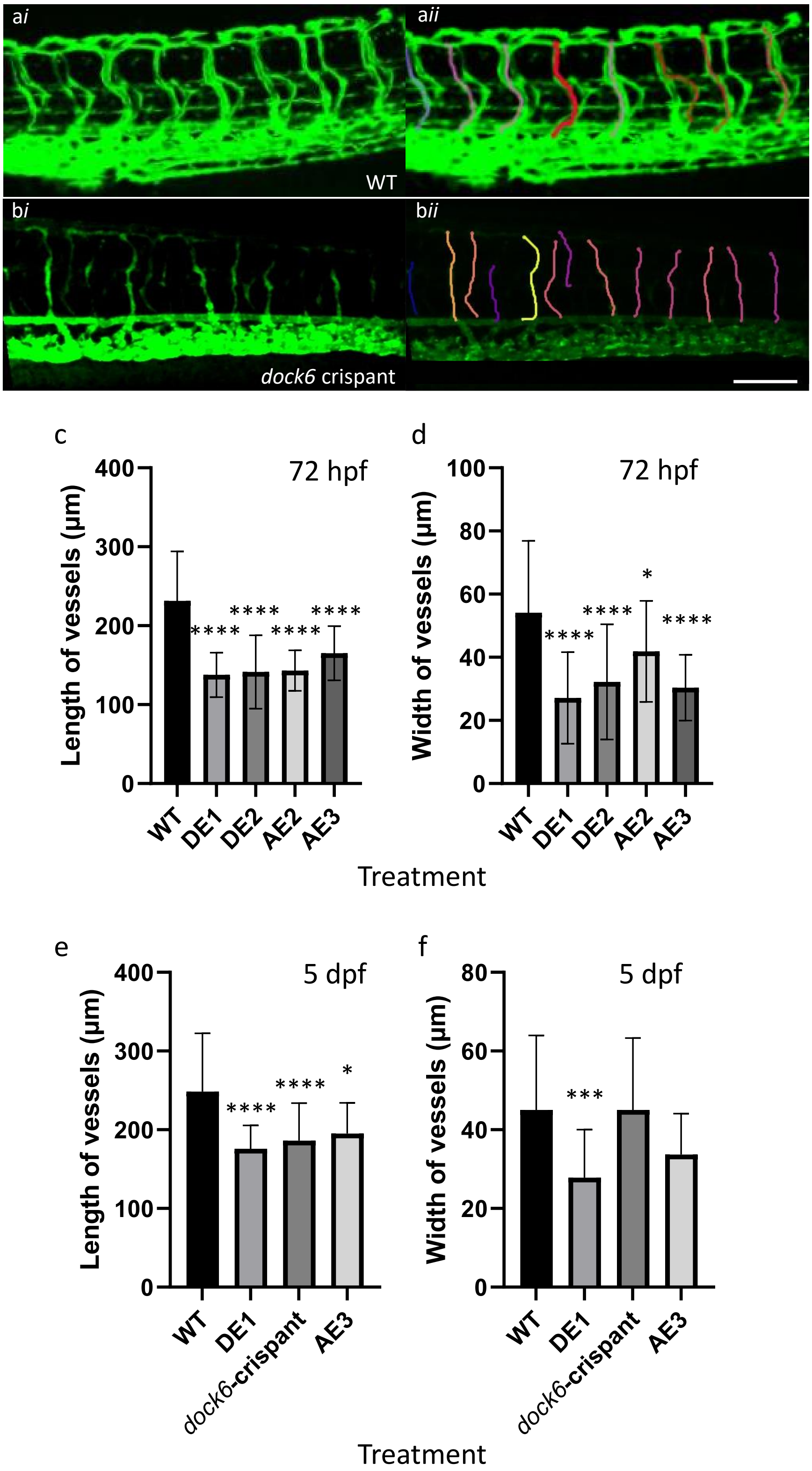

Figure 47: Quantification of vessel width and length in Rho dysregulation models.

An example of the vessel length and width quantification shows (**a**) a 72 hpf wild-type and (**b**) a *dock6*-crispant embryo. Both ***i.*** unmarked and ***ii.*** SNT software-annotated images of the trunk vasculature are shown. (**c-f**) Measurements of the length and width of vessels at 72 hpf (c,e) and 5 dpf (d,f). **p*<0.05, ****p*<0.001, *****p*<0.0001 indicate statistical significance by comparison to the wild-type. Error bars represent standard deviation. N=3-7 embryos/per condition. Scale bar, 100 µm.

At 5 dpf, the mean length of wild-type ISVs was 248.5 µm±72.1 µm (SD), and *dock6*-E1 (mean: 176.0 µm, SD: 26.6 µm), *dock6*-crispant (mean: 186.3 µm, SD: 47.7 µm) and *arhgap31*-E3 (mean: 195.0 µm, SD: 39 µm) ISVs remained significantly shorter (Figure 47d). However, the width of these vessels at 5 dpf was significantly reduced only in the *dock6*-E1 embryos (mean: 27.8 µm, SD: 12.2 µm) by comparison to the wild-type width (mean: 45.1 µm, SD: 18.9 µm) (Figure 47f). Following statistical analyses, the width of *dock6*-crispant (mean: 45.05 µm, SD:18.3 µm) and *arhgap31*-E3 (mean: 33.67 µm, SD: 10.4 µm) embryos was not found to be significantly decreased when compared to the wild-type (Figure 47f).

Together, these data show that knockdown of *arhgap31* or *dock6* significantly decreases the length and width of ISVs at 72 hpf, however this phenotype decreases in severity by 5 dpf.

5.6 Discussion

Previous chapters revealed localisation of *arhgap31* and *dock6* to numerous vascular structures over zebrafish embryogenesis and indicated potential vascular disruption upon depletion of *arhgap31* and *dock6* expression. Here, I sought to investigate the development of vascular structures under *arhgap31* and *dock6* knockdown through an analysis of *dll4*, *notch1a*, *kdrl* and *fli1* gene expression. Importantly, these experiments additionally aimed to delineate the potential mechanisms and regulatory mechanisms contributing to disorganised vascular development. For comprehensive examination of embryonic vascularisation upon *arhgap31* and *dock6* knockdown, microangiography and transgenic reporter techniques were employed with the aim of identifying structural changes induced by Rho dysregulation.

5.6.1 A novel interaction between the Notch and Rho signalling pathways

As a key contributor to early vascular development and a known causal pathway in AOS, investigation of Notch signalling in zebrafish provided a unique opportunity to further examine the molecular mechanisms behind aberrant vascularisation under Rho dysregulation and to identify a potential novel link between the two pathways in AOS pathogenesis.

Cranial *notch1a* expression in the 24 hpf zebrafish embryo appears inconsistent in the literature, as different studies have developed unique WISH probes which yielded slightly conflicting results (Banote et al., 2016; Gonzalez-Nunez, 2015; Kumar et al., 2017). For example, while one study displayed *notch1a* localisation to the eyes, forebrain, midbrain and hindbrain, another demonstrated confinement of *notch1a* expression to the rhombomeres, ventricles and hindbrain at 24 hpf (Banote et al., 2016; Kumar et al., 2017). However, despite these minor data discrepancies, all existing WISH data demonstrate localisation of *notch1a* to the developing forebrain, midbrain and hindbrain at 24 hpf. In this study, our WISH experiments in the 24 hpf wild-type embryo displayed strong, specific staining of *notch1a* expression to the forebrain, midbrain and hindbrain ventricles, with weaker staining in the otic vesicles and weaker staining to the more general hindbrain and midbrain regions. During mouse embryogenesis *Notch1* expression is accepted to be strongly localised to the ventricular zone, supporting these findings (Lindsell et al., 1996; Stump et al., 2002; Tokunaga et al., 2004). Endothelial staining by *notch1a* would also be expected during early zebrafish development, however it is likely that my *in situ* staining experiments did not undergo an adequate stain development time for endothelial staining, therefore we cannot infer a role for arhgap31 or dock6 knockdown in endothelial cells based on these experiments. Future experiments will include a longer stain development time so that the impact of *arhgap31* and *dock6* knockdown on *notch1a* signalling in endothelial cells can be observed.

5.6.1.1 Altered notch1a expression and ventricle patterning upon arhgap31 depletion

Upon *arhgap31* depletion, the strength of cranial *notch1a* expression was decreased and instead presented as a wider area of staining within the head due to *notch1a* expression no longer being confined to the ventricles. Previous studies have identified an essential role for *notch1a* in maintaining the neural stem cell pool; *notch1a* depletion leads to excessive differentiation of neural progenitors to neurons therefore reducing the neural stem cell population, whereas *notch1a* overexpression results in excessive neurogenesis and impaired cell proliferation (Banote et al., 2016;

Imayoshi et al., 2010; Kumar et al., 2017; Nikolaou et al., 2009). Increased Notch signalling induces expression of transcriptional repressor genes, including *Hes1* and *Hes5* (Imayoshi et al., 2010). Induction of these transcriptional effectors represses proneural gene expression, thereby inhibiting neuronal differentiation (Imayoshi et al., 2013, 2010). Therefore, Notch signalling is a key modulator in maintaining the neural stem cell population within the ventricles and negative regulation of this pathway promotes neuronal differentiation and cell proliferation (Wu et al., 2016).

The well-established role for *notch1a* in the zebrafish brain indicates that widened cranial *notch1a* staining upon *arhgap31* knockdown may lead to excessive neurogenesis and compromised cell proliferation (Nikolaou et al., 2009). Conversely, the poorly defined staining of the ventricles and line of *notch1a* staining over the presumptive ventricles could imply delayed or impaired enlargement of the neural tube into the ventricles in early embryogenesis, as the uninflated wild-type neural tube at 17 hpf exhibits a similar shape (Kimmel et al., 1995). Blood circulation has been identified as a contributing factor towards normal ventricle development, therefore it is worth noting that microangiography experiments (see Section 5.4.1) demonstrated compromised cranial vascular perfusion up to 5 dpf upon *arhgap31* reduction.

In wild-type zebrafish, the ventricles begin to develop from the neural tube at 17 hpf (Gibbs et al., 2017). This tube dilates in three different regions over time, giving rise to the forebrain, midbrain and hindbrain ventricles by 24 hpf, which coincides with the onset of blood circulation (Kimmel et al., 1995). Further opening of the hindbrain ventricles is facilitated by circulation, as noted in the *silent heart* zebrafish mutant which has impaired ventricle development beyond 24 hpf due to absent blood flow (Lowery and Sive, 2005). However, several mechanisms within the ventricles contribute to healthy ventricle expansion, including cerebrospinal fluid (CSF) accumulation leading to increased intraluminal pressure (Korzh, 2018) and, importantly, cell proliferation to regulate ventricle size (Lowery and Sive, 2005).

Interestingly, a regulatory mechanism involving ARHGAP31 and NOTCH1 has been identified in mice, whereby ARHGAP31 upregulates VEGF and induces SNAIL1 expression (Caron et al., 2016; Wu et al., 2014). NOTCH1 and DLL4 are then negatively regulated SNAIL1 (Wu et al., 2014). Thus, it is possible the delayed or impaired enlargement of the anterior neural tube into its three ventricles that was observed in *arhgap31* knockdown models may result from an increase in *notch1a* signalling. In support of this hypothesis, mice lacking neural-specific GSK-3, a positive regulator of ARHGAP31, exhibit a marked increase in Notch signalling as evidenced by widened *Hes1* expression, which is normally restricted to the ventricles and subventricular zones (Kim et al., 2009). This theory is further supported by the qPCR analysis in *arhgap31* morphant embryos, which demonstrated increased *notch1a* and *dll4* transcript levels at 24 hpf. Increased *notch1a* activity in this context likely maintains neurogenesis and impairs cell proliferation, leading to the observed under-developed ventricle phenotype upon *arhgap31* knockdown.

Of interest, autosomal dominant AOS can be caused by ARHGAP31 gain-of-function, NOTCH1 haploinsufficiency or DLL4 loss-of-function, therefore displaying different mechanisms of disease (Meester et al., 2015; Southgate et al., 2015, 2011). My data identify a novel link between opposing expression of *arhgap31* and *notch1a* which supports a mechanism for impaired vascular development. Quantification of protein expression for Notch pathway members is now required to comprehensively examine whether gene disruption translates into dysfunctional Notch signalling. In future, investigation of VEGF, SNAIL1 and GSK-3 activity in AOS-specific disease models, such as knock-in mice, may identify key targets for potential drug development in AOS.

5.6.1.2 Aberrant ventricular notch1a patterning under dock6 knockdown

Upon decreased *dock6* expression, cranial staining intensity was maintained, however expression in the midbrain-hindbrain boundary and forebrain ventricle was lost. It is unclear whether *dock6* knockdown has indeed affected *notch1a* expression patterns within the ventricles, or if there are structural defects in the forebrain ventricle and MHB caused by the loss of *dock6*. Of note, no direct links between *dock6* and *notch1a* signalling have been identified in the literature thus far.

Akin to the *arhgap31* morphants, impaired cranial blood circulation was identified in *dock6* knockdown models upon microangiography, which may have impacted ventricular development. Another potential mechanism is cell adhesion at the hinge-points of the MHB, which controls the opening between the midbrain and hindbrain ventricles (Kesavan et al., 2020). Defective cell adhesion at the MHB is known to impact the normal constriction of the neural tube, leading to aberrant shaping of the ventricles and impairs the development of other structures arising from the MHB, such as the cerebellum and the isthmic nuclei (Gibbs et al., 2017).

Interestingly, zebrafish mutations causing altered or reduced brain ventricle formation frequently coincide with heart and circulatory abnormalities, particularly affecting cranial circulation, as well as a loss of mobility which is generally associated with defective muscle development (Schier et al., 1996). These phenotypes strongly correlate with the observations in *dock6* knockdown models, which induced a stringy-heart phenotype and loss of circulation. Furthermore, *dock6* was expressed in the developing muscle fibres, suggesting a role for *dock6* in muscle development. However, it remains unclear whether abnormal ventricular formation induced these phenotypes or vice versa. Further work is required to ascertain whether these phenotypes cluster due to defective development from a cell type of common origin, for example the cranial NCCs, from which many structures in the head are derived.

5.6.1.3 Reduced arhgap31 or dock6 expression leads to loss of notch1a expression in the otic vesicle

A conserved role for Notch signalling in otic vesicle development exists in zebrafish, whereby the primary and secondary fates of hair cells and supporting cells, respectively, are decided through lateral inhibition in a Delta-Notch-dependent manner (Whitfield et al., 2002).

In both the *arhgap31* and *dock6* knockdown models, *notch1a* expression was lost from the otic vesicles. As previously noted in Sections 5.4.1 and 5.5.1, disruptions to *notch1a* expression could be due to a global developmental delay caused by Rho dysregulation and wild-type gene patterning may be restored later in embryogenesis. However, persistent disruption of Notch signalling in the otic vesicle can lead to perturbed otic development through aberrant cell specification in the inner ear. For example in the *mindbomb* mutant, which blocks Notch activation, cells do not differentiate to the secondary supporting cell fate, instead producing an excess of hair cells in early embryogenesis (Itoh et al., 2003). This leads to defective otic formation and the development of a smaller vesicle. However, as auditory impairment is not a common finding in AOS, *notch1a* loss at 24 hpf may be a zebrafish-specific effect of *arhgap31* and *dock6* knockdown, or there may be a compensatory mechanism at play that restores any malformation of the otic vesicles.

5.6.2 Impact of reduced *arhgap31* on early vascularisation

To further investigate the impact of *arhgap31* or *dock6* depletion on major angiogenic genes in zebrafish development, WISH was performed to examine the expression patterns of the ETS-associated *fli1* gene and the VEGF pathway gene *kdrl*. In the wild-type embryo at 24 hpf, *fli1* and *kdrl* expression patterns mirrored one another, with localisation to the PCV, CA, CV and ISVs. In both *arhgap31* morphants however, *fli1* and *kdrl* were expressed in these structures at a reduced level, perhaps indicative of a role for *arhgap31*-mediated regulation upstream of *fli1* and *kdrl*. Indeed, a previous study has identified increased *arhgap31* expression upon *etsrp* overexpression at 24 hpf, supporting involvement of *arhgap31* in the ETS signalling pathway at this time point (Gomez et al., 2012).

By contrast, qPCR experiments at 24 hpf did not support a global reduction of *fli1* and *kdrl* expression levels upon *arhgap31* knockdown. Despite large error bars, potentially indicating wide variability in expression levels across replicates, a general increase in *kdrl* was observed upon *arhgap31* knockdown. Expression levels of *fli1* also indicated an upward trend, similar to *notch1a* and *dll4* levels in *arhgap31* morphants (Figure 36, Figure 38). These results suggest that while *fli1* and *kdrl* appear reduced in trunk vascular structures at 24 hpf, there may be an upregulation of gene expression elsewhere, as qPCR experiments examined global *fli1* and *kdrl* expression.

Alternatively, the reduced WISH expression may be due to a loss of vascular structures caused by *arhgap31* knockdown.

5.6.2.1 arhgap31 knockdown impedes angiogenic initiation

Microangiography was used to quantify ISV development in *arhgap31* knockdown models, which indicated severely impaired ISV formation at 24 hpf (Figure 43). However, it should be noted that the smaller size of the morphant embryos may have been caused by morpholino-induced developmental delay and may have impacted the formation of ISVs at the correct time. Therefore, future experiments should assess morphant embryos that appear to be at the same stage of development by comparison to wild-type embryos. This is a limitation of morpholino technology. The increase in Notch pathway gene expression upon loss of *arhgap31* may point towards a Notch-mediated mechanism for the observed intersegmental vessel phenotype. Specifically, elevated *dll4* expression with a concomitant rise in ligand production may activate Notch signalling in adjacent cells. Historically, increased Dll4-Notch1 activity suppresses the tip cell phenotype and cells will instead default to stalk cell behaviour (Siekmann and Lawson, 2007b). As stalk cells do not develop filopodial structures, sprout development from the DA by 24 hpf is delayed. Therefore, increased Notch signalling in endothelial cells under reduced *arhgap31* expression may provide a potential explanation for the lack of developing ISVs seen at this timepoint in *arhgap31* knockdown models.

To assess tip and stalk cell ratios upon *arhgap31* depletion, a transgenic *kdrl* vascular reporter line in conjunction with light sheet microscopy from 12 hpf could be used to visualise cell differentiation and formation of the axial vessels, followed by endothelial cell migration and filopodia formation during ISV development. To delineate the impact of *arhgap31* reduction on vasculogenesis, WISH experiments could be performed to determine the arterial-venous specification of endothelial cells constituting the presumptive DA and PCV. Further examination of VEGF and Notch signalling specifically in the trunk vasculature using tissue-specific qPCR and WISH experiments beyond 24 hpf would clarify the relative expression of these genes under *arhgap31* depletion. Additionally, *hey1* and *hes1* levels could be used as a readout for Notch activity in the trunk vasculature to determine the likelihood for aberrant tip and stalk cell specification which may contribute towards delayed angiogenic sprout migration in ISV formation. These experiments would broaden our understanding for the role of *arhgap31* during vasculo- and angiogenesis on both a molecular and cellular level.

5.6.3 Early vascular defects induced upon *dock6* depletion

In *dock6* knockdown models, WISH experiments unveiled altered patterning of *fli1* and *kdrl* expression in the vasculature, particularly in the CVP. However, qPCR experiments did not reveal any significant changes in *fli1* and *kdrl* transcript levels at 24 hpf. Therefore, the altered gene expression in vascular structures may be due to *dock6*-induced patterning defects rather than a change in VEGF and Notch signalling. DOCK6 activity in humans and mice is regulated by PI3K/Akt-mediated phosphorylation, which is placed downstream of VEGF signalling (Miyamoto et al., 2013). Therefore, *dock6* knockdown is unlikely to directly impact *kdrl* expression levels.

As previously noted (see Section 5.3.2) the differences in *fli1* and *kdrl* expression levels observed between WISH and qPCR experiments may be due to the use of whole-organism RNA for cDNA analysis. As for the *arhgap31* knockdown models, tissue-specific mRNA extraction may provide more relevant insight towards the impact of *dock6* knockdown on *fli1* and *kdrl* expression levels in vascular structures. In addition, experiments assessing the impact of *dock6* knockdown on Rac1 and Cdc42 activity in the CVP may help to elucidate a role for *dock6* in CVP development and endothelial cell migration, a currently unexplored avenue.

5.6.3.1 Reduced dock6 expression impedes initiation of angiogenesis

To further assess the impact of *dock6* on angiogenesis, reduced *dock6* expression in the tg(*fli1*:GFP) line was examined at 24 hpf. As seen under *arhgap31* knockdown, *dock6* depletion severely impaired intersegmental vessel development by 24 hpf. However, the mechanisms underpinning impaired ISV development upon *dock6* downregulation are unclear. Interestingly, development of the CVP occurs in a similar manner to ISV, whereby venous endothelial cells of the PCV sprout and migrate ventrally to fuse with neighbouring tip cells and form a primitive vascular network (Wakayama et al., 2015). Therefore, it is possible that impaired CVP and ISV development under *dock6* knockdown share a common origin.

Various molecules associated with endothelial cell specification and angiogenesis have been found to interact with *dock6.* In particular, PI3K/Akt-mediated regulation of DOCK6 activity uncovered an essential role for DOCK6 in axonal elongation (Miyamoto et al., 2013). The striking mechanistic similarities between CNS and vascular development may suggest a common mode of action for DOCK6 in neuritogenesis and angiogenesis, namely cell extension and migration, in guiding and elongating sprouts. Therefore, loss of DOCK6 may impact Rac1/Cdc42-mediated cytoskeletal rearrangement in filopodial protrusion and adhesion, thus impairing ISV branch advancement and CVP development, as observed at 24 hpf (Figure 43).

To investigate the interactions between VEGF signalling and DOCK6 activity through PI3K/Akt-mediated phosphorylation, VEGF-stimulated endothelial cells could be examined *in vitro* and DOCK6 phosphorylation status analysed by Western blot with an anti-(pS1194)DOCK6 antibody. Further, G-LISA assays to quantify Cdc42 and Rac1 phosphorylation may identify whether VEGF stimulation impairs DOCK6 function to decrease Cdc42 and/or Rac1 activation. These experiments could reveal a novel interaction between VEGF signalling and DOCK6 GEF activity in angiogenesis.

5.6.4 Compromised trunk vascularisation upon Rho dysregulation

While numerous molecular mechanisms may be involved in the maldevelopment of ISVs under reduced *arhgap31* and *dock6* expression, further experiments are required to determine the true underlying causes. Having noted angiogenic abnormalities at 24 hpf in both *arhgap31* and *dock6* knockdown models, vascular development was tracked until 5 dpf, using a combination of microangiography and a transgenic vascular reporter line (tg[*fli1*:GFP]).

At 72 hpf, both *arhgap31* and *dock6* knockdown models demonstrated an ability to initiate angiogenesis, as ISVs in the tg(*fli1*:GFP) were present. However, microangiography experiments displayed a poor perfusion of some ISVs in addition to truncated or asymmetric ISV branching pairs, suggesting a failure of the tip cells to migrate properly, or to respond to angiogenic cues (Nasevicius et al., 2000).

Interestingly, the asymmetric phenotype observed strengthens an argument for impaired embryonic patterning under reduced *arhgap31* and *dock6* expression, as described in previously (see Sections 4.6.2 and 4.6.3). As the intersegmental vessel phenotypes were largely maintained by 5 dpf, it is unlikely that incomplete ISV development is caused solely by a generic developmental delay due to loss of *arhgap31* and *dock6*. Rather, these data point towards a direct negative effect of *arhgap31* and *dock6* knockdown on endothelial cell function.

Reduced ISV width and length were also observed at 5 dpf, although to a lesser extent. In particular, *dock6*-crispant and *arhgap31*-E3 models did not display a significantly decreased ISV width at 5 dpf. The observations of an improved vascular phenotype as the embryo develops may indicate compensatory mechanisms at play to offset the defects caused by aberrant Cdc42 and Rac1 regulation.

5.6.5 Poor blood circulation is induced by *arhgap31* or *dock6* knockdown

A large proportion of *dock6* knockdown embryos displayed impaired blood circulation (see Section 4.5), also seen in some microangiograms. Blood flow is known to play an important role in vascular development in both the pruning of developed vessels and the stabilisation of existing vessels (Chen et al., 2012). During ISV development, blood flow-induced shear stress on the cilia of the endothelial cells leads to the recruitment of mural cells to the developing vessel, which contributes towards lumen integrity (Chen et al., 2017). Of note, patient autopsies have identified impaired mural cell recruitment and distribution across vessels as a key mechanism in AOS pathogenesis (Patel et al., 2004).

Alternatively, poor perfusion and lack of blood circulation could be attributed to impaired vessel lumenisation. Transgenic reporter experiments (Figure 47) showed reduced ISV lumen width in *arhgap31* and *dock6* knockdown embryos aged 72 hpf by comparison to the wild-type. Correct formation of adherens junctions is essential in ISV lumenisation, as evidenced by compromised vascular integrity upon the loss of adhesion molecules, such as VE-cadherin (Montero-Balaguer et al., 2009). Critically, my microangiography experiments displayed leaking vessels upon dextran-conjugate injection (Figure 40), suggesting *arhgap31* and *dock6* may regulate adhesion molecules. Interestingly, previous studies have identified a role for ARHGAP31 in maintaining cadherin adhesion junctions through association with the scaffold protein Ajuba, in which ARHGAP31 overexpression lead to cell-cell contact disruption (McCormack et al., 2017).

In order to form an appropriately-sized lumen, endothelial cells must morph from a round cuboidal shape to an elongated squamous phenotype, which is dependent upon reorganisation of the actin cytoskeleton (Davis et al., 2002). Of interest, the DOCK-B family member DOCK4 has been reported to regulate the shape of endothelial cells in developing tubules *in vitro* (Abraham et al., 2015). *DOCK4*-depleted tubes were thinner with reduced adjacent cell-cell contacts, likely due to the loss of filopodia and protrusions caused by decreased Rac1 activity (Abraham et al., 2015). This was not found to be associated with defective migratory behaviour of the endothelial cells. Considering the similar phenotypes induced by *arhgap31* and *dock6* knockdown, it is possible that the compromised ISV and lumen formation may be caused by defective cell-cell adhesion in the sprouting intersegmental vessels, perhaps caused by Rac1 and/or Cdc42 activity disruption as a consequence of *arhgap31* or *dock6* knockdown.

5.6.6 Impaired cranial vascularisation at 72 hpf and 5 dpf

Hypovascularisation and poor perfusion of the brain upon *arhgap31* and *dock6* knockdown (Figure 39, Figure 40, Figure 45) is consistent with several AOS reports and with the phenotypes displayed in *ARHGAP31* knockout mouse models. MRI imaging of AOS patients has revealed ischaemia of the brain, in accordance with the compromised cranial perfusion seen in my Rho dysregulation models (Bilginer et al., 2008). Indeed, several studies have suggested that the onset of CNS abnormalities observed in some AOS patients, particularly those affected by *DOCK6* mutations, is due to the disruption of blood flow during critical periods of development (Lehman et al., 2014; Piazza et al., 2004).

There have also been several reports of periventricular calcifications in AOS patients, consistent with the onset of microbleeds due to compromised vascular integrity. Microangiography experiments unveiled impaired cranial vascular integrity across *arhgap31* and *dock6* models, to varying degrees (Figure 39, Figure 40). These findings further implicate *arhgap31* and *dock6* in the maintenance of cell adhesion and provide evidence for a conserved function between humans and zebrafish. Interestingly, *ARHGAP31* knockout in mouse models leads to lethality and haemorrhaging among other phenotypes, adding to the mounting evidence of a highly conserved function for *arhgap31* in maintaining vascular integrity through a role in cell-cell contact formation (Caron et al., 2016).

5.6.7 Conclusions

Depletion of *arhgap31* in zebrafish increases Notch signalling in both brain ventricle and vascular development, leading to impaired cell proliferation in the ventricle and therefore delayed enlargement of the ventricles. Additionally, impaired intersegmental vessel sprouting at 24 hpf may be due to Notch augmentation under *arhgap31* knockdown, leading to excessive stalk cell specification. Stalk cells exhibit a proliferative rather than migratory phenotype, therefore impairing angiogenic sprouting in ISV formation.

Similarly, *dock6* knockdown induces structural defects in brain ventricle formation, however this is unlikely to be caused by changes to the Notch signalling pathway. Instead, abnormal ventricle shaping may be due to impaired cell adhesion at the MHB due to reduced Rac1- and Cdc42-mediated filopodia and lamellipodia formation caused by *dock6* depletion.

Increasing evidence observed in microangiograms and vascular transgenic reporter experiments revealed phenotypes including poor vessel perfusion, angiogenic sprouting of the ISVs and vessel leakage. These data point towards a mechanism of impaired cell-cell adhesion in the vasculature under genetic disruption of *arhgap31* and *dock6.*

Chapter 6: *In vitro* analysis of *DOCK6* on angiogenic functions

6.1 Introduction

Previous chapters have demonstrated localisation of *dock6* and *arhgap31* to developing neural crest and vascular structures during normal zebrafish embryogenesis. Additionally, I identified poor vascular development upon reduction of *dock6* and *arhgap31*, indicating a critical role for these genes in early vascularisation. To further investigate the cellular mechanisms behind the phenotypes observed in zebrafish, *in vitro* studies were undertaken to examine the impact of *DOCK6* knockdown upon human vascular smooth muscle (VSMC) and human keratinocyte (HaCaT) cell line function. VSMCs were chosen due to the previously unexplored role for mural cells in the pathogenesis of AOS (see Section 1.1.1), whilst HaCaT cells were used to independently validate these findings and investigate *DOCK6* knockdown in the context of aplasia cutis congenita (ACC), a common feature of AOS.

Due to the role for DOCK6 as a GEF regulating the activity of Rac1 and Cdc42, it is hypothesised that reducing *DOCK6* expression will decrease levels of active Rac1 and Cdc42 and negatively impact actin cytoskeletal organisation. Indeed, it has previously been shown that patient fibroblasts harbouring biallelic *DOCK6* mutations display reduced lamellipodia formation and altered morphology (Shaheen et al., 2011). However, this has not yet been examined in other cell types. Therefore, I focussed on examining cytoskeletal organisation, cell adhesion, migration and proliferation in VSMCs and HaCaT cells. These cellular functions are heavily reliant upon correct lamellipodial and filopodial extension and critical for angiogenesis.

6.2 Generating DOCK6 knockdown models

To investigate the impact of DOCK6 loss-of-function *in vitro*, siRNA experiments were optimised to reduce *DOCK6* expression in VSMCs and HaCaTs. To confirm *DOCK6* knockdown, RNA and protein extracted from VSMCs and HaCaTs 72 hours post-transfection were analysed by qPCR and Western blotting. RNA quantification in VSMCs showed a significant decrease in transcript levels upon *DOCK6* siRNA treatment, displaying a 0.51-fold change (SD: 0.08) in RNA expression by comparison to the wild-type (Figure 48a). In VSMCs, the DOCK6 protein was visualised and displayed the expected molecular weight of approximately 230 kDa (Miyamoto et al., 2007). DOCK6 knockdown translated into reduced protein levels at 72 hours post-transfection, with a 0.54-fold-change (SD: 0.08) in the siRNA-treated cells by comparison to the wild-type (Figure 48b, c). DOCK6 protein levels were normalised to the total protein (Figure 48c, Figure 49c). The observed non-specific bands corresponded to those seen in other studies which used this DOCK6 primary (Miyamoto et al., 2007; Zhang et al., 2021).

Transcript levels in HaCaTs at 72 hours post-transfection displayed significantly reduced RNA expression under *DOCK6* siRNA treatment, which induced a 0.29-fold change (SD: 0.07) in expression by comparison to the wild-type (Figure 49a). At the protein level, *DOCK6* siRNA-treated HaCaTs displayed a 0.42-fold change (SD: 0.11) in expression by comparison to wild-type (Figure 49b, c). In both cell lines, *DOCK6* RNA and DOCK6 protein levels in the siRNA treated cells were significantly lower than the wild-type and negative control. Therefore, *DOCK6* siRNA-treated cells are a suitable model to investigate the impact of reduced *DOCK6* expression on cell function.

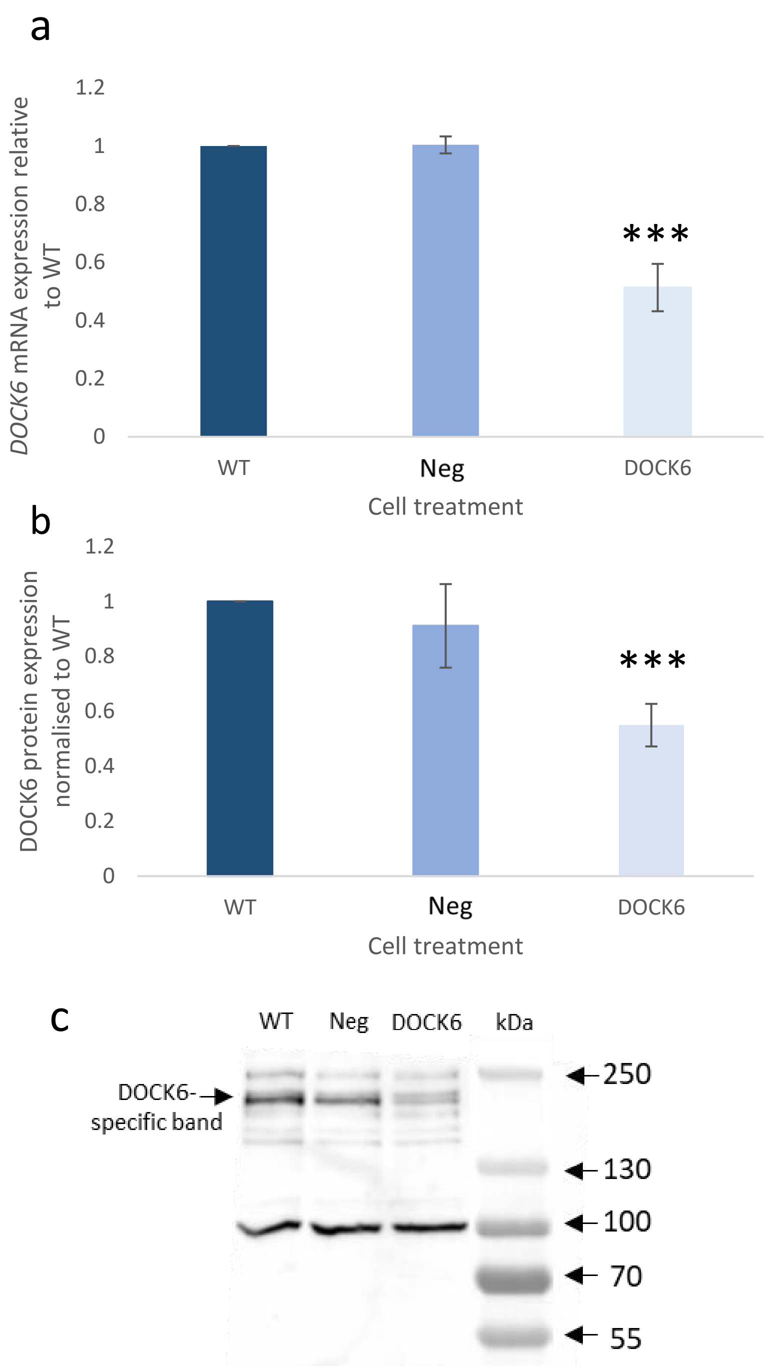

Figure 48: Knockdown of *DOCK6* in VSMCs.

Confirmation of *DOCK6* knockdown on the transcript and protein level in VSMCs by (**a**) quantitative PCR (n=5) and (**b, c**) Western blot (n=3). mRNA and protein analyses were carried out in wild-type (WT), negative siRNA control (Neg) and *DOCK6* siRNA-treated cells. Protein weight was determined using a PageRuler Plus Prestained Protein Ladder. Statistical analysis was conducted by one-way ANOVA with a Tukey's test for multiple comparisons. Error bars represent standard deviation. Significant differences are by comparison to the wild-type. ***, p<0.001.

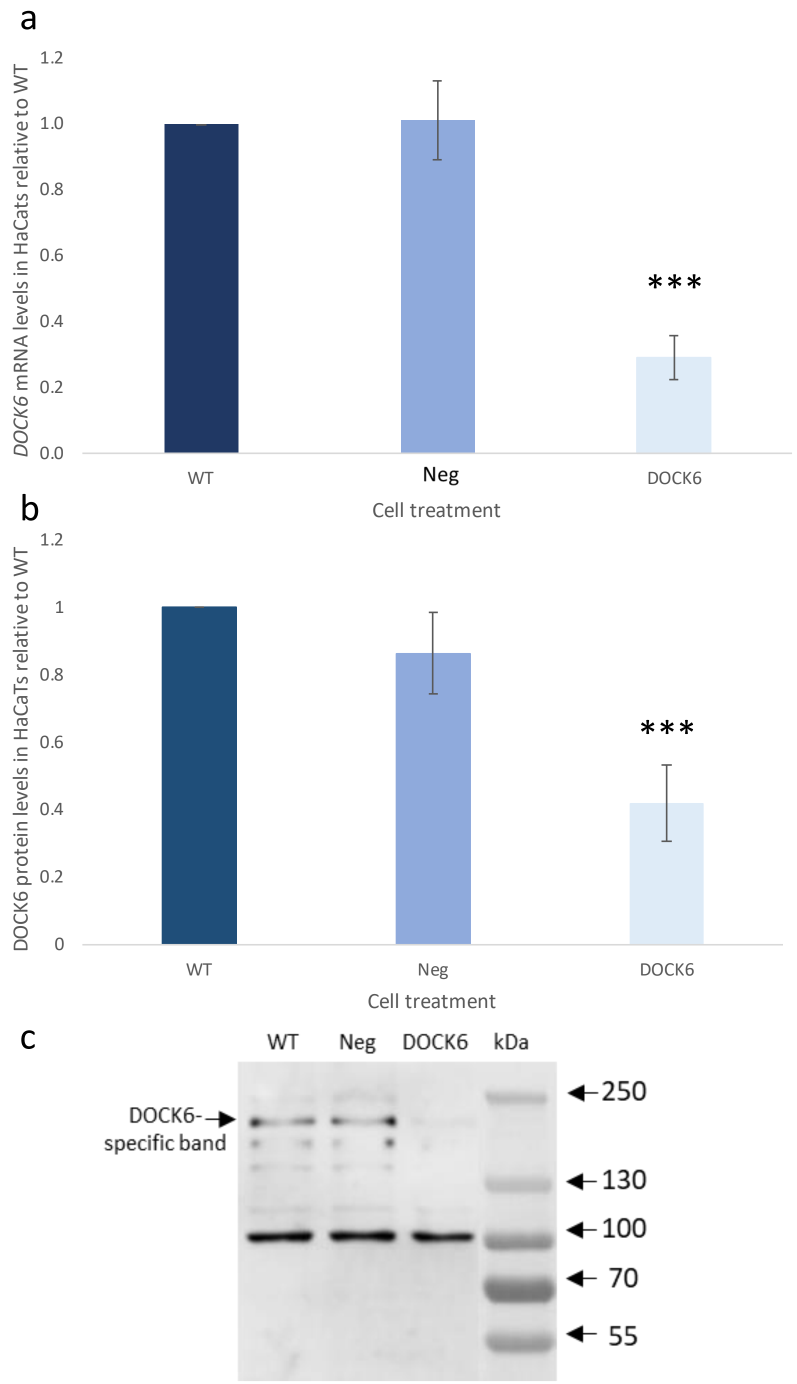

Figure 49: Confirmation of *DOCK6* knockdown in HaCaT cells.

Knockdown of *DOCK6* in HaCaT cells by siRNA confirmed by (**a**) quantitative PCR (n=3) and (**b, c**) Western blot (n=3). mRNA and protein analyses were carried out in the wild-type (WT), negative siRNA control (Neg) and *DOCK6* siRNA-treated cells. Protein weight was determined using a PageRuler Plus Prestained Protein Ladder. Statistical analysis was conducted by one-way ANOVA with a Tukey's test for multiple comparisons. Error bars represent standard deviation. Significant differences are by comparison to the wild-type (WT). ***, $p<0.001$.

6.3 Investigating cytoskeletal organisation

A previous study examining *DOCK6* loss-of-function in AOS patient fibroblasts identified cell rounding and a disorganised actin cytoskeleton upon reduced *DOCK6* expression (Shaheen et al., 2011). Therefore, I sought to investigate the impact of *DOCK6* knockdown on the actin cytoskeleton in VSMCs, a cell type which is relevant to angiogenesis and has shown aberrant behaviour in several AOS case reports (Maniscalco et al., 2005; Patel et al., 2004). Additionally, HaCaT cells were investigated to asses potential cell-specific effects in vascular and skin cells, both of which are relevant to the hallmark features of AOS.

6.3.1 *DOCK6* knockdown in VSMCs impairs cell surface attachment by disrupting the actin cytoskeleton

Upon transfection of VSMCs with *DOCK6* siRNA, a cell-rounding phenotype was observed in VSMCs depleted of *DOCK6* but not in the wild-type nor the cells treated with a negative siRNA control (Figure 50). Quantification of this phenotype revealed a significant increase in cell rounding in *DOCK6*-depleted cells (mean: 20.70%, SD: 3.57%) by comparison to wild-type (mean: 12.54%, SD: 1.89%) and negative control (mean: 10.52%, SD: 2.31%) cells (Figure 51a). Historically, cell rounding is associated

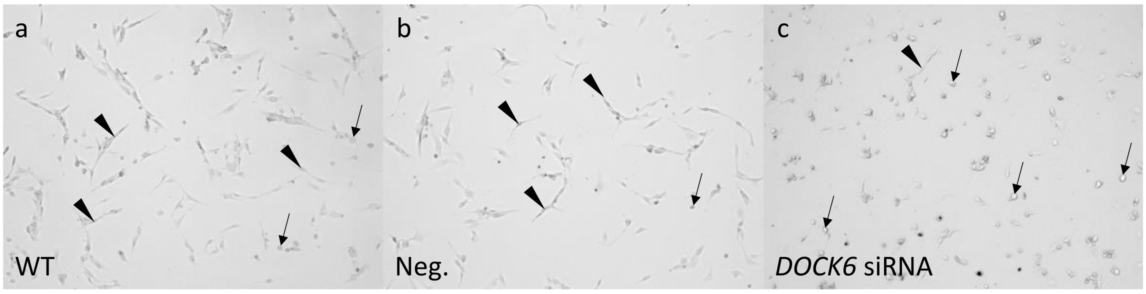

Figure 50: Representative images of cell rounding following *DOCK6* knockdown.

Images displaying typical VSMC morphology in (**a**) wild-type, (**b**) negative control and (**c**) *DOCK6*-depleted cells. Arrowheads and arrows indicate examples of the expected elongated VSMC morphology and the rounded cell phenotype, respectively.

with compromised cell adhesion, therefore the proportion of viable cells detached from the plate surface was calculated (Figure 51b). Of cells which detached from the cell surface after 24 hours, approximately seven times more cells were viable in the *DOCK6* siRNA-treated plates (mean: 24.51%, SD: 4.61%) than in the wild-type (mean: 3.62%, SD: 0.18%). Negative siRNA-treated plates had very few viable detached cells (mean: 1.31%, SD: 0.04%), indicating that a loss of adhesion in healthy VSMCs was specifically due to *DOCK6* knockdown. At 48 hours post-transfection, 8.36% ± 0.53% (SD) and 1.80% ± 0.07% (SD) of wild-type and negative control cells were viable, compared with 24.39% ± 4.15% (SD) of detached *DOCK6*-depleted cells. No significant difference was identified between the wild-type and negative control cells, confirming that the transfection method did not impact detached cell viability (Figure 51b).

To investigate the potential mechanism behind impaired VSMC adhesion, the actin cytoskeleton was visualised by phalloidin staining at 24 and 72 hours post *DOCK6* siRNA transfection. These two timepoints were used as they are before and after the critical 48 hour timepoint when *DOCK6*-depleted cells have been reported to recover by genetic compensation (Cerikan et al., 2016) At 24 and 72 hours, wild-type cells displayed expected actin filaments across the cell and normal filopodial protrusion and lamellipodial formation at the cell edges (Figure 52a, c). However, upon *DOCK6* reduction, VSMCs at 24 hours exhibited increased actin foci and decreased elongated actin filaments across the cell (Figure 52b). At the cell edges, filopodial protrusions were stunted and had a ragged appearance, suggesting that the supporting lamellipodial network has been disrupted. By 72 hours, these phenotypes had largely recovered, as filopodial protrusions and elongated actin filaments become apparent

(Figure 52d). These data provide support for the previously described genetic compensation following DOCK6 knockdown in cell culture models (see Section 6.7.4).

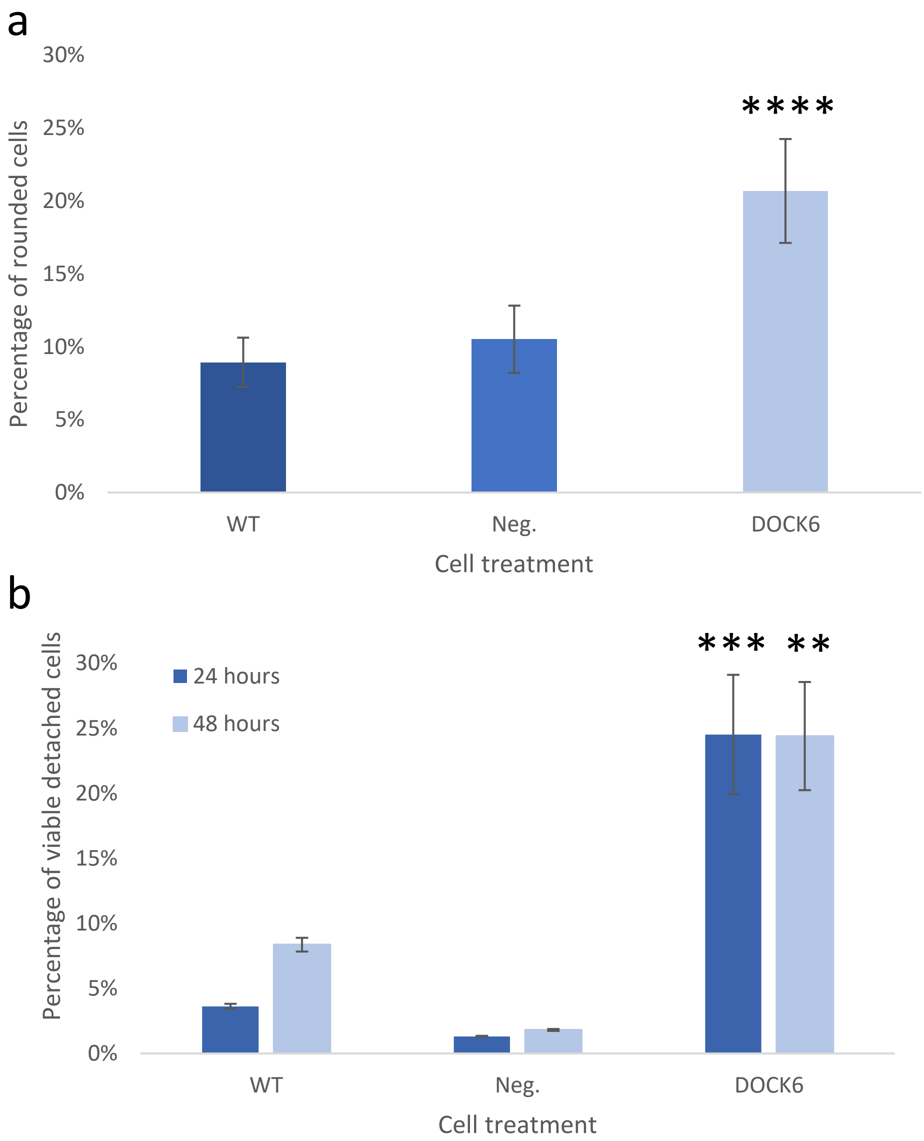

Figure 51: Cell rounding and detachment in *DOCK6* siRNA-treated VSMCs.

(**a**) Average percentage of rounded cells (n = 15 replicates) in wild-type (WT), negative siRNA control (Neg) and *DOCK6* siRNA-treated cells after 24 hours. (**b**) The percentage of detached cells which are viable (n = 2 replicates) at 24 and 48 hours post-transfection. Statistical analysis was performed by one-way ANOVA with a Tukey's test for multiple comparisons. Error bars represent standard deviation. Significant differences are marked by comparison to the wild-type. **, p<0.005, ***, p<0.001, ****, p<0.0001.

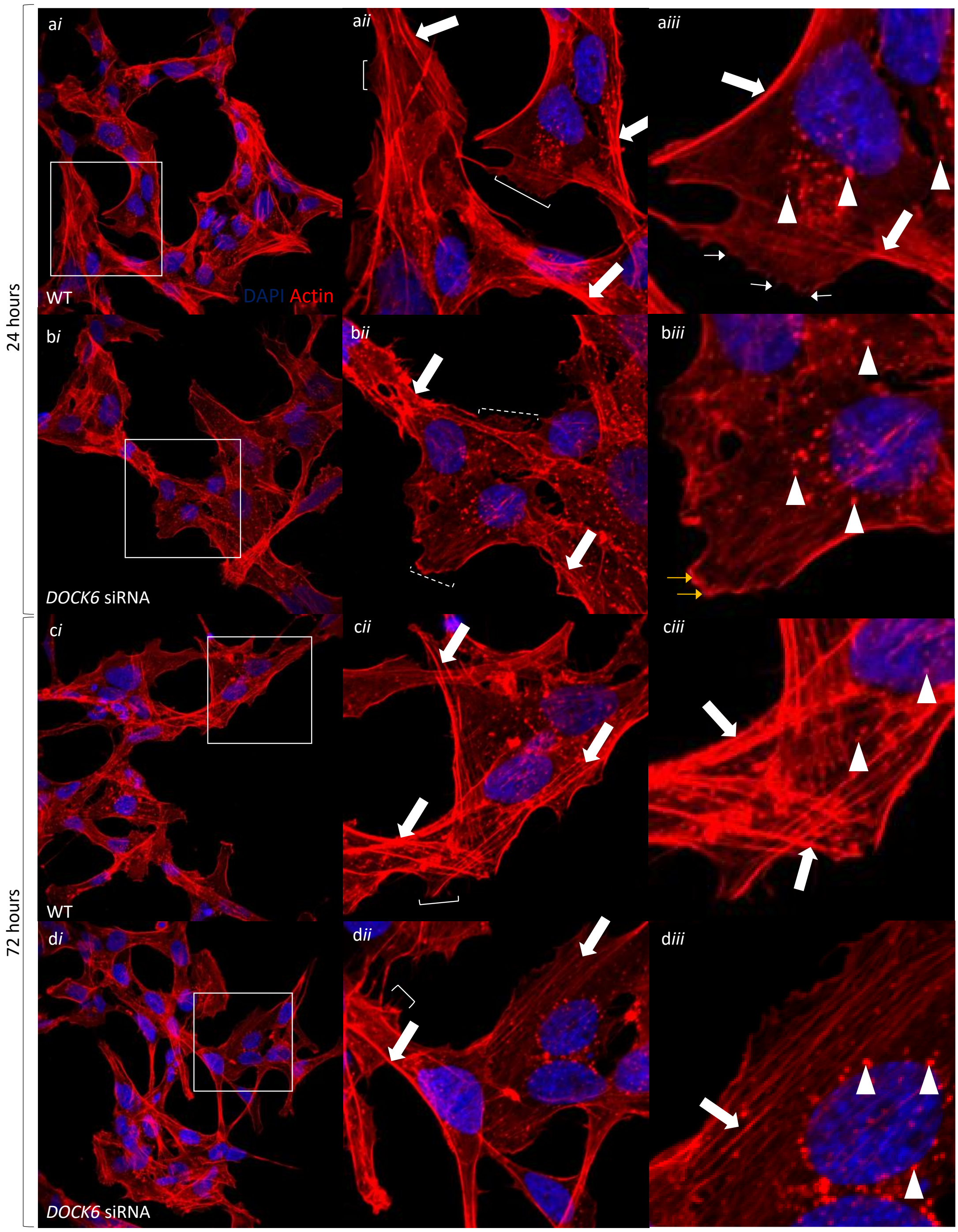

Figure 52: Disorganised actin cytoskeleton in VSMCs upon *DOCK6* knockdown.

Phalloidin-mediated actin staining in (**a, c**) wild-type (WT) and (**b, d**) *DOCK6*-depleted VSMCs at 24- and 72 hours post-transfection. Images show (*i*) representative cells (n=3 biological replicates) and (***ii***) magnified insets with (***iii***) lamellipodia and filopodia highlighted. Actin filaments (filled white arrows), actin foci (arrowhead), normal (thin white arrow) and defective filopodia (yellow arrow) are indicated.

The observation of increased actin foci was of interest due to its association with impaired cell spreading (Di Cio et al., 2020; Siu et al., 2011). Therefore, the number of actin foci per cell was quantified in both the wild-type and *DOCK6*-depleted cells at 24- and 72 hours post-transfection (Figure 53). While a significant increase in the number of actin foci was observed at 24 hours upon *DOCK6* depletion (98 ± 11.4 (SD)) by comparison to wild-type (40 ± 12.2 (SD)), the phenotype appeared to recover by 72 hours as no significant difference was observed, demonstrating 64 ± 9.9 (SD) and 68 ± 7 (SD) foci per cell in wild-type and *DOCK6*-depleted cells, respectively. This could be an indication of recovered *DOCK6* expression following siRNA treatment, this is unlikely due to the sustained loss of *DOCK6* RNA and protein expression seen up to 72 hours post-transfection. The recovery seen at 72 hour post-transfection may therefore be further evidence of genetic compensation (see Section 6.7.4)

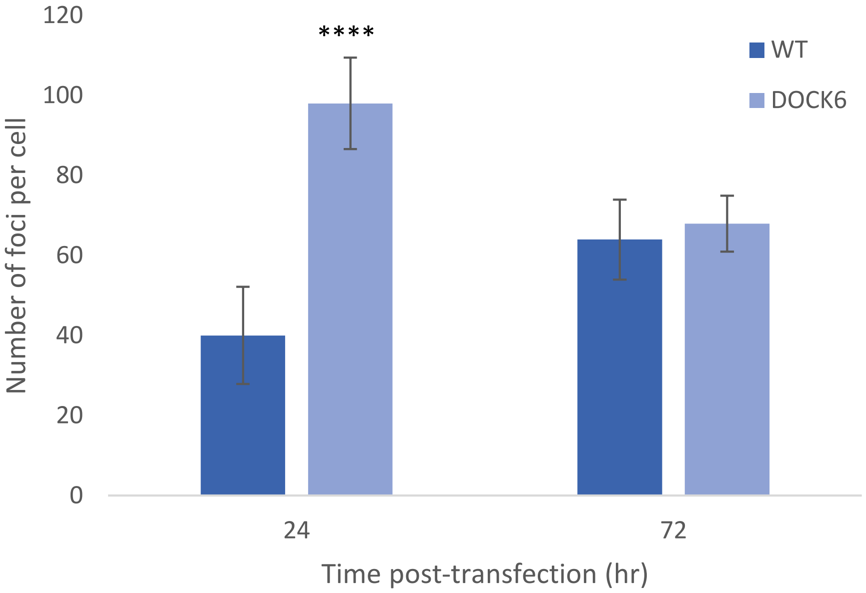

Figure 53: Quantification of actin foci in VSMCs under *DOCK6* depletion.

Mean number of actin foci in wild-type (n = 2 (4 cells/replicate)) and *DOCK6*-depleted (n = 4 (4 cells/replicate) VSMCs at 24 and 72 hours post-transfection. Statistical analysis was performed by two-way ANOVA with a Sidak's test for multiple comparisons. Error bars represent standard deviation. Asterisks represent a significant difference by comparison to the wild-type. ****, *p*<0.0001..

6.3.2 Reduced *DOCK6* expression impairs HaCaT cell spreading and actin cytoskeleton organisation

Following assessment of *DOCK6* knockdown in VSMCs, these experiments were repeated in HaCaT cells to examine the actin cytoskeleton in an alternative cell type relevant to AOS. Depletion of *DOCK6* in HaCaT cells exhibited a cell rounding phenotype, consistent with the observation in VSMCs following *DOCK6* knockdown. Upon quantification, 22.55% ± 6.21% (SD) of *DOCK6*-depleted HaCaT cells were rounded 24 hours after transfection, compared with 10.08% ± 2.54% (SD) and 10.58% ± 3.35% (SD) observed in wild-type and negative control HaCaTs (Figure 54a). The increased number of rounded *DOCK6*-depleted cells was highly significant ($p<0.0001$). Similar to the VSMC line, the viability of detached *DOCK6*-depleted HaCaT cells at 24 and 48 hours post-transfection was investigated (Figure 54b). Quantification revealed that 9.09% ± 12.86% (SD) of detached wild-type cells and 11.54% ± 16.32% (SD) of detached negative control cells were viable after 24 hours, compared with 38.52% ± 2.10% (SD) of *DOCK6* knockdown HaCaT cells. This increase in viability was maintained at 48 hours, with 38.08% ± 11.42% (SD) of detached *DOCK6*-depleted cells displaying viability, compared to 11.54% ± 16.32% (SD) and 7.69% ± 10.88% (SD) of detached wild-type and negative control cells, respectively. While reducing *DOCK6* expression led to an increase in viable detached cells at both timepoints, only the increase seen at 24 hours was significantly higher than that of the wild-type ($p<0.05$), largely due to wide variability across replicate control experiments.

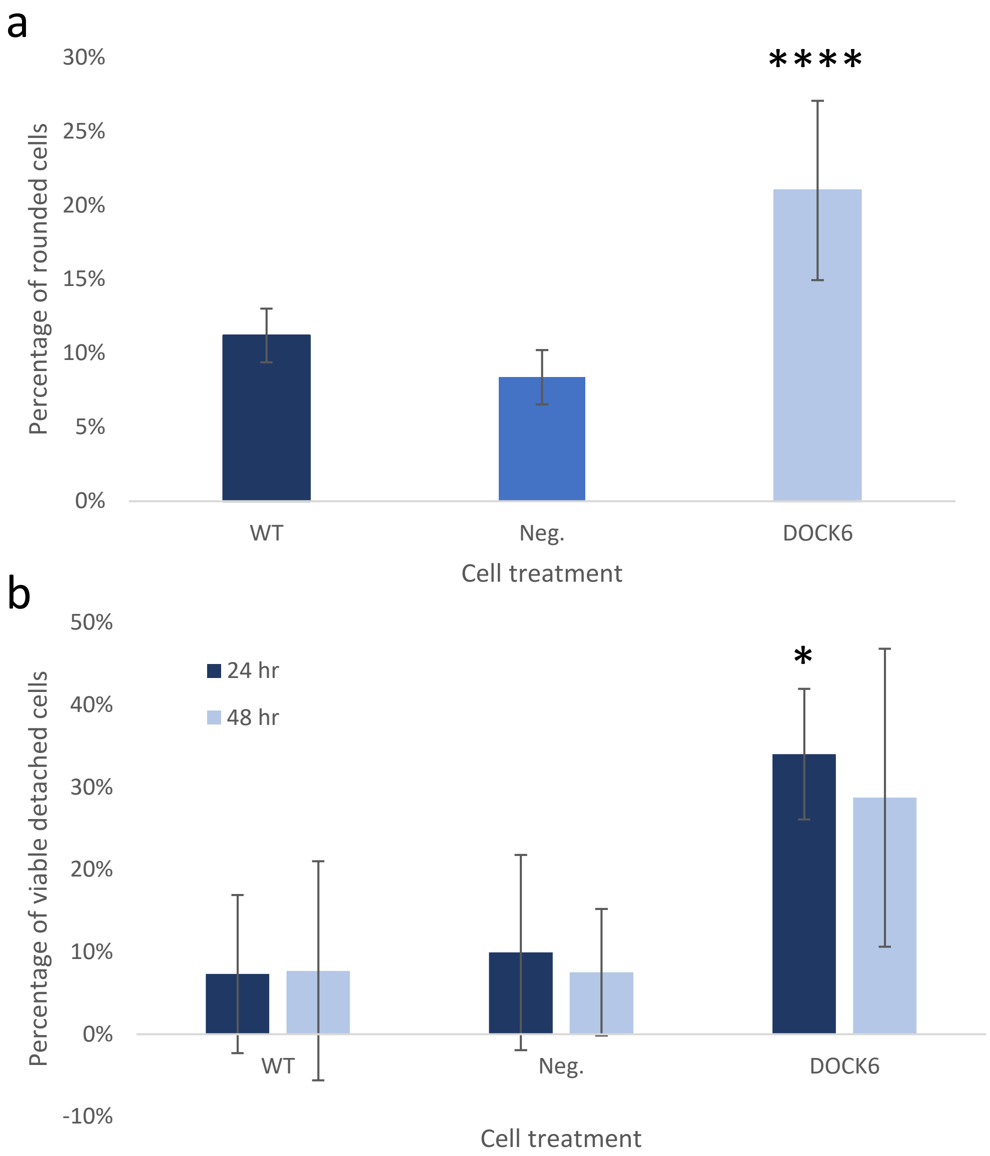

Figure 54: Cell rounding and detachment in *DOCK6* knockdown HaCaT cells.

The average percentage of (**a**) rounded HaCaT cells (n = 5 replicates) upon *DOCK6* knockdown after 24 hours and of (**b**) viable detached cells (n = 3 replicates) 24 and 48 hours post-transfection. Statistical analysis was performed by (a) one-way and (b) two-way ANOVA, followed by a Tukey's test for multiple comparisons. Error bars represent standard deviation. Asterisks indicate a significant difference by comparison to the wild-type. *, p<0.05, ****, p<0.0001.

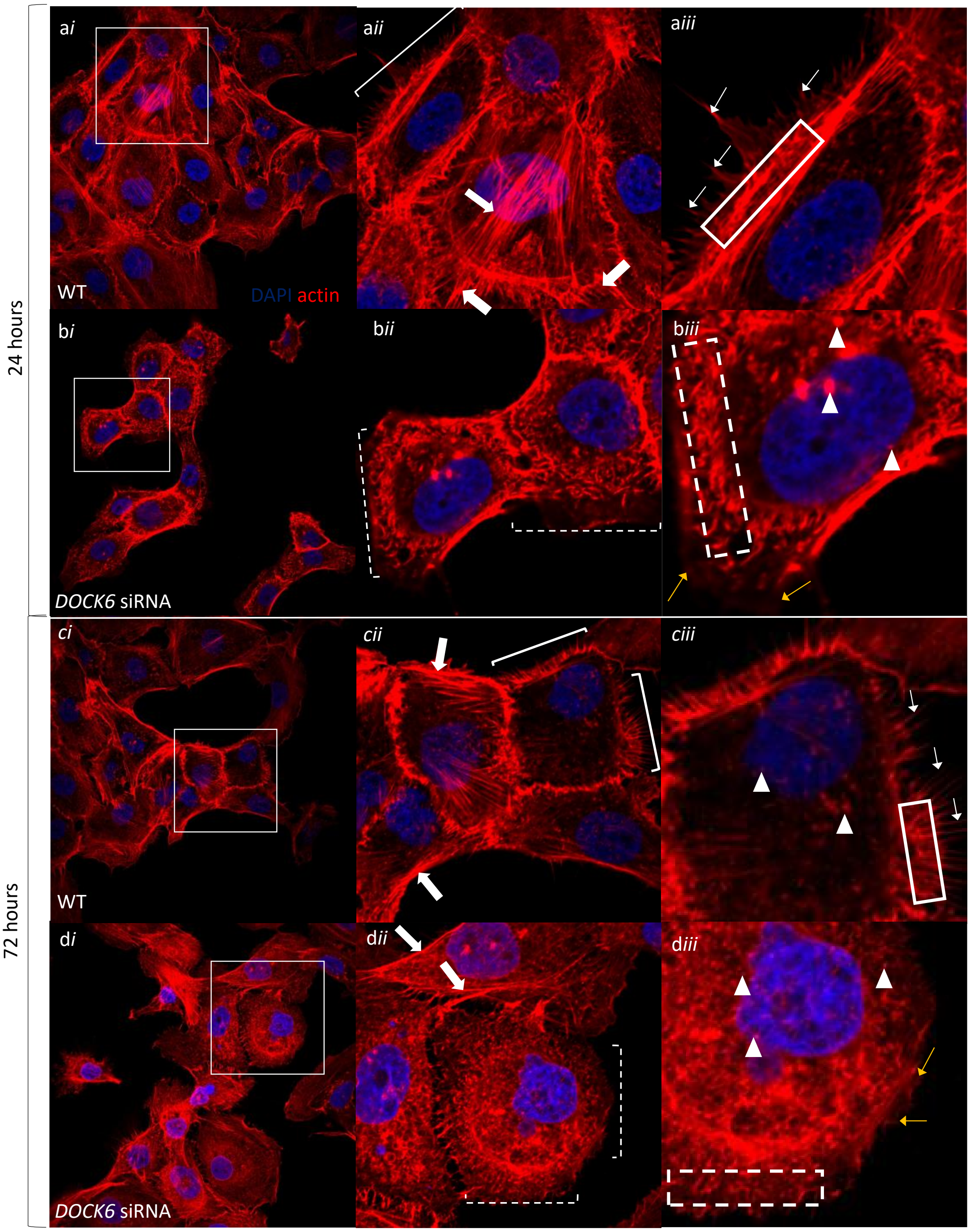

Figure 55: Actin cytoskeleton disruption in HaCaT cells under *DOCK6* knockdown.

Actin staining in (**a, c**) wild-type (WT) and (**b, d**) *DOCK6*-depleted HaCaT cells at (**a, b**) 24 hours and (**c, d**) 72 hours post-transfection. Representative cells (**i**) and magnified insets (**ii**) are displayed (n=3 biological replicates). Lamellipodia and filopodia formation in wild-type and DOCK6 knockdown cells are shown (**iii**). Actin filaments (filled white arrows), actin foci (arrowhead), normal (thin white arrow) and defective filopodia (yellow arrow) are indicated. Healthy and disorganised lamellipodia network formation are enclosed by continuous and dashed boxes, respectively.

Actin-staining of wild-type and *DOCK6* siRNA-treated HaCaT cells further highlighted differences in the actin cytoskeleton upon *DOCK6* depletion (Figure 55). In the wild-type, filopodial protrusions were successfully formed and expected actin filament distribution was exhibited across the cell (Figure 55a, c). However, in *DOCK6*-depleted cells, these actin filaments were observed at a much lower level, if at all, at both 24- and 72 hours post-transfection (Figure 55b, d). Additionally, filopodial protrusion appeared compromised and lamellipodial organisation at the cell edges was disrupted. Further, cells expressing reduced *DOCK6* displayed a speckled phenotype across the cell. These were identified as actin foci and appeared more severe in the HaCaT cells 72 hours after *DOCK6* depletion by comparison to 24 hours.

The increase in actin foci viewed under confocal microscopy upon *DOCK6* knockdown in HaCaT cells was quantified to assess significance (Figure 56). At 24 hours post transfection, *DOCK6*-depleted cells displayed a higher number of actin foci per cell

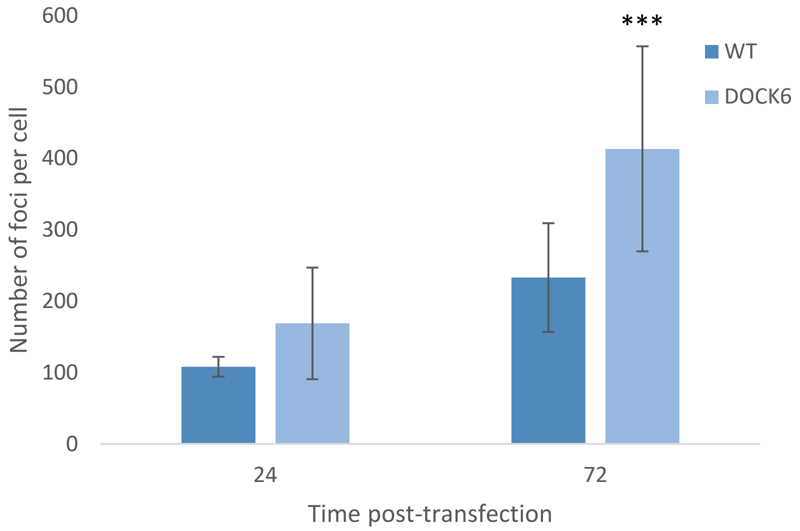

Figure 56: Reduced *DOCK6* expression increases number of actin foci in HaCaT cells.

The mean number of actin foci per cell 24- and 72 hours post-transfection in wild-type (n= 2 (3-4 cells/replicate) and *DOCK6* siRNA-treated (n = 3 (3-4 cells/replicate) HaCaT cells. Statistical analysis was performed by two-way ANOVA with a Sidak's test for multiple comparisons. Error bars represent standard deviation. Asterisks represent a significant difference by comparison to the wild-type. ***, $p<0.001$.

(mean: 168.9, SD: 78.2) by comparison to wild-type HaCaT cells (mean: 108, SD: 13.8). By contrast to the VSMCs, this difference was augmented at 72 hours post transfection, with *DOCK6*-depleted HaCaT cells displaying a significant increase in actin foci (mean: 413.5, SD: 143.8) compared to the wild-type (mean: 233.1, SD: 76.3).

6.4 *DOCK6* depletion does not impair proliferation in VSMCs

To determine whether cytoskeleton disruption impairs cell proliferation, cell growth of *DOCK6*-depleted VSMCs and HaCaT cells was monitored over 3-4 days by a combined approach of manual cell counting and MTT cell viability assays. As expected, manual cell counting experiments indicated a steady increase in cell number over time to 2.86-fold (SD: 0.89) in wild-type VSMCs and 2.72-fold (SD: 0.35) in negative siRNA control-treated cells, from 24- to 96 hours post transfection (Figure 57). A similar increase in cell count of 2.55-fold (SD: 1.29) was observed in the *DOCK6*-depleted VSMCs (Figure 57), indicating no significant deviation from the normal growth curve. As a method of independent validation, MTT assays were performed (Figure 58). Wild-type and *DOCK6*-depleted viable VSMC numbers displayed an increase between 0 hours at 72 hours, corresponding to fold-increases of 4.24 ± 0.13 (SD) and 4.6 ± 0.36 (SD), respectively, over 72 hours (Figure 58). Differences in cell number between the manual cell counting and MTT assays could be attributed to the use of 6 well and 96 well plates, respectively, resulting in differing cell densities and therefore altered cell proliferation. Based on my results, no significant differences were seen between wild-type and *DOCK6* siRNA-treated VSMCs, indicating that reducing the level of *DOCK6* expression did not impact VSMC proliferation.

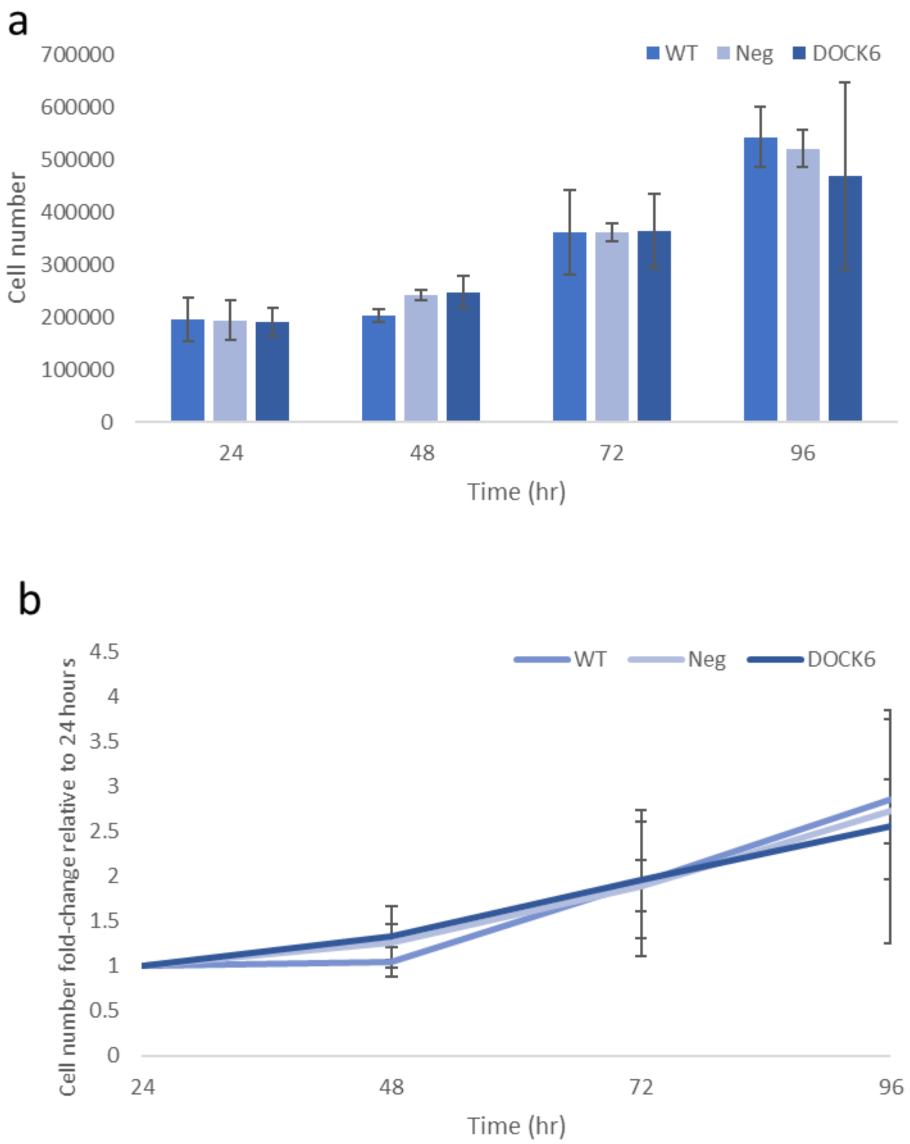

Figure 57: *DOCK6* depletion does not impact VSMC proliferation.

Cell proliferation of *DOCK6*-depleted VSMCs was calculated by (**a**) manual cell counting and (**b**) fold-change normalised to the starting cell number for each treatment. Statistical analysis was performed by two-way ANOVA followed by a Tukey’s test for multiple comparisons. N= 3 biological replicates, error bars represent standard deviation.

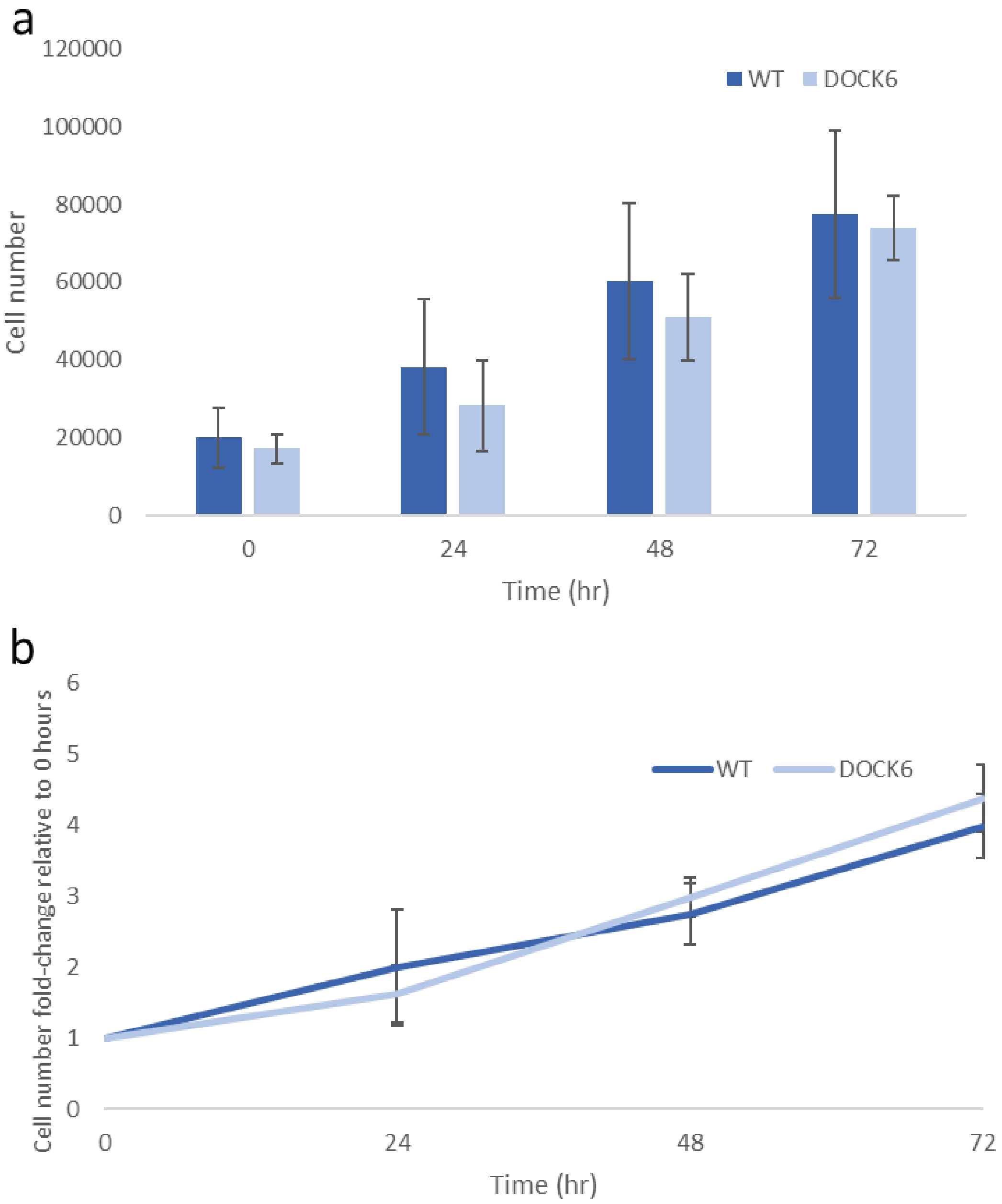

Figure 58: MTT assays display no difference in number of viable cells in VSMCs.

Cell viability calculated by (**a**) MTT assay (n=3 replicates). Cell fold-change normalised to the starting cell number of each treatment is displayed (**b**). Statistical analysis was performed between the wild-type and siRNA-treated cells at each timepoint by two-way ANOVA followed by a Tukey's test for multiple comparisons.

6.5 HaCaT proliferation is not impaired by *DOCK6* knockdown

HaCaT cell number as determined by manual cell counting showed a gradual increase of wild-type, negative control and *DOCK6* siRNA-treated HaCaTs (Figure 59a). When viewed as fold-change in cell number from 24 hours, wild-type, negative control and *DOCK6*-depleted cells displayed a fold-change increase of 8.99 ± 0.88 (SD), 9.47 ± 2.49 (SD) and 10.35 ± 2.24 (SD), respectively, by 96 hours (Figure 59b). Despite seeing a general trend towards increased fold-change in *DOCK6*-treated HaCaTs compared to the wild-type and negative control, at no timepoint were these differences significant. As no statistical difference was observed in the negative control compared to the wild-type, it can be concluded that the transfection method did not impact HaCaT cell proliferation. By contrast to manual cell counting, MTT assays did not display a general increase in viable cell number over time, instead demonstrating a decline in the first 24 hours followed by no cell growth (Figure 60a). The fold-change over 72 hours was ~0.8x the original cell number in both wild-type and *DOCK6* siRNA-treated cells (Figure 60b). As these results were consistent over three replicates, it is likely that an MTT assay was an inappropriate method for quantifying cell number in this cell type, perhaps due to toxicity or an inability of the cell type to metabolise MTT to formazan.

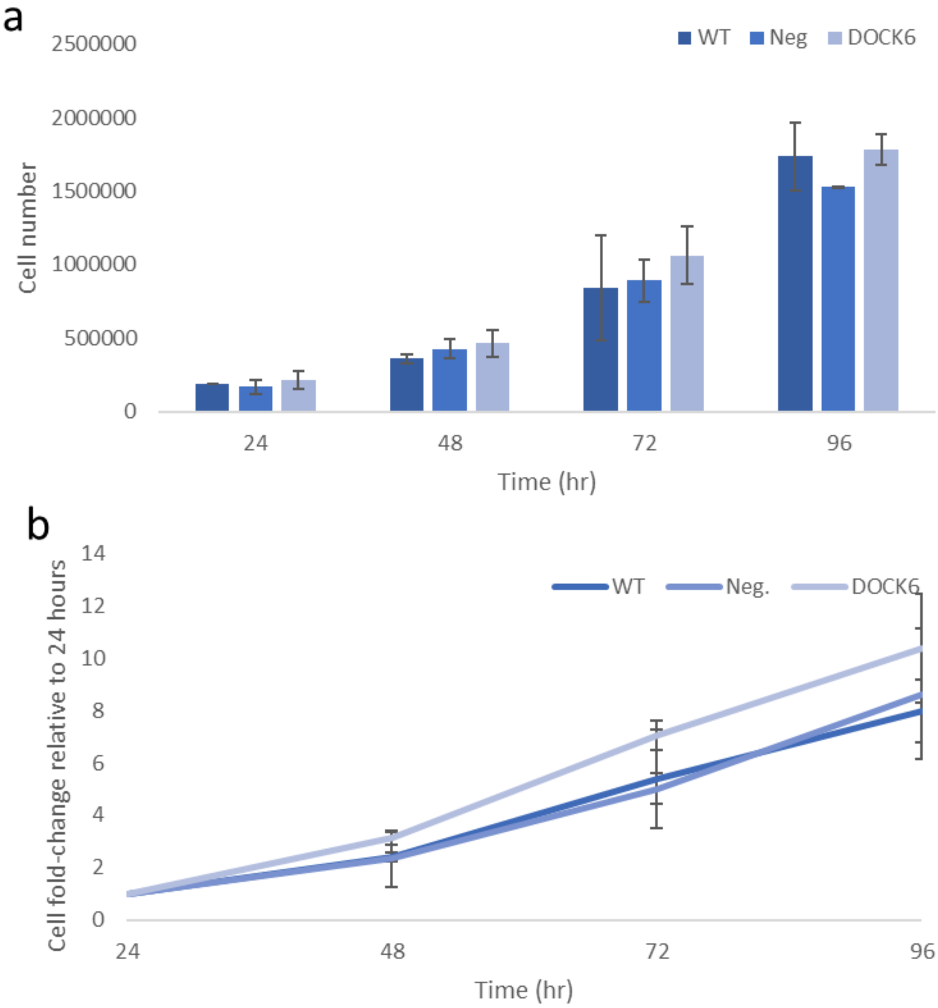

Figure 59: HaCaT proliferation is not altered by *DOCK6* depletion.

Cell proliferation in wild-type (WT) and *DOCK6*-depleted HaCaT cells was calculated by (**a**) manual cell counting (n=6 replicates) and (**b**) fold-change normalised to the starting cell number of each treatment. Statistical analysis was performed between the wild-type and siRNA-treated cells at each timepoint by two-way ANOVA followed by a Tukey’s test for multiple comparisons.

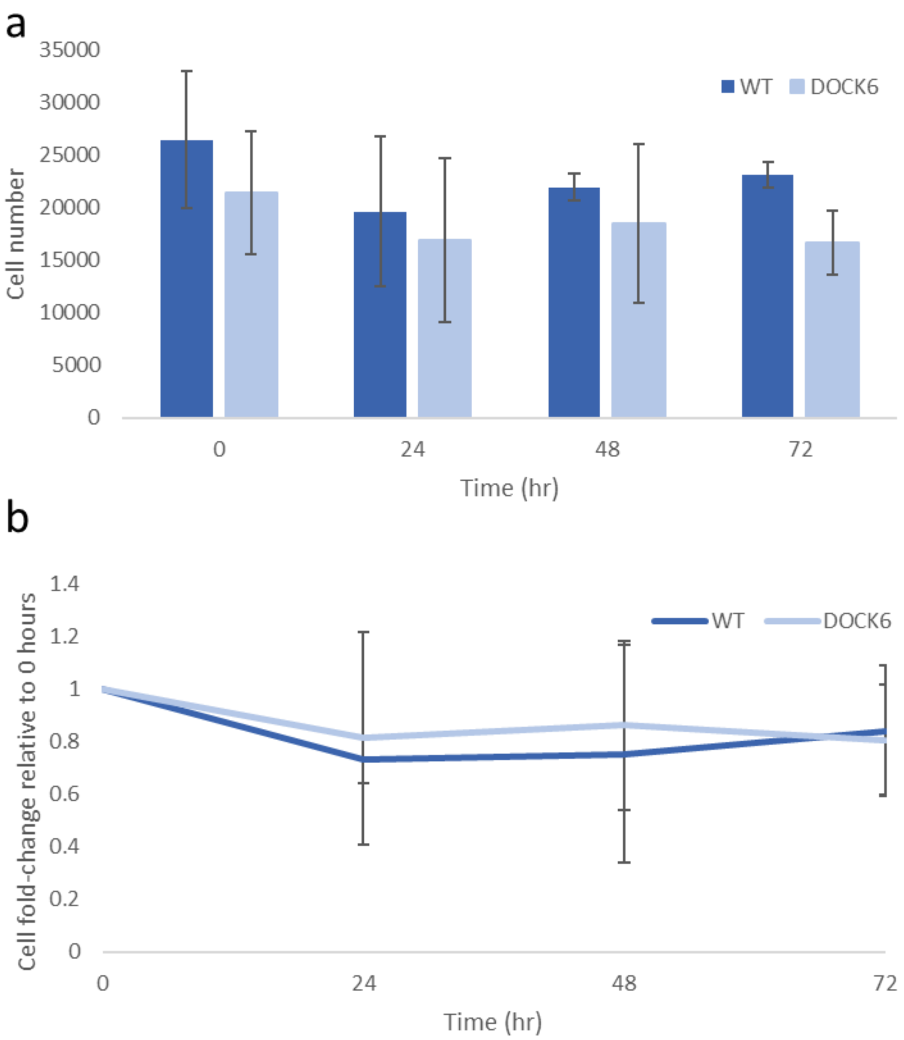

Figure 60: MTT assay calculating number of viable HaCaT cells over 72 hours.

Cell viability over time of wild-type (WT) and *DOCK6*-depleted HaCaT cells was calculated by (**a**) MTT assay (n=3 replicates) and (**b**) cell fold-change normalised to the starting cell number of each treatment. Statistical analysis between the wild-type and siRNA-treated cells at each timepoint was performed by two-way ANOVA followed by a Tukey's test for multiple comparisons.

6.6 Reduced *DOCK6* expression does not impact overall migration in VSMC and HaCaT cell lines

To assess the impact of *DOCK6* knockdown on VSMC and HaCaT migration, wound-healing and Ibidi chamber migration assays were optimised and analysed over 48 hours (Figure 61, Figure 62). In VSMCs, reducing *DOCK6* levels had no impact on cell migration as wild-type cell and *DOCK6*-depleted cell behaviour were

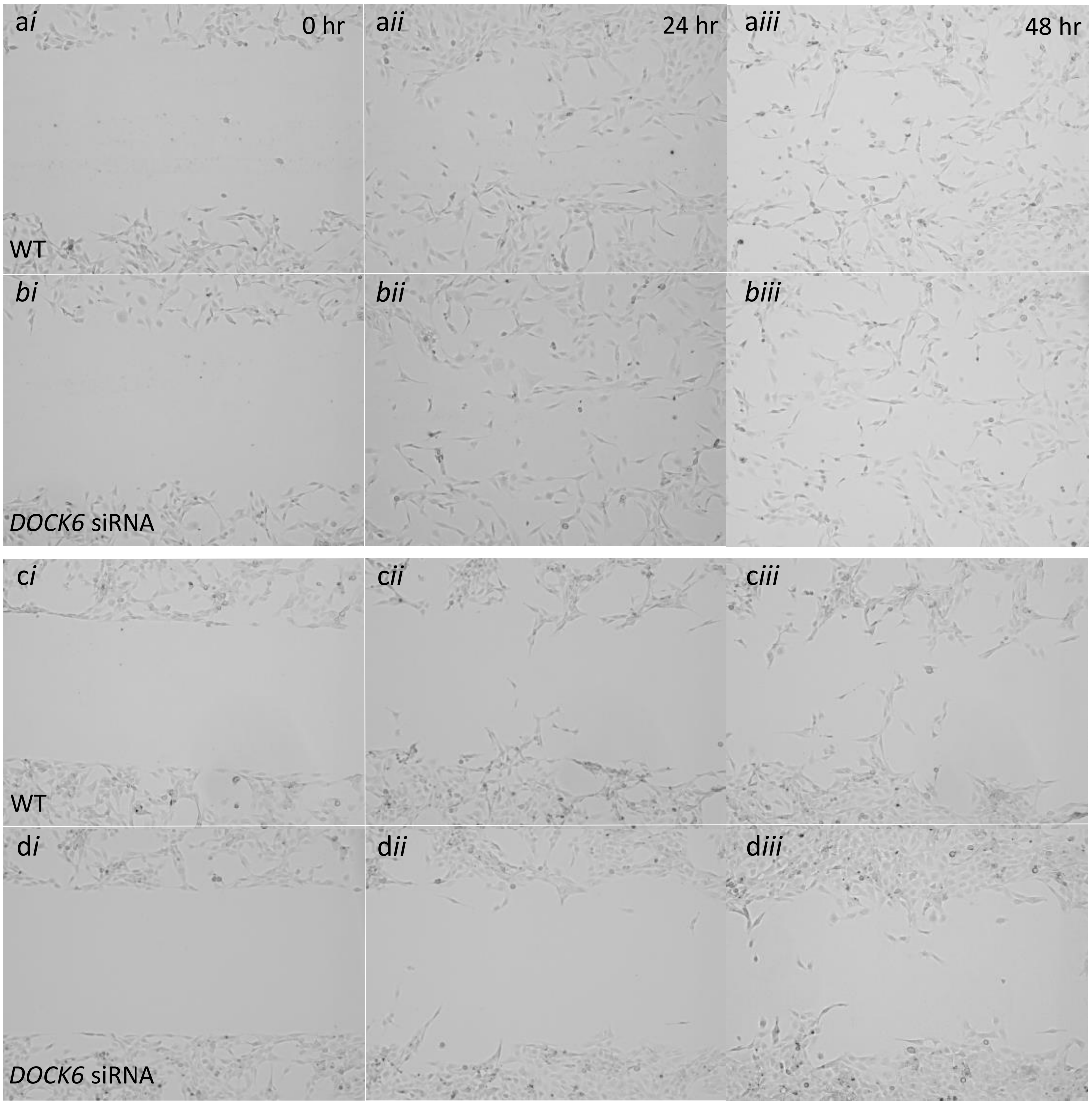

Figure 61: *DOCK6* depletion did not impact VSMC migration.

Migration was assessed in (**a, c**) wild-type and (**b, d**) *DOCK6*-depleted VSMCs by wound-healing (**a, b**) and Ibidi chamber (**c, d**) assays over 48 hours. N = 2 biological replicates, representative images are displayed.

indistinguishable in both wound-healing and Ibidi chamber assays at each timepoint (Figure 61).

By contrast in HaCaT cells, wild-type cells appear to begin closing the cell-free gap more effectively than *DOCK6* knockdown cells by 24 hours (Figure 62a*ii*-d*ii*). This phenotype appeared consistent in both wound-healing and Ibidi chamber assays. However, by 48 hours, the negative effect of *DOCK6* depletion on cell migration appeared to recover by comparison to the wild-type and the two conditions appear

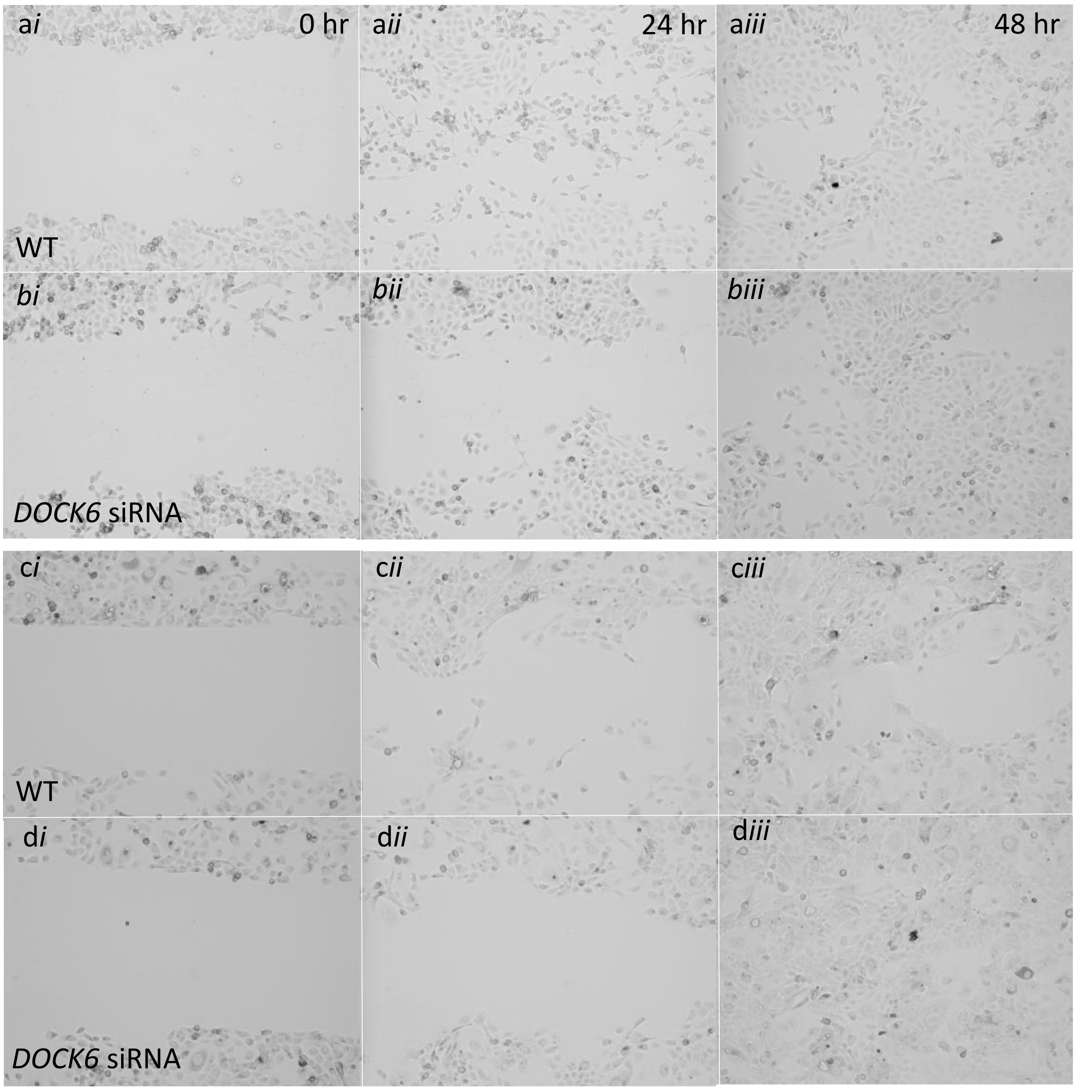

Figure 62: Assessing HaCaT migration upon *DOCK6* knockdown.

(**a, b**) Wound-healing and (**c, d**) Ibidi chamber assays examining the migration patterns of (**a, c**) wild-type and (**b, d**) *DOCK6*-depleted HaCaT cells. N = 2 biological replicates, representative images are displayed.

indistinguishable (Figure 62a*iii*-d*iii*). Taken together, these results indicate that *DOCK6* knockdown does not have any lasting impact on cell migration in these cell types.

6.7 Discussion

Following the identification of vascular disruption in Rho dysregulation zebrafish models (see Sections 5.4 and 5.5), *DOCK6* depletion was examined in VSMCs and HaCaT cell lines. These experiments aimed to elucidate the cellular mechanisms underlying impaired vascularisation by investigating the impact of *DOCK6* knockdown on actin cytoskeleton organisation, cell adhesion, cell proliferation and cell migration. This work was solely focussed on DOCK6 dysregulation as numerous studies have begun to characterise the cellular functions of ARHGAP31, however the role of DOCK6 in AOS pathogenesis remains poorly understood (Caron et al., 2016; Ishii, 2015; McCormack et al., 2017; Norden et al., 2016; Wormer et al., 2014).

6.7.1 *DOCK6* depletion disrupts actin cytoskeleton organisation

Transient knockdown of *DOCK6* induced a rounded phenotype in a significant proportion of VSMC and HaCaT cells, consistent with the phenotype observed under Cdc42 suppression, where filopodia formation is disrupted (Barry et al., 2015; Fantin et al., 2015). Similarly, previous studies have identified cell rounding in fibroblasts derived from AOS patients with pathogenic variants in either *ARHGAP31* or *DOCK6* and in HeLa cells transfected with mutagenised *DOCK6* plasmids (Cerikan et al., 2016; Ouadda et al., 2018; Shaheen et al., 2011; Southgate et al., 2011). My results provide an independent validation of these reports and indicate that this phenomenon may occur in multiple cell types relevant to AOS. It is likely that the reduction of *DOCK6* leads to a reduction in the availability of active Cdc42 and Rac1, which normally facilitate filopodia and lamellipodia formation, respectively (Allen et al., 1997; Miyamoto et al., 2007). Therefore, the cell rounding observed in both VSMCs and HaCaTs is likely to be caused by destabilisation of the actin cytoskeleton, resulting in disrupted lamellipodia network and impaired filopodial protrusion.

6.7.2 Reduced DOCK6 expression impairs cell attachment

Upon *DOCK6* depletion in both VSMCs and HaCaT cells, impaired attachment of the cells to the plate surface was observed, indicating that *DOCK6* expression is likely required in these cell types to facilitate Rac1- and/or Cdc42-mediated cell adhesion. This is supported by the observed association between reduced *DOCK6* expression and evidence of compromised filopodia and lamellipodia, both crucial structures in cell adhesion.

Correspondingly, numerous DOCK proteins have been implicated in facilitating cell attachment. Overexpression of the Rac1-specific active DOCK1 complex showed impaired detachment of 293F cells from a collagen coated surface, due to elongated cellular protrusions presumably induced by increased DOCK1 and therefore elevated Rac1 activity (Tachibana et al., 2009). Accordingly, Rac1-deficient cells typically display defective adhesion and cell spreading due to actin cytoskeleton disorganisation, coupled with reduced cell adhesion and decreased apoptosis (Duquette and Vane, 2014). While my experiments did not investigate the impact of *DOCK6* knockdown on apoptosis, future experiments using terminal deoxynucleotidyl transferase dUTP nick end labelling (TUNEL) staining may identify whether reducing *DOCK6* expression may affect cell death *in vitro* or *in vivo*. A hypothesised cause for TTLDs in AOS is failure of programmed interdigital apoptosis, therefore these experiments may also outline a potential mechanism for Rho dysregulation in the development of limb defects.

To investigate the specificity of DOCK6-mediated cell adhesion, adhesion assays using plates coated with different ECM proteins could be used. This may determine if *DOCK6* knockdown induces compromised adhesion to particular ECM proteins. Therefore, this technique could facilitate a tissue-specific analysis of the organs likely to be affected by reduced cell adhesion upon *DOCK6* knockdown. These findings could then be compared with areas commonly affected in *DOCK6*-related AOS patients, such as the vasculature, brain and eye (Alzahem et al., 2020; Lehman et al., 2014; Sukalo et al., 2015).

6.7.3 DOCK6 depletion compromises actin nucleation and polymerisation

The observation of increased actin foci in both VSMC and HaCaT cells upon reduced *DOCK6* expression corresponds with a defective cell spreading phenotype (Cheng and Mullins, 2020; Di Cio et al., 2020; Grabham et al., 2003). Of interest, ECM nanotopography sensing has identified a role for disrupted cytoskeleton and local collapse of the actin network in the formation of actin foci (Di Cio et al., 2020). Additionally, this technology captured cell retraction upon actin foci formation, providing a potential explanation for the rounded cell phenotype observed upon *DOCK6* knockdown. Activation of Rac1 and Cdc42 impacts their respective downstream effectors including the Arp2/3 complex and the WASP/WAVE family of proteins, which are essential in actin nucleation and polymerisation (Ma et al., 1998; Pollitt and Insall, 2009). Therefore, it is possible that reduced DOCK6 expression also affects the activity of Rac1 and Cdc42 effector proteins. This implies that *DOCK6* knockdown compromises actin nucleation by these effector proteins, which leads to the formation of actin foci and reduced actin polymerisation and filament formation, as observed in both VSMC and HaCaT cells. Interestingly, actin staining of *DOCK6*-related AOS patient fibroblasts also demonstrated the increased formation of actin foci, however this was not noted in the study (Shaheen et al., 2011). My findings suggest a mechanism the formation of actin foci upon *DOCK6* knockdown and for this and demonstrate a conserved role for *DOCK6* in correct actin filament formation across different cell types. This is important due to the variability of tissue types known to display abnormalities in *DOCK6*-related AOS.

Thus far the cellular localisation of DOCK6 has not been examined, therefore it would be useful to determine if wild-type DOCK6 co-localises to the lamellipodia and filopodia. Additionally, while DOCK6 is known to regulate both Rac1 and Cdc42, one study found that DOCK6-induced phenotypes in HeLa cells were mediated by reduced Rac1, critical for lamellipodia formation only (Cerikan et al., 2016). HeLa cells are an immortalised cervical carcinoma cell line and may not be as relevant to AOS pathogenesis. Therefore, it would be more pertinent to determine whether the compromised filopodia and lamellipodia formation observed upon *DOCK6* knockdown are solely Rac1-dependent, or if the GEF specificity of DOCK6 is cell type-dependent. This could be achieved using GTPase-specific G-LISA assays to independently measure the activity of Rac1 and Cdc42 following *DOCK6* knockdown. A targeted Cdc42 activation assay has previously been used successfully to identify a gain-of-function phenotype in HEK293 cells transiently transfected with mutant *ARHGAP31* constructs (Southgate et al., 2011).

6.7.4 Genetic compensation under *DOCK6* knockdown may be cell type-dependent

Due to the known role for genetic compensation upon *DOCK6* depletion, whereby chronic knockdown induced a cell rounding phenotype that recovered by 48 hours, VSMCs and HaCaTs were assessed 24 and 72 hours post-transfection (Cerikan et al., 2016). In VSMCs, the actin foci and reduced actin filament phenotypes appear to largely recover by 72 hours. However this was not seen in HaCaT cells, which appeared more affected by *DOCK6* depletion over time. This implies that the efficacy of genetic compensation may be cell type-dependent (Cerikan et al., 2016).

Genetic compensation under *DOCK6* knockdown is known to be driven largely by reduced RhoA activity and interferon-stimulated (ISG15) gene downregulation as an adaptive mechanism to restore active Rac1 and Cdc42 levels (Cerikan et al., 2016). Human *ISG15* deficiency presents as a type I interferonopathy inducing susceptibility to mycobacterial disease and autoinflammation, in addition to ulcerating skin lesions (Bogunovic et al., 2012). ISG15 was found to have an essential function in modulating reactive oxygen species (ROS) levels and upregulating cell adhesion molecules in both fibroblasts and HaCaT cells (Malik et al., 2022). However, ROS responses between cell types were inconsistent and increased ROS levels induced by ISG15 downregulation could not be recovered in HaCaT cells (Malik et al., 2022). This led to speculation that responses to increased ROS levels upon ISG15 downregulation were cell type-dependent, however this has not yet been examined following *DOCK6* knockdown.

To further examine the distinct phenotypic patterns and contrasting recovery times observed between cell types in this study, ISG15 levels could be examined in wild-type and *DOCK6* knockdown VSMCs and HaCaTs. Additional experiments to examine

ROS levels by flow cytometry in different cell types following *DOCK6* depletion may determine a potential mechanism for cell type-dependent phenotypic recovery. ROS inhibitors may be used to identify whether increased ROS levels have an impact on *DOCK6*-mediated phenotypes.

6.7.5 Reduced DOCK6 expression impacts HaCaT migration

In both VSMCs and HaCaT cells, migration was monitored over 48 hours. While no difference was observed between wild-type and *DOCK6*-depleted VSMCs, HaCaT cell migration initially decreased upon *DOCK6* knockdown. However, this phenotype appeared to recover by 48 hours. Given that the siRNA treatment has been confirmed to persist for ≥72 hours, this recovery phenotype further supports a likely role for genetic compensation upon *DOCK6* depletion. In addition to genetic compensation by ISG15 and RhoA as described in Section 6.7.4, other members of the DOCK family are potential candidates for offsetting the impact of DOCK6 knockdown, owing to redundancy in the small GTPases that are targeted (Benson and Southgate, 2021).

Two previous studies that measured the impact of *DOCK6* knockdown on migration both observed a decrease in migration in both cell types (Kim et al., 2015; Zhang et al., 2021). These experiments were carried out in pulmonary artery smooth muscle cells and oral squamous carcinoma cells. While this was emulated in HaCaT experiments, my VSMC data do not support this. As migration of wild-type and *DOCK6*-depleted VSMCs were indistinguishable in both wound-healing and Ibidi chamber assays, it is possible that contrasting results between cell lines may be due to cell type-dependent functions for *DOCK6*. Alternatively, the migration assays used may have generated alternative phenotypes that were not triggered by *DOCK6* knockdown. For example, the scraping process to generate a cell-free gap in wound-healing assays can cause cell injury to different extents between experiments, therefore misleading results (Riahi et al., 2012). In the Ibidi chamber assays, cell density was reduced by comparison to the wound-healing assay as a higher cell density resulted in cell death. The lower cell density may have impacted the ability of the cells to create a monolayer, which may explain why VSMCs in the Ibidi assays did not close the cell-free gap within 48 hours. Other aspects of cell migration may also be examined, for example cell directionality could be measured using Phasefocus Livecyte technology. Impaired cell directionality has previously been observed in fibroblasts derived from *ARHGAP31*-positive AOS patients (L Southgate 2018, personal communication).

My experiments showed no impact of *DOCK6* knockdown on cell proliferation in either HaCaT cells or VSMCs. This is in contrast to the existing literature which identified reduced cell proliferation in cancer stem cells upon *DOCK6* depletion (Chi et al., 2020). Although it is possible that the role for DOCK6 in cell proliferation is cell type-dependent, these differing outcomes may represent subtle differences between immortalised versus stem or primary cell cultures.

6.7.6 Potential impact of DOCK6 knockdown in a vascular context

As this work investigated the potential consequences of *DOCK6* knockdown in VSMCs in the context of AOS, it is important to consider how vascular development may be impacted by the observed phenotypes. Disrupted cell adhesion due to actin cytoskeleton disorganisation was the most prominent finding upon reduced *DOCK6* expression. In the developing vasculature, interactions between endothelial cells and mural cells are crucial to promote blood vessel stability (Rajan et al., 2020; Stratman et al., 2017). For example, while endothelial cells can produce basement membrane proteins, mural cells are required in building and maintaining the endothelial cell-associated basement membrane (Payne et al., 2019; Stratman et al., 2017). The basement membrane serves to support the vessels, as well as aiding in angiogenesis by promoting the enzymatic degradation of surrounding tissue to allow the migration of endothelial tip cells to form a new vessel (Stratman et al., 2017). Therefore, impaired interactions between VSMCs and endothelial cells caused by DOCK6 loss-of-function may impede complete vascularisation.

Additionally, the DOCK6 effector Rac1 has been implicated in the trafficking of N-cadherin to adherens junctions, necessary to stabilise endothelial-mural cell adhesion. Indeed, Rac1 deletion in the mouse lead to vascular integrity defects *in vivo* and a lack of vessel perfusion (Tan et al., 2008). This may suggest that the vascular impairments observed in the *dock6* zebrafish models could be caused by reduced levels of active Rac1.

Interestingly, ARHGAP31 is known to negatively regulate VE-cadherin in the epithelia (McCormack et al., 2017). VE-cadherin promotes adhesion between endothelial cells and other cell types, therefore ARHGAP31 gain-of-function mutations in AOS may compromise the function of VE-cadherin in vascular cell adhesion (Vestweber, 2008). Indeed, downregulation of VE-cadherin in the zebrafish causes vascular fragility, impaired perfusion, haemorrhaging and prevents vessels from establishing contacts (Montero-Balaguer et al., 2009). As DOCK6 is known to have antagonistic functions by comparison to ARHGAP31, it is possible that DOCK6 may play a role in regulating

VE-cadherin. Therefore, *DOCK6* knockdown-mediated cell adhesion defects in VSMCs may impact blood vessel stability and their ability to undergo angiogenic sprouting, as well as impaired perfusion. This directly corresponds with the impaired vascularisation phenotype seen in *dock6* knockdown zebrafish models and provides a potential mechanism underlying vascular defects upon Rho dysregulation in AOS.

6.7.7 Conclusions

Reducing *DOCK6* expression in VSMCs and HaCaT cell models mediated collapsed actin cytoskeletal organisation, as evidenced by reduced filopodia and lamellipodia formation. The formation of excess actin foci under *DOCK6* knockdown suggests that decreased actin polymerisation underpinned the abnormal development of lamellipodia and filopodia. While cell proliferation appeared unaffected, *DOCK6*-depleted cells displayed poor cell adhesion, consistent with phenotypes seen in other studies investigating DOCK protein function and with reports associating actin disassembly with disrupted cell focal contacts (Cerikan et al., 2016; Shaheen et al., 2011). Impaired cell adhesion in vascular structures upon *DOCK6* knockdown may provide a mechanism underlying defective vascular development in AOS patients. Additionally, these experiments highlighted the potential importance of differing cell types on genetic compensation following *DOCK6* knockdown. Further work is now required to identify the key proteins mediating this response and how this might modify phenotypic expression in AOS.

Chapter 7: General discussion and future directions

7.1 Introduction

Adams-Oliver syndrome is a rare developmental genetic disorder which is typically characterised by ACC, TTLD and vascular anomalies. While AOS is known to be caused by mutations in genes related to the Rho and Notch pathways, the cellular mechanisms underlying AOS pathology are poorly understood. I hypothesise that mutations in the Rho-related genes *ARHGAP31* and *DOCK6* lead to disrupted cytoskeletal organisation in AOS, precipitated by proliferation, migration or adhesion of vascular-derived cells. Consequently, the development of early embryonic blood vessels is impaired, impeding blood flow to the developing limb, scalp and cardiac structures. To investigate this hypothesis, I sought to model the impact of Rho dysregulation on early vascularisation during zebrafish embryogenesis and use human vascular and keratinocyte cell lines to examine the underlying cell functions contributing to AOS pathogenesis.

7.2 Embryonic expression of *arhgap31* and *dock6* correlates with vascular and neural crest development

To determine the roles of *arhgap31* and *dock6* in early vascularisation as a zebrafish model of AOS, a combination of qPCR, WISH and a novel *dock6* transgenic reporter line were initially used to assess the expression levels and patterns of *arhgap31* and *dock6* from 14 hpf to 5 dpf. Aside from one paper investigating *arhgap31* localisation at 24 hpf (Gomez et al., 2012), these data were previously unexplored.

Expression analyses observed *arhgap31* and *dock6* expression throughout early zebrafish embryogenesis and identified an overlapping tissue distribution, indicating a potential common regulatory mechanism modulating Rac1 and Cdc42 activity.

Localisation of *arhgap31* closely corresponded with early developing vascular structures, particularly migrating angioblasts at 16 hpf. This correlates with the estimated developmental point of vascular disruption in AOS (Swartz et al., 1999). In addition to the vascular distribution of gene expression, *arhgap31* showed localisation to the neural crest at 72 hpf, suggesting a potential role for *arhgap31* in the development of structures derived from the neural crest. Both WISH and transgenic experiments showed *dock6* localisation to the heart, vasculature, cranium and neural crest-derived structures. These findings loosely correlate with early *arhgap31* expression and are consistent with the characteristics of *DOCK6*-related AOS, including ocular and neurological pathologies, microcephaly and CHDs (Hassed et al., 2017). Of note, high *dock6* expression at 14 hpf corresponds with the onset of NCC migration. At this timepoint, *dock6* expression appeared localised to the neural tube, which is the origin of migrating NCCs.

Neural crest-derived structures include the anterior of the skull, correlating closely with the origin of ACC, and development of the digits, which are typically affected by TTLD in AOS patients. Additionally, NCCs give rise to the myocardium and aspects of the peripheral nervous system. These structures are known to be impacted in *DOCK6*-related AOS, supporting an argument for a potential neural crest-associated origin of AOS pathogenicity.

7.3 Reduced *arhgap31* and *dock6* expression promotes neural crest-associated defects

Having confirmed *arhgap31* and *dock6* expression during zebrafish development, I next generated and validated novel knockdown zebrafish models for both genes using morpholino technology and an additional CRISPR/Cas9-based method to independently verify *dock6* knockdown findings.

Knockdown of *arhgap31* promoted a relatively mild phenotype which is consistent with defective patterning. The blood accumulation and pericardial oedema observed mimic the characteristics of zebrafish embryos mutated for genes such as *tsg1* which establish the dorsal-ventral axis of the neural plate (Little and Mullins, 2004). Additionally, *arhgap31* knockdown led to impaired enlargement of the brain ventricles, likely due to increased Notch signalling. Similarly, reduced *dock6* expression induced impaired ventricle patterning as the forebrain ventricle and opening of the MHB appeared lost. The ventricles are an expansion of the neural tube which develops in concert with the neural crest, implicating Rho dysregulation in the disruption of neural crest or neural tube development and midline establishment (Lowery and Sive, 2005).

Further, *dock6* knockdown models displayed several phenotypes consistent with neural crest defects including aberrant cranial pigmentation and microphthalmia, which are directly associated with impaired NCC migration (Lister et al., 1999; Sedykh et al., 2017). Whilst pigment patterning defects have not been described in patients with AOS, biallelic *DOCK6* mutations are known to be strongly associated with ophthalmological defects, including microphthalmia (Sukalo et al., 2015). Additionally, defective heart looping and a curly-tailed phenotype were noted upon *dock6* depletion. These phenotypes are associated with impaired midline formation, in which the neural crest and neural tube play a critical role in establishing through signalling pathways including Hedgehog, FGF and BMP (Brand et al., 1996; Chen et al., 1997; Kalcheim, 2015; Lavine et al., 2006). Together, the phenotypes initiated under Rho dysregulation imply a critical role for *arhgap31* and *dock6* activity in early embryonic patterning, with a potential origin in the neural crest.

7.4 Reduced *arhgap31* and *dock6* expression impairs early vascularisation

Following the characterisation of the general morphology in my *arhgap31* and *dock6* knockdown models, I next sought to investigate the impact of reduced *arhgap31* and *dock6* expression on vasculo- and angiogenesis. This was carried out using a combination of vascular markers in WISH experiments, microangiography and a vascular transgenic reporter line.

Abnormal vessel patterning and defective intersegmental vessel sprouting were observed at 24 hpf in both *arhgap31* and *dock6* knockdown models, although it remains unclear if this was due to incorrect arterial and venous specification. Under *arhgap31* knockdown, the increased Notch signalling observed by qPCR may have suppressed the tip cell phenotype and subsequent impaired sprouting angiogenesis. A mechanism for *dock6* in intersegmental vessel sprouting was not identified in this work and therefore requires further investigation to determine the specific pathways involved.

By 72 hpf, the presence of truncated vessels in both *arhgap31* and *dock6* knockdown models indicated a failure of tip cells to migrate properly. An asymmetric vessel phenotype indicated impaired midline patterning, in accordance with previously described phenotypes (see Section 7.3). Additionally, Rho dysregulation precipitated an reduced blood flow phenotype, which can impact mural cell recruitment, vessel stabilisation and pruning (Bahrami and Childs, 2020; Chen et al., 2012; Kaufman et al., 2015). Notably, poor blood flow has been noted as an effect of defective lumen formation (Okuda and Hogan, 2020). Accordingly, I identified a significant decrease in the width of vessel lumens and embryos also displayed vessel leakage following *arhgap31* and *dock6* knockdown. Both compromised lumenisation and weakened vessel integrity point towards reduced cellular adhesion caused by loss of cell-cell contacts, likely due to impaired organisation of the actin cytoskeleton (Montero-Balaguer et al., 2009). The observed vascular phenotypes concur with reported vascular abnormalities in patients with AOS, namely vessel fragility leading to microbleeds and ischaemia caused by disrupted blood flow (Alsulaiman et al., 2020; Bilginer et al., 2008; Lehman et al., 2014; Meyer et al., 2020; Papadopoulou et al., 2008; Piazza et al., 2004).

7.5 Depletion of *DOCK6* impairs cell adhesion

Having identified impaired vascularisation as an outcome of *arhgap31* or *dock6* depletion in the zebrafish, I next aimed to elucidate the potential cellular mechanisms underlying poor vascular development upon Rho dysregulation. Therefore, *DOCK6* knockdown models were generated in VSMC and HaCaT cell lines and actin cytoskeletal organisation, cell adhesion, migration and proliferation were examined. Visualisation of the actin cytoskeleton identified a significantly increased number of actin foci upon *DOCK6* depletion, which was associated with impaired lamellipodial and filopodial formation in both VSMCs and HaCaT cells. The increase in actin foci implies compromised actin nucleation and therefore reduced actin polymerisation, likely due to decreased Rac1 and Cdc42 activity however this is yet to be confirmed (Di Cio et al., 2020).

These observations of cytoskeletal disruption upon *DOCK6* depletion indicated a potential downstream effect on filopodia- and lamellipodia-dependent cellular functions, implicating a disruption of cell adhesion, migration or proliferation. While migration and proliferation assays identified no significant difference between wild-type and *DOCK6*-depleted cells, *DOCK6* knockdown induced a significant increase in the proportion of rounded cells and viable detached VSMCs and HaCaT cells. These findings correspond with previous observations following loss of Rac1, which leads to defective adhesion and cell spreading due to actin cytoskeleton disorganisation (Hajdo-Milašinović et al., 2007; Katoh and Negishi, 2003; Zoughlami et al., 2013).

In the context of embryonic vascularisation, it is likely that cell adhesion defects in VSMCs will impact blood vessel stability, perfusion and angiogenic sprouting through decreased adhesion and interaction with endothelial cells. By combining results from the zebrafish and cell model data, these finding support a mechanism of impaired VSMC adhesion may promoting vascular disruption in AOS.

The slightly contrasting phenotypes observed in HaCaT cells and VSMCs provide the first indication that the impact of depleted *DOCK6* expression may be cell type-dependent. In particular, the compensation mechanisms that have been identified in previous studies may be driven by cell type-specific adaptation to reduced *DOCK6* expression (Cerikan et al., 2016; Malik et al., 2022). This is important as it may reveal insight behind the varying severity of phenotypes seen across AOS patients.

These data suggest a hypothesis for impaired cell adhesion impeding neural crest development and function, leading to a secondary effect of disrupted vascularisation in Adams-Oliver syndrome. These are novel findings which advance our understanding of the poorly elucidated cellular mechanisms underpinning Adams-Oliver syndrome.

7.6 Future work

This work identified novel findings of impaired vascularisation likely due to defective cell adhesion and a potential new role for neural crest development in AOS. To examine this further, additional experiments are now required to elucidate the finer molecular intricacies underpinning the role for Rho dysregulation in neural crest and vascular development. Importantly, by defining the regulatory pathways and molecular mechanisms that contribute to the characteristics of AOS, we will gain a deeper understanding of potential avenues for novel drug development and improved clinical management of this disorder.

7.6.1 The impact of Rho dysregulation on the neural crest

In humans, AOS is caused by either DOCK6 loss-of-function or ARHGAP31 gain-of-function. Therefore, stable zebrafish models demonstrating either *dock6* knockout or *arhgap31* overexpression could be developed to replicate the molecular mechanisms of AOS. Ideally, zebrafish mutant lines containing knock-in variants of conserved AOS-causing mutations would provide the most appropriate models to recapitulate disease. Cell fate mapping of the neural crest, combined with transgenic reporter lines for *arhgap31* and *dock6*, may delineate associations between *arhgap31* and *dock6* expression and neural crest-derived structures. To further investigate the roles of these genes in the neural crest, a transgenic NCC reporter line, such as *sox10*, may be used to assess the impact of altered *arhgap31* and *dock6* expression on NCC migration, adhesion and development into NCC-derived structures. Correlating these results against reported clinical features in AOS may determine the likelihood for an origin of neural crest defects in AOS pathogenesis.

To examine the development of structures derived from the neural crest under Rho dysregulation, Alcian Blue and Alizarin Red experiments could be used to stain the developing cartilage and skeleton, respectively. This may identify if there is a downstream impact on neural crest-derived structures upon aberrant *arhgap31* and *dock6* expression and, through a specific analysis of cranial anatomy including the scalp vertex, may be directly related to the ACC phenotype observed in AOS patients.

7.6.2 Identifying the mechanisms behind disrupted vascularisation in zebrafish development

To comprehensively examine the vascular abnormalities identified in Rho dysregulation models, transgenic reporter lines marking endothelial cell, VSMC and pericyte development should be used in conjunction with *arhgap31* and *dock6* disease models. These embryos would then be monitored over early development using lightsheet microscopy. This may determine whether migration, proliferation and adhesion of these cell types are impacted by Rho dysregulation and at what timepoint any divergence from the wild-type occurs.

Having identified impaired intersegmental vessel sprouting in both *arhgap31* and *dock6* knockdown models, a *kdrl* reporter line could be used to examine endothelial tip cell specification in early angiogenesis. This will likely elucidate whether disrupted vessel sprouting is caused by aberrant tip and stalk cell specification and may reveal whether dysregulated *arhgap31* and *dock6* expression impact filopodia formation on migrating tip cells. Additionally, experiments investigating the arterial-venous specification of endothelial cells at this timepoint will determine if *arhgap31* or *dock6* play a role in early endothelial vessel patterning.

7.6.3 Investigating novel links between the Rho and Notch pathway

To interrogate my findings of altered *notch1a* expression pattern in the zebrafish brain ventricle following *arhgap31* and *dock6* knockdown, several avenues can be explored. Injections of a dye into the ventricles will quickly reveal whether the brain ventricle shape itself has been altered by *arhgap31* or *dock6* disruption, rather than any change to *notch1a* localisation. WISH experiments to visualise *engrailed-2* will demarcate the MHB and identify if there have been any structural changes to this boundary upon reduced *arhgap31* or *dock6* expression, perhaps lending an explanation for the altered ventricle shape in *dock6* knockdown. Repeating the experiment at later stages of development will determine if the impact of depleted *arhgap31* or *dock6* expression on Notch expression patterns and levels can be restored, perhaps by compensatory mechanisms or through recovery of Rho-mediated developmental delay over time.

To further probe the interactions between the Rho and Notch signalling pathways, a *notch1a* qPCR of Rho knockdown brain tissue would determine expression level changes in the brain caused by loss of *arhgap31* or *dock6*, which may indicate a regulatory mechanism between the two pathways. Similarly, investigating the expression levels of Notch pathway effector genes *hey1* and *hes1* in these models will ascertain if the Rho pathway is able to impact Notch activity. Additional experiments to investigate the impact of Rho dysregulation on other AOS-related Notch pathway genes, such as *dll4*, *rbpj* and *eogt*, would further elucidate any putative links between the Rho and Notch pathways in AOS pathogenesis, shedding light on a potential shared aetiology across the different sub-types of disease.

7.6.4 Further investigation of the cellular mechanisms underlying AOS characteristics

The experiments in this study provide preliminary evidence for a mechanism of impaired cell adhesion in AOS. To investigate this further, a stable *DOCK6* knockout model should be generated and an overexpression or knock-in model of *ARHGAP31* optimised. These may be developed via stable transfection or using CRISPR-Cas9 technology, which has proven reliable in zebrafish. Relevant primary cell lines such as cardiomyocytes, endothelial cells, human aortic smooth muscle cell, chondrocytes and keratinocytes should be investigated to assess the impact of Rho dysregulation in cell types associated with AOS characteristics. Of interest, these cell types have also been reported to be derived from the neural crest (Le Douarin and Dupin, 2003). Repeating the angiogenic assays optimised in this study in these primary cell types may provide insight into how DOCK6 loss-of-function and ARHGAP31 gain-of-function impact other cell types relevant to this disorder.

To further examine the role for DOCK6 in lamellipodia and filopodia formation, the GTP-bound forms of Rac1 and Cdc42 could be overexpressed to determine whether restoring Rho GTPase activity will rescue the disrupted cytoskeleton and cell detachment phenotype observed upon *DOCK6* knockdown. Additionally, experiments assessing endothelial tubule formation could be performed in an *ARHGAP31* overexpression and/or *DOCK6* knockout model. This will examine whether ARHGAP31 and DOCK6 have a role in initiating tube and lumen development, providing further insight into the cellular impact of Rho dysregulation upon endothelial tube formation.

As impaired cell adhesion has been identified as a key molecular mechanism contributing to *DOCK6*-related AOS pathogenesis, it will be imperative to investigate the impact of DOCK6 loss-of-function and ARHGAP31 gain-of-function on the formation of focal adhesions, cell-cell contacts, tight junctions and gap junctions. This could be achieved by staining key molecules in the formation of adherens junctions, such as N-cadherin and VE-cadherin to visualise points of cell adhesion (Hartsock and Nelson, 2008; Vestweber, 2008). These experiments would reveal whether Rho dysregulation compromises vessel integrity in the vasculature through poor cell-cell adhesion.

Taken together, this work provides novel evidence for the role of impaired cell adhesion in promoting vascular disruption in AOS and proffers a foundation for investigating the neural crest as a previously unexplored origin in AOS pathogenesis.

References

Abraham, S., Scarcia, M., Bagshaw, R.D., McMahon, K., Grant, G., Harvey, T., Yeo, M., Esteves, F.O.G., Thygesen, H.H., Jones, P.F., Speirs, V., Hanby, A.M., Selby, P.J., Lorger, M., Dear, T.N., Pawson, T., Marshall, C.J., Mavria, G., 2015. A Rac/Cdc42 exchange factor complex promotes formation of lateral filopodia and blood vessel lumen morphogenesis. Nat. Commun. 6.

Adams, F.H., Oliver, C.P., 1945. Hereditary deformities in man: due to arrested development. J. Hered. 36, 3–7.

Albert, S., Müller, F., Fischer, N., Biellmann, D., Neumann, C., Blader, P., Strähle, U., 2003. Cyclops-independent floor plate differentiation in zebrafish embryos. Dev. Dyn. 226, 59–66.

Allen, W.E., Jones, G.E., Pollard, J.W., Ridley, A.J., 1997. Rho, Rac and Cdc42 regulate actin organization and cell adhesion in macrophages. J. Cell Sci. 110, 707–720.

Alsulaiman, A.M., Alsulaiman, H.M., Almousa, A., Alsulaiman, S.M., 2020. Adams Oliver syndrome: A mimicker of familial exudative vitreoretinopathy. Am. J. Ophthalmol. Case Reports 19, 100715.

Alzahem, T., Alsalamah, A.K., Mura, M., Alsulaiman, S.M., 2020. A novel variant in DOCK6 gene associated with Adams–Oliver syndrome type 2. Ophthalmic Genet. 41, 377–380.

Anderson, M.J., Pham, V.N., Vogel, A.M., Weinstein, B.M., Roman, B.L., 2008. Loss of unc45a precipitates arteriovenous shunting in the aortic arches. Dev. Biol. 318, 258–267.

Antkiewicz, D.S., Burns, C.G., Carney, S.A., Peterson, R.E., Heideman, W., 2005. Heart malformation is an early response to TCDD in embryonic zebrafish. Toxicol. Sci. 84, 368–377.

Arcidiacono, P., Webb, C.M., Brooke, M.A., Zhou, H., Delaney, P.J., Ng, K.E., Blaydon, D.C., Tinker, A., Kelsell, D.P., Chikh, A., 2018. P63 is a key regulator of iRHOM2 signalling in the keratinocyte stress response. Nat. Commun. 9.

Bahrami, N., Childs, S.J., 2020. Development of vascular regulation in the zebrafish embryo. Dev. 147, 1–12.

Balls, M., Goldberg, A.M., Fentem, J.H., Broadhead, C.L., Burch, R.L., Festing, M.F.W., Frazier, J.M., Hendriksen, C.F.M., Jennings, M., Kamp, argot D.O. van der, Morton, D.B., Rowan, A.N., Russell, C., Russell, W.M.S., Spielmann, H., Stephens, M.L., Stokes, W.S., Straughan, D.W., Yager, J.D., Zurlo, J., Zutphen, B.F.M. van, 1995. The Three Rs: The Way Forward: The Report and Recommendations of ECVAM Workshop 11. Altern. to Lab. Anim. 6, 838–866.

Banote, R.K., Edling, M., Eliassen, F., Kettunen, P., Zetterberg, H., Abramsson, A., 2016. β-Amyloid precursor protein-b is essential for Mauthner cell development in the zebrafish in a Notch-dependent manner. Dev. Biol. 413, 26–38.

Barry, D.M., Xu, K., Meadows, S.M., Zheng, Y., Norden, P.R., Davis, G.E., Cleaver, O., 2015. Cdc42 is required for cytoskeletal support of endothelial cell adhesion during blood vessel formation in mice. Dev. 142, 3058–3070.

Bauer, H.C., Krizbai, I.A., Bauer, H., Traweger, A., 2014. “You shall not pass”-tight junctions of the blood brain barrier. Front. Neurosci. 8, 1–21.

Bayless, K.J., Davis, G.E., 2002. The Cdc42 and Rac1 GTPases are required for capillary lumen formation in three-dimensional extracellular matrices. J. Cell Sci. 115, 1123–1136.

Bear IV, J.E., 1998. SCAR defines a new family of WASP-related actin cytoskeleton regulators (Doctoral dissertation, Emory University).

Bedell, V.M., Westcot, S.E., Ekker, S.C., 2011. Lessons from morpholino-based screening in zebrafish. Brief. Funct. Genomics 10, 181–188.

Benson, C.E., Southgate, L., 2021. The DOCK protein family in vascular development and disease. Angiogenesis 24, 417–433.

Bilginer, B., Önal, M.B., Bahadir, S., Akalan, N., 2008. Aplasia cutis congenita of the scalp, skull and dura associated with Adams-Oliver Syndrome. Turk. Neurosurg. 18, 191–193.

Bisgrove, B.W., Yost, H.J., 2001. Classification of Left ± Right Patterning Defects in Zebrafish , Mice , and Humans. Am. J. Med. Genet. 315–323.

Blanco, R., Gerhardt, H., 2013. VEGF and Notch in tip and stalk cell selection. Cold Spring Harb. Perspect. Med. 3, 1–20.

Bogunovic, D., Byun, M., Durfee, L.A., Abhyankar, A., Sanal, O., Mansouri, D., Salem, S., Radovanovic, I., Grant, A. V., Adimi, P., Mansouri, N., Okada, S., Bryant, V.L., Kong, X.F., Kreins, A., Velez, M.M., Boisson, B., Khalilzadeh, S., Ozcelik, U., Darazam, I.A., Schoggins, J.W., Rice, C.M., Al-Muhsen, S., Behr, M., Vogt, G., Puel, A., Bustamante, J., Gros, P., Huibregtse, J.M., Abel, L., Boisson-Dupuis, S., Casanova, J.L., 2012. Mycobacterial disease and impaired IFN-γ immunity in humans with inherited ISG15 deficiency. Science (80-.). 337, 1684–1688.

Brancati, F., Garaci, F.G., Mingarelli, R., Dallapiccola, B., 2008. Abnormal neuronal migration defect in the severe variant subtype of Adams-Oliver syndrome. Am. J. Med. Genet. Part A 146, 1622–1623.

Brand, M., Heisenberg, C.P., Warga, R.M., Pelegri, F., Karlstrom, R.O., Beuchle, D., Picker, A., Jiang, Y.J., Furutani-Seiki, M., Van Eeden, F.J.M., Granato, M., Haffter, P., Hammerschmidt, M., Kane, D.A., Kelsh, R.N., Mullins, M.C., Odenthal, J., Nüsslein-Volhard, C., 1996. Mutations affecting development of the midline and general body shape during zebrafish embryogenesis. Development 123, 129–142.

Brown, L.A., Rodaway, A.R.F., Schilling, T.F., Jowett, T., Ingham, P.W., Patient, R.K., Sharrocks, A.D., 2000. Insights into early vasculogenesis revealed by expression of the ETS-domain transcription factor Fli-1 in wild-type and mutant zebrafish embryos. Mech. Dev. 90, 237–252.

Brugnera, E., Haney, L., Grimsley, C., Lu, M., Walk, S.F., Tosello-Trampont, A.C., Macara, I.G., Madhani, H., Fink, G.R., Ravichandran, K.S., 2002. Unconventional Rac-GEF activity is mediated through the Dock180-ELMO complex. Nat. Cell Biol. 4, 574–582.

Bryan, B.A., D'Amore, P.A., 2007. What tangled webs they weave: Rho-GTPase control of angiogenesis. Cell. Mol. Life Sci. 64, 2053–2065.

Bryan, B.A., Dennstedt, E., Mitchell, D.C., Walshe, T.E., Noma, K., Loureiro, R., Saint-Geniez, M., Campaigniac, J., Liao, J.K., Patricia, D.A., 2010. RhoA/ROCK signaling is essential for multiple aspects of VEGF-mediated angiogenesis. FASEB J. 24, 3186–3195.

Byrd, N., Grabel, L., 2004. Hedgehog signaling in murine vasculogenesis and angiogenesis. Trends Cardiovasc. Med. 14, 308–313.

Caron, C., Degeer, J., Fournier, P., Duquette, P.M., Luangrath, V., Ishii, H., Karimzadeh, F., Lamarche-Vane, N., Royal, I., 2016. CdGAP/ARHGAP31, a Cdc42/Rac1 GTPase regulator, is critical for vascular development and VEGF-mediated angiogenesis. Sci. Rep. 6, 1–10.

Cascone, I., Giraudo, E., Caccavari, F., Napione, L., Bertotti, E., Collard, J.G., Serini, G., Bussolino, F., 2003. Temporal and spatial modulation of Rho GTPases during in vitro formation of capillary vascular network: Adherens junctions and myosin light chain as targets of Rac1 and RhoA. J.

Biol. Chem. 278, 50702–50713.

Cau, J., Hall, A., 2005. Cdc42 controls the polarity of the actin and microtubule cytoskeletons through two distinct signal transduction pathways. J. Cell Sci. 118, 2579–2587.

Cerikan, B., Schiebel, E., 2019. Mechanism of cell-intrinsic adaptation to Adams-Oliver Syndrome gene DOCK6 disruption highlights ubiquitin-like modifier ISG15 as a regulator of RHO GTPases. Small GTPases 10, 210–217.

Cerikan, B., Shaheen, R., Colo, G.P., Gläßer, C., Hata, S., Knobeloch, K.P., Alkuraya, F.S., Fässler, R., Schiebel, E., 2016. Cell-Intrinsic Adaptation Arising from Chronic Ablation of a Key Rho GTPase Regulator. Dev. Cell 39, 28–43.

Chapouton, P., Skupien, P., Hesl, B., Coolen, M., Moore, J.C., Madelaine, R., Kremmer, E., Faus-Kessler, T., Blader, P., Lawson, N.D., Bally-Cuif, L., 2010. Notch activity levels control the balance between quiescence and recruitment of adult neural stem cells. J. Neurosci. 30, 7961–7974.

Charnock-Jones, D.S., Kaufmann, P., Mayhew, T.M., 2004. Aspects of human fetoplacental vasculogenesis and angiogenesis. I. Molecular regulation. Placenta 25, 103–113.

Chen, F., Ma, L., Parrini, M.C., Mao, X., Lopez, M., Wu, C., Marks, P.W., Davidson, L., Kwiatkowski, D.J., Kirchhausen, T., Orkin, S.H., Rosen, F.S., Mayer, B.J., Kirschner, M.W., Alt, F.W., 2000. Cdc42 is required for PIP2-induced actin polymerization end early development but not for cell viability. Curr. Biol. 10, 758–765.

Chen, J.N., Van Eeden, F.J.M., Warren, K.S., Chin, A., Nüsslein-Volhard, C., Haffter, P., Fishman, M.C., 1997. Left-right pattern of cardiac BMP4 may drive asymmetry of the heart in zebrafish. Development 124, 4373–4382.

Chen, P.C., Hsueh, Y.W., Lee, Y.H., Tsai, H.W., Tsai, K.J., Chiang, P.M., 2021. FGF primes angioblast formation by inducing ETV2 and LMO2 via FGFR1/BRAF/MEK/ERK. Cell. Mol. Life Sci. 78, 2199–2212.

Chen, Q., Jiang, L., Li, C., Hu, D., Bu, J. wen, Cai, D., Du, J. lin, 2012. Haemodynamics-Driven Developmental Pruning of Brain Vasculature in Zebrafish. PLoS Biol. 10, 1–16.

Chen, S., Lechleider, R.J., 2004. Transforming growth factor-β-induced differentiation of smooth muscle from a neural crest stem cell line. Circ. Res. 94, 1195–1202.

Chen, Y., Ju, L., Rushdi, M., Ge, C., Zhu, C., 2017. Receptor-mediated cell mechanosensing. Mol. Biol. Cell 28, 3134–3155.

Cheng, K.W., Mullins, R.D., 2020. Initiation and disassembly of filopodia tip complexes containing VASP and lamellipodin. Mol. Biol. Cell 31, 2021–2034.

Cherfils, J., Zeghouf, M., 2013. Regulation of small GTPases by GEFs, GAPs, and GDIs. Physiol. Rev. 93, 269–309.

Chi, H.-C., Tsai, C.-Y., Wang, C.-S., Yang, H.-Y., Lo, C.-H., Wang, W.-J., Lee, K.-F., Lai, L.-Y., Hong, J.-H., Chang, Y.-F., Tsai, M.-M., Yeh, C.-T., Wu, C.H., Hsieh, C.-C., Wang, L.-H., Chen, W.-J., Lin, K.-H., 2020. DOCK6 promotes chemo- and radioresistance of gastric cancer by modulating WNT/β-catenin signaling and cancer stem cell traits. Oncogene 29, 5933–5949.

Choi, S.Y., Baek, J.I., Zuo, X., Kim, S.H., Dunaief, J.L., Lipschutz, J.H., 2015. Cdc42 and sec10 are required for normal retinal development in Zebrafish. Investig. Ophthalmol. Vis. Sci. 56, 3361–3370.

Choi, S.Y., Chacon-Heszele, M.F., Huang, L., McKenna, S., Wilson, F.P., Zuo, X., Lipschutz, J.H., 2013. Cdc42 deficiency causes ciliary abnormalities and cystic kidneys. J. Am. Soc. Nephrol. 24, 1435–1450.

Chu, V.T., Weber, T., Wefers, B., Wurst, W., Sander, S., Rajewsky, K., Kühn, R., 2015. Increasing the efficiency of homology-directed repair for CRISPR-Cas9-induced precise gene editing in mammalian cells. Nat. Biotechnol. 33, 543–548.

Ciuffetelli Alamo, I. V., Kwartler, C.S., Regalado, E.R., Afifi, R.O., Parkash, S., Rideout, A., Guo, D. chuan, Milewicz, D.M., 2019. Grange syndrome due to homozygous YY1AP1 missense rare variants. Am. J. Med. Genet. Part A 179, 2500–2505.

ClinVar [WWW Document], 2022. URL https://www.ncbi.nlm.nih.gov/clinvar (accessed 5.9.22).

Cohen, I., Silberstein, E., Perez, Y., Landau, D., Elbedour, K., Langer, Y., Kadir, R., Volodarsky, M., Sivan, S., Narkis, G., Birk, O.S., 2014. Autosomal recessive Adams-Oliver syndrome caused by homozygous mutation in EOGT, encoding an EGF domain-specific O-GlcNAc transferase. Eur. J. Hum. Genet. 22, 374–378.

Coles, E.G., Lawlor, E.R., Bronner-Fraser, M., 2008. EWS-FLI1 Causes Neuroepithelial Defects and Abrogates Emigration of Neural Crest Stem Cells. Stem Cells 26, 2237–2244.

Côté, J.F., Vuori, K., 2002. Identification of an evolutionary conserved superfamily of DOCK180-related proteins with guanine nucleotide exchange activity. J. Cell Sci. 115, 4901–4913.

Coultas, L., Nieuwenhuis, E., Anderson, G.A., Cabezas, J., Nagy, A., Henkelman, R.M., Hui, C.C., Rossant, J., 2010. Hedgehog regulates distinct vascular patterning events through VEGF-dependent and -independent mechanisms. Blood 116, 653–660.

Cox, C.M., Poole, T.J., 2000. Angioblast differentiation is influenced by the local environment: FGF-2 induces angioblasts and patterns vessel formation in the quail embryo. Dev. Dyn. 218, 371–382.

Dadzie, O.E., Tyszczuk, L., Holder, S.E., Teixeira, F., Charakida, A., Scarisbrick, J., Chu, A., 2007. Adams-Oliver syndrome with widespread CMTC and fatal pulmonary vascular disease. Pediatr. Dermatol. 24, 651–653.

Dana, H., Chalbatani, G.M., Mahmoodzadeh, H., Karimloo, R., Rezaiean, O., Moradzadeh, A., Mehmandoost, N., Moazzen, F., Mazraeh, A., Marmari, V., Ebrahimi, M., Rashno, M.M., Abadi, S.J., Gharagouzlo, E., 2017. Molecular Mechanisms and Biological Functions of siRNA. Int. J. Biomed. Sci. 13, 48–57.

Danek, E.I., Tcherkezian, J., Triki, I., Meriane, M., Lamarche-Vane, N., 2007. Glycogen synthase kinase-3 phosphorylates CdGAP at a consensus ERK 1 regulatory site. J. Biol. Chem. 282, 3624–3631.

Davis, G.E., Bayless, K.J., Mavila, A., 2002. Molecular basis of endothelial cell morphogenesis in three-dimensional extracellular matrices. Anat. Rec. 268, 252–275.

Di Cio, S., Iskratsch, T., Connelly, J.T., Gautrot, J.E., 2020. Contractile myosin rings and cofilin-mediated actin disassembly orchestrate ECM nanotopography sensing. Biomaterials 232, 119683.

Doench, J., Sharp, P.A., Alema, L.M., 2007. Comparison of siRNA-induced off-target RNA and protein effects. Rna 385–395.

Drake, C.J., 2003. Embryonic and adult vasculogenesis. Birth Defects Res. Part C - Embryo Today Rev. 69, 73–82.

Dudoignon, B., Huber, C., Michot, C., Di Rocco, F., Girard, M., Lyonnet, S., Rio, M., Rabia, S.H., Daire, V.C., Baujat, G., 2020. Expanding the phenotype in Adams–Oliver syndrome correlating with the genotype. Am. J. Med. Genet. Part A 182, 29–37.

Duquette, P.M., Vane, N.L., 2014. Rho GTPases in embryonic development. Small GTPases 5.

Eisen, J.S., Smith, J.C., 2008. Controlling morpholino experiments: Don't stop making antisense. Development 135, 1735–1743.

Ellenbroek, S.I.J., Collard, J.G., 2007. Rho GTPases: Functions and association with cancer. Clin. Exp. Metastasis 24, 657–672.

Ellertsdóttir, E., Lenard, A., Blum, Y., Krudewig, A., Herwig, L., Affolter, M., Belting, H.G., 2010. Vascular morphogenesis in the zebrafish embryo. Dev. Biol. 341, 56–65.

Endris, V., Wogatzky, B., Leimer, U., Bartsch, D., Zatyka, M., Latif, F., Maher, E.R., Tariverdian, G., Kirsch, S., Karch, D., Rappold, G.A., 2002. The novel Rho-GTPase activating gene MEGAP/srGAP3 has a putative role in severe mental retardation. Proc. Natl. Acad. Sci. U. S. A. 99, 11754–11759.

Engelse, M.A., Laurens, N., Verloop, R.E., Koolwijk, P., Van Hinsbergh, V.W.M., 2008. Differential gene expression analysis of tubule forming and non-tubule forming endothelial cells: CDC42GAP as a counter-regulator in tubule formation. Angiogenesis 11, 153–167.

Epting, D., Slanchev, K., Boehlke, C., Hoff, S., Loges, N.T., Yasunaga, T., Indorf, L., Nestel, S., Lienkamp, S.S., Omran, H., Kuehn, E.W., Ronneberger, O., Walz, G., Kramer-zucker, A., Epting, D., Slanchev, K., Boehlke, C., Hoff, S., Loges, N.T., Yasunaga, T., Indorf, L., Nestel, S., Lienkamp, S.S., Omran, H., Kuehn, E.W., 2015. Erratum to: Rac1 regulator ELMO controls basal body migration and docking in multiciliated cells through interaction with Ezrin (Development, 142, (174-184)). Dev. 142, 1553.

Epting, D., Wendik, B., Bennewitz, K., Dietz, C.T., Driever, W., Kroll, J., 2010. The Rac1 regulator ELMO1 controls vascular morphogenesis in zebrafish. Circ. Res. 107, 45–55.

Fantin, A., Lampropoulou, A., Gestri, G., Raimondi, C., Senatore, V., Zachary, I., Ruhrberg, C., 2015. NRP1 Regulates CDC42 Activation to Promote Filopodia Formation in Endothelial Tip Cells. Cell Rep. 11, 1577–1590.

Fong, G.-H., Rossant, J., Gertsenstein, M., Breitman, M.L., 1995. Role of the Flt-1 receptor tyrosine kinase in regulating the assembly of vascular endothelium. Nature 376, 66–70.

Fuchs, S., Herzog, D., Sumara, G., Büchmann-Møller, S., Civenni, G., Wu, X., Chrostek-Grashoff, A., Suter, U., Ricci, R., Relvas, J.B., Brakebusch, C., Sommer, L., 2009. Stage-Specific Control of Neural Crest Stem Cell Proliferation by the Small Rho GTPases Cdc42 and Rac1. Cell Stem Cell 4, 236–247.

Furutani-Seiki, M., Jiang, Y.J., Brand, M., Heisenberg, C.P., Houart, C., Beuchle, D., Van Eeden, F.J.M., Granato, M., Haffter, P., Hammerschmidt, M., Kane, D.A., Kelsh, R.N., Mullins, M.C., Odenthal, J., Nüsslein-Volhard, C., 1996. Neural degeneration mutants in the zebrafish, Danio rerio. Development 123, 229–239.

Gaengel, K., Genové, G., Armulik, A., Betsholtz, C., 2009. Endothelial-mural cell signaling in vascular development and angiogenesis. Arterioscler. Thromb. Vasc. Biol. 29, 630–638.

Gerhardt, H., Golding, M., Fruttiger, M., Ruhrberg, C., Lundkvist, A., Abramsson, A., Jeltsch, M., Mitchell, C., Alitalo, K., Shima, D., Betsholtz, C., 2003. VEGF guides angiogenic sprouting utilizing endothelial tip cell filopodia. J. Cell Biol. 161, 1163–1177.

Gibbs, H.C., Chang-Gonzalez, A., Hwang, W., Yeh, A.T., Lekven, A.C., 2017. Midbrain-hindbrain boundary morphogenesis: At the intersection of wnt and Fgf signaling. Front. Neuroanat. 11, 1–17.

Girard, M., Amiel, J., Fabre, M., Pariente, D., Lyonnet, S., Jacquemin, E., 2005. Adams-Oliver syndrome and hepatoportal sclerosis: Occasional association or common mechanism? Am. J. Med. Genet. 135 A, 186–189.

Gomez, G., Lee, J.H., Veldman, M.B., Lu, J., Xiao, X., Lin, S., 2012. Identification of Vascular and Hematopoietic Genes Downstream of etsrp by Deep Sequencing in Zebrafish. PLoS One 7, 1–12.

Gonzalez-Nunez, V., 2015. Role of gabra2, GABAA receptor alpha-2 subunit, in CNS development. Biochem. Biophys. Reports 3, 190–201.

Gore, A. V., Monzo, K., Cha, Y.R., Pan, W., Weinstein, B.M., 2012. Vascular development in zebrafish. Cold Spring Harb Perspect Med. 2.

Grabham, P.W., Reznik, B., Goldberg, D.J., 2003. Microtubule and Rac 1-dependent F-actin in growth cones. J. Cell Sci. 116, 3739–3748.

Guang, S., Bochner, A.F., Pavelec, D.M., Burkhart, K.B., Harding, S., Lachowiec, J., Kennedy, S., 2009. An Argonaute Transports siRNAs from the Cytoplasm to the Nucleus. Science (80-.). 321.

Guo, D. chuan, Duan, X.Y., Regalado, E.S., Mellor-Crummey, L., Kwartler, C.S., Kim, D., Lieberman, K., de Vries, B.B.A., Pfundt, R., Schinzel, A., Kotzot, D., Shen, X., Yang, M.L., Bamshad, M.J., Nickerson, D.A., Gornik, H.L., Ganesh, S.K., Braverman, A.C., Grange, D.K., Milewicz, D.M., 2017. Loss-of-Function Mutations in YY1AP1 Lead to Grange Syndrome and a Fibromuscular Dysplasia-Like Vascular Disease. Am. J. Hum. Genet. 100, 21–30.

Gupta-Rossi, N., Six, E., LeBail, O., Logeat, F., Chastagner, P., Olry, A., Israël, A., Brou, C., 2004. Monoubiquitination and endocytosis direct γ-secretase cleavage of activated Notch receptor. J. Cell Biol. 166, 73–83.

Hajdo-Milašinović, A., Ellenbroek, S.I.J., van Es, S., van der Vaart, B., Collard, J.G., 2007. Rac1 and rac3 have opposing functions in cell adhesion and differentiation of neuronal cells. J. Cell Sci. 120, 555–566.

Harris, L.K., Keogh, R.J., Wareing, M., Baker, P.N., Cartwright, J.E., Aplin, J.D., Whitley, G.S.J., 2006. Invasive trophoblasts stimulate vascular smooth muscle cell apoptosis by a Fas ligand-dependent mechanism. Am. J. Pathol. 169, 1863–1874.

Hartsock, A., Nelson, W.J., 2008. Adherens and tight junctions: Structure, function and connections to the actin cytoskeleton. Biochim. Biophys. Acta - Biomembr. 1778, 660–669.

Hassed, S., Li, S., Mulvihill, J., Aston, C., Palmer, S., 2017. Adams–Oliver syndrome review of the literature: Refining the diagnostic phenotype. Am. J. Med. Genet. Part A 173, 790–800.

Hassed, S.J., Wiley, G.B., Wang, S., Lee, J.Y., Li, S., Xu, W., Zhao, Z.J., Mulvihill, J.J., Robertson, J., Warner, J., Gaffney, P.M., 2012. RBPJ mutations identified in two families affected by Adams-Oliver syndrome. Am. J. Hum. Genet. 91, 391–395.

Heasman, J., 2002. Morpholino oligos: Making sense of antisense? Dev. Biol. 243, 209–214.

Hellström, M., Phng, L.K., Hofmann, J.J., Wallgard, E., Coultas, L., Lindblom, P., Alva, J., Nilsson, A.K., Karlsson, L., Gaiano, N., Yoon, K., Rossant, J., Iruela-Arispe, M.L., Kalén, M., Gerhardt, H., Betsholtz, C., 2007. Dll4 signalling through Notch1 regulates formation of tip cells during angiogenesis. Nature 445, 776–780.

Hen, G., Nicenboim, J., Mayseless, O., Asaf, L., Shin, M., Busolin, G., Hofi, R., Almog, G., Tiso, N., Lawson, N.D., Yaniv, K., 2015. Venous-derived angioblasts generate organ-specific vessels during zebrafish embryonic development. Dev. 142, 4266–4278.

Hernández-García, R., Iruela-Arispe, M.L., Reyes-Cruz, G., Vázquez-Prado, J., 2015. Endothelial RhoGEFs: A systematic analysis of their expression profiles in VEGF-stimulated and tumor endothelial cells. Vascul. Pharmacol. 74, 60–72.

Hernández-Vásquez, M.N., Adame-García, S.R., Hamoud, N., Chidiac, R., Reyes-Cruz, G., Gratton, J.P., Côté, J.F. and Vázquez-Prado, J., 2017. Cell adhesion controlled by adhesion G protein–coupled receptor GPR124/ADGRA2 is mediated by a protein complex comprising intersectins and Elmo–Dock. Journal of Biological Chemistry, 292, 12178-12191.

Hill, A.J., Bello, S.M., Prasch, A.L., Peterson, R.E., Heideman, W., 2004. Water permeability and TCDD-induced edema in Zebrafish early-life stages. Toxicol. Sci. 78, 78–87.

Hong, C.C., Peterson, Q.P., Hong, J.Y., Peterson, R.T., 2006. Artery/Vein Specification Is Governed by Opposing Phosphatidylinositol-3 Kinase and MAP Kinase/ERK Signaling. Curr. Biol. 16, 1366–1372.

Hu, Y., Xie, S., Yao, J., 2016. Identification of novel reference genes suitable for qRT-PCR normalization with respect to the zebrafish developmental stage. PLoS One 11, 1–13.

Hung, I.C., Chen, T.M., Lin, J.P., Tai, Y.L., Shen, T.L., Lee, S.J., 2020. Erratum: Wnt5b integrates Fak1a to mediate gastrulation cell movements via Rac1 and Cdc42 (Open Biology (2020) 10 (190273) DOI: 10.1098/rsob.190273). Open Biol. 10.

Ibrahim, M., Richardson, M.K., 2017. In vitro development of zebrafish vascular networks. Reprod. Toxicol. 70, 102–115.

Imayoshi, I., Sakamoto, M., Yamaguchi, M., Mori, K., Kageyama, R., 2010. Essential roles of Notch signaling in maintenance of neural stem cells in developing and adult brains. J. Neurosci. 30, 3489–3498.

Imayoshi, I., Shimojo, H., Sakamoto, M., Ohtsuka, T., Kageyama, R., 2013. Genetic visualization of notch signaling in mammalian neurogenesis. Cell. Mol. Life Sci. 70, 2045–2057.

Ishii, H., 2015. Role of CdGAP / ARHGAP31 in Metabolism , and Functional Characterization of the CdGAP C-terminal Regulatory Region .

Isogai, S., Lawson, N.D., Torrealday, S., Horiguchi, M., Weinstein, B.M., 2003. Angiogenic network formation in the developing vertebrate trunk. Development 130, 5281–5290.

Isrie, M., Wuyts, W., Van Esch, H., Devriendt, K., 2014. Isolated terminal limb reduction defects: Extending the clinical spectrum of Adams-Oliver syndrome and ARHGAP31 mutations. Am. J. Med. Genet. Part A 164, 1576–1579.

Itoh, M., Kim, C.H., Palardy, G., Oda, T., Jiang, Y.J., Maust, D., Yeo, S.Y., Lorick, K., Wright, G.J., Ariza-McNaughton, L., Weismann, A.M., Lewis, J., Chandrasekharappa, S.C., Chitnis, A.B., 2003. Mind bomb is a ubiquitin ligase that is essential for efficient activation of notch signaling by delta. Dev. Cell 4, 67–82.

Jinek, M., Chylinski, K., Fonfara, I., Hauer, M., Doudna, J.A., Charpentier, E., 2012. A Programmable Dual-RNA–Guided DNA Endonuclease in Adaptive Bacterial Immunity. Science (80-.). 337, 816–822.

Jones, K.M., Silfvast-Kaiser, A., Leake, D.R., Diaz, L.Z., Levy, M.L., 2017. Adams–Oliver Syndrome Type 2 in Association with Compound Heterozygous DOCK6 Mutations. Pediatr. Dermatol. 34, e249–

e253.

Kalcheim, C., 2015. Epithelial–mesenchymal transitions during neural crest and somite development. J. Clin. Med. 5, 1–15.

Kamai, T., Tsujii, T., Arai, K., Takagi, K., Asami, H., Ito, Y., Oshima, H., 2003. Significant association of Rho/ROCK pathway with invasion and metastasis of bladder cancer. Clin. Cancer Res. 9, 2632–2641.

Kang, M.H., Oh, S.C., Lee, H.J., Kang, H.N., Kim, J.L., Kim, J.S., Yoo, Y.A., 2011. Metastatic function of BMP-2 in gastric cancer cells: The role of PI3K/AKT, MAPK, the NF-KB pathway, and MMP-9 expression. Exp. Cell Res. 317, 1746–1762.

Katoh, H., Negishi, M., 2003. RhoG activates Rac1 by direct interaction with the Dock180-binding protein Elmo. Nature 424, 461–464.

Katt, M.E., Placone, A.L., Wong, A.D., Xu, Z.S., Searson, P.C., 2016. In vitro tumor models: Advantages, disadvantages, variables, and selecting the right platform. Front. Bioeng. Biotechnol. 4.

Kaufman, R., Weiss, O., Sebbagh, M., Ravid, R., Gibbs-Bar, L., Yaniv, K., Inbal, A., 2015. Development and origins of Zebrafish ocular vasculature. BMC Dev. Biol. 15, 1–9.

Kesavan, G., Machate, A., Hans, S., Brand, M., 2020. Cell-fate plasticity, adhesion and cell sorting complementarily establish a sharp midbrain-hindbrain boundary. Development 147.

Kesavan, G., Sand, F.W., Greiner, T.U., Johansson, J.K., Kobberup, S., Wu, X., Brakebusch, C., Semb, H., 2009. Cdc42-Mediated Tubulogenesis Controls Cell Specification. Cell 139, 791–801.

Kim, K., Yang, D.K., Kim, S., Kang, H., 2015. MIR-142-3p Is a Regulator of the TGFβ-Mediated Vascular Smooth Muscle Cell Phenotype. J. Cell. Biochem. 116, 2325–2333.

Kim, W.Y., Wang, X., Wu, Y., Doble, B.W., Patel, S., Woodgett, J.R., Snider, W.D., 2009. GSK-3 is a master regulator of neural progenitor homeostasis. Nat. Neurosci. 12, 1390–1397.

Kimmel, C., Ballard, W.W., Kimmel, S.R., Ullmann, B., Schilling, T.F., 1995. Stages of Embryonic Development of the Zebrafish. Dev. Dyn. 3, 253–310.

Kirby, M.L., Waldo, K.L., 1995. Neural crest and cardiovascular patterning. Circ. Res. 77, 211–215.

Kochhan, E., Lenard, A., Ellertsdottir, E., Herwig, L., Affolter, M., Belting, H.G., Siekmann, A.F., 2013. Blood Flow Changes Coincide with Cellular Rearrangements during Blood Vessel Pruning in Zebrafish Embryos. PLoS One 8, 1–7.

Korzh, V., 2018. Development of brain ventricular system. Cell. Mol. Life Sci. 75, 375–383.

Krah, K., Mironov, V., Risau, W., Flamme, I., 1994. Induction of Vasculogenesis in Quail Blastodisc-Derived Embryoid Bodies. Dev. Biol. 164, 123–132.

Krebs, L.T., Shutter, J.R., Tanigaki, K., Honjo, T., Stark, K.L., Gridley, T., 2004. Haploinsufficient lethality and formation of arteriovenous malformations in Notch pathway mutants. Genes Dev. 18, 2469–2473.

Kroll, F., Powell, G.T., Ghosh, M., Gestri, G., Antinucci, P., Hearn, T.J., Tunbak, H., Lim, S., Dennis, H.W., Fernandez, J.M., Whitmore, D., Dreosti, E., Wilson, S.W., Hoffman, E.J., Rihel, J., 2021. A simple and effective f0 knockout method for rapid screening of behaviour and other complex phenotypes, eLife.

Krueger, J., Liu, D., Scholz, K., Zimmer, A., Shi, Y., Klein, C., Siekmann, A., Schulte-Merker, S., Cudmore, M., Ahmed, A., le Noble, F., 2011. Flt1 acts as a negative regulator of tip cell formation and branching morphogenesis in the zebrafish embryo. Development 138, 2111–2120.

Kubis, N., Levy, B.I., 2003a. Vasculogenesis and angiogenesis: Molecular and cellular controls: Part 1: Growth factors. Interv. Neuroradiol. 9, 227–237.

Kubis, N., Levy, B.I., 2003b. Vasculogenesis and angiogenesis: Molecular and cellular controls: Part 2: Interactions between cell and extracellular environment. Interv. Neuroradiol. 9, 239–248.

Kugler, E., Snodgrass, R., Bowley, G., Plant, K., Serbanovic-Canic, J., Hamilton, N., Evans, P.C., Chico, T., Armitage, P., 2021. The effect of absent blood flow on the zebrafish cerebral and trunk vasculature. Vasc. Biol. 3, 1–16.

Kühn, S., Erdmann, C., Kage, F., Block, J., Schwenkmezger, L., Steffen, A., Rottner, K., Geyer, M., 2015. The structure of FMNL2-Cdc42 yields insights into the mechanism of lamellipodia and filopodia formation. Nat. Commun. 6.

Kumar, A., Huh, T.L., Choe, J., Rhee, M., 2017. Rnf152 is essential for neurod expression and delta-notch signaling in the zebrafish embryos. Mol. Cells 40, 945–953.

Lai, E.C., 2002. Keeping a good pathway down: Transcriptional repression of Notch pathway target genes by CSL proteins. EMBO Rep. 3, 840–845.

Lamarche-Vane, N., Hall, A., 1998. CdGAP, a novel proline-rich GTPase-activating protein for Cdc42 and Rac. J. Biol. Chem. 273, 29172–29177.

Lavine, K.J., White, A.C., Park, C., Smith, C.S., Choi, K., Long, F., Hui, C.C., Ornitz, D.M., 2006. Fibroblast growth factor signals regulate a wave of Hedgehog activation that is essential for coronary vascular development. Genes Dev. 20, 1651–1666.

Lawson, N.D., Scheer, N., Pham, V.N., Kim, C.H., Chitnis, A.B., Campos-Ortega, J.A., Weinstein, B.M., 2001. Notch signaling is required for arterial-venous differentiation during embryonic vascular development. Development 128, 3675–3683.

Lawson, N.D., Vogel, A.M., Weinstein, B.M., 2002. Sonic hedgehog and vascular endothelial growth factor act upstream of the Notch pathway during arterial endothelial differentiation. Dev. Cell 3, 127–136.

Le Borgne, R., Bardin, A., Schweisguth, F., 2005. The roles of receptor and ligand endocytosis in regulating Notch signaling. Development 132, 1751–1762.

Le Douarin, N.M., Dupin, E., 2003. Multipotentiality of the neural crest. Curr. Opin. Genet. Dev. 13, 529–536.

Lehman, A., Stittrich, A.B., Glusman, G., Zong, Z., Li, H., Eydoux, P., Senger, C., Lyons, C., Roach, J.C., Patel, M., 2014. Diffuse angiopathy in Adams-Oliver syndrome associated with truncating DOCK6 mutations. Am. J. Med. Genet. Part A 164, 2656–2662.

Liang, X., Potter, J., Kumar, S., Ravinder, N., Chesnut, J.D., 2017. Enhanced CRISPR/Cas9-mediated precise genome editing by improved design and delivery of gRNA, Cas9 nuclease, and donor DNA. J. Biotechnol. 241, 136–146.

Lieber, T., Kidd, S., Young, M.W., 2002. Kuzbanian-mediated cleavage of Drosophila Notch. Genes Dev. 16, 209–221.

Lieschke, G.J., Oates, A.C., Paw, B.H., Thompson, M.A., Hall, N.E., Ward, A.C., Ho, R.K., Zon, L.I., Layton, J.E., 2002. Zebrafish SPI-1 (PU.1) marks a site of myeloid development independent of primitive erythropoiesis: Implications for axial patterning. Dev. Biol. 246, 274–295.

Lindsell, C.E., Boulter, J., DiSibio, G., Gossler, A., Weinmaster, G., 1996. Expression patterns of Jagged, Delta1, Notch1, Notch2, and Notch3 genes identify ligand-receptor pairs that may function in neural development. Mol. Cell. Neurosci. 8, 14–27.

Linnerz, T., Bertrand, J.Y., 2021. Dlc1 controls cardio-vascular development downstream of Vegfa/Kdrl/Nrp1 signaling in the zebrafish embryo. BioRxiv.

Lister, J.A., Robertson, C.P., Lepage, T., Johnson, S.L., Raible, D.W., 1999. Nacre Encodes a Zebrafish Microphthalmia-Related Protein That Regulates Neural-Crest-Derived Pigment Cell Fate. Development 126, 3757–3767.

Little, S.C., Mullins, M.C., 2004. Twisted gastrulation promotes BMP signaling in zebrafish dorsal-ventral axial patterning. Development 131, 5825–5835.

Liu, F., Walmsley, M., Rodaway, A., Patient, R., 2008. Fli1 Acts at the Top of the Transcriptional Network Driving Blood and Endothelial Development. Curr. Biol. 18, 1234–1240.

Lobov, I.B., Cheung, E., Wudali, R., Cao, J., Halasz, G., Wei, Y., Economides, A., Lin, H.C., Papadopoulos, N., Yancopoulos, G.D., Wiegand, S.J., 2011. The Dll4/notch pathway controls postangiogenic blood vessel remodeling and regression by modulating vasoconstriction and blood flow. Blood 117, 6728–6737.

Lowery, L.A., Sive, H., 2005. Initial formation of zebrafish brain ventricles occurs independently of circulation and requires the nagie oko and snakehead/atp1a1a.1 gene products. Development 132, 2057–2067.

Lu, S., Hu, M., Wang, Z., Liu, H., Kou, Y., Lyu, Z., Tian, J., 2020. Generation and application of the zebrafish heg1 mutant as a cardiovascular disease model. Biomolecules 10, 1–15.

Ma, L., Rohatgi, R., Kirschner, M.W., 1998. The Arp2/3 complex mediates actin polymerization induced by the small GTP-binding protein Cdc42. Proc. Natl. Acad. Sci. U. S. A. 95, 15362–15367.

Mack, C.P., 2011. Signaling mechanisms that regulate smooth muscle cell differentiation. Arterioscler. Thromb. Vasc. Biol. 31, 1495–1505.

Mack, N.A. and Georgiou, M., 2014. The interdependence of the Rho GTPases and apicobasal cell polarity. Small GTPases, 5, 973768.

Malik, M.N.H., Waqas, S.F.U.H., Zeitvogel, J., Cheng, J., Geffers, R., Gouda, Z.A.E., Elsaman, A.M., Radwan, A.R., Schefzyk, M., Braubach, P., Auber, B., Olmer, R., Müsken, M., Roesner, L.M., Gerold, G., Schuchardt, S., Merkert, S., Martin, U., Meissner, F., Werfel, T., Pessler, F., 2022. Congenital deficiency reveals critical role of ISG15 in skin homeostasis. J. Clin. Invest. 132.

Maniscalco, M., Zedda, A., Faraone, S., De Laurentiis, G., Verde, R., Molese, V., Lapiccirella, G., Sofia, M., 2005. Association of Adams-Oliver syndrome with pulmonary arterio-venous malformation in the same family: A further support to the vascular hypothesis. Am. J. Med. Genet. 136 A, 269–274.

Mao, Z., Bozzella, M., Seluanov, A., Gorbunova, V., 2008. Comparison of nonhomologous end joining and homologous recombination in human cells. DNA Repair (Amst). 7, 1765–1771.

Martin-Belmonte, F., Gassama, A., Datta, A., Yu, W., Rescher, U., Gerke, V., Mostov, K., 2007. PTEN-Mediated Apical Segregation of Phosphoinositides Controls Epithelial Morphogenesis through Cdc42. Cell 128, 383–397.

Marziano, C., Genet, G., Hirschi, K.K., 2021. Vascular endothelial cell specification in health and disease. Angiogenesis 24, 213–236.

McCormack, J.J., Bruche, S., Ouadda, A.B.D., Ishii, H., Lu, H., Garcia-Cattaneo, A., Chávez-Olórtegui, C., Lamarche-Vane, N., Braga, V.M.M., 2017. The scaffold protein Ajuba suppresses CdGAP activity in epithelia to maintain stable cell-cell contacts. Sci. Rep. 7, 1–14.

Meester, J.A.N., Southgate, L., Stittrich, A.B., Venselaar, H., Beekmans, S.J.A., Den Hollander, N., Bijlsma, E.K., Helderman-Van Den Enden, A., Verheij, J.B.G.M., Glusman, G., Roach, J.C., Lehman, A., Patel, M.S., De Vries, B.B.A., Ruivenkamp, C., Itin, P., Prescott, K., Clarke, S., Trembath, R., Zenker, M., Sukalo, M., Van Laer, L., Loeys, B., Wuyts, W., 2015. Heterozygous Loss-of-Function Mutations in DLL4 Cause Adams-Oliver Syndrome. Am. J. Hum. Genet. 97, 475–482.

Meester, J.A.N., Sukalo, M., Schröder, K.C., Schanze, D., Baynam, G., Borck, G., Bramswig, N.C., Duman, D., Gilbert-Dussardier, B., Holder-Espinasse, M., Itin, P., Johnson, D.S., Joss, S., Koillinen, H., McKenzie, F., Morton, J., Nelle, H., Reardon, W., Roll, C., Salih, M.A., Savarirayan, R., Scurr, I., Splitt, M., Thompson, E., Titheradge, H., Travers, C.P., Van Maldergem, L., Whiteford, M., Wieczorek, D., Vandeweyer, G., Trembath, R., Van Laer, L., Loeys, B.L., Zenker, M., Southgate, L., Wuyts, W., 2018. Elucidating the genetic architecture of Adams–Oliver syndrome in a large European cohort. Hum. Mutat. 39, 1246–1261.

Meyer, B.I., Williams, P.J., Hanif, A.M., Lenhart, P.D., Hubbard, G.B., Jain, N., 2020. Proliferative Retinopathy in a 13-Year-Old with Adams-Oliver Syndrome. Retin. Cases Brief Rep. Publish Ah.

Mikdache, A., Fontenas, L., Albadri, S., Revenu, C., Loisel-Duwattez, J., Lesport, E., Degerny, C., Del Bene, F., Tawk, M., 2020. Elmo1 function, linked to Rac1 activity, regulates peripheral neuronal numbers and myelination in zebrafish. Cell. Mol. Life Sci. 77, 161–177.

Miki, Y., Ono, K., Hata, S., Suzuki, T., Kumamoto, H., Sasano, H., 2012. The advantages of co-culture over mono cell culture in simulating in vivo environment. J. Steroid Biochem. Mol. Biol. 131, 68–75.

Minoux, M., Rijli, F.M., 2010. Molecular mechanisms of cranial neural crest cell migration and patterning in craniofacial development. Development 137, 2605–2621.

Miyamoto, Y., Torii, T., Yamamori, N., Ogata, T., Tanoue, A., Yamauchi, J., 2013. Akt and PP2A reciprocally regulate the guanine nucleotide exchange factor Dock6 to control axon growth of sensory neurons. Sci. Signal. 6, 1–13.

Miyamoto, Y., Yamauchi, J., Sanbe, A., Tanoue, A., 2007. Dock6, a Dock-C subfamily guanine nucleotide exchanger, has the dual specificity for Rac1 and Cdc42 and regulates neurite outgrowth. Exp. Cell Res. 313, 791–804.

Montero-Balaguer, M., Swirsding, K., Orsenigo, F., Cotelli, F., Mione, M., Dejana, E., 2009. Stable vascular connections and remodeling require full expression of VE-cadherin in zebrafish embryos. PLoS One 4.

Morris, J.K., Chomyk, A., Song, P., Parker, N., Deckard, S., Trapp, B.D., Pimplikar, S.W., Dutta, R., 2015. Decrease in levels of the evolutionarily conserved microRNA miR-124 affects oligodendrocyte numbers in Zebrafish, Danio rerio. Invertebr. Neurosci. 15, 1–7.

Mullins, R.D., 2000. How WASP-family proteins and the Arp2/3 complex convert intracellular signals into cytoskeletal structures. Current opinion in cell biology, 12, 91-96.

Nadif Kasri, N., Van Aelst, L., 2008. Rho-linked genes and neurological disorders. Pflugers Arch. Eur. J. Physiol. 455, 787–797.

Nagase, T., Nagase, M., Machida, M., Fujita, T., 2008. Hedgehog signalling in vascular development. Angiogenesis 11, 71–77.

Nasevicius, A., Larson, J., Ekker, S.G., 2000. Distinct requirements for zebrafish angiogenesis revealed by a VEGF-A morphant. Yeast 17, 294–301.

Nikolaou, N., Watanabe-Asaka, T., Gerety, S., Distel, M., Köster, R.W., Wilkinson, D.G., 2009. Lunatic fringe promotes the lateral inhibition of neurogenesis. Development 136, 2523–2533.

Norden, P.R., Kim, D.J., Barry, D.M., Cleaver, O.B., Davis, G.E., 2016. Cdc42 and k-ras control endothelial tubulogenesis through apical membrane and cytoskeletal polarization: Novel stimulatory roles for GTPase effectors, the small GTPases, Rac2 and Rap1b, and inhibitory influence of Arhgap31 and Rasa1. PLoS One 11, 1–27.

Okuda, K.S., Hogan, B.M., 2020. Endothelial Cell Dynamics in Vascular Development: Insights From Live-Imaging in Zebrafish. Front. Physiol. 11.

Ouadda, A.B.D., He, Y., Calabrese, V., Ishii, H., Chidiac, R., Gratton, J.P., Roux, P.P., Lamarche-Vane, N., 2018. CdGAP/ARHGAP31 is regulated by RSK phosphorylation and binding to 14-3-3β adaptor protein. Oncotarget 9, 11646–11664.

Outtandy, P., Russell, C., Kleta, R., Bockenhauer, D., 2019. Zebrafish as a model for kidney function and disease. Pediatr. Nephrol. 34, 751–762.

Papadopoulou, E., Sifakis, S., Raissaki, M., Germanakis, I., Kalmanti, M., 2008. Antenatal and postnatal evidence of periventricular leukomalacia as a further indication of vascular disruption in Adams-Oliver syndrome. Am. J. Med. Genet. Part A 146, 2545–2550.

Papasani, M.R., Robison, B.D., Hardy, R.W., Hill, R.A., 2006. Early developmental expression of two insulins in zebrafish (Danio rerio). Physiol. Genomics 27, 79–85.

Parlow, M.H., Bolender, D.L., Kokan-Moore, N.K., Lough, J., 1991. Localization of bFGF-like proteins as punctate inclusions in the preseptation myocardium of the chicken embryo. Dev. Biol. 146, 139–147.

Parri, M., Chiarugi, P., 2010. Rac and Rho GTPases in cancer cell motility control. Cell Commun. Signal. 8, 1–14.

Patan, S., 2000. Vasculogenesis and angiogenesis as mechanisms of vascular network formation, growth and remodeling. J. Neurooncol. 50, 1–15.

Patel-Hett, S., D'Amore, P.A., 2011. Signal transduction in vasculogenesis and developmental angiogenesis. Int. J. Dev. Biol. 55, 353–369.

Patel, M.S., Taylor, G.P., Bharya, S., Al-Sanna'a, N., Adatia, I., Chitayat, D., Lewis, M.E.S., Human, D.G., 2004. Abnormal pericyte recruitment as a cause for pulmonary hypertension in Adams-Oliver syndrome. Am. J. Med. Genet. 129 A, 294–299.

Payne, L.B., Zhao, H., James, C.C., Darden, J., McGuire, D., Taylor, S., Smyth, J.W., Chappell, J.C., 2019. The pericyte microenvironment during vascular development. Microcirculation 26, 1–11.

Pepicelli, C. V., Lewis, P.M., McMahon, A.P., 1998. Sonic hedgehog regulates branching morphogenesis in the mammalian lung. Curr. Biol. 8, 1083–1086.

Persson, A.B., Buschmann, I.R., 2011. Vascular Growth in Health and Disease. Front. Mol. Neurosci. 4, 1–15.

Pertz, O., Fritz, R.D., 2016. The dynamics of spatio-temporal Rho GTPase signaling: Formation of signaling patterns. F1000Research 5, 1–12.

Pfaffl, M.W., Tichopad, A., Prgomet, C., Neuvians, T.P., 2004. Determination of stable housekeeping genes , differentially regulated target genes and sample integrity : BestKeeper – Excel-based tool using pair-wise correlations 509–515.

Piazza, A.J., Blackston, D., Sola, A., 2004. A case of Adams-Oliver syndrome with associated brain and pulmonary involvement: Further evidence of vascular pathology? Am. J. Med. Genet. 130 A, 172–175.

Pisciotta, L., Capra, V., Accogli, A., Giacomini, T., Prato, G., Tavares, P., Pinto-Basto, J., Morana, G., Mancardi, M.M., 2018. Epileptic Encephalopathy in Adams–Oliver Syndrome Associated to a New DOCK6 Mutation: A Peculiar Behavioral Phenotype. Neuropediatrics 49, 217–221.

Pollitt, A.Y., Insall, R.H., 2009. WASP and SCAR/WAVE proteins: The drivers of actin assembly. J. Cell Sci. 122, 2575–2578.

Poole, T.J., Coffin, D.J., 1989. Vasculogenesis and angiogenesis: Two distinct morphogenetic mechanisms establish embryonic vascular pattern. J. Exp. Zool. 251, 224–231.

Poole, T.J., Finkelstein, E.B., Cox, C.M., 2001. The role of FGF and VEGF in angioblast induction and migration during vascular development. Dev. Dyn. 220, 1–17.

Proulx, K., Lu, A., Sumanas, S., 2010. Cranial vasculature in zebrafish forms by angioblast cluster-derived angiogenesis. Dev. Biol. 348, 34–46.

Pursglove, S.E., Mackay, J.P., 2005. CSL: A notch above the rest. Int. J. Biochem. Cell Biol. 37, 2472–2477.

Raggio, V., Dell'Oca, N., Simoes, C., Tapié, A., Medici, C., Costa, G., Rodriguez, S., Greif, G., Garrone, E., Rovella, M.L., Gonzalez, V., Halty, M., González, G., Shin, J.Y., Shin, S.Y., Kim, C., Seo, J.S., Graña, M., Naya, H., Spangenberg, L., 2021. Whole genome sequencing reveals a frameshift mutation and a large deletion in YY1AP1 in a girl with a panvascular artery disease. Hum. Genomics 15, 1–9.

Rajan, A.M., Ma, R.C., Kocha, K.M., Zhang, D.J., Huang, P., 2020. Dual function of perivascular fibroblasts in vascular stabilization in zebrafish, PLoS Genetics.

Ran, F.A., Hsu, P.D., Wright, J., Agarwala, V., Scott, D.A., Zhang, F., 2013. Genome engineering using the CRISPR-Cas9 system. Nat. Protoc. 8, 2281–2308.

Randi, A.M., Sperone, A., Dryden, N.H., Birdsey, G.M., 2009. Regulation of angiogenesis by ETS transcription factors. Biochem. Soc. Trans. 37, 1248–1253.

Rath, M., Spiegler, S., Strom, T.M., Trenkler, J., Kroisel, P.M., Felbor, U., 2019. Identification of pathogenic YY1AP1 splice variants in siblings with Grange syndrome by whole exome sequencing. Am. J. Med. Genet. Part A 179, 295–299.

Renfree, K.J., Dell, P.C., 2016. Distal Limb Defects and Aplasia Cutis: Adams–Oliver Syndrome. J. Hand Surg. Am. 41, e207–e210.

Riahi, R., Yang, Y., Zhang, D.D., Wong, P.K., 2012. Advances in wound-healing assays for probing collective cell migration. J. Lab. Autom. 17, 59–65.

Ridley, A.J., 2015. Rho GTPase signalling in cell migration. Curr. Opin. Cell Biol. 36, 103–112.

Salas-Vidal, E., Meijer, A.H., Cheng, X., Spaink, H.P., 2005. Genomic annotation and expression analysis of the zebrafish Rho small GTPase family during development and bacterial infection.

Genomics 86, 25–37.

Sastre, A.A., Montoro, M.L., Gálvez-Martín, P., Lacerda, H.M., Lucia, A., Llavero, F., Zugaza, J.L., 2020. Small gtpases of the ras and rho families switch on/off signaling pathways in neurodegenerative diseases. Int. J. Mol. Sci. 21, 1–23.

Sato, M., Yost, H.J., 2003. Cardiac neural crest contributes to cardiomyogenesis in zebrafish. Dev. Biol. 257, 127–139.

Schier, A.F., Neuhauss, S.C.F., Harvey, M., Malicki, J., Solnica-krezel, L., Stainier, D.Y.R., Zwartkruis, F., Abdelilah, S., Stemple, D.L., Rangini, Z., Yang, H., 1996. Mutations affecting the development of the embryonic zebrafish brain. Development 165-178m.

Schmidt, A., Brixius, K., Bloch, W., 2007. Endothelial precursor cell migration during vasculogenesis. Circ. Res. 101, 125–136.

Sedykh, I., Yoon, B., Roberson, L., Moskvin, O., Dewey, C.N., Grinblat, Y., 2017. Zebrafish zic2 controls formation of periocular neural crest and choroid fissure morphogenesis. Dev. Biol. 429, 92–104.

Semenza, G.L., 2007. Vasculogenesis, angiogenesis, and arteriogenesis: Mechanisms of blood vessel formation and remodeling. J. Cell. Biochem. 102, 840–847.

Shah, N.M., Groves, A.K., Anderson, D.J., 1996. Alternative neural crest cell fates are instructively promoted by TGFβ superfamily members. Cell 85, 331–343.

Shaheen, R., Aglan, M., Keppler-Noreuil, K., Faqeih, E., Ansari, S., Horton, K., Ashour, A., Zaki, M.S., Al-Zahrani, F., Cueto-González, A.M., Abdel-Salam, G., Temtamy, S., Alkuraya, F.S., 2013. Mutations in EOGT confirm the genetic heterogeneity of autosomal-recessive Adams-Oliver syndrome. Am. J. Hum. Genet. 92, 598–604.

Shaheen, R., Faqeih, E., Sunker, A., Morsy, H., Al-Sheddi, T., Shamseldin, H.E., Adly, N., Hashem, M., Alkuraya., F.S., 2011. Recessive mutations in DOCK6, Encoding the guanidine nucleotide exchange factor DOCK6, lead to abnormal actin cytoskeleton organization and Adams-Oliver syndrome. Am. J. Hum. Genet. 89, 328–333.

Shalaby, F., Ho, J., Stanford, W.L., Fischer, K.D., Schuh, A.C., Schwartz, L., Bernstein, A., Rossant, J., 1997. A requirement for Flk1 in primitive and definitive hematopoiesis and vasculogenesis. Cell 89, 981–990.

Shalaby, F., Rossant, J., Yamaguchi, T.P., Gertsenstein, M., Wu, X.-F., Breitman, M.L., Schuh, A.C., 1995. Failure of blood-island formation and vasculogenesis in Flk-1-deficient mice. Nature 376, 62–66.

Siekmann, A.F., Lawson, N.D., 2007a. Notch signalling and the regulation of angiogenesis. Cell Adh. Migr. 1, 104–105.

Siekmann, A.F., Lawson, N.D., 2007b. Notch signalling limits angiogenic cell behaviour in developing zebrafish arteries. Nature 445, 781–784.

Silva, G., Braga, A., Leitão, B., Mesquita, A., Reis, A., Duarte, C., Barbot, J., Silva, E.S., 2012. Adams-Oliver syndrome and portal hypertension: Fortuitous association or common mechanism? Am. J. Med. Genet. Part A 158 A, 648–651.

Siu, K.Y., Yu, M.K., Wu, X., Zong, M., Roth, M.G., Chan, H.C., Yu, S., 2011. The non-catalytic carboxyl-terminal domain of ARFGAP1 regulates actin cytoskeleton reorganization by antagonizing the activation of Rac1. PLoS One 6.

Six, E., Ndiaye, D., Laâbi, Y., Brou, C., Gupta-Rossi, N., Israël, A., Logeat, F., 2003. The Notch ligand

Delta1 is sequentially cleaved by an ADAM protease and γ-secretase. Proc. Natl. Acad. Sci. U. S. A. 100, 7638–7643.

Southgate, L., 2019. Current opinion in the molecular genetics of Adams-Oliver syndrome. Expert Opin. Orphan Drugs 7, 21–26.

Southgate, L., Machado, R.D., Snape, K.M., Primeau, M., Dafou, D., Ruddy, D.M., Branney, P.A., Fisher, M., Lee, G.J., Simpson, M.A., He, Y., Bradshaw, T.Y., Blaumeiser, B., Winship, W.S., Reardon, W., Maher, E.R., Fitzpatrick, D.R., Wuyts, W., Zenker, M., Lamarche-Vane, N., Trembath, R.C., 2011. Gain-of-function mutations of ARHGAP31, a Cdc42/Rac1 GTPase regulator, cause syndromic cutis aplasia and limb anomalies. Am. J. Hum. Genet. 88, 574–585.

Southgate, L., Sukalo, M., Karountzos, A.S.V., Taylor, E.J., Collinson, C.S., Ruddy, D., Snape, K.M., Dallapiccola, B., Tolmie, J.L., Joss, S., Brancati, F., Digilio, M.C., Graul-Neumann, L.M., Salviati, L., Coerdt, W., Jacquemin, E., Wuyts, W., Zenker, M., Machado, R.D., Trembath, R.C., 2015. Haploinsufficiency of the NOTCH1 Receptor as a Cause of Adams-Oliver Syndrome with Variable Cardiac Anomalies. Circ. Cardiovasc. Genet. 8, 572–581.

Srinivas, B.P., Woo, J., Leong, W.Y., Roy, S., 2007. A conserved molecular pathway mediates myoblast fusion in insects and vertebrates. Nat. Genet. 39, 781–786.

Stainier, D.Y.R., Raz, E., Lawson, N.D., Ekker, S.C., Burdine, R.D., Eisen, J.S., Ingham, P.W., Schulte-Merker, S., Yelon, D., Weinstein, B.M., Mullins, M.C., Wilson, S.W., Ramakrishnan, L., Amacher, S.L., Neuhauss, S.C.F., Meng, A., Mochizuki, N., Panula, P., Moens, C.B., 2017. Guidelines for morpholino use in zebrafish. PLoS Genet. 13, 6–10.

Stittrich, A.B., Lehman, A., Bodian, D.L., Ashworth, J., Zong, Z., Li, H., Lam, P., Khromykh, A., Iyer, R.K., Vockley, J.G., Baveja, R., Silva, E.S., Dixon, J., Leon, E.L., Solomon, B.D., Glusman, G., Niederhuber, J.E., Roach, J.C., Patel, M.S., 2014. Mutations in NOTCH1 Cause Adams-Oliver Syndrome. Am. J. Hum. Genet. 95, 275–284.

Stratman, A.N., Pezoa, S.A., Farrelly, O.M., Castranova, D., Dye, L.E., Butler, M.G., Sidik, H., Talbot, W.S., Weinstein, B.M., 2017. Interactions between mural cells and endothelial cells stabilize the developing zebrafish dorsal aorta. Dev. 144, 115–127.

Stump, G., Durrer, A., Klein, A.L., Lütolf, S., Suter, U., Taylor, V., 2002. Notch1 and its ligands Delta-like and Jagged are expressed and active in distinct cell populations in the postnatal mouse brain. Mech. Dev. 114, 153–159.

Sukalo, M., Tilsen, F., Kayserili, H., Müller, D., Tüysüz, B., Ruddy, D.M., Wakeling, E., Ørstavik, K.H., Snape, K.M., Trembath, R., De Smedt, M., van der Aa, N., Skalej, M., Mundlos, S., Wuyts, W., Southgate, L., Zenker, M., 2015. DOCK6 Mutations Are Responsible for a Distinct Autosomal-Recessive Variant of Adams-Oliver Syndrome Associated with Brain and Eye Anomalies. Hum. Mutat. 36, 593–598.

Summerton, J., Weller, D., 1997. Morpholino Antisense Oligomers: Design, Preparation, and Properties. Antisense Nucleic Acid Drug Dev. 187–195.

Suzuki, D., Yamada, A., Kamijo, R., 2013. The essential roles of the small GTPase Rac1 in limb development. J. Oral Biosci. 55, 116–121.

Swartz, E.N., Sanatani, S., Sandor, G.G.S., Schreiber, R.A., 1999. Vascular abnormalities in Adams-Oliver syndrome: Cause or effect? Am. J. Med. Genet. 82, 49–52.

Tachibana, M., Kiyokawa, E., Hara, S., Iemura, S. ichiro, Natsume, T., Manabe, T., Matsuda, M., 2009. Ankyrin repeat domain 28 (ANKRD28), a novel binding partner of DOCK180, promotes cell migration by regulating focal adhesion formation. Exp. Cell Res. 315, 863–876.

Tan, W., Palmby, T.R., Gavard, J., Amornphimoltham, P., Zheng, Y., Gui, J.S., 2008. An essential role for Rac1 in endothelial cell function and vascular development. FASEB J. 22, 1829–1838.

Tang, G., 2005. siRNA and miRNA: An insight into RISCs. Trends Biochem. Sci. 30, 106–114.

Tao, Z., Bu, S., Lu, F., 2021. Two AOS genes attributed to familial exudative vitreoretinopathy with microcephaly: Two case reports. Medicine (Baltimore). 100, e24633.

Tapon, N., Hall, A., 1997. Rho, Rac and Cdc42 GTPases regulate the organization of the actin cytoskeleton. Curr. Opin. Cell Biol. 9, 86–92.

Tcherkezian, J., Danek, E.I., Jenna, S., Triki, I., Lamarche-Vane, N., 2005. Extracellular Signal-Regulated Kinase 1 Interacts with and Phosphorylates CdGAP at an Important Regulatory Site. Mol. Cell. Biol. 25, 6314–6329.

Tcherkezian, J., Lamarche-Vane, N., 2007. Current knowledge of the large RhoGAP family of proteins. Biol. Cell 99, 67–86.

Tcherkezian, J., Triki, I., Stenne, R., Danek, E.I., Lamarche-Vane, N., 2006. The human orthologue of CdGAP is a phosphoprotein and a GTPase-activating protein for Cdc42 and Rac1 but not RhoA. Biol. Cell 98, 445–456.

Tessadori, F., Tsingos, E., Colizzi, E.S., Kruse, F., Van Den Brink, S.C., Van Den Boogaard, M., Christoffels, V.M., Merks, R.M.H., Bakkers, J., 2021. Twisting of the zebrafish heart tube during cardiac looping is a tbx5-dependent and tissue-intrinsic process. Elife 10, 1–34.

Tokunaga, A., Kohyama, J., Yoshida, T., Nakao, K., Sawamoto, K., Okano, H., 2004. Mapping spatio-temporal activation of Notch signaling during neurogenesis and gliogenesis in the developing mouse brain. J. Neurochem. 90, 142–154.

Toriello, H. V., Graff, R.G., Florentine, M.F., Lacina, S., Moore, W.D., 1988. Scalp and limb defects with cutis marmorata telangiectatica congenita: Adams-Oliver syndrome? Am. J. Med. Genet. 29, 269–276.

Van Aelst, L. and D'Souza-Schorey, C., 1997. Rho GTPases and signaling networks. Genes & development, 11, 2295-2322.

Van Buul, J.D., Geerts, D., Huveneers, S., 2014. Rho GAPs and GEFs: Controling switches in endothelial cell adhesion. Cell Adhes. Migr. 8, 108–124.

Verma, A., Bhattacharya, R., Remadevi, I., Li, K., Pramanik, K., Samant, G. V., Horswill, M., Chun, C.Z., Zhao, B., Wang, E., Miao, R.Q., Mukhopadhyay, D., Ramchandran, R., Wilkinson, G.A., 2010. Endothelial cell-specific chemotaxis receptor (ecscr) promotes angioblast migration during vasculogenesis and enhances VEGF receptor sensitivity. Blood 115, 4614–4622.

Verma, A., Prasad, K.N., Singh, A.K., Nyati, K.K., Gupta, R.K. and Paliwal, V.K., 2010. Evaluation of the MTT lymphocyte proliferation assay for the diagnosis of neurocysticercosis. Journal of microbiological methods, 81, 175-178.

Vestweber, D., 2008. VE-cadherin: The major endothelial adhesion molecule controlling cellular junctions and blood vessel formation. Arterioscler. Thromb. Vasc. Biol. 28, 223–232.

Vokes, S.A., Yatskievych, T.A., Heimark, R.L., McMahon, J., McMahon, A.P., Antin, P.B., Krieg, P.A., 2004. Hedgehog signaling is essential for endothelial tube formation during vasculogenesis. Development 131, 4371–4380.

Wakayama, Y., Fukuhara, S., Ando, K., Matsuda, M., Mochizuki, N., 2015. Cdc42 mediates Bmp - Induced sprouting angiogenesis through Fmnl3-driven assembly of endothelial filopodia in zebrafish. Dev. Cell 32, 109–122.

Wang, S., Watanabe, T., Matsuzawa, K., Katsumi, A., Kakeno, M., Matsui, T., Ye, F., Sato, K., Murase, K., Sugiyama, I., Kimura, K., Mizoguchi, A., Ginsberg, M.H., Collard, J.G., Kaibuchi, K., 2012. Tiam1 interaction with the PAR complex promotes talin-mediated Rac1 activation during polarized cell migration. J. Cell Biol. 199, 331–345.

Wang, Z., Wang, X., Guiyu Lou, Litao Qin, Shasha Bian, Tang, X., Hongjie Zhu, Shengran Wang, Bingtao Hao, Shixiu Liao, 2019. Novel compound heterozygous mutations of the DOCK6 gene in a familial case of Adams-Oliver syndrome 2. Gene 700, 65–69.

Waterman-Storer, C.M., Worthylake, R.A., Liu, B.P., Burridget, K., Salmon, E.D., 1999. Microtubule growth activates Rac1 to promote lamellipodial protrusion in fibroblasts. Nat. Cell Biol. 1, 45–50.

Weinstein, B.M., Stemple, D.L., Driever, W., Fishman, M.C., 1995. gridlock, a localized heritable vascular patterning defect in the zebrafish 1, 1143–1147.

White, A.C., Lavine, K.J., Ornitz, D.M., 2007. FGF9 and SHH regulate mesenchymal Vegfa expression and development of the pulmonary capillary network. Development 134, 3743–3752.

Whitfield, T.T., Riley, B.B., Chiang, M.Y., Phillips, B., 2002. Development of the zebrafish inner ear. Dev. Dyn. 223, 427–458.

Wormer, D.B., Davis, K.A., Henderson, J.H., Turner, C.E., 2014. The focal adhesion-localized CdGAP regulates matrix rigidity sensing and durotaxis. PLoS One 9.

Wu, R.S., Lam, I.I., Clay, H., Duong, D.N., Deo, R.C., Coughlin, S.R., 2018. A Rapid Method for Directed Gene Knockout for Screening in G0 Zebrafish. Dev. Cell 46, 112-125.e4.

Wu, X., Fleming, A., Ricketts, T., Pavel, M., Virgin, H., Menzies, F.M., Rubinsztein, D.C., 2016. Autophagy regulates Notch degradation and modulates stem cell development and neurogenesis. Nat. Commun. 7.

Wu, Y., Liang, D., Wang, Y., Bai, M., Tang, W., Bao, S., Yan, Z., Li, D., Li, J., 2013. Correction of a genetic disease in mouse via use of CRISPR-Cas9. Cell Stem Cell 13, 659–662.

Wu, Y.T., Yu, I.S., Tsai, K.J., Shih, C.Y., Hwang, S.M., Su, I.J., Chiang, P.M., 2015. Defining Minimum Essential Factors to Derive Highly Pure Human Endothelial Cells from iPS/ES Cells in an Animal Substance-Free System. Sci. Rep. 5, 1–9.

Wu, Z.Q., Rowe, R.G., Lim, K.C., Lin, Y., Willis, A., Tang, Y., Li, X.Y., Nor, J.E., Maillard, I., Weiss, S.J., 2014. A Snail1/Notch1 signalling axis controls embryonic vascular development. Nat. Commun. 5.

Xia, H., Mao, Q., Paulson, H.L., Davidson, B.L., 2002. Sirna-mediated gene silencing in vitro and in vivo. Nat. Biotechnol. 20, 1006–1010.

Xu, X., Meiler, S.E., Zhong, T.P., Mohideen, M., Crossley, D.A., Burggren, W.W., Fishman, M.C., 2002. Cardiomyopathy in zebrafish due to mutation in an alternatively spliced exon of titin. Nat. Genet. 30, 205–209.

Yang, J., Zhang, Z., Roe, S.M., Marshall, C.J., Barford, D., 2009. Activation of Rho GTPases by DOCK Exchange Factors Is Mediated by a Nucleotide Sensor 1398–1403.

Zennaro, C., Mariotti, M., Carraro, M., Pasqualetti, S., Corbelli, A., Armelloni, S., Li, M., Ikehata, M., Clai, M., Artero, M., Messa, P., Boscutti, G., Rastaldi, M.P., 2014. Podocyte developmental defects caused by adriamycin in zebrafish embryos and larvae: A novel model of glomerular damage. PLoS One 9.

Zhang, J.P., Li, X.L., Li, G.H., Chen, W., Arakaki, C., Botimer, G.D., Baylink, D., Zhang, L., Wen, W., Fu, Y.W., Xu, J., Chun, N., Yuan, W., Cheng, T., Zhang, X.B., 2017. Efficient precise knockin with a double cut HDR donor after CRISPR/Cas9-mediated double-stranded DNA cleavage. Genome Biol. 18, 1–18.

Zhang, Z.-Y., Sun, Y.-Y., Wang, H.-C., Fu, W.-N., Sun, C.-F., 2021. Overexpression of DOCK6 in oral squamous cell cancer promotes cellular migration and invasion and is associated with poor prognosis. Arch. Oral Biol. 133, 105297.

Zoughlami, Y., van Stalborgh, A.M., van Hennik, P.B., Hordijk, P.L., 2013. Nucleophosmin1 Is a Negative Regulator of the Small GTPase Rac1. PLoS One 8.

Appendix

Optimisation of qPCR protocols

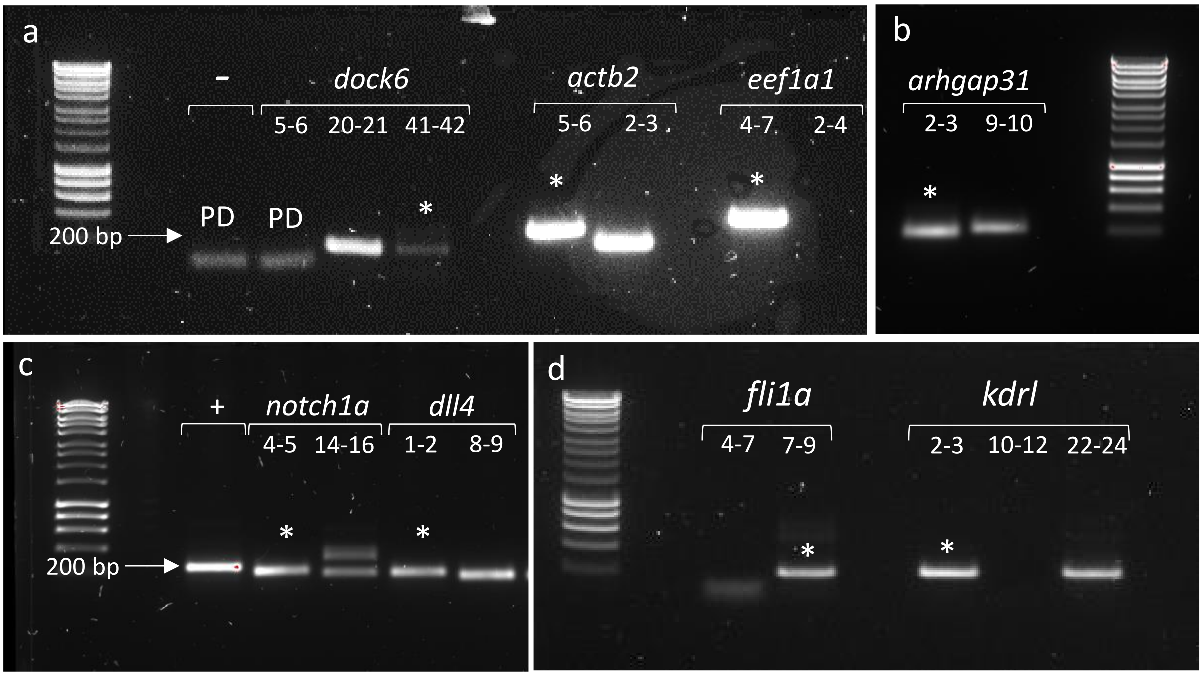

Figure 63: Optimisation of SYBR-based qPCR primers.

Gel electrophoresis of PCR products using SYBR-specific qPCR primers. Primers amplifiying regions of (**a**) *dock6*, *actb2*, *eef1a1*, (**b**) *arhgap31*, (c) *notch1a*, *dll4*, (d) *fli1a* and *kdrl* are shown. The numbers above each band describe the exonic region amplified by each primer pair. The bands chosen for use in SYBR-based qPCR experiments are indicated by an asterisk. PD denotes primer-dimer formation. A plus sign indicates a positive control. Meridian BioScience HyperLadder 1 Kb was used to determine the band sizes.

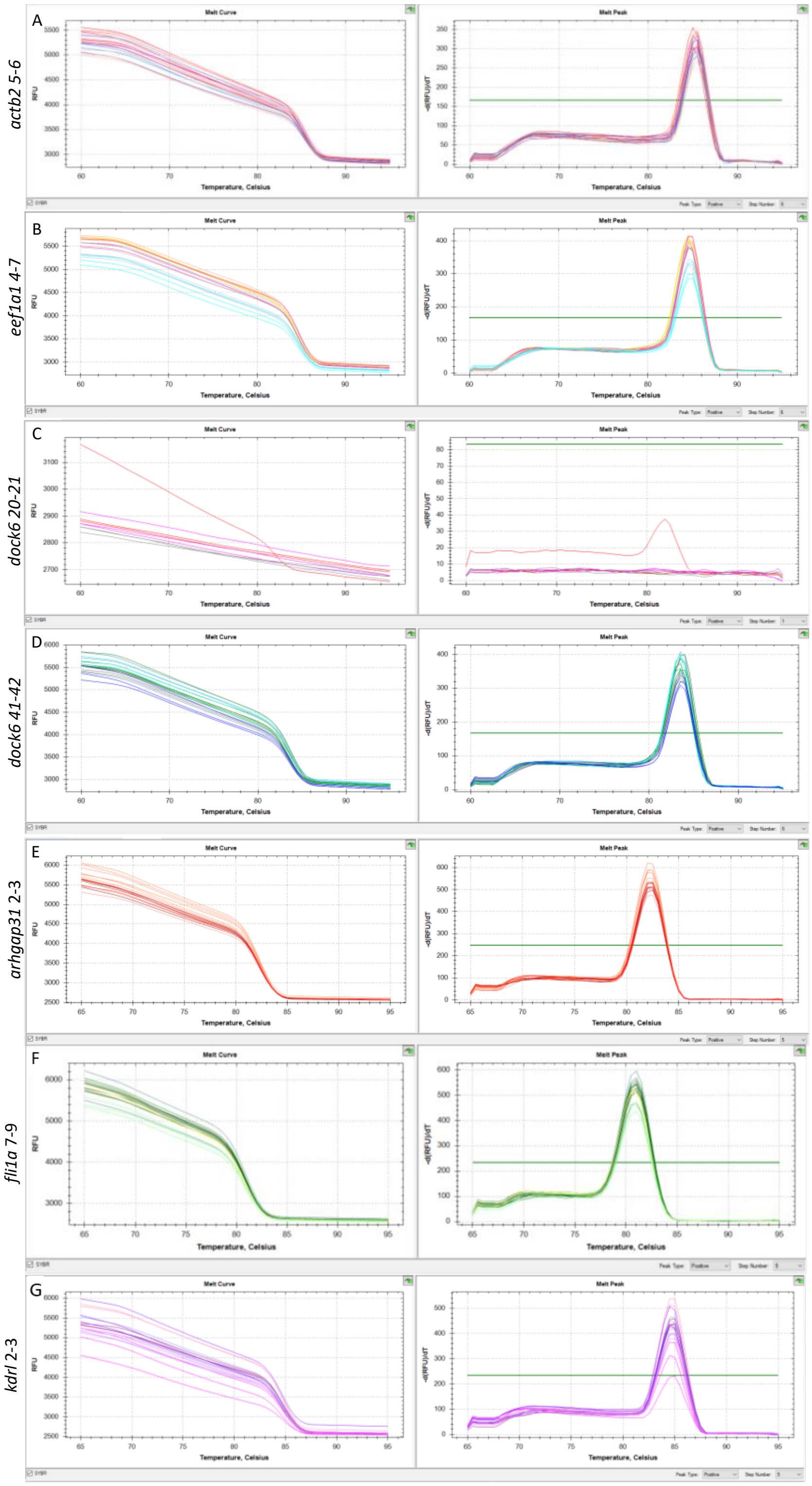

Figure 64: Melt curve analyses of qPCR primer pairs amplifying genes *actb2*, *eef1a1*, *dock6*, *arhgap31*, *fli1* and *kdrl*.

Panels **A, B** and **E** display the melt curves generated by primer pairs amplifying regions of genes *actb2*, *eef1a1* and *arhgap31*. Panels **C** and **D** show melt curve analyses of two primer pairs amplifying exonic regions 20-21 and 41-42, respectively, of *dock6*. The primer pair in **C** produced a poor melt curve, therefore the primers producing melt curve **D** were used to measure *dock6* transcript levels. **F** and **G** display the melt curves and peaks generated by primer pairs targeting exons 7-9 of *fli1* and 2-3 of *kdrl*, respectively.

A

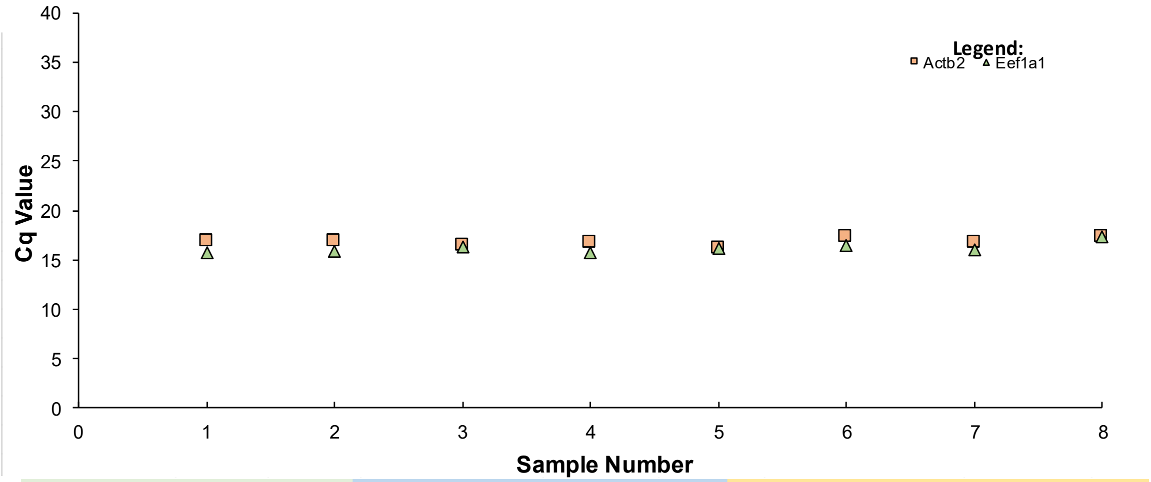

B

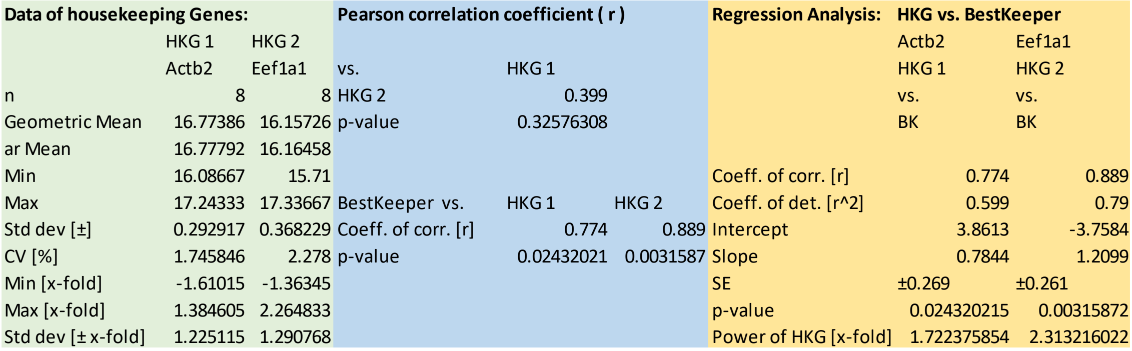

Data of housekeeping Genes:			Pearson correlation coefficient (r)			Regression Analysis:	HKG vs. BestKeeper	
	HKG 1	HKG 2					Actb2	Eef1a1
	Actb2	Eef1a1	vs.	HKG 1			HKG 1	HKG 2
n	8	8	HKG 2	0.399			vs.	vs.
Geometric Mean	16.77386	16.15726	p-value	0.32576308			BK	BK
ar Mean	16.77792	16.16458						
Min	16.08667	15.71				Coeff. of corr. [r]	0.774	0.889
Max	17.24333	17.33667	BestKeeper vs.	HKG 1	HKG 2	Coeff. of det. [r^2]	0.599	0.79
Std dev [±]	0.292917	0.368229	Coeff. of corr. [r]	0.774	0.889	Intercept	3.8613	-3.7584
CV [%]	1.745846	2.278	p-value	0.02432021	0.0031587	Slope	0.7844	1.2099
Min [x-fold]	-1.61015	-1.36345				SE	±0.269	±0.261
Max [x-fold]	1.384605	2.264833				p-value	0.024320215	0.00315872
Std dev [± x-fold]	1.225115	1.290768				Power of HKG [x-fold]	1.722375854	2.313216022

Figure 65: Stable mRNA expression of qPCR housekeeping genes *actb2* and *eef1a1*.

A. Graph displaying the C_q values of *actb2* and *eef1a1* collected from 8 cohorts of 50 embryos, from 14 hpf to 4 dpf. **B.** Table showing a summary of the statistical analyses performed on these C_q values using BestKeeper software.

Validation of *in situ* hybridisation probes

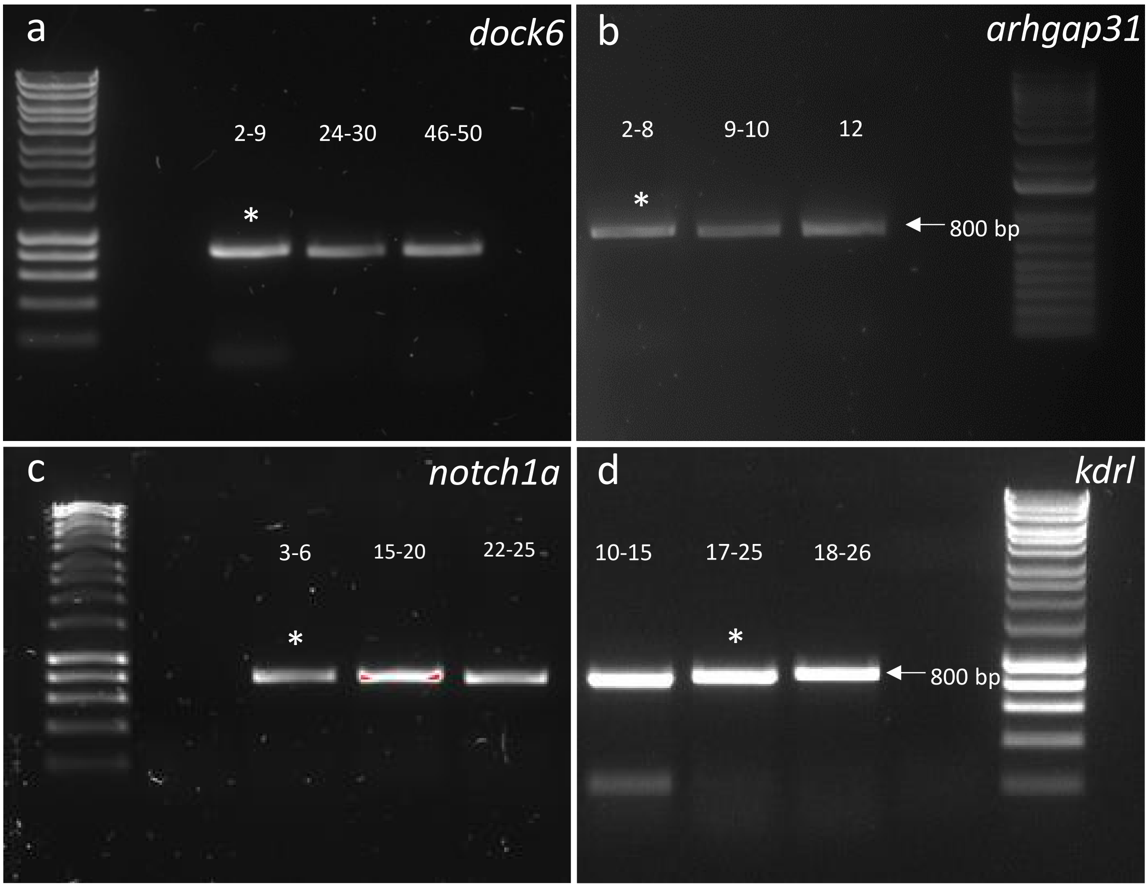

Figure 66: Amplification of *dock6*, *arhgap31*, *notch1a* and *kdrl in situ* hybridisation probes.

Gel electrophoresis of cDNA probe targets for each gene. The bands chosen for use as WISH probes are indicated by an asterisk. The numbers above each band describe the exonic region amplified by each primer pair. Meridian BioScience HyperLadder 1 Kb (**a, c, d**) and Invitrogen 1 Kb Plus DNA (**b**) ladders was used to determine the band sizes.

Visualisation of the zebrafish circulation in real-time

Movie 1: *dock6* knockdown impairs blood circulation at 72 hpf.

Representative movies of typical blood circulation in wild-type and *dock6* depleted zebrafish embryos are displayed. Movies can be accessed in a separate folder provided. Healthy blood circulation in the (**a**) wild-type (n=55) is demonstrated. Absent blood flow is observed in (**b**) *dock6*-E1 (17), (**c**) dock6-E2 (18) and (**d**) dock6-crispant (40) embryos.